

UC San Diego

UC San Diego Electronic Theses and Dissertations

Title

Heterogeneous chemistry of atmospheric organic acids and other organic compounds with oxide surfaces representative of mineral dust and indoor surfaces

Permalink

<https://escholarship.org/uc/item/4wn282rd>

Author

Fang, Yuan

Publication Date

2018

Peer reviewed|Thesis/dissertation

UNIVERSITY OF CALIFORNIA SAN DIEGO

**Heterogeneous chemistry of atmospheric organic acids and other organic
compounds with oxide surfaces representative of mineral dust and indoor surfaces**

A dissertation submitted in partial satisfaction of the
requirements for the degree
Doctor of Philosophy

in

Chemistry

by

Yuan Fang

Committee in charge:

Professor Vicki H. Grassian, Chair
Professor Francesco Paesani
Professor Jeffery Rinehart
Professor Donald Sirbuly
Professor Wei Xiong

Copyright

Yuan Fang, 2018

All rights reserved.

The dissertation of Yuan Fang is approved, and it is acceptable in quality and form for publication on microfilm and electronically:

Chair

University of California San Diego

2018

DEDICATION

To my parents.

TABLE OF CONTENTS

SIGNATURE PAGE	iii
DEDICATION	iv
TABLE OF CONTENTS.....	v
LIST OF FIGURES	ix
LIST OF TABLES	xv
LIST OF SCHEMES.....	xvii
ACKNOWLEDGMENTS	xviii
VITA.....	xxii
ABSTRACT OF THE DISSERTATION	xxiii
Chapter 1 INTRODUCTION.....	1
1.1 Atmospheric Aerosols.....	1
1.2 Mineral Dust Aerosols	3
1.3 Gases in the Atmosphere	5
1.3.1 Trace Gases of Interest.....	5
1.3.2 Water.....	9
1.4 Surface Chemistry of Indoor Air	11
1.4.1 Indoor Air.....	11
1.4.2 Indoor Surface Chemistry	13
1.4.3 Relevant Gas-Phase Molecules Present in Indoor Air	15
1.5 Thesis Objectives	17
1.6 References.....	20
Chapter 2 EXPERIMENTAL METHODS.....	28

2.1	Methods for Infrared Studies	28
2.1.1	Teflon Coated Fourier Transform Infrared (FTIR) Spectroscopy	28
2.1.2	Heated Infrared System.....	31
2.1.3	Transmission FTIR Spectroscopy: Photochemical Studies	32
2.1.4	Flowing Board and ATR-FTIR coupled System	33
2.1.5	Gas Phase Diffusion Measurements and Correction	36
2.2	Complementary Physicochemical Characterization Methods	37
2.2.1	Mass Spectroscopy (MS)	37
2.2.2	BET Surface Area Measurement	38
2.3	Chemicals.....	39
2.3.1	Particle Samples.....	39
2.3.2	Liquid and Gas Reagents	39
2.4	References.....	40

Chapter 3 COMPETITION BETWEEN SURFACE DISPLACEMENT AND

DISSOCIATIVE ADSORPTION OF A STRONG ACID COMPARED TO A WEAK

ACID ON SILICA PARTICLE SURFACES: THE ROLE OF ADSORBED WATER ..41

3.1	Abstract.....	41
3.2	Introduction.....	42
3.3	Experimental Section.....	44
3.4	Results and Discussion	46
3.4.1	Adsorption of HNO ₃ on silica.....	46
3.4.2	Adsorption of HCOOH on silica	55
3.4.3	Role of Adsorbed Water in Surface Displacement and Dissociation Reactions of Acids on Silica Surfaces	60
3.5	Conclusion	62
3.6	Acknowledgement	63
3.7	References.....	63

Chapter 4 HETEROGENEOUS REACTIONS OF ACETIC ACID WITH OXIDE

SURFACES: EFFECTS OF MINERALOGY AND RELATIVE HUMIDITY69

4.1	Abstract.....	69
4.2	Introduction.....	70
4.3	Experimental section.....	72
4.4	Results and Discussion	74
4.4.1	Heterogeneous reaction with γ -Al ₂ O ₃	75
4.4.2	Heterogeneous reaction with CaO	81
4.4.3	Heterogeneous uptake on SiO ₂	83
4.4.4	Discussion.....	86
4.5	Conclusion	87
4.6	Acknowledgement	88
4.7	Appendix.....	89

4.7.1	FTIR spectra (800-4000 cm ⁻¹) of γ -Al ₂ O ₃ , CaO, and SiO ₂ after interaction with acetic acid	89
4.7.2	Langmuir isotherm for acetic acid adsorption on silica particles	92
4.8	References.....	94
Chapter 5 HETEROGENEOUS INTERACTIONS BETWEEN GAS-PHASE PYRUVIC ACID AND HYDROXYLATED SILICA SURFACES: A COMBINED EXPERIMENTAL AND THEORETICAL STUDY		
		100
5.1	Abstract.....	100
5.2	Introduction.....	100
5.3	Methods.....	103
5.3.1	Experimental Setup.....	103
5.3.2	Theoretical Methods	104
5.4	Results and Discussion	105
5.4.1	Adsorption of Pyruvic Acid on SiO ₂ Surfaces.....	105
5.4.2	Theoretical Modeling.....	112
5.4.3	Curve fitting based on theoretical simulation	117
5.5	Conclusion	122
5.6	Acknowledgement	123
5.7	Reference	124
Chapter 6 SURFACE ADSORPTION AND HETEROGENEOUS PHOTOCHEMISTRY OF PYRUVIC ACID ON OXIDE SURFACES: AL ₂ O ₃ AND TiO ₂		
		130
6.1	Abstract.....	130
6.2	Introduction.....	131
6.3	Experimental Methods	134
6.4	Results and Discussion	137
6.4.1	Pyruvic acide adsorption on Al ₂ O ₃	137
6.4.2	Surface adsorption of pyruvic acid on TiO ₂	140
6.4.3	Photochemistry of Adsorbed Pyruvic Acid on Al ₂ O ₃ and TiO ₂	141
6.5	Conclusion	149
6.6	Acknowledgement	149
6.7	References.....	150
Chapter 7 UNDERSTANDING THE INTERACTION BETWEEN INDOOR AIR RELEVANT VOLATILE ORGANIC COMPOUNDS WITH SILICA SURFACES....		
		158
7.1	Abstract.....	158
7.2	Introduction.....	158
7.3	Experimental Section	161
7.4	Results and Discussion	163

7.4.1	Limonene Adsorption and Desorption Kinetics on Silica	163
7.4.2	Limonene Adsorption as a Function of RH	182
7.4.3	Adsorption and Desorption of Other Indoor Relevant Molecules	184
7.5	Conclusion and Implications for Indoor Air	187
7.6	Acknowledgement	188
7.7	References	188
Chapter 8 THE DRIVING FORCE BEHIND ADSORPTION OF HYDROPHOBIC		
MOLECULES ON HYDROPHILIC SURFACES		
		192
8.1	Abstract	192
8.2	Introduction	193
8.3	Methods	195
8.4	Results and Discussion	197
8.4.1	FTIR Studies and Ab Initio Molecular Dynamics Study for Limonene Adsorption on SiO ₂	197
8.4.2	Study of Other Cyclic Compounds on SiO ₂ using FTIR and MD	206
8.4.3	Study of Limonene Adsorption Using Flowing System	213
8.5	Conclusion	216
8.6	Acknowledgement	217
8.7	References	219
Chapter 9 CONCLUSION AND FUTURE WORK		
		222

LIST OF FIGURES

Figure 1.1. Schematic of the major processes contributing to atmospheric aerosols. Examples of the natural and anthropogenic processes producing gas and particles in the atmosphere are shown. Subsequent processes can transform and age these particles during their transportation through the atmosphere. From: Prather et al. (2008).	2
Figure 1.2. Mineral dust and its impact on local process including climate and ocean biogeochemical cycles. From: Usher et al. (2003).	5
Figure 1.3. Details of the photolysis mechanism for aqueous pyruvic acid. From: Griffith et al. (2013).	9
Figure 1.4. Schematic of complex interactions of mineral dust particles with atmospheric trace gases and water, as well as impacts on cloud formation. Reactions involved are defined as follows: Chemical aging of mineral dust aerosol particles due to reactions with trace gases (R1).....	11
Figure 1.5. Major reactants, products and reaction pathways of indoor chemistry. From: Morrison et al. (2015).	13
Figure 2.1. Schematic of the Teflon coated transmission FTIR experimental setup. (a) Tungsten grid held by the Teflon coated sample holder with half of the grid covered by the surface sample. (b) Transmission FTIR spectrometer with FTIR cell mounted inside, glass mixing chamber and evacuation system.	30
Figure 2.2. Schematic of the stainless-steel transmission FTIR heated sample holder connected to the temperature controller and heater power supply.	32
Figure 2.3. Schematic of the optical light path from the Hg arc lamp to the FTIR cell mounted inside the FTIR spectrometer. The sample was irradiated for the desired time, followed by collection of surface and gas phase spectra.	33
Figure 2.4. Schematic of the flow system which allows for measurements using the Quartz Crystal Microbalance (QCM) and the ATR – FTIR spectrometer simultaneously. Note that only the ATR – FTIR portion was used in the dissertation research. (Adapt from Schuttlefield et al. (2007))	35
Figure 3.1. (a) A typical FTIR spectrum (1200 to 4000 cm^{-1}) of silica particles after exposure to 100 mTorr $\text{HNO}_3(\text{g})$ under dry condition. (b) FTIR spectra (1200 to 1800 cm^{-1}) of silica particles after exposure to 100 mTorr $\text{HNO}_3(\text{g})$ at different RH.	46
Figure 3.2. Peak areas of infrared absorption bands for $\text{H}_2\text{O}(\text{a})$ (1627 cm^{-1} , open squares) and $\text{HNO}_3(\text{a})$ (1315 cm^{-1} , open circles) on silica as a function of RH, after exposure to 100	

mTorr HNO ₃ (g). For comparison H ₂ O(a) (solid squares) in the absence of HNO ₃ (a) is plotted as a function of RH.	48
Figure 3.3. Peak fitting results of IR absorption in the range of (a) 1550 to 1800 cm ⁻¹ and (b) 1250 to 1550 cm ⁻¹ for silica particles after exposure to 100 mTorr HNO ₃ (g) at 10% RH. These bands correspond to multiple species present on the surface.	50
Figure 3.4. FTIR spectra (between 1550 and 1750 cm ⁻¹) of silica particles after exposure to HNO ₃ (g) of different pressure at 10% RH.	51
Figure 3.5. Intensities (represented by peak area) of IR absorption peaks at 1627 cm ⁻¹ for H ₂ O(a) (open squares), 1315 cm ⁻¹ for HNO ₃ (a) (open triangles), and 1727 cm ⁻¹ for H ₃ O ⁺ (a) (open circles) as a function of HNO ₃ (g) pressure at 10% RH. For comparison HNO ₃ (a) (solid triangles) at dry conditions is also plotted as a function of HNO ₃ (g) pressure.	53
Figure 3.6. (a) FTIR spectrum of silica particles in the presence of 100 mTorr HCOOH(g) under dry conditions. The spectral range between 1200 and 4000 cm ⁻¹ is shown. (b) FTIR spectra in the spectral range from 1500 to 1850 cm ⁻¹ after exposure to 100 mTorr HCOOH(g) at different RH.	56
Figure 3.7. IR peak intensities (represented as peak areas) for H ₂ O(a) (1627 cm ⁻¹ , open square) and HCOOH(a) (1724 cm ⁻¹ , open circle) on silica surface as a function of RH, after exposure to 100 mTorr HCOOH(g). For comparison adsorbed water, H ₂ O(a) (solid square), in the absence of HCOOH(g) is also plotted as a function of RH.	57
Figure 3.8. (a) FTIR spectra (1500-1850 cm ⁻¹) of silica particles after exposure to HCOOH(g) of different pressure at 10% RH. (b) Intensities (represented by peak areas) of IR absorption bands for H ₂ O(a) (1627 cm ⁻¹ , open squares) and HCOOH(a) (1724 cm ⁻¹ , open triangles) on silica particles at 10% RH, as a function of HCOOH(g) pressure.	59
Figure 4.1. FTIR spectra (shown above from 1600 to 1900 cm ⁻¹) of CH ₃ COOH(g) as a function of pressure (5, 55, and 117 mTorr) at 296 K.	75
Figure 4.2. FTIR spectra (900-1900 cm ⁻¹) of γ-Al ₂ O ₃ after reaction with CH ₃ COOH(g) under dry conditions. (a) Spectra of γ-Al ₂ O ₃ after reaction with 27, 79, 293, and 1190 mTorr CH ₃ COOH(g). (b) A typical spectrum of reacted γ-Al ₂ O ₃ after evacuation of the reaction cell.	76
Figure 4.3. FTIR spectra (900-1900 cm ⁻¹) of CaO after reaction with CH ₃ COOH(g) under dry conditions. (a) Spectra of CaO after reaction with 25, 82, 298, and 1175 mTorr CH ₃ COOH(g). (b) A typical spectrum of reacted CaO after evacuation of the reaction cell.	82
Figure 4.4. FTIR spectra (900-1900 cm ⁻¹) of SiO ₂ after interaction with CH ₃ COOH(g) with pressure of 5, 21, 55, and 117 mTorr in the gas phase under dry conditions. Please note that SiO ₂ is opaque below 1250 cm ⁻¹	84

Figure 4.5. FTIR spectra (1500-1800 cm^{-1}) of SiO_2 after exposure to $\text{CH}_3\text{COOH}(\text{g})$ of 5 mTorr in the gas phase at different RH.....	85
Figure 4.6. FTIR spectra (800-4000 cm^{-1}) of $\gamma\text{-Al}_2\text{O}_3$ after reaction with $\text{CH}_3\text{COOH}(\text{g})$ under dry conditions. (a) Spectra of $\gamma\text{-Al}_2\text{O}_3$ after reaction with 27, 79, 293, and 1190 mTorr $\text{CH}_3\text{COOH}(\text{g})$. (b) A typical spectrum of reacted $\gamma\text{-Al}_2\text{O}_3$ after evacuation of the reaction cell.....	89
Figure 4.7. FTIR spectra (800-4000 cm^{-1}) of CaO after reaction with $\text{CH}_3\text{COOH}(\text{g})$ under dry conditions. (a) Spectra of CaO after reaction with 25, 82, 298, and 1175 mTorr $\text{CH}_3\text{COOH}(\text{g})$. (b) A typical spectrum of reacted CaO after evacuation of the reaction cell.....	90
Figure 4.8. FTIR spectra (800-4000 cm^{-1}) of SiO_2 after exposure to $\text{CH}_3\text{COOH}(\text{g})$ with pressure of 5, 21, 55, and 117 mTorr in the gas phase under dry conditions. Please note that SiO_2 is opaque below 1250 cm^{-1}	91
Figure 4.9. Plotting of P/N as a function of $\text{CH}_3\text{COOH}(\text{g})$ pressure (P) for SiO_2 under dry conditions.....	92
Figure 5.1. Conformers of pyruvic acid. (a) Tc and (b) Tt conformer.	101
Figure 5.2. FTIR spectrum of gas-phase pyruvic acid in the spectral range of 800 to 4000 cm^{-1} and inset from 1650 to 1900 cm^{-1} . The small shoulder observed in the inset (at 1760 cm^{-1} , shown in red) corresponds to the non-hydrogen bonded Tt conformer.....	106
Figure 5.3. (a) Absorbance spectra (1280 to 4000 cm^{-1}) of pyruvic acid adsorbed on silica under dry conditions (RH < 1%). Note that SiO_2 is opaque below 1280 cm^{-1} due to lattice vibrations. Spectral subtraction was performed using gas-phase absorption spectra. Shown as a dashed line (- - -) is the surface spectrum following overnight evacuation.....	108
Figure 5.4. Absorbance spectra (1280 to 1900 cm^{-1}) of silica particles after first exposure to 100 mTorr pyruvic acid and then water vapor as a function of relative humidity (RH). The dashed line (- - -) indicates the surface adsorbed species disappear after evacuation of both water and pyruvic acid.....	110
Figure 5.5. Normalized intensity (peak height at 1737 cm^{-1}) of 10, 50, 100 mTorr pyruvic acid adsorbed on the silica surface as a function of RH (< 1%, 5%, 10%, 15% and 20%).	111
Figure 5.6. (a) – (c) Tc conformer interacting with silica surface from geometry optimization: the lowest three energy minima. (d) – (e) The two lowest energy minima of Tt conformer interacting with silica surface. (From Dr. Dominika Lesnicki).....	115
Figure 5.7. Interaction between Tt-Ct pyruvic acid dimer on silica surface from (a) top and (b) side view. (From Dr. Dominika Lesnicki)	116

Figure 5.8. Pyruvic acid (a) Tc and (b) Tt conformer interacting with wet silica surface through a water bridge (dark blue). (From Dr. Dominika Lesnicki)	117
Figure 5.9. (a) Absorbance spectra (1550 – 1900 cm^{-1}) after peak fitting, for SiO_2 particles following exposure to 100 mTorr pyruvic acid ($\text{RH} < 1\%$). Absorbance bands correspond to C=O stretching of multiple species present on the surface, including: adsorbed pyruvic acid Tc conformer C=O acid stretch (1756 cm^{-1}).	119
Figure 5.10. Absorbance spectra (1500 – 1900 cm^{-1}) after peak fitting, for SiO_2 particles following exposure to 100 mTorr pyruvic acid ($\text{RH} = 50\%$). Absorbance bands correspond to C=O stretching of multiple species present on the surface, including: the adsorbed pyruvic acid Tc conformer (1756 cm^{-1}); Tt conformer (1736 cm^{-1}).	122
Figure 6.1. FTIR spectra of (a) Al_2O_3 following exposure to pyruvic acid for 20 minutes under dry conditions as a function of pyruvic acid pressure (5, 10, 20, 50, 100, 634, 856 and 1124 mTorr) in the spectral range of 850 to 4000 cm^{-1} and (b) 20 mTorr Al_2O_3 adsorption as a function of time in the spectral range of 900 to 1950 cm^{-1}	138
Figure 6.2. (a) FTIR spectra (800 to 4000 cm^{-1}) of TiO_2 following exposure to pyruvic acid under dry conditions as a function of pressure (10, 30, 75, 190, 310 and 625 mTorr). Each spectrum was taken 20 minutes after introduction of each pressure.	140
Figure 6.3. FTIR difference spectra (950 – 1900 cm^{-1}) of 100 mTorr adsorbed pyruvic acid on the (a) Al_2O_3 and (b) TiO_2 surface, respectively, as a function of irradiation time. Difference spectra were obtained by subtracting the spectrum taken prior to irradiation.	142
Figure 7.1. FTIR spectrum of gas phase limonene (1.6 Torr) from 800 to 4000 cm^{-1}	164
Figure 7.2. Absorbance spectra of limonene adsorbed on silica under dry conditions ($\text{RH} < 1\%$) as a function of limonene pressure (1, 5, 10, 25, 50, 100, 200, 500 and 1000 mTorr) in the 1280 ~ 4000 cm^{-1} spectral regions. Note that SiO_2 is opaque below 1280 cm^{-1} due to lattice vibrations.	165
Figure 7.3. Temporal evolution of (a) 25 mTorr (3 replicates) limonene on silica. Gas-phase contribution has been subtracted.	167
Figure 7.4. [P/N] versus pressure for limonene adsorbed on silica using integrated peak area from 2785 to 3115 cm^{-1}	172
Figure 7.5. Temporal evolution of limonene (16 mTorr) adsorption and desorption for the following temperatures: 298, 300.5, 303, 305.5, 308 K ($\pm 1\text{K}$).	173
Figure 7.6. Schematic of the K2-SURF model for adsorption and desorption of limonene to a silica surface. The subscripts ‘ads’ and ‘gs’ represent adsorbed molecules and near surface gas-phase molecules, respectively. (From Dr. Pascale Lakey)	175

Figure 7.7. (a) Example of experimental kinetics data (×) at 3 different pressures (8, 16 and 25 mTorr, triplicate measurements) fitted with K2–SURF model (—). (Fitted curve from Dr. Pascale Lakey)	176
Figure 7.8. Adsorbed limonene concentrations on silica as a function of time at an equilibrium pressure of 16 mTorr and at five different temperatures (a) 298 K, (b) 300.5 K, (c) 303 K, (d) 305.5 K and (e) 308 K. (From Dr. Pascale Lakey)	181
Figure 7.9. FTIR spectra (a) 2400 to 4000 cm ⁻¹ and (b) 1250 to 1800 cm ⁻¹ for silica particles following initial exposure to 100 mTorr limonene, then water vapor at varying RH (5%, 10%, 20%, 35%, 50% and 75% RH).	182
Figure 7.10. FTIR spectra over the spectral range (a) 2600 to 4000 cm ⁻¹ and (b) 1250 to 1850 cm ⁻¹ for silica particles following exposure to 100 mTorr carvone, then evacuation.	183
Figure 7.11. Absorbance spectra of dihydromyrcenol adsorbed on silica under dry conditions (RH < 1 %) as a function of dihydromyrcenol pressure (16, 34, 100 and 150 mTorr) in the 1280 ~ 4000 cm ⁻¹ spectral regions. The surface spectrum following evacuation is shown as a dashed line (---).	185
Figure 7.12. Temporal evolution of (a) 34 mTorr and (b) 150 mTorr dihydromyrcenol on silica. Gas-phase contribution has been subtracted.....	186
Figure 8.1. Absorbance spectra of 1000 mTorr limonene in gas phase (—) and adsorbed (—) on silica under dry conditions (RH < 1%) in the 1280 to 4000 cm ⁻¹ spectral region. Gas-phase limonene has been subtracted from adsorbed limonene spectra.	199
Figure 8.2. Baseline-corrected FTIR spectra displaying the loss of surface hydroxyl groups (at 3742 cm ⁻¹) as a function of coverage. The broad band from 3200 to 3700 cm ⁻¹ , which is assigned to the OH stretching mode of hydrogen bonding, also shifts with increasing coverage.	202
Figure 8.3. Interaction between limonene and hydroxyl groups on the silica surface. (a) Chiral carbon points down, forming 1 hydrogen bond. (b) Chiral carbon points up, forming 2 hydrogen bonds. Si (●), O (●), H (○), non-chiral C (●) and chiral C (●).(From Saleh Riahi).....	203
Figure 8.4. Simulated vibrational frequency, ω (cm ⁻¹) for the interaction of limonene with surface hydroxyl groups via 1 (—) or 2 (---) hydrogen bonds. (From Saleh Riahi).....	204
Figure 8.5. Peak fitting results for experimental FTIR spectra in the 3000 – 4000 cm ⁻¹ spectral region, with 13% of the silica surface covered with limonene (based on theoretical calculated vibrational frequencies and assignments).	205
Figure 8.6. Force field MD simulations of (a) enthalpy and (b) free energy of desorption of organic molecules from the silica surface. (From Saleh Riahi).....	207

Figure 8.7. Radical distribution functions (RDFs) of hydrogen atoms on the silica surface and the carbon atoms on the organic molecules (benzene (—): center of the ring; limonene (1HB (—) and 2HB (—)) and cyclohexene (—): C=C atoms; cyclohexane (—): all carbon atoms) calculated by ab initio (DFT) MD simulations. (From Saleh Riahi) 208

Figure 8.8. Graphical representation of (a) cyclohexane, (b) benzene, and (c) cyclohexene on the silica surface. Si (●), O (●), H (○), C (double bond from cyclohexene, ●) and C (●). Hydrogen bonding between organic molecules and the silica surface is represented by (---). (From Saleh Riahi) 210

Figure 8.9. FTIR spectra of: (a) cyclohexane (3000 to 4000 cm^{-1}); (b) benzene (3200 to 4000 cm^{-1}); and (c) cyclohexene (3080 to 4000 cm^{-1}). (From Saleh Riahi) 211

Figure 8.10. Normalized peak area of surface hydroxyl group (integrated using peak centered at 3745 cm^{-1}) loss as a function of pressure for the adsorption of the cyclic molecules of interest on the silica surface: (a) cyclohexane; (b) benzene; and (c) cyclohexene..... 213

Figure 8.11. ATR-FTIR spectra for limonene adsorption (—) and desorption (---) on SiO_2 in the spectral range of 1280 – 4000 cm^{-1} 214

Figure 8.12. ATR-FTIR spectra for limonene adsorption (—) and desorption (---) on (a) TiO_2 and (b) $\text{CaSO}_4 \cdot 2\text{H}_2\text{O}$ 215

LIST OF TABLES

Table 1.1. Abundance of Major Oxides found in the Continental Crust. From: Usher et al. (2003).....	4
Table 4.1. Vibrational mode assignments for species formed on the surfaces of γ -Al ₂ O ₃ , SiO ₂ , and CaO after heterogeneous interactions with CH ₃ COOH(g).....	77
Table 4.2. Uptake coefficients of CH ₃ COOH(g) on γ -Al ₂ O ₃ particles at different acetic acid pressure and RH.....	81
Table 5.1. Vibrational mode assignment for pyruvic acid (PA), CH ₃ COCOOH(g) and adsorbed species on SiO ₂ particle surfaces.....	109
Table 5.2. Calculated binding energies of different pyruvic acid species on hydroxylated silica. (From Dr. Dominika Lesnicki).....	114
Table 5.3. Calculated vibrational frequencies of different adsorbed pyruvic acid species. (Adapted from Dr. Dominika Lesnicki).....	114
Table 6.1. Vibrational mode assignments for species formed on the surface of Al ₂ O ₃ and TiO ₂ , respectively, following heterogeneous interaction with pyruvic acid.....	137
Table 6.2. Selected Compiled Photochemistry HRMS Data of Adsorbed Pyruvic Acid on Al ₂ O ₃ . (From Michael Alves).....	143
Table 6.3. Selected Compiled Photochemistry HRMS Data of Adsorbed Pyruvic Acid on TiO ₂ . (From Michael Alves).....	144
Table 7.1. Vibrational mode assignment for limonene and adsorbed species on SiO ₂ particle surfaces.	166
Table 7.2. Calculated coverages of limonene on silica for different pressures using volumetric measurements.	170
Table 7.3. Parameters used in the K2-SURF model. (From Dr. Pascale Lakey).....	179
Table 8.1. Vibrational mode assignment for limonene, cyclohexane, benzene and cyclohexene on SiO ₂ particle surfaces.....	200
Table 8.2. Vibrational mode assignment for limonene on SiO ₂ particle surfaces. (From Saleh Riahi).....	206
Table 8.3. Vibrational mode assignments for limonene adsorption on SiO ₂ , TiO ₂ and CaSO ₄ ·2H ₂ O, respectively using the flowing system coupled with ATR-FTIR.	216

Table 8.4. Summary of ATR-FTIR studies of limonene adsorption on various surfaces conducted herein. 216

LIST OF SCHEMES

Scheme 6.1. Pyruvic acid dimerized to form parapyruvic acid and zymonic acid. (Adapted from Perkins et al (2016)).	145
--	-----

ACKNOWLEDGMENTS

First and foremost, I would like to thank my research advisor, Dr Vicki Grassian. She has a wide knowledge of heterogeneous reactions and surface chemistry. I am grateful that she gave me the opportunity to work with her and be her student. During my Ph.D. study, I have gradually expanded my horizon, deepened my understanding of chemistry and learned to think critically and work independently through her help. Vicki encouraged me to take on the challenge and work on several projects at the same time. Whenever I needed help, I always knew that she would be around to help me. Without her, none of the works presented in this dissertation study would be possible. Additionally, I am willing to thank her for providing me with the opportunity to work with other researchers in the field.

I appreciate the help, support and advice from my committee members, Professor Francesco Paesani, Professor Jeffrey Rinehart, Professor Donald Sirbuly and Professor Wei Xiong.

I would like to thank Professor Jianjun Cheng from University of Illinois Urbana-Champaign. You encouraged me to become a scientist and helped me with applying for graduate school in the United States.

A couple members (past and present) of the Grassian research group deserve recognition. I would like to thank Dr. Aruni Gankanda for being patient with me during my first year in the lab explaining how every system works and how to troubleshoot the system. You guided me through the vacuum system step by step, shared your experience with me and help me with the data collection and analysis.

I would like to thank Dr. Mingjin Tang, who worked with me to overcome the difficulties during experiments. I truly appreciate the way you taught me by not giving the direct answer to my questions but rather explaining how to get the answer on my own. You were always ready to talk when I needed someone to talk to. Even now, you are busy professor far in China, you still have time to talk and guide me through the hard times I met in my life.

I would like to thank Dr. Mona Shrestha who worked with me on the indoor air project. We rebuilt the flowing system together and customized the Telfon flowing cell as needed. I enjoyed all my discussions with you and we brought up a lot of good ideas.

I would like to thank Dr. Kristin Wall for improving my writing skills through revising my manuscripts. I also appreciate all the help and the suggestions you gave me.

I would like to thank all my former and current group members. It was a pleasure to work with all and each of you during these years. I would like to especially thank Dr. Armando Estillore and Dr. Olga Laskina who helped me practice and get through my comprehensive exams. I would like to thank Dr. Liubin Huang for all our discussions about heterogeneous reactions. I would like to thank Michael Alves for mass spectrometry analysis and Haibin Wu for helping me with BET analysis. I would like to thank Andrew McDonald, my first mentee, for doing a wonderful job in the lab.

I would like to thank Dr. Grassian for making me a member of the Indoor Air project and providing me with the opportunity to collaborate with other researchers, especially the theoretical calculation groups. My understanding of surface heterogeneous chemistry has been elevated by working with them.

I would like to thank all Indoor Air collaborators: Dr. Pascal Lakey (Professor Manabu Shiraiwa group from UC Irvine) and Saleh Riahi (Professor Douglas Tobias group from UC Irvine). We worked together on the Indoor Air project for kinetics and simulation studies.

I also would like to thank my other collaborators: Dr. Dominika Lesnicki (Professor Marialore Sulpizi group from Johannes Gutenberg-Universität Mainzfor) carrying out the theoretical simulations for me to better understand the behavior of pyruvic acid on silica surfaces.

I would like to thank all the staff members that make it more convenient to do research in the Department of Chemistry and Biochemistry, including Jeanine Kolinko and Amy Tran for helping with registration and enrollment. Richard Thomas and Steve George for lab safety and installations. Dr. Grassian's assistant Carmen Alfaro for being responsive and helping with traveling and placing orders.

There are many people outside of school to whom I owe thanks for their support. My family back in China, especially my parents, Tuoye Fang and Jing Yao, who are always proud of me and believe in me. I know they will always be supportive and love me no matter who I am. I am so grateful that they brought me into this world and become my first life mentors. I would like to thank all my friends during the past years. They never hesitated to assist me when I needed help. We had a lot of happy times together and we shared the joy and sadness in our life and support each other.

Chapter 3, in full, is a reprint of the material published by American Chemical Society in: Yuan Fang, Mingjin Tang, Vicki H. Grassian, "Competition between Displacement and Dissociation of a Strong Acid Compared to a Weak Acid Adsorbed on

Silica Particle Surfaces: The Role of Adsorbed Water”, *The Journal of Physical Chemistry A* **2016** *120* (23), 4016-4024. The dissertation author was the primary investigator and author of this paper.

Chapter 4, in full, is a reprint of the material published by American Chemical Society in: Mingjin Tang, Whitney A. Larish, Yuan Fang, Aruni Gankanda, and Vicki H. Grassian, “Heterogeneous Reactions of Acetic Acid with Oxide Surfaces: Effects of Mineralogy and Relative Humidity”, *The Journal of Physical Chemistry A* **2016** *120* (28), 5609-5616. The dissertation author was the investigator and author of all experimental measurements and data analysis of gas phase and adsorbed acetic acid on silica.

Chapter 5, in full is currently being prepared for submission for publication of the material. Yuan Fang, Dominika Lesnicki, Kristin Wall, Marialore Sulpizi and Vicki H. Grassian. The dissertation author was the primary investigator and author of this material.

Chapter 6, in full is currently being prepared for submission for publication of the material. Yuan Fang, Michael Alves, Kristin Wall and Vicki H. Grassian. The dissertation author was the primary investigator and author of this material.

Chapter 7, in full is currently being prepared for submission for publication of the material. Yuan Fang, Pascale Lakey, Saleh Riahi, Mona Shrestha, Andrew McDonald, Manabu Shiraiwa, Douglas J. Tobias, and Vicki H. Grassian. The dissertation author was the primary investigator and author of this material.

Chapter 8, in full is currently being prepared for submission for publication of the material. Yuan Fang, Saleh Riahi, Mona Shrestha, Andrew McDonald, Douglas J. Tobias, and Vicki H. Grassian. The dissertation author was the primary investigator and author of this material.

VITA

- 2013 B.S. in Chemistry, University of Science and Technology of China
- 2013 – 2015 Graduate Teaching/Research Assistant, University of Iowa
- 2016 – 2018 Graduate Teaching/Research Assistant, University of California, San Diego
- 2018 Ph.D. in Chemistry, University of California San Diego

PUBLICATIONS

Fang, Y., Tang, M., & Grassian, V. H. (2016). Competition between Displacement and Dissociation of a Strong Acid Compared to a Weak Acid Adsorbed on Silica Particle Surfaces: The Role of Adsorbed Water. *The Journal of Physical Chemistry A*, 120(23), 4016-4024.

Tang, M., Larish, W. A., Fang, Y., Gankanda, A., & Grassian, V. H. (2016). Heterogeneous Reactions of Acetic Acid with Oxide Surfaces: Effects of Mineralogy and Relative Humidity. *The Journal of Physical Chemistry A*, 120(28), 5609-5616.

ABSTRACT OF THE DISSERTATION

Heterogeneous chemistry of atmospheric organic acids and other organic compounds with oxide surfaces representative of mineral dust and indoor surfaces

by

Yuan Fang

Doctor of Philosophy in Chemistry

University of California San Diego 2018

Professor Vicki H. Grassian, Chair

Atmospheric aerosols significantly affect the chemical balance of the atmosphere, the Earth's climate, biogeochemical cycles and human health. Although these effects have been extensively investigated in previous studies, there is still substantial uncertainty associated with the heterogeneous chemical processes involved. In industrialized nations, people spend most of their time indoors. Given the fact that there is a myriad of available

indoor surfaces having large surface to volume ratios (S/V), investigation of the heterogeneous reactions between gas and surfaces of indoor relevance is crucial. However, the detailed chemistry of molecular processes involving indoor surfaces remain poorly understood.

In this dissertation study, laboratory studies have been carried out using transmission Fourier transform infrared spectroscopy (FTIR) to help better understand the heterogeneous reactions between atmospheric acidic gases and mineral dust surfaces. Adsorption and desorption processes of nitric acid, formic acid, acetic acid and pyruvic acid, respectively, on silica (SiO_2) were found to be reversible, physisorbed processes via hydrogen bonding. However, adsorption of pyruvic acid on alumina (Al_2O_3) and titanium dioxide (TiO_2), respectively, formed adsorbed pyruvate, zymonic acid and other pyruvic acid oligomers. Additionally, the role of adsorbed water was studied systematically. Water can compete for surface adsorption sites as well as assist the dissociation of adsorbed strong acid. Photochemical reactions of adsorbed aqueous- and gas-phase pyruvic acid, respectively, on oxide surfaces formed different compounds, suggesting the complex nature of surface-adsorbed systems needs to be addressed.

An additional focus of this dissertation was to investigate the indoor surface chemistry between gases and model surfaces of indoor relevance. We developed a method to study the adsorption/desorption kinetics of gases of indoor relevance on model surfaces of indoor relevance by combining experimental measurements, kinetics modeling, as well as molecular dynamic (MD) simulations. The detailed chemistry between limonene with indoor model surfaces was studied. The interaction mode between a hydrophilic surface

with hydrophobic compounds (i.e., limonene) was studied using a combination of transmission FTIR spectroscopy and molecular dynamic simulations.

Overall, the research described in this dissertation study provides valuable insights into heterogeneous reactions between atmospheric gases and mineral dust as well as indoor surface chemistry.

CHAPTER 1 INTRODUCTION

1.1 Atmospheric Aerosols

Atmospheric aerosol particles are solid or liquid particles suspended in the atmosphere, with diameters between 10^{-9} and 10^{-4} m.^{1,2} They originate from a large variety of natural and anthropogenic sources, including: combustion; biomass burning; fossil fuel combustion; volcanic eruption; wave action to form sea spray; and soil blown to form mineral dust.^{1,3} The particles directly emitted into the atmosphere are defined as primary particles, while secondary particles are formed via gas-to-particle conversion.⁴ Gas can also be shifted to the particle phase by changing temperature, as well as during heterogeneous uptake and multiphase processes.³ The major processes contributing to atmospheric aerosols are displayed in Figure 1.1.³

The average lifetime of atmospheric aerosol particles can vary from less than 1 day to ~2 - 4 weeks depending on the particle size.⁵ Therefore, aerosol particles can undergo long range transportation during their lifetime in the atmosphere. Irradiation by sunlight, chemical and photochemical reactions with reactive atmospheric trace gases, as well as uptake of water in clouds (also during nucleation) can occur during the transport of aerosol particles.⁶ Wet deposition associated with precipitation and dry deposition processes including turbulent collisions and gravitational settling of aerosols are the two major processes for the removal of atmospheric aerosols.⁵

Atmospheric aerosols can directly and indirectly effect the atmospheric radiative balance and climate by three main processes: (1) scattering and adsorption by solar; (2) scattering, adsorption and emission by thermal radiation; and (3) cloud condensation.^{5,7,8}

The first two processes are direct climate effects, which are related to the physical and chemical properties of aerosol particles such as size, shape and chemical nature.

Aerosols can also have effects on human health including: mortality, cardiovascular, respiratory and allergic disease.^{1,8,9} The toxicity of aerosols is determined by particle size, morphology and reactions occurring on the surface.⁸ In 1997, the U.S. Environmental Protection Agency used the PM (particulate matter) 2.5 standard which emphasizes the importance of aerosols having diameters $\leq 2.5 \mu\text{m}$ in causing severe health problems.⁸

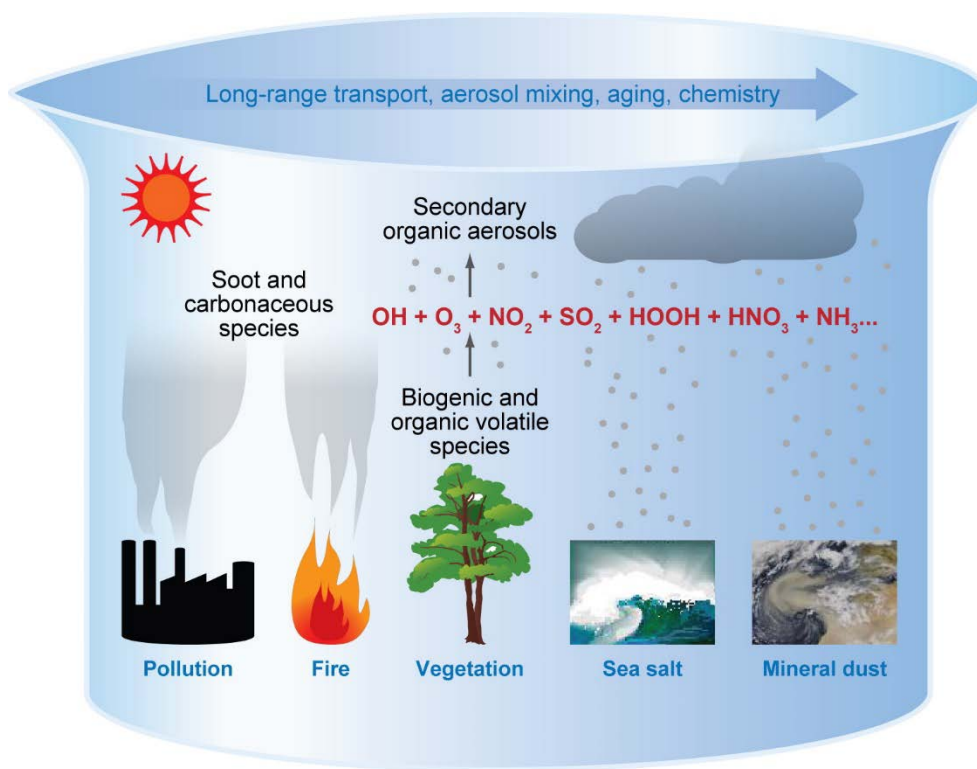


Figure 1.1. Schematic of the major processes contributing to atmospheric aerosols. Examples of the natural and anthropogenic processes producing gas and particles in the atmosphere are shown. Subsequent processes can transform and age these particles during their transportation through the atmosphere. From: Prather et al. (2008).

1.2 Mineral Dust Aerosols

Mineral dust aerosol is the largest mass fraction of total aerosol emissions, with, 1000 ~ 3000 Tg/yr of mineral dust is emitted into the atmosphere.⁸ The major source of mineral dust is wind-blown soil from arid and semiarid desert regions, which cover approximately 36 % of the Earth's continental surface.¹⁰ The so-called "dust belt" region from North Africa, through Middle East and Central and South Asia to China¹⁰ contributes to most of the global mineral dust emissions. Human activities such as surface land modification also contribute up to ~ 30 to 50 % of the total atmospheric dust loading.¹¹ The inappropriate land use driven by economic, social and political circumstances could cause the expansion of arid and semiarid regions, continuously increasing the mineral dust loading in the atmosphere.⁸ Mineral dust aerosol particles are similar in composition to continental crustal rocks as they are wind-blown eroded soils. The major components of mineral dust include: quartz, mica, oxides, carbonates and clay minerals⁸, with the exact composition of mineral dust depending on the source region. Table 1.1 displays the typical abundance of the major oxides found in global continental crust. Among the different oxides, silica (SiO_2 , > 60%) and aluminium oxide (Al_2O_3 , > 15%) are the two major components of the oxide fraction. Silica is a neutral oxide with abundant surface hydroxyl groups.^{12,13} Titanium dioxide (TiO_2), a photoactive semiconductor oxide, also exists in mineral dust.

Table 1.1. Abundance of Major Oxides found in the Continental Crust. From: Usher et al. (2003).

Oxide	Percentage (%)
Silica (SiO ₂)	61.5
Aluminium oxide (Al ₂ O ₃)	15.1
Iron (III) oxide (Fe ₂ O ₃)	6.28
Calcium oxide (CaO)	5.5
Sodium oxide (Na ₂ O)	3.2
Magnesium oxide (MgO)	3.7
Potassium oxide (K ₂ O)	2.4
Titanium dioxide (TiO ₂)	0.68
Barium oxide (BaO)	0.0584
Manganese (II) oxide (MnO)	0.1

In addition to the effect on climate, atmospheric aerosols can significantly alter the biogeochemical cycles by varying the loss/gain of nutrients through the atmosphere.⁵ Approximately 300-500 Tg/yr of mineral dust is deposited into the oceans, with 50% of the total deposition occurring in the north Atlantic Ocean.⁸ Mineral dust can also affect ocean phytoplankton by offering soluble iron as a micronutrient supply.^{8,14} Figure 1.2 gives a summary of the different impacts of mineral dust on climate and ocean biogeochemical cycles.⁸

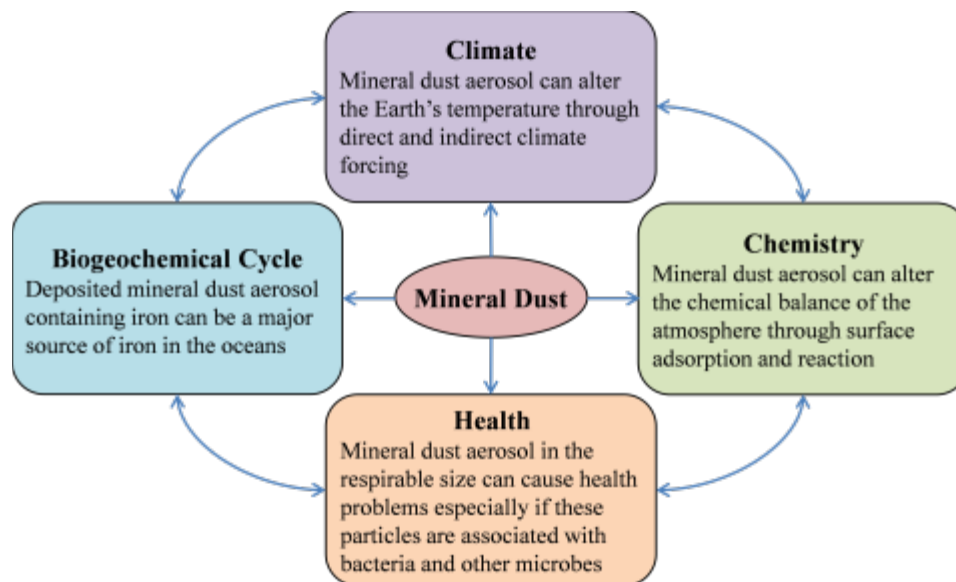


Figure 1.2. Mineral dust and its impact on local process including climate and ocean biogeochemical cycles. Reprinted with permission from Usher et al. (2003). Copyright (2003) American Chemical Society.

Heterogeneous and photochemical reactions occurring on aerosol particle surfaces can change the properties of atmospheric particles, as well as gas-phase chemistry in the atmosphere. Heterogeneous reactions on mineral dust surfaces can impart the concentration of important trace gases and radicals^{15,16}, partially modifying the aerosol composition^{17,18}, hence changing their ability to serve as cloud condensation nuclei (CCN)^{19–23} and ice nuclei (IN)^{23–26}. This study focused on: (1) understanding the heterogeneous reactions between mineral dust aerosols and atmospheric acidic gases; (2) the role that adsorbed water plays in the heterogeneous reactions. These topics are discussed in detail below.

1.3 Gases in the Atmosphere

1.3.1 Trace Gases of Interest

The Earth's atmosphere is composed of 78% nitrogen (N₂) and 21 % oxygen (O₂) — water vapor (H₂O), argon (Ar) and other noble gases constitute the remaining

components. The atmosphere also contains less than 1% trace gases.⁷ Trace gases in the atmosphere include: carbon dioxide (CO₂), nitrogen oxides (NO_x), nitric acid (HNO₃), sulfur dioxide (SO₂), ozone (O₃), hydrogen peroxide (H₂O₂) and volatile organic compounds (VOCs). As a result of the growth of both the world population and industrial activities since the industrial revolution, the composition of trace gases is changing rapidly.

Gaseous nitric acid (HNO₃), a stable product thought to be removed via wet or dry deposition, can be formed by atmospheric oxidation of nitrogen oxides (NO_x). Reactions between HNO₃ and oxide surfaces result in adsorbed nitrate via different coordination modes.¹² However, recent studies of adsorbed nitrate photochemistry on Al₂O₃, TiO₂, and Fe₂O₃ have shown the potential renoxification (leading to NO_x formation) under different environmental conditions.²⁷⁻²⁹

There are also numerous volatile organic compounds (VOCs) present in the atmosphere.⁷ Major sources of VOCs include natural biogenic processes and human activities.⁷ Biogenic processes (including the emissions from plants, wild animals, forest burning, and anaerobic processes occurring in bogs and marshes) increase the ambient levels of organic compounds substantially. Human activities (automobile emissions, lead abrasion, wood smoke, gas combustion and petrol evaporation) increase VOCs levels by directly releasing organic matter (OM) into the atmosphere.⁷ VOCs affect the production of tropospheric ozone and secondary organic aerosols, thus raising great environmental concern. Once emitted into the atmosphere, VOCs undergo a variety of physical and chemical processes leading to deposition or transformation.³⁰ Following reactions of VOCs on aerosol surfaces, a potential removal pathway is adsorption. Volatile organic acids (VOAs), including formic acid, acetic acid and pyruvic acid, are the most abundant species

among VOCs.⁷ Precipitation chemistry studies have found that organic acids may account for up to 64% of the total acidity in non-urban environments.³¹ Sources of atmospheric organic acids include anthropogenic and biogenic emissions, as well as photochemical oxidation of organic compounds in the atmosphere.⁷ Sinks of atmospheric organic acids mainly include wet/dry deposition, as well as reaction with OH radicals.

Formic acid (HCOOH) and acetic acid (CH₃COOH), the two most abundant organic acids in the atmosphere, have been found in concentration ranges from 0.1 ~ 40 ppbv and 0.5 ~ 16 ppbv, respectively.³² Formic and acetic acid can be found in all types of precipitation including rain, cloud, fog, snow and ice water, contributing from ~16 up to 35% of the free acidity in U.S. precipitation.³² The major sources of carboxylic acids include anthropogenic and biogenic processes, which involve direct emission from plastics combustion, chemical plant emissions, biomass burning, as well as emissions from soil and vegetation.^{32,33} Motor exhaust, another important source of carboxylic acid, has an acetic acid concentration approximately 17 times higher than found in air.³³ Carboxylic acids have also been found in aerosol particles and cloud droplets.³⁴ The acidity of aerosol particles and cloud droplets are also significantly affected by the partitioning of carboxylic acids in the gas and condensed phases.³⁴

Pyruvic acid (CH₃COCOOH) an important atmospheric α -keto acid, is mainly formed from the particle-phase aqueous reaction between the hydroxyl radical (\bullet OH) and hydrated methylglyoxal (CH₃CCHO).³⁵ Pyruvic acid has been found in the gas phase (10 – 100 ppt), in aerosols (up to 140 ng m⁻³), in snow and rainwater.³⁶ The primary sink of atmospheric pyruvic acid is through direct photolysis. Pyruvic acid can also be removed via reaction with \bullet OH and wet deposition.^{37,38} Under most atmospheric conditions,

photolysis of pyruvic acid in the gas phase dominates over aqueous photolysis, with products including CO₂ and acetaldehyde^{39,40}, or acetic acid and CO.^{36,38,41} Photolysis of pyruvic acid in the aqueous phase undergoes a completely different mechanism since 60% of pyruvic acid hydrates to 2,2-dihydroxypropanoic acid (DHPA), the geminal-diol of pyruvic acid, when dissolved in water.⁴² Acetic acid, CO₂, dimethyl tartaric acid (DMHA) and zymonic acid have been detected as major products when the multiphase photochemistry of pyruvic acid was studied.³⁵ Pyruvic acid photolysis products could contribute to the secondary organic aerosol (SOA) loading into atmosphere. Understanding SOA formation and aging is important to climate studies owing to the current lack of knowledge concerning SOAs in global models^{35,43}, as well as, the importance of surface composition and heterogeneous reactions of SOA.^{44,45} Figure 1.3 displays the details of the photolysis mechanism for aqueous pyruvic acid.³⁸ The structure of pyruvic acid is also interesting as it possesses several conformers due to the intramolecular rotation along the C-C and C-O bonds.⁴⁶ The lowest energy conformer is labelled as trans-cis (Tc) conformer while the one 2.08 kcal mol⁻¹ higher in energy is the trans-trans (Tt) conformer. There is a significant thermal population of both conformers at ambient temperatures as the energy between the two conformers is sufficiently close.^{46,47} To date, there remains a lack of knowledge concerning how adsorption on surfaces would impact the molecular configurations of pyruvic acid.

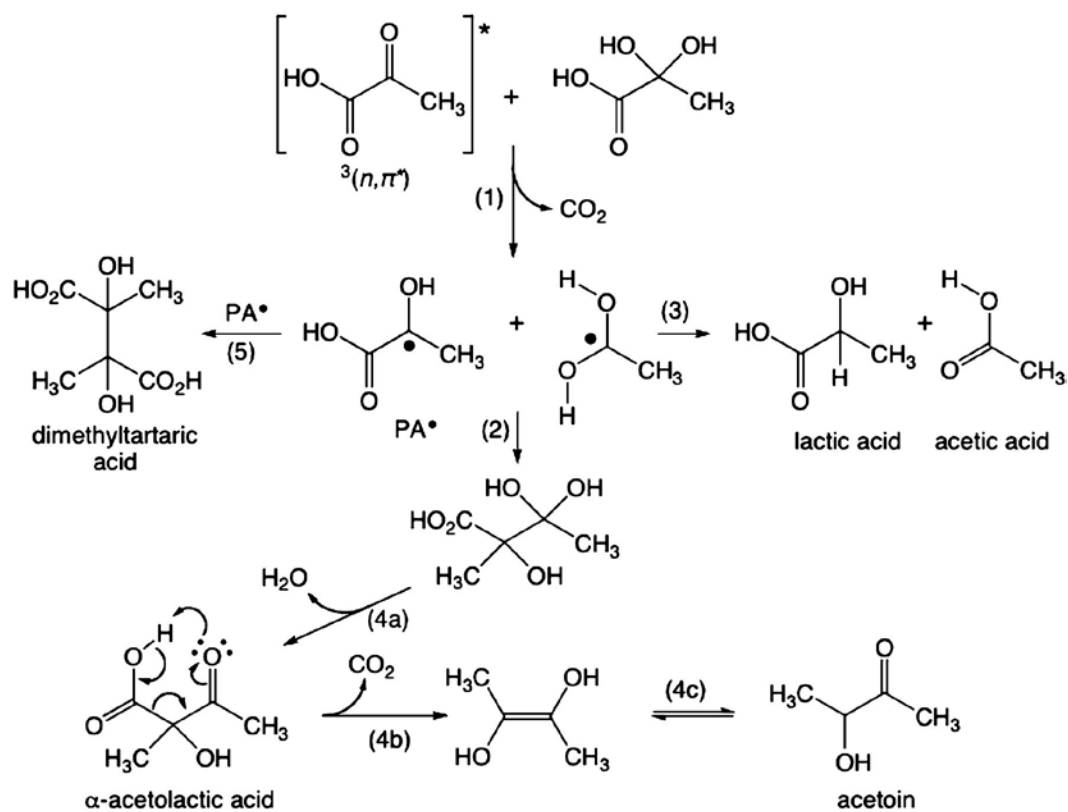


Figure 1.3. Details of the photolysis mechanism for aqueous pyruvic acid. From: Griffith et al. (2013).

Trace atmospheric acidic gases, such as nitric acid, formic acid, acetic acid, and pyruvic acid, can interact with mineral oxide surfaces in the atmosphere forming surface adsorbed species, which may undergo photochemical reactions in the presence of irradiation. Even though most aerosols originate from remote regions, they can be transported and encounter atmospheric trace gases during their lifetime.

1.3.2 Water

Water vapor plays a critical role in the heterogeneous reaction chemistry of oxide surfaces with atmospheric gases.⁴⁸ Relative humidity (RH) is usually used to describe the

amount of water vapor in air, typically in percentage (%), as the ratio of its partial pressure to saturated water vapor pressure at the same temperature (T),

$$RH = 100 \times \frac{P(\text{water})}{P_s(\text{water})} \quad (\text{E1})$$

where: $P(\text{water})$ is the partial pressure of water vapor, and $P_s(\text{water})$ is the saturated vapor pressure of water.²³ Water vapor can partition into/onto mineral dust particles under subsaturated conditions ($RH < 100\%$), defined as water adsorption. Water also affects the cloud condensation nucleation process of mineral dust aerosols being activated to cloud droplets under supersaturated conditions ($RH > 100\%$).

Heterogeneous reactions between water and mineral dust aerosols can impact the reactivity of mineral dust toward atmospheric trace gases.²³ In addition, change in the composition and hygroscopicity of mineral dust aerosol may affect the refractive index⁴⁹, optical diameters, and the probability of wet deposition^{50,51}, thus impacting their atmospheric lifetime.^{23,51} Furthermore, heterogeneous chemistry also has an influence on the solubility and/or bioavailability of elements within individual mineral dust particles. Figure 1.4 shows a schematic of interactions of mineral dust particles with trace gases and water, as well as their impacts on cloud formation.²³ However, there remains a lack of knowledge concerning how adsorbed water will affect the heterogeneous reactions between strong and weak atmospheric acidic gases and mineral dust aerosols, as well as the role of water on the molecular configurations of adsorbed species. Therefore, studying the role of water vapor on heterogeneous reactions between trace atmospheric gases on mineral dust oxide surfaces is an important objective of this dissertation research.

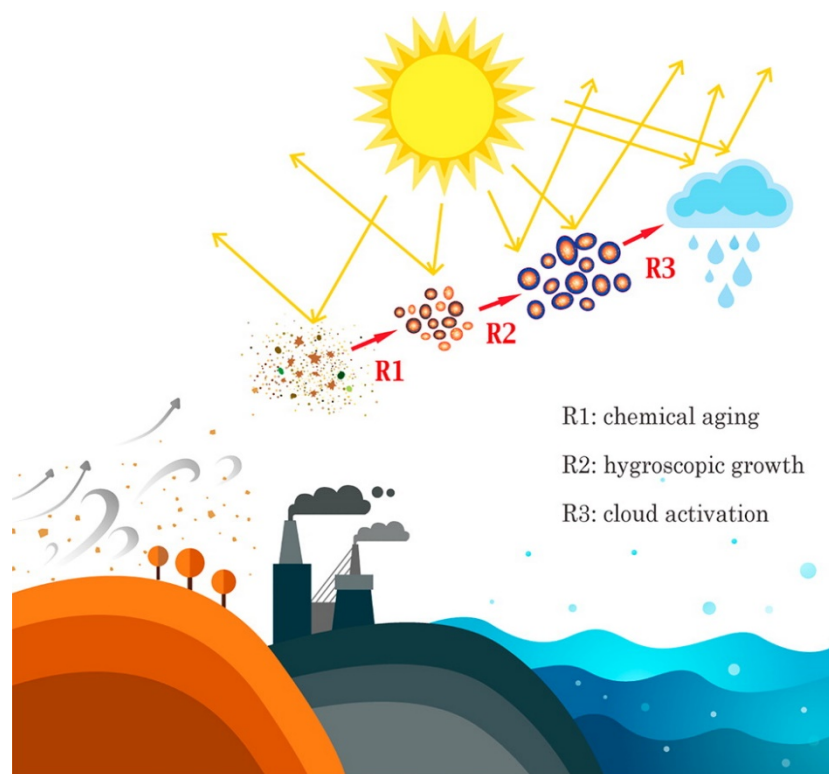


Figure 1.4. Schematic of complex interactions of mineral dust particles with atmospheric trace gases and water, as well as impacts on cloud formation. Reactions involved are defined as follows: Chemical aging of mineral dust aerosol particles due to reactions with trace gases (R1); aged mineral dust aerosol particles increase hydroscopic growth (R2); and activation of mineral dust particles to cloud droplets and ice particles (R3). Reprinted with permission from Tang et al. (2016) Copyright (2016) American Chemical Society.

1.4 Surface Chemistry of Indoor Air

1.4.1 Indoor Air

People have focused on atmospheric heterogeneous reactions for decades. However, over the course of a human’s entire life, most of the encountered air is “indoor air”.⁵² In industrialized nations, people spend approximately 90% of their total time indoors, especially in one’s own residence. Humans have a large direct contribution to indoor air chemistry via body metabolism, skin, hair, clothing, and human activities such as cooking and printing as well as use of personal care products.⁵² Local outdoor air pollution can be introduced indoors as buildings are exchanging air with surroundings via

ventilation and leaking.⁵² In addition, indoor air contaminants are removed from ventilation, a crucial removal process for pollutants emitted from indoor sources. The rate of indoor reactions can be affected by the concentrations of the reactants, the nature of the reactants, temperature and relative humidity. The relative humidity influences the gas-phase concentration of water as well as the absence/presence/thickness of surface aqueous films which affect the removal rate of hydrophilic gas-phase chemicals.⁵² Photolysis is important outdoors and given the fact that buildings are equipped with windows, photolysis is another indoor reaction pathway. In addition, indoor illumination (especially fluorescent lights) could photolyze the nitrate radical (NO_3^\bullet , $\lambda < 580 \text{ nm}$) and nitrogen dioxide (NO_2 , $\lambda < 398 \text{ nm}$).⁵³ The major indoor reactants, products and reaction pathways are shown in Figure 1.5.⁵⁴

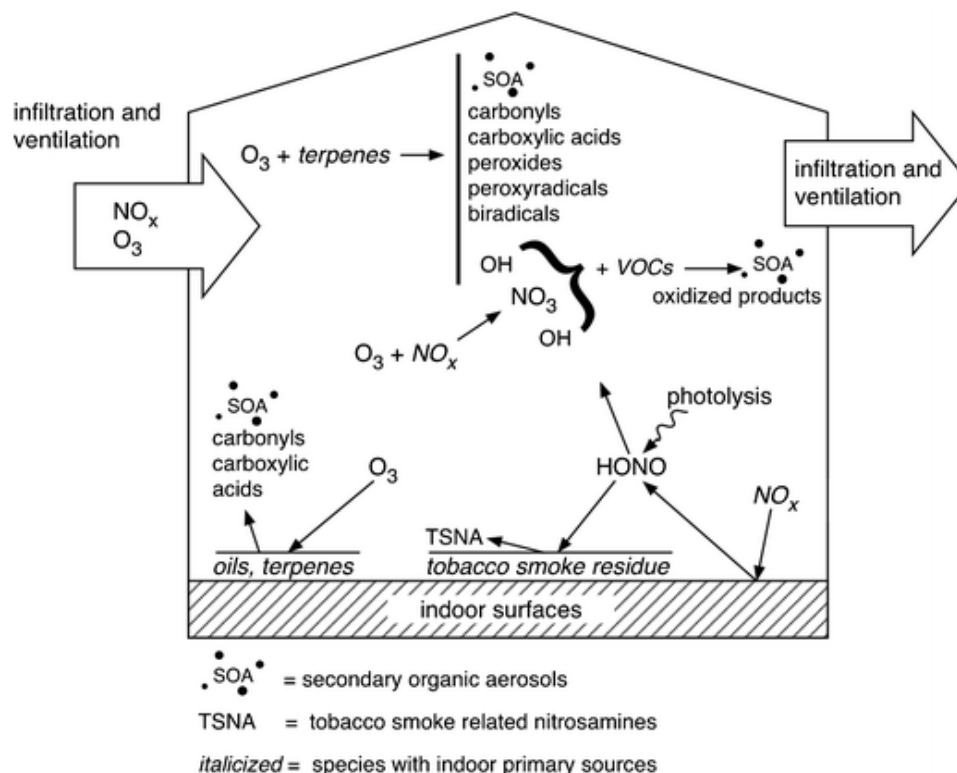


Figure 1.5. Major reactants, products and reaction pathways of indoor chemistry. From: Morrison et al. (2015).

1.4.2 Indoor Surface Chemistry

Indoor environments consist of a myriad of surfaces such as walls, windows and floors, and have large surface-to-volume (S/V) ratios.^{52,55} Singer et al.⁵⁶ studied a sample of ten residential rooms, observing nominal S/V values in the range of 2.9 – 4.6 m² per m³. Surface reactions could serve as both indoor pollutants sinks and sources.⁵³ Indoor surfaces are also coated with adsorbed molecules such as high-molecular-weight organics, salts, water and other contaminants.⁵⁴

Indoor pollutants in the form of particles can originate from indoor and outdoor pollution sources. The composition and concentration of indoor particles varies with

different pollution sources. For example, fine particles are released from cooking or smoking, with coarse particles arising from sweeping and vacuuming.⁵⁷ Harmful gases and liquids can also adsorb on these pollutant particles, affecting human health.^{57,58} Pollutants introduced from outdoor air and contaminants emitted from indoor environments constitute the major indoor air impurities. Numerous factors affect indoor air quality including temperature, relative humidity (RH), ventilation, air exchange rate, particles, biological and gaseous pollutants.⁵⁷ Indoor gaseous pollutants including: primary gaseous pollutants such as CO, CO₂, SO₂, NO_x, O₃ and VOCs; and secondary gaseous pollutants generated from reactions between ozone and unsaturated hydrocarbons (free radicals, aldehydes, ketones, alcohols, carboxylic acids and fine particulate matter).^{57,59} Indoor VOCs mainly come from building and décor materials including carpet, boards, composite floor, cork, paint and heat pipeline.^{57,60} Models have been developed to study the surface emission as well as adsorption of VOCs from building and decor materials.^{61,62} However, the molecular details of the chemical processes occurring indoors are still poorly understood.

Secondary indoor gaseous pollutants could be more irritating than the primary reactants.⁶³ Outdoor reactive chemistry is mostly driven by the hydroxyl radical, as well as higher photochemistry levels during daytime. Photon flux densities indoors are much smaller. Therefore, indoor reactive chemistry is possibly driven by ozone and nitrate radicals.⁵² Ozone chemistry has been widely studied on indoor surfaces.⁵⁵ Ozone uptakes on surfaces as well as oxidized organic matter (OM) on surfaces⁶⁴, generating VOCs from carpet, paint, ventilation duct material⁶⁵, and surfaces in a simulated aircraft cabin.^{55,66,67} Investigations carried out on ozone reacting with limonene (C₁₀H₁₆)^{68,69}, terpene⁷⁰, α -terpene⁷¹, VOCs⁷² and airborne particulate⁷³, the major contributors to secondary indoor

pollution, raises the significant research needed to improve our understanding of the chemical reactions occurring on indoor surfaces (large S/V indoors).⁵⁷

1.4.3 Relevant Gas-Phase Molecules Present in Indoor Air

Terpenes, from vegetation and trees, are naturally occurring, unsaturated VOCs widely found indoors, with the following sources: emission of wood products; solvents (based on pine oil) usage; cleaning products; and air fresheners usage.⁶³ Limonene, a terpene with a citrus/lemon fragrance, is commonly found in the indoor environment, and widely used in consumer products (such as detergents, soaps, perfumes and beverages as a flavor and fragrance additive) and is also used in household cleaning products.^{63,74,75} The average reported indoor concentration of limonene is 5-15 ppb^{69,76}, however, after product use, the concentration can increase up to 175 ppb.⁶³ Limonene, an unsaturated hydrocarbon, has the potential to form secondary organic aerosols as well as hydrogen peroxide (H₂O₂) via reactions with oxidants such as ozone, producing both stable species and free radicals including many aldehydes (saturated and unsaturated) and organic acids with low odor thresholds.^{63,69,77,78} Some of the products may be more irritating than their precursors, with low vapor pressure products contributing to the growth of secondary organic aerosols (SOA) indoors.⁶⁹

In addition, the toxicity of limonene has been investigated.⁷⁴ As one of the most often used fragrant terpenes, limonene is known to be easily oxidized.⁷⁴ Several studies have found that limonene and limonene oxidation products have allergenic and toxicity properties on mammals.^{74,79,80} Therefore, oxidized limonene has been added to the test series for potential fragrance allergy patients by the current European regulation on

fragrances.⁷⁴ With a high vapor pressure, limonene can be readily adsorbed on indoor surfaces and is directly applied to interior surfaces when used in consumer products.⁸¹ Using a model framework developed to predict the mass formation of SOA from ozone/adsorbed limonene surface reactions, it has been found that on nonreactive surfaces, such as glass, sealed materials or smooth metals, adsorbed limonene and ozone can also form SOA due to surface reactions.⁸¹ The molecular details for the interactions between limonene and indoor surfaces remains poorly understood.

Carboxylic acids can be harmful to tissues and organs during occupational exposure by irritating eyes, skin, and mucous membrane.⁸² In addition, carboxylic acids were found to be responsible for the corrosion of some indoor facilities.⁸³ Lactic acid, a water-soluble gas, is an α -hydroxy acid which consists of a carboxylic acid substituted with a hydroxyl group on the adjacent carbon. Lactic acid is one of the major constituents of human perspiration and is also found in various personal health products.^{84,85} Most importantly, it has been recently detected as one of the dominant gas-phase carboxylic acids in occupied classrooms with a concentration of 4.7 ppm.⁸² Indoor concentration of lactic acid was reported to be 10 times as its outdoor concentrations on average, most likely because of human perspiration.⁸²

Relative humidity is known to be the one factor that can alter indoor reaction pathways by affecting the aqueous surface films and the surface removal ability of hydrophilic gas phase species.⁵³ It has been found that relative humidity can strongly impact the perception of indoor air quality by decreasing the perceived air quality with increasing humidity.⁸⁶ However, there remains a large lack of knowledge concerning the mechanisms of water vapor with indoor relevant gases on indoor surfaces.

In this dissertation study, model surfaces were chosen to represent the chemistry on: glass surfaces (SiO_2); components of paint and self-cleaning wall surfaces (TiO_2); and components of drywall surfaces ($\text{CaSO}_4 \cdot 2\text{H}_2\text{O}$). These model surfaces are in the form of powders with high surface areas to obtain a better understanding of surface adsorption mechanisms.

1.5 Thesis Objectives

The research presented herein focuses on understanding the heterogeneous chemistry and photochemistry that occurs between the surface of mineral dust aerosols and atmospheric trace gases, as well as between gases present in indoor environments with relevant indoor surfaces. Furthermore, the role of adsorbed water is also investigated. Several different types of interactions have been explored in the research, including: heterogeneous reactions of nitric acid and formic acid on silica surfaces; acetic acid dimer formation on silica surfaces; pyruvic acid interaction with SiO_2 , Al_2O_3 and TiO_2 surfaces, as well as photochemical surface reactions; limonene adsorption on different relevant indoor surfaces; and the interaction of limonene with silica surfaces, incorporating a limonene adsorption kinetics study.

Multiple experimental methods were used in this study to investigate the heterogeneous reactions between atmospheric and indoor gases with surfaces. These experimental techniques include transmission Fourier transform infrared (FTIR) spectroscopy and attenuated total reflectance (ATR) – FTIR spectroscopy to understand gas phase and surface changes caused by heterogeneous interactions. Oxide samples were

characterized by BET surface area measurements. In addition, analysis using Mass Spectroscopy (MS) was applied to identify the reaction products for photochemical reactions between gases and mineral dust surfaces. All the experimental methods used are described in detail in Chapter 2.

In Chapter 3, the focus is to understand the role of adsorbed water between strong and weak atmospheric acidic gases on the silica surface using FTIR spectroscopy. As will be discussed, nitric acid, a strong acid, and formic acid, a weak acid, both molecularly and reversibly adsorb on the silica surface by hydrogen bonding. Adsorbed water competes with adsorbed acids for surface adsorption sites and can also assist their dissociation on the surface. However, the extent of dissociation is significantly smaller for HCOOH than for HNO₃ because of the much weaker acidity of HCOOH.

In Chapter 4, the heterogeneous reactions between an organic atmospheric trace gas, acetic acid (a carboxylic acid) with the silica surface is discussed. The formation of dimer in both gas phase and surface phase is observed. The monomer is observed to be more favorable in the gas phase (under low gas phase concentrations), while the dimer dominates when adsorbed on surfaces. Adsorbed water is found to compete for surface adsorption sites with adsorbed acetic acid.

In Chapter 5, heterogeneous interactions between gas phase pyruvic acid and hydroxylated silica surfaces is discussed. Pyruvic acid adsorption on silica is a molecular, reversible process. Configurations of adsorbed pyruvic acid have been well investigated from both experimental and theoretical modeling perspectives. It is shown here that both Tt and Tc conformers still exist on the surface after adsorption. As will be discussed, the Tt and Tc conformers hydrogen bond with surface hydroxyl groups via different functional

groups. In the presence of adsorbed water, both Tt and Tc conformer binds with silica surface via a 'water bridge'.

Heterogeneous reactions of pyruvic acid heterogeneous reactions with Al_2O_3 and TiO_2 , as well as photochemical reactions are discussed in Chapter 6. Pyruvic acid irreversibly adsorbs on Al_2O_3 and TiO_2 forming adsorbed pyruvate, zymonic acid and other species. Upon irradiation, parapyruvic and zymonic acid, pyruvic acid dimers, as well as trimers are observed using MS analysis. Observed differences in the photochemical mechanisms of adsorbed pyruvic acid on surfaces for the gas phase in comparison to the aqueous phase is discussed in detail in Chapter 6.

In Chapter 7, surface adsorption measurements obtained from vibrational spectroscopy are integrated with kinetic modeling and theoretical calculations. The interaction type and strength of limonene adsorption on SiO_2 is investigated, along with the kinetics of the adsorption/desorption process. Limonene is found to reversibly adsorb on silica via hydrogen bonding. A kinetics model is built for limonene adsorption/desorption at different coverages and can be expanded to study other indoor organic vapors and surfaces.

The driving force behind adsorption of hydrophobic molecules, such as limonene, on hydrophilic surfaces (SiO_2) is studied using a combination of vibrational spectroscopy measurements and molecular dynamic (MD) simulation modeling in Chapter 8. As will be discussed, limonene adsorbs on silica via one or two hydrogen bonds. Other cyclic molecules such as cyclohexane, benzene and cyclohexene were studied to further understand the interactions between hydrophobic molecules and hydrophilic surfaces. Heterogeneous reactions between the adsorption of relevant indoor gases (limonene) on

relevant indoor surfaces (SiO_2 , $\text{CaSO}_4 \cdot 2\text{H}_2\text{O}$ and TiO_2 which are representative of glass, gypsum, wall and paintings) are investigated using ATR-FTIR. The adsorption on TiO_2 is observed to be mostly irreversible for both relevant indoor gases, while on SiO_2 and $\text{CaSO}_4 \cdot 2\text{H}_2\text{O}$ surfaces, the process is found to be reversible.

1.6 References

- (1) Pöschl, U. Atmospheric Aerosols: Composition, Transformation, Climate and Health Effects. *Angew. Chemie - Int. Ed.* **2005**, *44* (46), 7520–7540.
- (2) Prospero, J. M.; Mohnen, V.; Jaenicke, R.; Charlson, R. J.; Delany, A. C.; Moyers, J.; Zoller, W.; Rahn, R. The Atmospheric Aerosol System: An Overview. *Rev. Geophys.* **1983**, *21* (7), 1607–1630.
- (3) Prather, K. A.; Hatch, C. D.; Grassian, V. H. Analysis of Atmospheric Aerosols. *Annu. Rev. Anal. Chem.* **2008**, *1* (1), 485–514.
- (4) Turpin, B. J.; Huntzicker, J. J. Identification of Secondary Organic Aerosol Episodes and Quantitation of Primary and Secondary Organic Aerosol Concentrations during SCAQS. *Atmos. Environ.* **1995**, *29* (23), 3527–3544.
- (5) Mahowald, N.; Ward, D. S.; Kloster, S.; Flanner, M. G.; Heald, C. L.; Heavens, N. G.; Hess, P. G.; Lamarque, J.-F.; Chuang, P. Y. Aerosol Impacts on Climate and Biogeochemistry. *Annu. Rev. Environ. Resour.* **2011**, *36* (1), 45–74.
- (6) Cwiertny, D. M.; Young, M. A.; Grassian, V. H. Chemistry and Photochemistry of Mineral Dust Aerosol. *Annu. Rev. Phys. Chem.* **2008**, *59* (1), 27–51.
- (7) Steinfeld, J. I. Atmospheric Chemistry and Physics: From Air Pollution to Climate Change. *Environ. Sci. Policy Sustain. Dev.* **1998**, *40* (7), 26–26.
- (8) Usher, C. R.; Michel, A. E.; Grassian, V. H. Reactions on Mineral Dust. *Chem. Rev.* **2003**, *103* (12), 4883–4939.
- (9) Seaton, A.; MacNee, W.; Donaldson, K.; Godden, D. Particulate Air Pollution and Acute Health Effects. *Lancet* **1995**, *345* (8943), 176–178.
- (10) Hatch, C. D.; Grassian, V. H. 10th Anniversary Review: Applications of Analytical Techniques in Laboratory Studies of the Chemical and Climatic Impacts of Mineral Dust Aerosol in the Earth's Atmosphere. *J. Environ. Monit.* **2008**, *10* (8), 919–934.

- (11) Sokolik, I. N.; Toon, O. B. Direct Radiative Forcing by Anthropogenic Airborne Mineral Aerosols. *Nature*. 1996, pp 681–683.
- (12) Goodman, A. L.; Bernard, E. T.; Grassian, V. H. Spectroscopic Study of Nitric Acid and Water Adsorption on Oxide Particles: Enhanced Nitric Acid Uptake Kinetics in the Presence of Adsorbed Water. *J. Phys. Chem. A* **2001**, *105* (26), 6443–6457.
- (13) Fang, Y.; Tang, M.; Grassian, V. H. Competition between Displacement and Dissociation of a Strong Acid Compared to a Weak Acid Adsorbed on Silica Particle Surfaces: The Role of Adsorbed Water. *J. Phys. Chem. A* **2016**, *120* (23), 4016–4024.
- (14) Meskhidze, N. Iron Mobilization in Mineral Dust: Can Anthropogenic SO₂ Emissions Affect Ocean Productivity? *Geophys. Res. Lett.* **2003**, *30* (21), 2085.
- (15) Dentener, F. J.; Carmichael, G. R.; Zhang, Y.; Lelieveld, J.; Crutzen, P. J. Role of Mineral Aerosol as a Reactive Surface in the Global Troposphere. *J. Geophys. Res. Atmos.* **1996**, *101* (D17), 22869–22889.
- (16) Tang, Y.; Carmichael, G. R.; Kurata, G.; Uno, I.; Weber, R. J.; Song, C. H.; Guttikunda, S. K.; Woo, J. H.; Streets, D. G.; Wei, C.; et al. Impacts of Dust on Regional Tropospheric Chemistry during the ACE-Asia Experiment: A Model Study with Observations. *J. Geophys. Res. D Atmos.* **2004**, *109* (19), 1–21.
- (17) Sullivan, R. C.; Guazzotti, S. A.; Sodeman, D. A.; Prather, K. A. Direct Observations of the Atmospheric Processing of Asian Mineral Dust. *Atmos. Chem. Phys.* **2007**, *7* (5), 1213–1236.
- (18) Li, W. J.; Shao, L. Y. Observation of Nitrate Coatings on Atmospheric Mineral Dust Particles. *Atmos. Chem. Phys.* **2009**, *9* (6), 1863–1871.
- (19) Krueger, B. J. The Transformation of Solid Atmospheric Particles into Liquid Droplets through Heterogeneous Chemistry: Laboratory Insights into the Processing of Calcium Containing Mineral Dust Aerosol in the Troposphere. *Geophys. Res. Lett.* **2003**, *30* (3), 1148.
- (20) Laskin, A.; Iedema, M. J.; Ichkovich, A.; Graber, E. R.; Taraniuk, I.; Rudich, Y. Direct Observation of Completely Processed Calcium Carbonate Dust Particles. *Faraday Discuss.* **2005**, *130*, 453–468.
- (21) Sullivan, R. C.; Moore, M. J. K.; Petters, M. D.; Kreidenweis, S. M.; Roberts, G. C.; Prather, K. A. Effect of Chemical Mixing State on the Hygroscopicity and Cloud Nucleation Properties of Calcium Mineral Dust Particles. *Atmos. Chem. Phys.* **2009**, *9* (10), 3303–3316.
- (22) Tang, M. J.; Whitehead, J.; Davidson, N. M.; Pope, F. D.; Alfarra, M. R.; McFiggans, G.; Kalberer, M. Cloud Condensation Nucleation Activities of Calcium Carbonate and Its Atmospheric Ageing Products. *Phys. Chem. Chem. Phys.* **2015**,

17 (48), 32194–32203.

- (23) Tang, M.; Cziczo, D. J.; Grassian, V. H. Interactions of Water with Mineral Dust Aerosol: Water Adsorption, Hygroscopicity, Cloud Condensation, and Ice Nucleation. *Chem. Rev.* **2016**, *116* (7), 4205–4259.
- (24) Sullivan, R. C.; Petters, M. D.; Demott, P. J.; Kreidenweis, S. M.; Wex, H.; Niedermeier, D.; Hartmann, S.; Clauss, T.; Stratmann, F.; Reitz, P.; et al. Irreversible Loss of Ice Nucleation Active Sites in Mineral Dust Particles Caused by Sulphuric Acid Condensation. *Atmos. Chem. Phys.* **2010**, *10* (23), 11471–11487.
- (25) Kulkarni, G.; Sanders, C.; Zhang, K.; Liu, X.; Zhao, C. Journal of Geophysical Research : Atmospheres. **2014**, 1–19.
- (26) Sihvonen, S. K.; Schill, G. P.; Lykтей, N. A.; Veghte, D. P.; Tolbert, M. A.; Freedman, M. A. Chemical and Physical Transformations of Aluminosilicate Clay Minerals Due to Acid Treatment and Consequences for Heterogeneous Ice Nucleation. *J. Phys. Chem. A* **2014**, *118* (38), 8787–8796.
- (27) Rubasinghege, G.; Grassian, V. H. Photochemistry of Adsorbed Nitrate on Aluminum Oxide Particle Surfaces. *J. Phys. Chem. A* **2009**, *113* (27), 7818–7825.
- (28) Ndour, M.; Conchon, P.; D’Anna, B.; Ka, O.; George, C. Photochemistry of Mineral Dust Surface as a Potential Atmospheric Renoxification Process. *Geophys. Res. Lett.* **2009**, *36* (5), 2–5.
- (29) Tuazon, E. C.; Aschmann, S. M.; Atkinson, R. Atmospheric Degradation of Volatile Methyl-Silicon Compounds. *Environ. Sci. Technol.* **2000**, *34* (10), 1970–1976.
- (30) Atkinson, R.; Arey, J. Atmospheric Degradation of Volatile Organic Compounds. *Chem. Rev.* **2003**, *103* (12), 4605–4638.
- (31) Keene, W. C.; Galloway, J. N.; Holden, J. D. From Remote Areas of the World. **1983**, *88* (3), 5122–5130.
- (32) Chebbi, a; Carlier, P. Carboxylic Acids in the Troposphere, Occurrence, Sources and Sinks: A Review. *Atmos. Environ.* **1996**, *30* (24), 4223–4249.
- (33) Talbot, R. W.; Beecher, K. M.; Harriss, R. C.; Cofer III, W. R. Atmospheric Geochemistry of Formic and Acetic Acids at a Mid-Latitude Temperature Site. *J. Geophys. Res.* **1988**, *93* (D2), 1638–1652.
- (34) Puja, K.; N., K.; M., K. K.; S., S. S. Atmospheric Formic and Acetic Acids: An Overview. *Rev. Geophys.* **1999**, *37* (2), 227–248.
- (35) Reed Harris, A. E.; Pajunoja, A.; Cazaunau, M.; Gratien, A.; Pangui, E.; Monod, A.; Griffith, E. C.; Virtanen, A.; Doussin, J. F.; Vaida, V. Multiphase Photochemistry of Pyruvic Acid under Atmospheric Conditions. *J. Phys. Chem. A* **2017**, *121* (18),

3327–3339.

- (36) Reed Harris, A. E.; Doussin, J. F.; Carpenter, B. K.; Vaida, V. Gas-Phase Photolysis of Pyruvic Acid: The Effect of Pressure on Reaction Rates and Products. *J. Phys. Chem. A* **2016**, *120* (51), 10123–10133.
- (37) Mellouki, A.; Mu, Y. On the Atmospheric Degradation of Pyruvic Acid in the Gas Phase. *J. Photochem. Photobiol. A Chem.* **2003**, *157* (2–3), 295–300.
- (38) Reed Harris, A. E.; Ervens, B.; Shoemaker, R. K.; Kroll, J. A.; Rapf, R. J.; Griffith, E. C.; Monod, A.; Vaida, V. Photochemical Kinetics of Pyruvic Acid in Aqueous Solution. *J. Phys. Chem. A* **2014**, *118* (37), 8505–8516.
- (39) Leermakers, P. A.; Vesley, G. F. The Photochemistry of α -Keto Acids and α -Keto Esters. I. Photolysis of Pyruvic Acid and Benzoylformic Acid. *J. Am. Chem. Soc.* **1963**, *85* (23), 3776–3779.
- (40) Yamamoto, S.; Back, R. A. The Photolysis and Thermal Decomposition of Pyruvic Acid in the Gas Phase. *Can. J. Chem.* **1985**, *63* (2), 549–554.
- (41) Epstein, S. A.; Nizkorodov, S. A. A Comparison of the Chemical Sinks of Atmospheric Organics in the Gas and Aqueous Phase. *Atmos. Chem. Phys.* **2012**, *12* (17), 8205–8222.
- (42) Maroń, M. K.; Takahashi, K.; Shoemaker, R. K.; Vaida, V. Hydration of Pyruvic Acid to Its Geminal-Diol, 2,2-Dihydroxypropanoic Acid, in a Water-Restricted Environment. *Chem. Phys. Lett.* **2011**, *513* (4–6), 184–190.
- (43) Jimenez, J. L.; Canagaratna, M. R.; Donahue, N. M.; Pósfelt, A. S. H.; Zhang, Q.; Kroll, J. H.; DeCarlo, P. F.; Allan, J. D.; Coe, H.; Ng, N. L.; et al. Evolution of Organic Aerosols in the Atmosphere: A New Framework Connecting Measurements to Models. *Science* (80-.). **2009**, *326* (December), 1525–1529.
- (44) George, C.; Ammann, M.; D’Anna, B.; Donaldson, D. J.; Nizkorodov, S. A. Heterogeneous Photochemistry in the Atmosphere. *Chem. Rev.* **2015**, *115* (10), 4218–4258.
- (45) Nozière, B. Don’t Forget the Surface. *Science* (80-.). **2016**, *351* (6280), 1396 LP-1397.
- (46) Saito, K.; Sasaki, G.; Okada, K.; Tanaka, S. Unimolecular Decomposition of Pyruvic Acid: An Experimental and Theoretical Study. *J. Phys. Chem.* **1994**, *98*, 3756–3761.
- (47) Plath, K. L.; Takahashi, K.; Skodje, R. T.; Vaida, V. Fundamental and Overtone Vibrational Spectra of Gas-Phase Pyruvic Acid. *J. Phys. Chem. A* **2009**, *113* (26), 7294–7303.

- (48) Rubasinghege, G.; Grassian, V. H. Role(s) of Adsorbed Water in the Surface Chemistry of Environmental Interfaces. *Chem. Commun.* **2013**, 49 (30), 3071–3094.
- (49) Laskina, O.; Young, M. A.; Kleiber, P. D.; Grassian, V. H. Infrared Extinction Spectroscopy and Micro-Raman Spectroscopy of Select Components of Mineral Dust Mixed with Organic Compounds. *J. Geophys. Res. Atmos.* **2013**, 118 (12), 6593–6606.
- (50) Abdelkader, M.; Metzger, S.; Mamouri, R. E.; Astitha, M.; Barrie, L.; Levin, Z.; Lelieveld, J. Dust-Air Pollution Dynamics over the Eastern Mediterranean. *Atmos. Chem. Phys.* **2015**, 15 (16), 9173–9189.
- (51) Fan, S. M.; Horowitz, L. W.; Levy, H.; Moxim, W. J. Impact of Air Pollution on Wet Deposition of Mineral Dust Aerosols. *Geophys. Res. Lett.* **2004**, 31 (2), 2–5.
- (52) Nazaroff, W. W.; Goldstein, A. H. Indoor Chemistry: Research Opportunities and Challenges. *Indoor Air* **2015**, 25 (4), 357–361.
- (53) Weschler, C. J.; Shields, H. C. Potential Reactions among Indoor Pollutants. *Atmos. Environ.* **1997**, 31 (21), 3487–3495.
- (54) Morrison, G. Recent Advances in Indoor Chemistry. *Curr. Sustain. Energy Reports* **2015**, 2 (2), 33–40.
- (55) Morrison, G. Interfacial Chemistry in Indoor Environments. *Environ. Sci. Technol.* **2008**, 42 (10), 3495–3499.
- (56) Singer, B. C.; Hodgson, A. T.; Hotchi, T.; Ming, K. Y.; Sextro, R. G.; Wood, E. E.; Brown, N. J. Sorption of Organic Gases in Residential Rooms. *Atmos. Environ.* **2007**, 41 (15), 3251–3265.
- (57) Yu, B. F.; Hu, Z. B.; Liu, M.; Yang, H. L.; Kong, Q. X.; Liu, Y. H. Review of Research on Air-Conditioning Systems and Indoor Air Quality Control for Human Health. *Int. J. Refrig.* **2009**, 32 (1), 3–20.
- (58) Tham, K. W.; Zuraimi, M. S. Size Relationship between Airborne Viable Bacteria and Particles in a Controlled Indoor Environment Study. *Indoor Air* **2005**, 15 Suppl 9 (Suppl 9), 48–57.
- (59) Sarwar, G.; Corsi, R.; Allen, D.; Weschler, C. The Significance of Secondary Organic Aerosol Formation and Growth in Buildings: Experimental and Computational Evidence. *Atmos. Environ.* **2003**, 37 (9–10), 1365–1381.
- (60) Cox, S. S.; Little, J. C.; Hodgson, A. T. Predicting the Emission Rate of Volatile Organic Compounds from Vinyl Flooring. *Environ. Sci. Technol.* **2002**, 36 (4), 709–714.
- (61) Won, D.; Corsi*, R. L.; Rynes, M. Sorptive Interactions between VOCs and Indoor

Materials. *Indoor Air* **2001**, *11* (4), 246–256.

- (62) Li, F.; Niu, J. An Inverse Approach for Estimating the Initial Distribution of Volatile Organic Compounds in Dry Building Material. *Atmos. Environ.* **2005**, *39* (8), 1447–1455.
- (63) Wainman, T.; Zhang, J.; Weschler, C. J.; Lioy, P. J. Ozone and Limonene in Indoor Air: A Source of Submicron Particle Exposure. *Environ. Health Perspect.* **2000**, *108* (12), 1139–1145.
- (64) Grøntoft, T.; Raychaudhuri, M. R. Compilation of Tables of Surface Deposition Velocities for O₃, NO₂ and SO₂ to a Range of Indoor Surfaces. *Atmos. Environ.* **2004**, *38* (4), 533–544.
- (65) J., W. C. Chemical Reactions among Indoor Pollutants: What We've Learned in the New Millennium. *Indoor Air* *14* (s7), 184–194.
- (66) Weschler, C. J.; Wisthaler, A.; Cowlin, S.; Tamás, G.; Strøm-Tejsen, P.; Hodgson, A. T.; Destailats, H.; Herrington, J.; Zhang, J.; Nazaroff, W. W. Ozone-Initiated Chemistry in an Occupied Simulated Aircraft Cabin. *Environ. Sci. Technol.* **2007**, *41* (17), 6177–6184.
- (67) Wisthaler, A.; Tamás, G.; Wyon, D. P.; Strøm-Tejsen, P.; Space, D.; Beauchamp, J.; Hansel, A.; Märk, T. D.; Weschler, C. J. Products of Ozone-Initiated Chemistry in a Simulated Aircraft Environment. *Environ. Sci. Technol.* **2005**, *39* (13), 4823–4832.
- (68) Sarwar, G.; Corsi, R. The Effects of Ozone/Limonene Reactions on Indoor Secondary Organic Aerosols. *Atmos. Environ.* **2007**, *41* (5), 959–973.
- (69) Tamás, G.; Weschler, C. J.; Toftum, J.; Fanger, P. O. Influence of Ozone-Limonene Reactions on Perceived Air Quality. *Indoor Air* **2006**, *16* (3), 168–178.
- (70) Sarwar, G.; Olson, D. A.; Corsi, R. L.; Weschler, C. J. Indoor Fine Particles: The Role of Terpene Emissions from Consumer Products. *J. Air Waste Manage. Assoc.* **2004**, *54* (3), 367–377.
- (71) Pommer, L.; Fick, J.; Nilsson, C.; Andersson, B. An Experimental Comparison of a Kinetic Model for the Reaction of Alpha-Pinene and Delta(3)-Carene with Ozone and Nitrogen Oxides. *Indoor Air* **2004**, *14 Suppl 8* (Suppl 8), 75–83.
- (72) Fan, Z.; Lioy, P.; Weschler, C.; Fiedler, N.; Kipen, H.; Zhang, J. Ozone-Initiated Reactions with Mixtures of Volatile Organic Compounds under Simulated Indoor Conditions. *Environ. Sci. Technol.* **2003**, *37* (9), 1811–1821.
- (73) Møhlhave, L.; Kjærgaard, S. K.; Sigsgaard, T.; Lebowitz, M. Interaction between Ozone and Airborne Particulate Matter in Office Air. *Indoor Air* **2005**, *15* (6), 383–392.

- (74) Erasto, P.; Viljoen, A. Limonene - A Review : Biosynthetic , Ecological and Pharmacological Relevance This Issue Is Dedicated to Professor Gerhard Buchbauer on the Occasion of His 65Th Birthday. **2008**, No. January.
- (75) Nazaroff, W. W.; Weschler, C. J. Cleaning Products and Air Fresheners: Exposure to Primary and Secondary Air Pollutants. *Atmos. Environ.* **2004**, *38* (18), 2841–2865.
- (76) Wolkoff, P.; Wilkins, C. K.; Clausen, P. A.; Nielsen, G. D. Organic Compounds in Office Environments - Sensory Irritation, Odor, Measurements and the Role of Reactive Chemistry. *Indoor Air* **2006**, *16* (1), 7–19.
- (77) Weschler, C. J.; Shields, H. C. Indoor Ozone/Terpene Reactions as a Source of Indoor Particles. *Atmos. Environ.* **1999**, *33* (15), 2301–2312.
- (78) Li, T. H.; Turpin, B. J.; Shields, H. C.; Weschler, C. J. Indoor Hydrogen Peroxide Derived from Ozone/d-Limonene Reactions. *Environ. Sci. Technol.* **2002**, *36* (15), 3295–3302.
- (79) Wei, Q.; Harada, K.; Ohmori, S.; Minamoto, K.; Wei, C.; Ueda, A. Toxicity Study of the Volatile Constituents of Myoga Utilizing Acute Dermal Irritation Assays and the Guinea-Pig Maximization Test. *J. Occup. Health* **2006**, *48* (6), 480–486.
- (80) Matura, M.; Sköld, M.; Börje, A.; Andersen, K. E.; Bruze, M.; Frosch, P.; Goossens, A.; Johansen, J. D.; Svedman, C.; White, I. R.; et al. Not Only Oxidized R-(+)- but Also S-(-)-Limonene Is a Common Cause of Contact Allergy in Dermatitis Patients in Europe. *Contact Dermatitis* **2006**, *55* (5), 274–279.
- (81) Waring, M. S.; Siegel, J. A. Indoor Secondary Organic Aerosol Formation Initiated from Reactions between Ozone and Surface-Sorbed d -Limonene. *Environ. Sci. Technol.* **2013**, *47* (12), 6341–6348.
- (82) Liu, S.; Thompson, S. L.; Stark, H.; Ziemann, P. J.; Jimenez, J. L. Gas-Phase Carboxylic Acids in a University Classroom: Abundance, Variability, and Sources. *Environ. Sci. Technol.* **2017**, *51* (10), 5454–5463.
- (83) Niklasson, A.; Langer, S.; Arrhenius, K.; Rosell, L.; Bergsten, C.; Johansson, L.; Svensson, J. Air Pollutant Concentrations and Atmospheric Corrosion of Organ Pipes in European Church Environments. *Stud. Conserv.* **2008**, *53* (1), 24–40.
- (84) Piccoli, A.; Fiori, J.; Andrisano, V.; Orioli, M. Determination of Triclosan in Personal Health Care Products by Liquid Chromatography (HPLC). *Farmaco* **2002**, *57* (5), 369–372.
- (85) Yokoyama, Y.; Aragaki, M.; Sato, H.; Tsuchiya, M. Determination of Sweat Constituents by Liquid Ionization Mass Spectrometry. *Anal. Chim. Acta* **1991**, *246* (2), 405–411.

- (86) Fang, L.; Clausen, G.; Fanger, P. O. Impact of Temperature and Humidity on the Perception of Indoor Air Quality. *Indoor Air* **1998**, 8 (2), 80–90.

CHAPTER 2 EXPERIMENTAL METHODS

The research presented in this dissertation used several different experimental methods and techniques to investigate the heterogeneous reactions between atmospheric trace gases with mineral dust aerosol surfaces, and indoor gases with indoor surfaces. In this chapter, multiple experimental methods are discussed in detail, including transmission and attenuated total reflection (ATR) – Fourier Transform Infrared (FTIR) spectroscopy, as well as Quartz Crystal Microbalance (QCM) measurements.

2.1 Methods for Infrared Studies

Infrared (IR) spectroscopy is useful for both gas phase and surface analysis. IR spectroscopy provides invaluable information including: the structure of surface compounds; the characteristic features such as chemical and physical properties of bonds formed between the surface and adsorbed molecules; as well as the existence of gas phase molecules and adsorbed species on the surface. Experiments involving the tested atmospheric acidic gases, and limonene were conducted using a Teflon coated customized infrared cell connected to a glass mixing chamber. Temperature-dependent experiments were conducted using a stainless steel heated sample holder coupled to a heater.

2.1.1 Teflon Coated Fourier Transform Infrared (FTIR) Spectroscopy

Transmission FTIR spectroscopy was used in various experiments including outdoor air with mineral dust surface studies, as well as indoor surface studies. Infrared spectra were collected using a single beam FTIR spectrometer (Thermo Fisher, iS50),

equipped with a liquid nitrogen-cooled narrowband mercury cadmium telluride (MCT) detector having a spectral region from 800 to 4000 cm^{-1} . A commercially available purge air generator (Nano Purification Solutions, CO_2 Adsorption Dryer NDC-600) was used to purge the spectrometer as well as the sample compartment to reduce the H_2O and CO_2 concentrations. The customized FTIR cell used in this setup is made from a Teflon coated stainless steel cube (total inner volume of 177 ± 2 mL) to avoid decomposition of corrosive acidic gases on the walls. A schematic of the FTIR cell and sample holder is shown in Figure 2.1(a). The Teflon coated stainless steel FTIR cell is equipped with two BaF_2 windows (ISP Optics), which were sealed by two stainless steel holders with rubber O-rings. The FTIR cell also consists a Teflon coated sample holder. The sample holder can hold a tungsten grid ($3 \text{ cm} \times 2 \text{ cm}$, 100 mesh/in., 0.002" wire dia., Alfa Aesar) via two removable Teflon coated nickel jaws. In typical experiments, only one half of the tungsten grid is coated with the solid sample of interest, with the other half left blank. Mounted on a linear translator, the surface coated or blank half of the tungsten grid could be probed by the infrared beam after moving the cell to the appropriate position through the IR beam path. The FTIR cell is connected with a glass mixing chamber (volume of 1329 ± 2 mL) via Teflon tubing (75 cm long, 3.3 mm diameter). The mixing chamber contains valves and gas supply bulbs, two absolute pressure transducers (MKS instruments) having ranges from 0.001 to 10.00 Torr and from 0.1 to 1000 Torr, as shown in the schematic in Figure 2.1(b). The mixing chamber is also connected to a two-stage pumping system which consists of a mechanical rough pump for use until 10^{-3} Torr (Alcatel), and a turbo molecular pump for further pumping down to 10^{-5} Torr (Alcatel, 5150 CP). The vacuum system was used before

experiments to clean the entire system and the surfaces by removing the weakly-bonded species. The experimental apparatus has been described previously in detail.^{1,2}

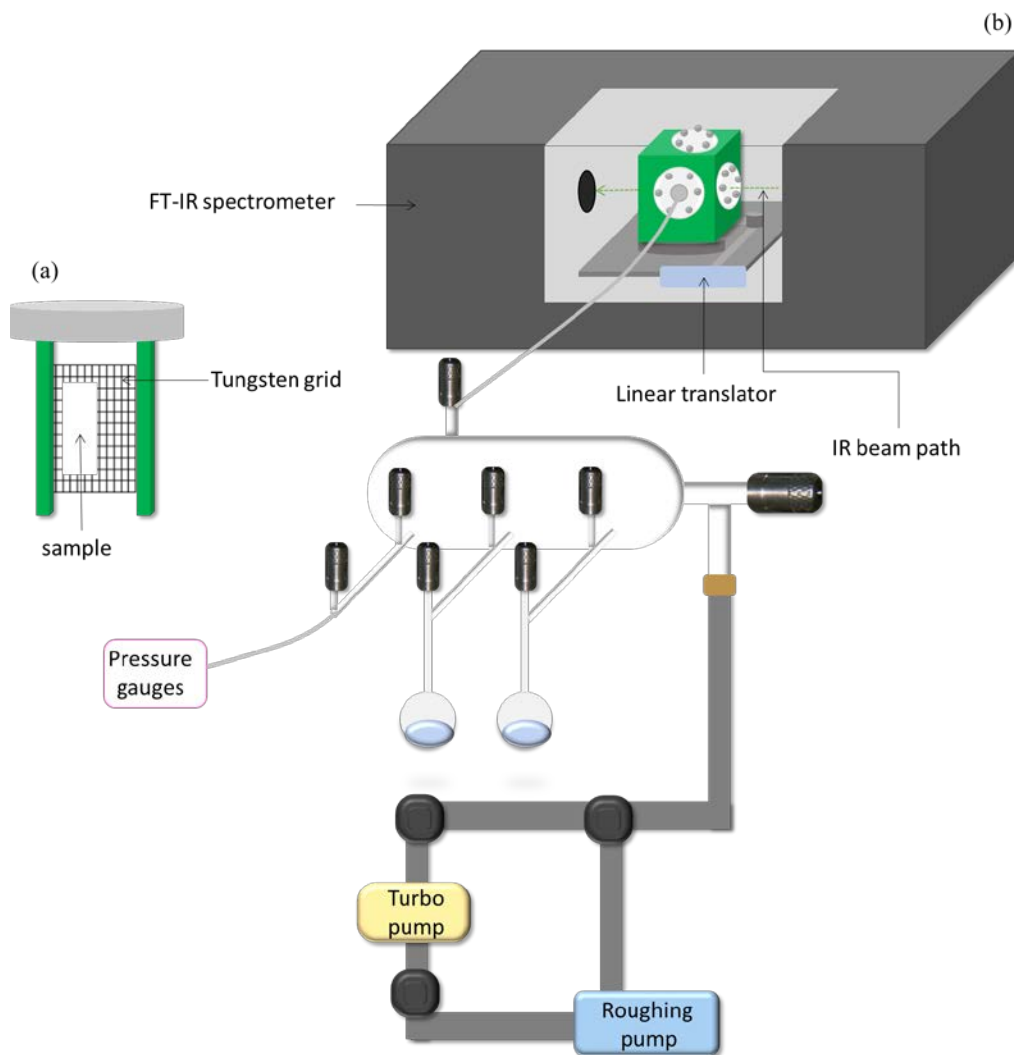


Figure 2.1. Schematic of the Teflon coated transmission FTIR experimental setup. (a) Tungsten grid held by the Teflon coated sample holder with half of the grid covered by the surface sample. (b) Transmission FTIR spectrometer with FTIR cell mounted inside, glass mixing chamber and evacuation system.

For a typical FTIR experiment, about 5 mg of solid surface sample powder: mineral dust samples (SiO_2 , Al_2O_3 and TiO_2); and indoor modeling surfaces (SiO_2 , $\text{CaSO}_4 \cdot 2\text{H}_2\text{O}$, TiO_2), were pressed directly onto one half of a tungsten grid. The tungsten grid, held by

the Teflon coated sample holder, is then placed in the FTIR cell. Usually 300 scans were collected and averaged using OMNIC software using a resolution of 4 cm^{-1} . Absorbance spectra for gas phase and surface species were acquired by reprocessing single beam spectra of the blank half grid and the sample coated half grid after exposure of the reactant gas to the single beam collected prior to gas introduction. To obtain the absorbance spectra of adsorbed surface species after gas phase reactant adsorption, the gas was introduced into the mixing chamber at desired pressures. Equilibrium between the gas phase and adsorbed surface species was achieved when a constant pressure was reached. Spectra of adsorbed surface species were obtained by subtracting gas phase spectra acquired under the same conditions. All FTIR experiments were carried out at 296 K unless otherwise indicated.

2.1.2 Heated Infrared System

The basic design of the heated stainless steel FTIR setup is similar to the FTIR cell with the glass mixing chamber system discussed previously in Section 2.1.1. As shown in Figure 2.2, the heated infrared system has a different sample holder which is specifically designed to carry out temperature dependence experiments. The sample holder can hold a tungsten grid ($3\text{ cm} \times 2\text{ cm}$, 100 mesh/in., 0.002" wire diameter, Alfa Aesar) by two removable nickel jaws. The sample temperature is measured by thermocouple wires are spot-welded to the tungsten grid and an external heater. The external heater (connected with nickel jaws) can resistively heat the tungsten grid as well as the sample coated on the grid. The total volume of the FTIR cell is $327 \pm 3\text{ mL}$. The remainder of the FTIR cell (Teflon coated cube), glass mixing chamber, as well as the vacuum system are identical to those used in the reaction system described earlier (in Section 2.1.1).

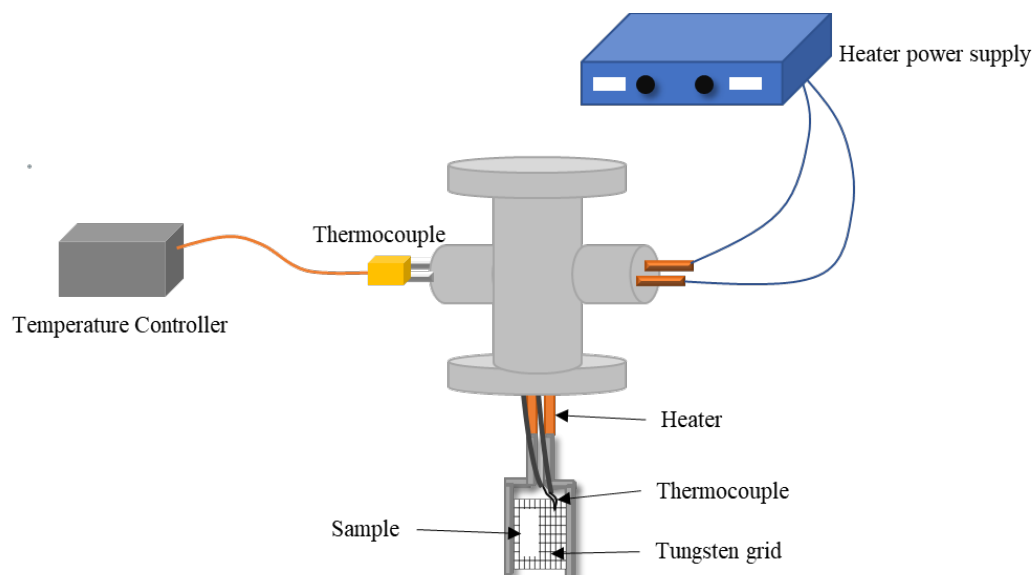


Figure 2.2. Schematic of the stainless-steel transmission FTIR heated sample holder connected to the temperature controller and heater power supply.

2.1.3 Transmission FTIR Spectroscopy: Photochemical Studies

The transmission FTIR setup described in Section 2.1.1 was slightly modified to perform photochemical experiments as shown in Figure 2.3. A 500-Watt mercury arc lamp (Oriel, model no. 66033), containing ultra-violet, visible, and infrared light, was used as a broadband light source. A water filter is applied to remove the unwanted infrared radiation from the Hg arc lamp. The valve connecting the FTIR cell and the mixing chamber was closed after sample preparation and introduction of the reactant gas. Samples were irradiated with full broadband irradiation. During the irradiation, infrared spectra of both surface and gas phase were collected using the same single - beam spectrometer as mentioned in Section 2.1.1. The broadband light source was blocked using a plastic shutter to record the FTIR spectra of surface and gas phase.

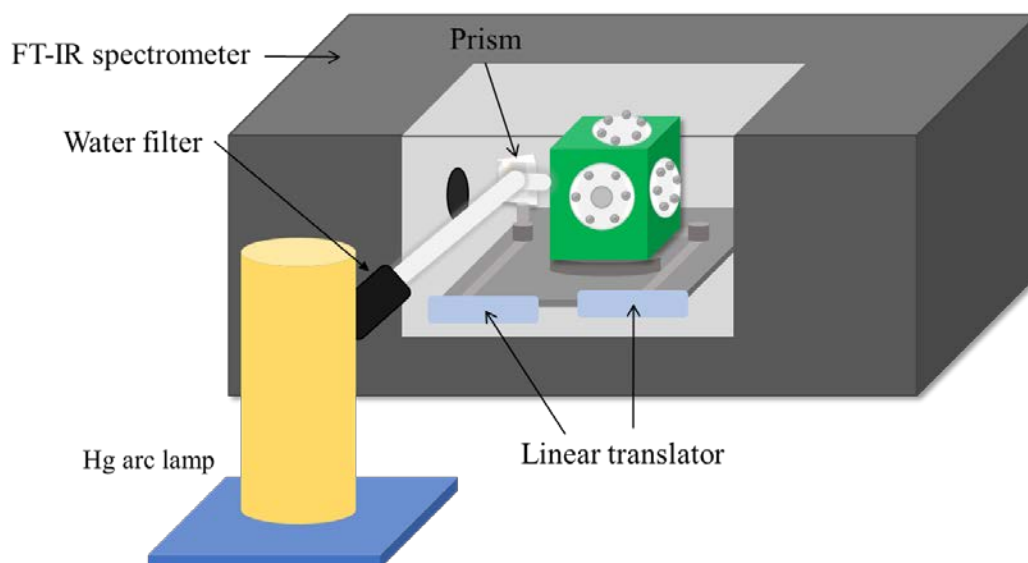


Figure 2.3. Schematic of the optical light path from the Hg arc lamp to the FTIR cell mounted inside the FTIR spectrometer. The sample was irradiated for the desired time, followed by collection of surface and gas phase spectra.

2.1.4 Flowing Board and ATR-FTIR coupled System

Limonene adsorption and the role of adsorbed water were studied using a custom-built flow system. The details of the flow system can be found elsewhere.³ A commercial attenuated total reflection (ATR) horizontal liquid cell apparatus (AMTIR, Pike Technology) was placed in the internal compartment of the FTIR spectrometer. The optics attachment and bottom portion of the liquid cell were used as received, while the top portion of the liquid cell was customized by adding a Teflon cover which contains inlet and outlet ports for gas introduction and a relative humidity sensor. As shown in Figure 2.4, the customized horizontal ATR cell was connected to a flow system. A commercial purge air generator (Nano Purification Solutions, CO₂ Adsorption Dryer NDC-600) was used as the dry air source for the flow system. Dry air was initially passed through Hydro-purge filters (Altech Associates, Inc) to remove any remaining moisture, oil and organics.

The relative humidity (RH) was measured using a relative humidity sensor (EK-H4, Sensirion) The flow system was continuously purged with dry air ($\text{RH} < 3 \%$) for heterogenous experiments performed under dry conditions. The reactant gas was generated by flowing dry air through the reactant bubbler. For relative humidity experiments, wet air was generated by water bubblers and mixed with dry air and equilibrated in a mixing chamber. The flow rate was controlled and measured using mass flow controller/meter(s) (MKS instruments). The desired relative humidity was achieved by reducing the amount of dry air and increasing the amount of wet air flowing through the system. An RH sensor was used to monitor the real time relative humidity inside the Teflon cover during the experiments. Once the desired relative humidity was reached, it was allowed to stabilize for at least 20 minutes.

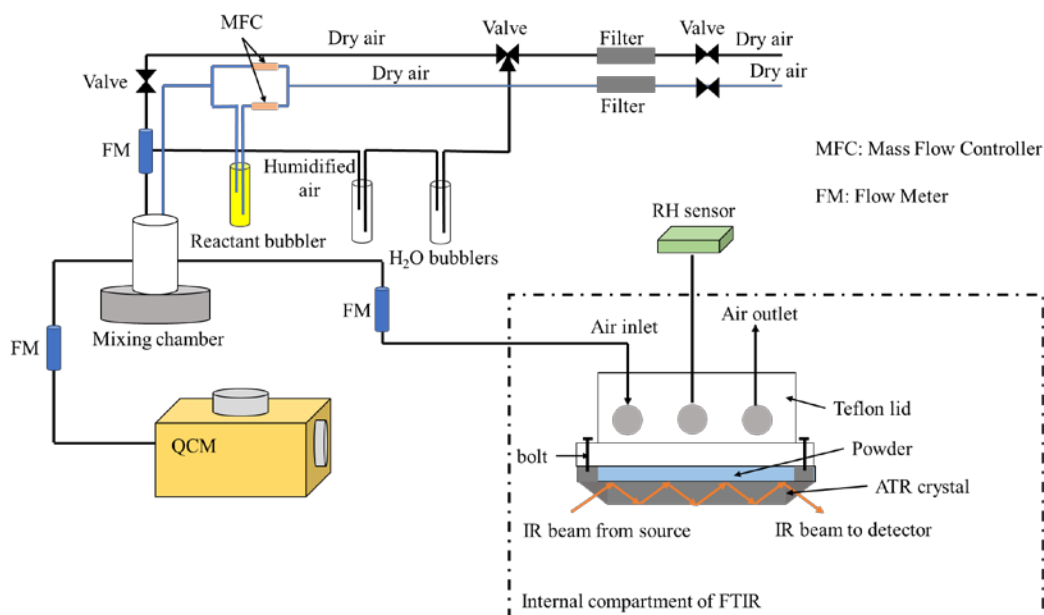


Figure 2.4. Schematic of the flow system which allows for measurements using the Quartz Crystal Microbalance (QCM) and the ATR – FTIR spectrometer simultaneously. Note that only the ATR – FTIR portion was used in the dissertation research. (Adapt from Schuttlefield et al. (2007))

ATR-FTIR infrared spectra were collected using a single beam Thermo Nicolet 6700 FTIR Spectrometer, equipped with a liquid-nitrogen-cooled narrow-band mercury cadmium telluride (MCT) detector. The purge air generator mentioned previously was used to purge the FTIR spectrometer and the sample compartment. Typically, 300 scans were acquired with a resolution of 4 cm^{-1} over the spectral region from 750 to 4000 cm^{-1} using the AMTIR ATR crystal. A thin film (15 mg) of the sample (SiO_2 , TiO_2 and $\text{CaSO}_4 \cdot 2\text{H}_2\text{O}$) was prepared by suspending the particles in 1mL milli-Q water (Milli-Q Advantage A10 System, Millipore SAS, resistivity = $18.2\text{ M}\Omega\cdot\text{cm}$, 298 K). The suspension was sonicated for at least 10 minutes and then applied to the horizontal cell. The water was allowed to evaporate under dry air purge overnight in the sample compartment, allowing a uniform

dispersion of particles on the cell. Spectra were referenced to the AMTIR ATR-FTIR crystal without applying any sample under dry conditions ($RH < 3\%$).

2.1.5 Gas Phase Diffusion Measurements and Correction

The integrated absorbance peak area from the adsorbed species only was acquired via correction using spectral subtraction of the gas-phase spectra at adsorption equilibrium, as expressed in (E2.1)

$$A_{\text{ads, eq}} = A_{\text{c, eq}} - A_{\text{g, eq}} \quad (\text{E2.1}),$$

where: $A_{\text{ads, eq}}$ represents the integrated peak area of surface adsorbate on the surface at adsorption equilibrium; $A_{\text{g, eq}}$ represents the gaseous phase integrated peak area; and $A_{\text{c, eq}}$ is the integrated peak area collected with the infrared beam probing surface.

However, unlike equilibrium measurements, gas-phase spectra were not collected during the kinetics experiments. Therefore, real-time gas-phase contribution can only be corrected by gas-phase diffusion measurements. Gas-phase diffusion studies were carried out under the same conditions as the kinetics measurements which required correction via spectral subtraction. The desired amount of limonene was introduced into the infrared cell as described above for surface measurement, while infrared beam probes the gas phase during the experiments.

The gas-phase spectra were collected using a Macro by averaging 10 scans. $A_{\text{g, T}}$ is obtained from averaged triplicate gas-phase diffusion measurements by integrating absorbance peak areas of the same vibrational modes from the spectrum collected at time T. The integrated peak area of the adsorbed species at time T ($A_{\text{ads, T}}$) can then be corrected using equation (E2.2):

$$A_{\text{ads}, T} = A_{c, T} - A_{g, T} \quad (\text{E2.2}),$$

where: $A_{\text{ads}, T}$ represents the integrated peak area of the adsorbate on the surface at time T; $A_{g, T}$ is the integrated peak area of the gas-phase contribution at time T; and $A_{c, T}$ denotes the integrated peak area collected during the kinetics measurements at the same time.

In addition, temporal evolution of the gas-phase pressure inside the infrared cell can also be obtained from gas-phase diffusion experiments. A conversion factor (C_f) can be obtained by dividing the adsorption equilibrium pressure (P_{eq}) (recorded from the pressure gauge) by $A_{g, \text{eq}}$:

$$C_f = \frac{P_{\text{eq}}}{A_{g, \text{eq}}} \quad (\text{E2.3})$$

The gas-phase pressure at time T (P_T) can subsequently be calculated using (E2.4):

$$P_T = C_f \times A_{g, T} \quad (\text{E2.4})$$

2.2 Complementary Physicochemical Characterization Methods

2.2.1 Mass Spectroscopy (MS)

Insight into the precise chemical composition of the oxidation products observed in the study was obtained using direct-injection linear ion trap (ThermoFisher Orbitrap) mass spectrometry (MS). Samples taken prior to and following absorption-desorption processes for the selected solid nanoparticles were removed from the substrate using acetonitrile (LC-MS Optima-grade) and methanol (Fisher Scientific). Sample vial, syringe, and all other glassware used in the transfer process were cleaned prior to use with acetonitrile and Milli-Q water [18.2 M Ω .cm] and baked in an oven at 500 °C to further remove trace organics. All samples were stored at -20 °C and analyzed within 24 hours of collection.

Analysis in both positive and negative mode was used. Most detected ions were observed in negative mode ($[M-H]^-$). The heated electrospray ionization (HESI) source was operated at 50°C. The ESI capillary was set to a voltage of 2.8 kV at 325°C. Internal standards in negative mode included high-purity deuterated Hexanoic-d₁₁ Acid and Octanoic-d₁₅ Acid (CDN Isotopes). Positive mode internal standards included Hexylamine (99%) and Hexadecylamine (98%) (both purchased from Sigma-Aldrich). The HESI-Orbitrap MS was calibrated prior to use. Spectra were acquired with a mass range of 80-2000 Da. Peaks with a mass error > 2 ppm were rejected and were calculated for composition with the following element ranges: ¹²C, 0-30; ¹H, 0-50; ¹⁶O, 0-10. Contamination was minimized by employing method and instrumental blanks.

2.2.2 BET Surface Area Measurement

Surface areas of surface particle samples were measured using a BET surface area analyzer (Quantachrome 4200e). In this study, N₂ is introduced into a calibrated sample cell (cooled by liquid nitrogen) that allows dedicated study of the adsorption of the N₂. Relative pressures, (P/P₀), of the N₂ introduced and the adsorption of N₂ (W) is measured. Total surface areas were calculated using the cross-section of N₂ molecules.

A surface area per unit mass is given by dividing the total surface area by the sample mass. Seven-point N₂-BET adsorption isotherm measurements were used to determine the specific surface area of particles using the following equation (E2.5) among the limited linear range of the BET isotherm:

$$\frac{1}{\left(\frac{P_0}{P}\right)-1} = \frac{1}{W_m C} + \frac{C-1}{W_m C} \left(\frac{P}{P_0}\right) \quad (\text{E2.5})$$

In (E2.5): W_m is the weight of adsorbate constituting one monolayer of coverage; and C is a constant. W_m and C are determined by the slope and intercept obtained by plotting $\frac{1}{W\left(\frac{P_0}{P}\right)-1}$ versus $\frac{P}{P_0}$. Samples were degassed overnight prior to analysis.

2.3 Chemicals

2.3.1 Particle Samples

To study the heterogenous interactions between outdoor and indoor relevant gases on surfaces, oxide particles were used as received. The surface oxide samples included: SiO₂ (Degussa, OX50), γ - Al₂O₃ (Degussa, AlumOxid C), TiO₂ (P25, Sigma Aldrich) and CaSO₄ · 2H₂O (MP Biomedicals).

2.3.2 Liquid and Gas Reagents

Milli-Q water was generated by Milli-Q Advantage A10 System (Millipore SAS). Dry gaseous nitric acid vapor was produced from the vapor of a 1 : 3 ratio mixture of concentrated nitric acid (HNO₃, 70%, Sigma Aldrich) and sulfuric acid (H₂SO₄, 95.9% Mallinckrodt). Formic acid (HCOOH, 97%, Alfa Aesar), acetic acid (CH₃COOH, ≥99.7% w/w, Fisher Scientific), pyruvic acid (CH₃COCOOH, 97%, Alfa Aesar), (+) - Limonene (C₁₀H₁₆, > 99%, Fisher Scientific), cyclohexane (C₆H₁₂, 99.9%, Fisher Scientific), benzene (C₆H₆, ≥ 99.9, Sigma Aldrich) and cyclohexene (C₆H₁₀, 99%, Sigma Aldrich) were degassed at least three times with consecutive freeze-pump-thaw cycles prior to use.

Varying concentrations of lactic acid (CH₃C(OH)₂COOH, 85% w/w, Fisher Chemical) (1, 5, 10, 25, 50 and 100 mM) were prepared via dissolution in Milli-Q water prior to experiments.

2.4 References

- (1) Goodman, A. L.; Bernard, E. T.; Grassian, V. H. Spectroscopic Study of Nitric Acid and Water Adsorption on Oxide Particles: Enhanced Nitric Acid Uptake Kinetics in the Presence of Adsorbed Water. *J. Phys. Chem. A* **2001**, *105* (26), 6443–6457.
- (2) Fang, Y.; Tang, M.; Grassian, V. H. Competition between Displacement and Dissociation of a Strong Acid Compared to a Weak Acid Adsorbed on Silica Particle Surfaces: The Role of Adsorbed Water. *J. Phys. Chem. A* **2016**, *120* (23), 4016–4024.
- (3) Schuttlefield, J.; Al-Hosney, H.; Zachariah, A.; Grassian, V. H. Attenuated Total Reflection Fourier Transform Infrared Spectroscopy to Investigate Water Uptake and Phase Transitions in Atmospherically Relevant Particles. *Appl. Spectrosc.* **2007**, *61* (3), 283–292.

CHAPTER 3 COMPETITION BETWEEN SURFACE DISPLACEMENT AND DISSOCIATIVE ADSORPTION OF A STRONG ACID COMPARED TO A WEAK ACID ON SILICA PARTICLE SURFACES: THE ROLE OF ADSORBED WATER

3.1 Abstract

The adsorption of nitric (HNO_3) and formic (HCOOH) acid on silica particle surfaces and the effect of adsorbed water have been investigated at 296 K using transmission FTIR spectroscopy. Under dry conditions, both nitric and formic acids adsorb reversibly on silica. Additionally, the FTIR spectra show that both of these molecules remain in the protonated form. At elevated relative humidities (RH), adsorbed water competes both for surface adsorption sites with these acids as well as promotes their dissociation to hydronium ions and corresponding anions. Compared to HNO_3 , the extent of dissociation is much smaller for HCOOH , very likely due to its weaker acidity. This study provides valuable insights into the interaction of HNO_3 and HCOOH with silica surface on the molecular level, and further reveals the complex roles of surface-adsorbed water in atmospheric heterogeneous chemistry of mineral dust particles – many of these containing silica.

3.2 Introduction

Mineral dust aerosol is ubiquitous in the atmosphere,¹ and reactions on the surface of mineral dust particles play an important role in atmospheric chemistry.^{2,3} Heterogeneous reactions of mineral dust particles can impact the concentrations of important trace gases and radicals (such as NO_x, O₃, and HO_x)^{4,5} and modify aerosol particle composition,^{6,7} which in turn leads to changes in the ability of dust particles to serve as cloud condensation nuclei (CCN)⁸⁻¹² and ice nuclei (IN).¹²⁻¹⁵ Nitric acid (HNO₃) and formic acid (HCOOH) are among the most abundant acidic gases in the troposphere,^{16,17} and their heterogeneous reactions are of great interest. As such, a number of studies have investigated the heterogeneous reactions of mineral dust particles with HNO₃¹⁸⁻²³ and HCOOH.²⁴⁻²⁹

Silica (SiO₂) is a major component of mineral dust particles in the atmosphere.^{2,30,31} It is a neutral oxide with abundant surface hydroxyl groups¹⁸ and several studies have investigated heterogeneous reaction of silica with acidic atmospheric gases. For example, using a Knudsen cell reactor, the uptake coefficient of HNO₃, $\gamma(\text{HNO}_3)$, was reported to be $(2.9 \pm 2) \times 10^{-5}$ for silica particles.²⁰ Vlasenko et al.²³ investigated the uptake of HNO₃ onto silica aerosol particles at room temperature using an aerosol flow tube, and $\gamma(\text{HNO}_3)$ was found to be smaller than 5×10^{-4} at 33% RH. Goodman et al.¹⁸ used transmission FTIR to study the heterogeneous reaction of HNO₃ with silica, and found that HNO₃ is molecularly and reversibly adsorbed on silica surface although the effect of RH was not thoroughly investigated. However, previous studies suggested that exposure to HNO₃ could enhance the water uptake by silica particles.^{32,33}

The uptake of HCOOH by CaCO₃,²⁴ clay minerals,^{25,28} TiO₂,²⁹ Al₂O₃,²⁶⁻²⁸ and silica²⁸ has been examined previously. Using diffuse reflectance infrared Fourier transform

spectroscopy (DRIFTS), Tong et al.²⁶ studied the uptake of HCOOH by α -Al₂O₃ at room temperature, and found that the uptake coefficients increase with RH for RH below 20%, and then decrease with RH. The effect of temperature on the uptake of HCOOH by α -Al₂O₃ was also explored.²⁷ Attenuated Total Reflection-Fourier Transmission Infrared Spectroscopy (ATR-FTIR) and Quartz Crystal Microbalance (QCM) were used to investigate the heterogeneous uptake of HCOOH by silica and γ -Al₂O₃.²⁸ It was found that under dry conditions (RH <1%), HCOOH is reversibly and molecularly adsorbed on silica surface. In contrast, the adsorption of HCOOH on γ -Al₂O₃ is not entirely reversible under dry conditions, and the irreversibly adsorbed HCOOH is dissociated, leading to the formation of a thin layer of adsorbed formate.²⁸ HCOOH was also found to be both irreversibly and reversibly adsorbed on TiO₂ surface under dry conditions, and increasing RH could enhance the uptake of HCOOH.²⁹

Despite the fact that heterogeneous interactions of silica with HNO₃ and HCOOH have been investigated in several previous studies, mechanisms for these reactions at the molecular level are still not completely understood. Specifically, it is still largely unknown how adsorbed water will affect their heterogeneous reactions with silica particle surfaces. In this study, transmission FTIR spectroscopy has been used to study the adsorption of HNO₃ and HCOOH at different RH. These two acids were chosen because HNO₃ is considered as a strong acid with complete dissociation in bulk water while HCOOH is considered a weaker acid with protonated and deprotonated forms existing in equilibrium and the extent of deprotonation being pH dependent in bulk solution. This study of their interactions with silica particle surfaces may shed light on mechanisms of interactions of silica and other surfaces with acidic gases of varying strength of acidity.

3.3 Experimental Section

Nitric acid (HNO_3) and formic acid (HCOOH) adsorption on hydroxylated silica surfaces at different relative humidity (RH) was studied using a modified Teflon coated infrared cell coupled with transmission Fourier transform infrared (FTIR) spectroscopy, as described in previous studies.^{18,34} All the experiments were carried out at 296 ± 1 K. For these experiments, around 10 mg silica (Degussa, with a BET surface area of $230 \text{ m}^2 \text{ g}^{-1}$) were pressed onto one half of a tungsten grid which was held by two Teflon-coated jaws in the Teflon-coated reaction cell. The reaction cell was connected to a Pyrex glass mixing chamber via two short Teflon tubes joint by a fluorinated ethylene propylene (FEP) valve. The following steps were used to start and terminate the gas-particle interactions:

First, the reaction cell and the mixing chamber were evacuated for 6 hours using a turbo-molecular pump to clean the cell and sample surface. Second, after evacuation, the reaction cell and the mixing chamber were isolated by closing the FEP valve. HNO_3 or HCOOH vapor with a given pressure was introduced into the mixing chamber. For relative humidity experiments, water vapor of a given pressure was subsequently introduced into the mixing chamber. The pressure changes due to introduction of vapors into the mixing chamber was monitored by two absolute pressure transducers. Third, the FEP valve was opened in order to introduce the gas mixture into the reaction cell. This resulted in a small pressure drop, which was taken into account when we reported initial pressures of HNO_3 , HCOOH , and water vapor. Pressures of gaseous acids are reported as initial pressures, as we did in our previous studies.^{18,28,29,34} Finally, after no significant changes were observed for silica particles by FTIR (with a typical exposure time of 20 min), the reaction cell and the mixing chamber were evacuated so that the heterogeneous interaction was terminated.

The evacuation was carried out overnight using a turbo-molecular pump to remove the weakly bonded surface species.

Three different types of experiments were conducted in our work: i) silica particles were exposed to $\text{HNO}_3(\text{g})$ or $\text{HCOOH}(\text{g})$ of different pressure under dry conditions; ii) particles were exposed to $\text{HNO}_3(\text{g})$ or $\text{HCOOH}(\text{g})$ of different pressures at a given elevated RH; and iii) silica was exposed to $\text{HNO}_3(\text{g})$ or $\text{HCOOH}(\text{g})$ of a given pressure at different RH. It should be emphasized that using the experimental procedures described above, silica particles were always simultaneously exposed to one of the gaseous acid and water vapor when water vapor was used.

The single beam spectra of surface and gas phase (250 scans) were acquired at a resolution of 4 cm^{-1} at 298 K in the $800\text{ to }4000\text{ cm}^{-1}$ spectral range prior to and after the exposure of acidic gases. Silica is opaque below $\sim 1200\text{ cm}^{-1}$ and therefore only spectra above 1200 cm^{-1} are shown. During the exposure, single beam spectra of surface (10 scans) were acquired by using a Macro (FTIR software) with an interval of 10 seconds. Absorbance spectra of HNO_3 or HCOOH on silica particles were reported as the difference in spectra of silica before and after exposure to HNO_3 or HCOOH . Absorption bands due to $\text{HNO}_3(\text{g})$ or $\text{HCOOH}(\text{g})$, measured through the blank half of the tungsten grid, were subtracted in order to get FTIR spectra of particles loaded on the tungsten grid.

Dry gaseous HNO_3 , HCOOH , and water vapor were produced from the vapor of a 1:3 mixture of concentrated HNO_3 (70%, Sigma-Aldrich) and H_2SO_4 (95.9%, Mallinckrodt), HCOOH (97%, Alfa Aesar), and HPLC grade water (Fisher Chemicals), respectively. Prior to use, all the liquid samples were degassed several times with consecutive freeze-pump-thaw cycles.

3.4 Results and Discussion

3.4.1 Adsorption of HNO₃ on silica

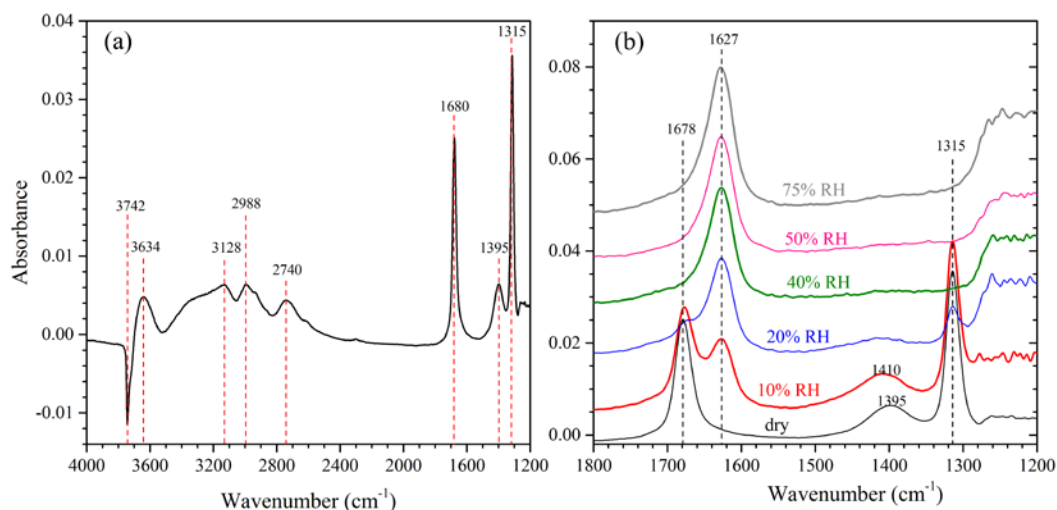


Figure 3.1. (a) A typical FTIR spectrum (1200 to 4000 cm⁻¹) of silica particles after exposure to 100 mTorr HNO₃(g) under dry condition. (b) FTIR spectra (1200 to 1800 cm⁻¹) of silica particles after exposure to 100 mTorr HNO₃(g) at different RH.

Figure 3.1a shows a spectrum of silica particles after being exposed to HNO₃(g) at dry condition (RH <1%). The spectral features at 1680, 1395, and 1315 cm⁻¹ can be assigned to $\nu_a(\text{NO}_2)$, $\delta(\text{OH})$, and $\nu_s(\text{NO}_2)$ of molecularly adsorbed HNO₃ on the surface.^{18,35,36} The broad absorption band extending from 2600 to 3800 cm⁻¹, with peaks at 2740, 2988, 3128, and 3634 cm⁻¹, is attributed to the O-H vibration mode of HNO₃(a) (i.e. molecularly adsorbed nitric acid) and surface hydroxyl groups involved in hydrogen-bonding interactions.¹⁸ As shown in Figure 3.1a, exposure of silica surface to HNO₃(g) under dry condition leads to a negative peak at 3742 cm⁻¹. This is due to isolated silanol groups on the silica surface hydrogen bonding with HNO₃(a) which causes a shift in the vibrational frequency.^{26,37}

All of these bands disappeared upon evacuation of the reaction chamber. In particular, absorption peaks at 1680, 1395, and 1315 cm^{-1} , due to $\text{HNO}_3(\text{a})$, disappeared as well as the bands at 2740, 2988 and 3128 cm^{-1} , while the 3742 cm^{-1} peak due to isolated O-H groups reappeared, suggesting that HNO_3 was reversibly adsorbed on silica surface. These results are in agreement with the earlier work of Goodman et al.¹⁸

3.4.1.1 Effect of relative humidity

The adsorption of HNO_3 on silica was then systematically studied at different RH (<1%, 10%, 20%, 40%, 50%, and 75%) to investigate the effect of surface adsorbed water, $\text{H}_2\text{O}(\text{a})$. In these experiments, the silica surface was exposed to 100 mTorr $\text{HNO}_3(\text{g})$ and RH was varied. The IR spectra of silica particles between 1200 and 1800 cm^{-1} , after exposure to 100 mTorr $\text{HNO}_3(\text{g})$ and different RH, are shown in Figure 3.1b. For comparison, the spectrum of adsorbed nitric acid under dry condition is also included.

The amount of $\text{H}_2\text{O}(\text{a})$ increases with RH, as suggested by the increase of absorption band at 1627 cm^{-1} in Figure 3.1b, which is attributed to the water bending mode.³⁸ In contrast, the intensities of peaks near 1680, 1395, and 1315 cm^{-1} due to $\text{HNO}_3(\text{a})$ decrease with increasing RH. Above 40% RH these peaks disappear completely and cannot be distinguished from the baseline. Furthermore, as shown in Figure 3.1b, the three IR peaks for $\text{HNO}_3(\text{a})$, were observed to shift from 1680, 1395, and 1315 cm^{-1} under dry condition to 1678, 1410, and 1310 cm^{-1} at 10% RH, respectively. This suggests that nitric acid molecules adsorbed on the silica surface are interacting with adsorbed water.

In this study, peaking fitting has been applied to peaks which have significant overlaps (for example, the two peaks at 1627 and 1678 cm^{-1} shown in Figure 3.1b), in order to determine correct peak areas. Though the peak at 1627 cm^{-1} is asymmetric, fitting it with

a single Gaussian function generates fairly similar results for fitting it with two Gaussian functions with a constant ratio. Thus, for simplicity, the results with the single Gaussian function fitting are reported. Peak areas of the infrared bands for H₂O(a) (1627 cm⁻¹) and HNO₃(a) (1315 cm⁻¹), as a function of RH, are shown in Figure 3.2, suggesting that the overall trend is that the amount of H₂O(a) increases while the amount of HNO₃(a) decreases with increasing RH. Peak areas of H₂O(a) on silica particles in the absence of HNO₃(g) at several different RH are also plotted in Figure 3.2. It is observed that at 10% and 20% RH, the amounts of H₂O(a) on silica particles in the presence of 100 mTorr HNO₃(g) are larger than those in the absence of HNO₃(g) at the same RH. As RH increases to 40%, the amounts of H₂O(a) become equal within the experimental uncertainties.

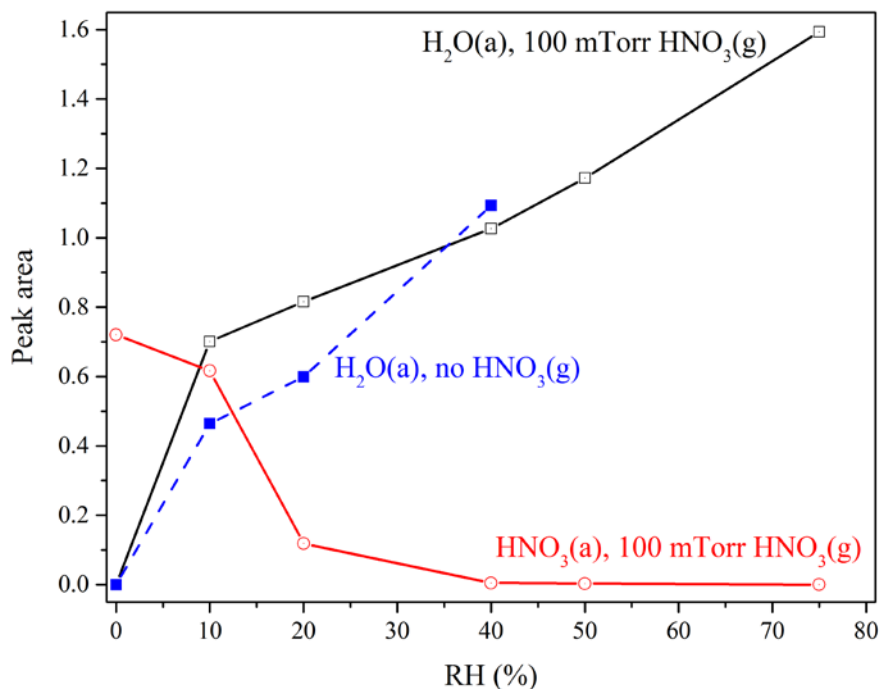


Figure 3.2. Peak areas of infrared absorption bands for H₂O(a) (1627 cm⁻¹, open squares) and HNO₃(a) (1315 cm⁻¹, open circles) on silica as a function of RH, after exposure to 100 mTorr HNO₃(g). For comparison H₂O(a) (solid squares) in the absence of HNO₃(a) is plotted as a function of RH.

Peak fitting was applied to IR spectra in the ranges of 1280 to 1800 cm^{-1} of silica particles after exposure to $\text{HNO}_3(\text{g})$ at 10% RH. In the region for $\text{H}_2\text{O}(\text{a})$ (1550-1800 cm^{-1}), three IR peaks can be identified, as shown in Figure 3.3a. In addition to the peak at 1627 cm^{-1} for $\text{H}_2\text{O}(\text{a})$ and 1678 cm^{-1} for $\text{HNO}_3(\text{a})$, a new peak at 1727 cm^{-1} can be identified, which is assigned to adsorbed hydronium ions, $\text{H}_3\text{O}^+(\text{a})$.³⁹⁻⁴² The presence of this band suggests that some of the $\text{HNO}_3(\text{a})$ are dissociated on the surface leading to the formation of $\text{H}_3\text{O}^+(\text{a})$ and $\text{NO}_3^-(\text{a})$, possibly as ion contact pairs on the surface. The dissociation of $\text{HNO}_3(\text{a})$ to $\text{H}_3\text{O}^+(\text{a})$ and $\text{NO}_3^-(\text{a})$ has been previously observed on $\gamma\text{-Al}_2\text{O}_3$ surface.³⁹ Figure 3.3b reveals that the broad absorption band in the range of 1280-1550 cm^{-1} can be fitted with four IR peaks, among which the two at 1315 and 1405 cm^{-1} are due to $\nu_s(\text{NO}_2)$ and $\delta(\text{OH})$ of $\text{HNO}_3(\text{a})$. The other two peaks at 1455 and 1355 cm^{-1} can be assigned to the splitting of the symmetric stretching mode of $\text{NO}_3^-(\text{a})$, formed from the solvation and dissociation of $\text{HNO}_3(\text{a})$ by $\text{H}_2\text{O}(\text{a})$ on the surface,³⁹ further suggesting that some of $\text{HNO}_3(\text{a})$ on silica surface are dissociated in the presence of $\text{H}_2\text{O}(\text{a})$.³⁹

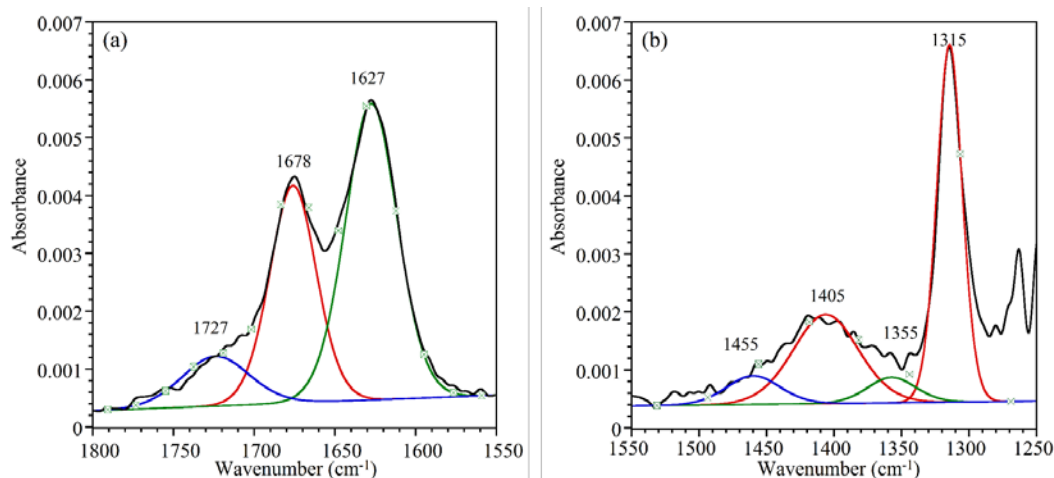


Figure 3.3. Peak fitting results of IR absorption in the range of (a) 1550 to 1800 cm^{-1} and (b) 1250 to 1550 cm^{-1} for silica particles after exposure to 100 mTorr $\text{HNO}_3(\text{g})$ at 10% RH. These bands correspond to multiple species present on the surface, including $\text{HNO}_3(\text{a})$ at 1315, 1405 and 1678 cm^{-1} , $\text{H}_2\text{O}(\text{a})$ at 1627 cm^{-1} , $\text{H}_3\text{O}^+(\text{a})$ at 1727 cm^{-1} , and $\text{NO}_3^-(\text{a})$ at 1355 and 1455 cm^{-1} .

3.4.1.2 Effect of HNO_3 gas-phase concentration

To further understand the interaction of $\text{HNO}_3(\text{a})$ with the silica surface in the presence of $\text{H}_2\text{O}(\text{g})$, a series of experiments were carried out by maintaining the RH at 10% while varying the $\text{HNO}_3(\text{g})$ pressure (50, 100, 200, 300, and 500 mTorr). A complete monolayer of $\text{H}_2\text{O}(\text{a})$ is formed on silica surface at around 20% RH,¹⁸ largely limiting the amount of $\text{HNO}_3(\text{a})$ (and $\text{HCOOH}(\text{a})$ as well) formed on the surface; in order to increase the signal of $\text{HNO}_3(\text{a})$, 10% RH was used in our experiments under which only a sub-monolayer of $\text{H}_2\text{O}(\text{a})$ is formed on the surface. FTIR spectra between 1550 and 1750 cm^{-1} of silica particles exposed to $\text{HNO}_3(\text{g})$ of different pressures at 10% RH are shown in Figure 3.4. In addition to the peak at 1627 cm^{-1} assigned to $\text{H}_2\text{O}(\text{a})$ and that at 1678 cm^{-1} assigned to $\text{HNO}_3(\text{a})$, a third peak at 1727 cm^{-1} which can be attributed to $\text{H}_3\text{O}^+(\text{a})$ becomes evident. As discussed below, the $\text{H}_3\text{O}^+(\text{a})$ peak intensity increases with $\text{HNO}_3(\text{g})$ pressure.

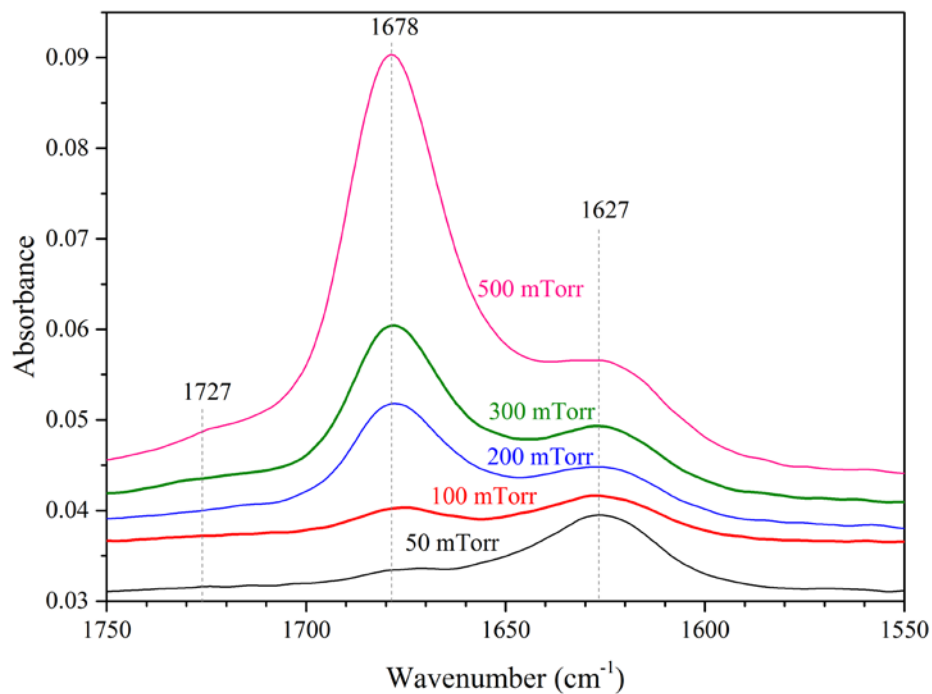


Figure 3.4. FTIR spectra (between 1550 and 1750 cm^{-1}) of silica particles after exposure to $\text{HNO}_3(\text{g})$ of different pressure at 10% RH.

As shown in Figure 3.4, peaks assigned to $\text{H}_3\text{O}^+(\text{a})$ at 1727 cm^{-1} , $\text{HNO}_3(\text{a})$ at 1678 cm^{-1} , and $\text{H}_2\text{O}(\text{a})$ at 1627 cm^{-1} are significantly overlapped. Therefore, peak fitting has been applied to IR spectra (of silica being exposure to $\text{HNO}_3(\text{g})$ of different pressure at 10% RH) in the range of 1550 to 1800 cm^{-1} to better determine peak areas, with a typical peaking fitting shown in Figure 3.3a for 100 mTorr $\text{HNO}_3(\text{g})$.

These peak areas are plotted for $\text{H}_3\text{O}^+(\text{a})$ (1727 cm^{-1} , open circles), $\text{HNO}_3(\text{a})$ (1315 cm^{-1} , open triangles), and $\text{H}_2\text{O}(\text{a})$ (1627 cm^{-1} , open squares) in Figure 3.5 as a function of $\text{HNO}_3(\text{g})$ pressure. As $\text{HNO}_3(\text{g})$ pressure increases, the amounts of $\text{HNO}_3(\text{a})$ and $\text{H}_3\text{O}^+(\text{a})$ on the silica surface both increase. Though the occurrence of the two peaks attributed to $\text{NO}_3^-(\text{a})$ at 1455 and 1355 cm^{-1} is evident from Figure 3.3b, these two peaks have large overlaps with two much more intensive peaks at 1315 and 1405 cm^{-1} due to

HNO₃(a), precluding us from further quantitative analysis. In addition, peak areas of HNO₃(a) as a function of HNO₃(g) pressure under dry conditions are also included in Figure 3.5.

While all the experiments were all carried out at 10% RH, Figure 3.5 shows that the amount of H₂O(a) first decreases when HNO₃(g) pressure increases from 50 to 100 mTorr, potentially due to competition of sites. However, after that the amount of H₂O(a) increases with increasing HNO₃(g) pressure, suggesting that partitioning of water to the surface changes with nitric acid dissociation leading to more adsorbed water when ions are present on the surface. This indicates that there is a minimum number of water molecules needed for dissociation and solvation. Earlier studies^{18,38,43} suggest that ~20% RH corresponds to one monolayer coverage of water on the surface of SiO₂. However, the question is how uniform this layer is. Molecular dynamic simulations^{44,45} have shown that water layers in dynamic equilibrium with water vapor at room temperature can be quite “patchy” with the co-existence between isolated water molecules, water clusters and even bare sites on the surface – even at RH much greater than the expected fully covered, complete monolayer of adsorbed water is not achieved. This is also supported by experimental work in which sum frequency generation spectroscopy was used to study water adsorption on Al₂O₃⁴⁶ and SiO₂,⁴⁷ suggesting that the distribution of adsorbed water is not uniform on mineral surfaces.

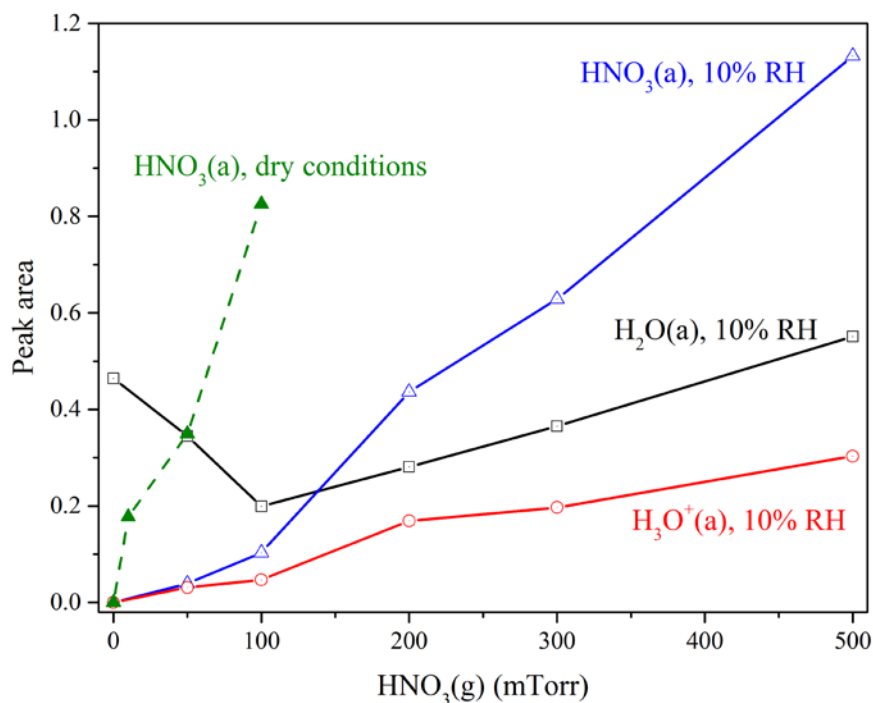
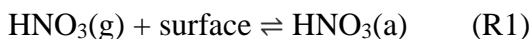


Figure 3.5. Intensities (represented by peak area) of IR absorption peaks at 1627 cm^{-1} for $\text{H}_2\text{O}(\text{a})$ (open squares), 1315 cm^{-1} for $\text{HNO}_3(\text{a})$ (open triangles), and 1727 cm^{-1} for $\text{H}_3\text{O}^+(\text{a})$ (open circles) as a function of $\text{HNO}_3(\text{g})$ pressure at 10% RH. For comparison $\text{HNO}_3(\text{a})$ (solid triangles) at dry conditions is also plotted as a function of $\text{HNO}_3(\text{g})$ pressure.

3.4.1.3 Mechanisms

It has been suggested¹⁸ that HNO_3 can be irreversibly adsorbed on surfaces of metal oxides (e.g., TiO_2 and $\alpha\text{-Al}_2\text{O}_3$) and then dissociate to nitrate ions which can be solvated by $\text{H}_2\text{O}(\text{a})$ at elevated RH, as described by Reactions R1 and R2:



It is not clear yet if HNO_3 adsorbed on silica surface will be dissociated to $\text{NO}_3^-(\text{a})$ and then be solvated by $\text{H}_2\text{O}(\text{a})$. In a recent study, Tang et al.⁴⁸ used single particle optical levitation-Raman spectroscopy to explore the gas-particle partitioning of HNO_3 which was formed in the heterogeneous reaction of N_2O_5 with silica particles, and reported that the amount of

nitrate associated with silica particles is not observed under dry condition and increases largely at elevated RH. The enhancement of partitioning of HNO₃ onto silica particles under humidified conditions is suggested to be due to dissociation of HNO₃(a) to nitrate in the presence of H₂O(a),^{48,49} as shown by Reactions R1 and R2. However in another study, Du et al.⁵⁰ utilized Brewster angle cavity ring-down spectroscopy to investigate the co-adsorption of HNO₃ and H₂O on silica surfaces at 294 K. They⁵⁰ found that a multicomponent Langmuir adsorption isotherm can be used to adequately describe the co-adsorption of HNO₃ and H₂O on silica, suggesting that HNO₃ and H₂O are competing for adsorption sites on silica surface. This competition mechanism can be described by Reaction (R3):



In our current study, we found that HNO₃(a) decreases while H₂O(a) increases with increasing RH after exposure of silica particles to 100 mTorr HNO₃(g), as revealed by Figure 3.2. Similarly, Figure 3.5 suggests that for 50 and 100 mTorr HNO₃(g), the amounts of HNO₃(a) at dry conditions are also larger than those at 10%. These observations can be explained by both mechanisms. The dissociation mechanism, assisted by H₂O(a), suggests that increase of RH leads to the increase of H₂O(a), enhancing the dissociation of HNO₃(a); therefore, HNO₃(a) may decrease with RH. The competition mechanism means that H₂O and HNO₃ compete for surface adsorption sites; as a result, increase of RH will increase H₂O(a) and subsequently decrease the amount of HNO₃(a).

The dissociation mechanism is directly supported by our observation of H₃O⁺(a) at 1727 cm⁻¹ and NO₃⁻(a) at 1455 and 1355 cm⁻¹, as evident from Figures 3.3 and 3.4. In addition, Figure 3.2 shows that at 10% and 20% RH, the amounts of H₂O(a) in the presence

of 100 mTorr $\text{HNO}_3(\text{g})$ are larger than those in the absence of $\text{HNO}_3(\text{g})$ for the same RH. The increase of $\text{H}_2\text{O}(\text{a})$ in the presence of $\text{HNO}_3(\text{g})$ can be explained by the dissociation of $\text{HNO}_3(\text{a})$ to $\text{NO}_3^-(\text{a})$, which will increase the surface hydrophilicity. This observation also supports the occurrence of the dissociation mechanism. The effect of $\text{HNO}_3(\text{g})$ exposure may become much smaller at higher RH and thus the difference in $\text{H}_2\text{O}(\text{a})$ is not significant for conditions with and without the presence of 100 mTorr $\text{HNO}_3(\text{g})$, as we notice in Figure 3.2.

Figure 3.5 shows that at 10% RH, the amounts of $\text{HNO}_3(\text{a})$, $\text{H}_3\text{O}^+(\text{a})$, and $\text{H}_2\text{O}(\text{a})$ all increase with increasing $\text{HNO}_3(\text{g})$ pressure when $\text{HNO}_3(\text{g})$ pressure is above 100 mTorr. If in this region the competition mechanism dominated, the amount of $\text{H}_2\text{O}(\text{a})$ would decrease with increasing $\text{HNO}_3(\text{g})$ pressure; therefore, at 10% RH, the dissociation mechanism should play a major role for HNO_3 pressure above 100 mTorr. Figure 3.5 also suggests that at 10% RH, increase of $\text{HNO}_3(\text{g})$ pressure from 50 mTorr to 100 mTorr leads to a decrease of $\text{H}_2\text{O}(\text{a})$, indicating that the competition mechanism may be more important in this region. Therefore, for the first time, these experimental data confirm both the dissociation mechanism^{18,48} and competition mechanism⁵⁰ proposed by previous studies for the adsorption of HNO_3 and H_2O on silica surface, further revealing the complex roles of RH and $\text{H}_2\text{O}(\text{a})$ in heterogeneous reactions of trace gases with mineral dust.^{49,51}

3.4.2 Adsorption of HCOOH on silica

A typical spectrum of silica particles after being exposed to $\text{HCOOH}(\text{g})$ at dry condition (RH <1%) is displayed in Figure 3.6a. The IR peaks at 3066, 2933, 1724, and 1360 cm^{-1} can be assigned to $\nu(\text{OH})(\text{COH})$, $\nu(\text{CH})$, $\nu(\text{C}=\text{O})$, and $\delta(\text{CH})$ of $\text{HCOOH}(\text{a})$ (i.e. molecularly adsorbed HCOOH) on the surface.^{28,29,52,53} After exposure to $\text{HCOOH}(\text{g})$,

isolated surface OH groups on silica surface are hydrogen bonded with HCOOH(a), resulting in a negative peak at 3742 cm^{-1} and the growth of a broad absorption band extending approximately from 2700 to 3800 cm^{-1} . Similar phenomena were observed for the adsorption of HCOOH on TiO_2 and Al_2O_3 in previous work^{26,28,29} and for the adsorption of HNO_3 on silica in our current work as discussed in Section 3.1. Upon evacuation, the IR peak at 1724 cm^{-1} , due to HCOOH(a), decreases significantly.

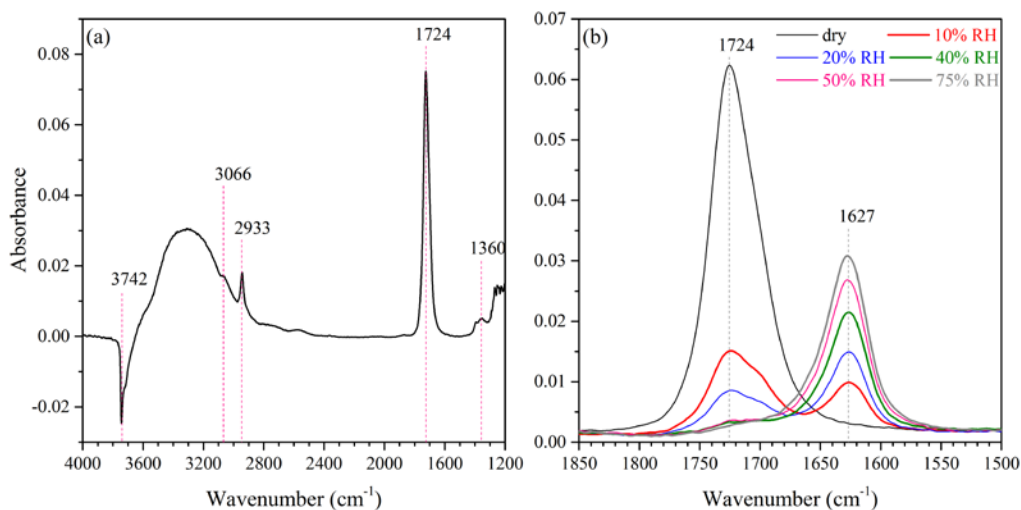


Figure 3.6. (a) FTIR spectrum of silica particles in the presence of 100 mTorr HCOOH(g) under dry conditions. The spectral range between 1200 and 4000 cm^{-1} is shown. (b) FTIR spectra in the spectral range from 1500 to 1850 cm^{-1} after exposure to 100 mTorr HCOOH(g) at different RH. The peaks at 1724 and 1627 cm^{-1} are assigned to $\nu(\text{C}=\text{O})$ of HCOOH(a) and $\delta(\text{H}_2\text{O})$ of H_2O (a) on the silica surface.

3.4.2.1 Effect of relative humidity

RH was varied in a series of experiments in which silica was exposed to 100 mTorr HCOOH(g), and the spectra of silica (1500 - 1850 cm^{-1}) after exposure are shown in Figure 3.6b. The intensity of the IR peak at 1627 cm^{-1} , attributed to the OH bending mode of H_2O (a), increases with RH. In contrast, the intensity of the IR peak at 1724 cm^{-1} , due to HCOOH(a), decreases rapidly with increasing RH and becomes undistinguishable from the

baseline for RH above 40%. In addition, no $\text{H}_3\text{O}^+(\text{a})$ (at 1727 cm^{-1})³⁹ or formate (at 1600 and 1378 cm^{-1})^{24,26} ions were observed.

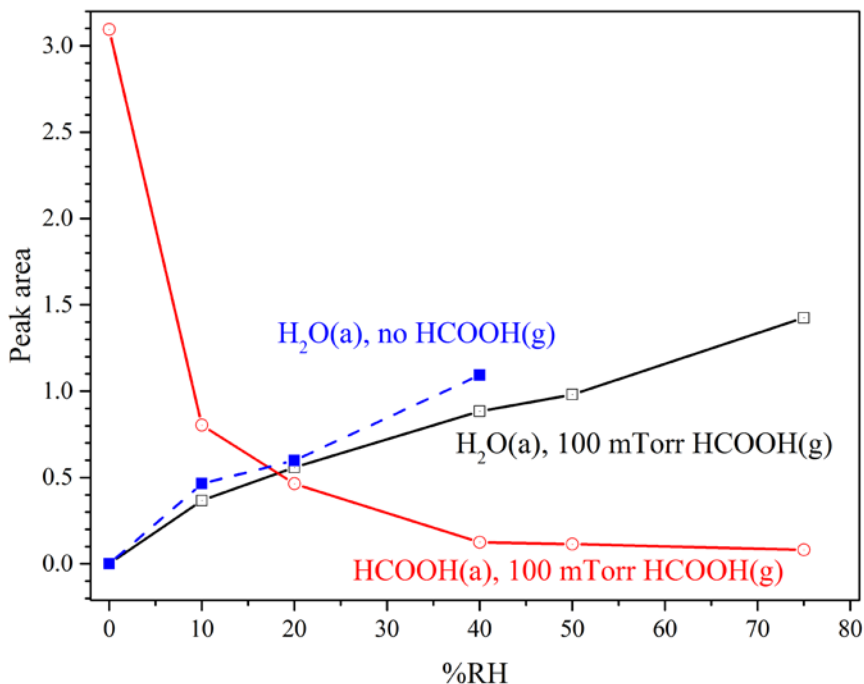


Figure 3.7. IR peak intensities (represented as peak areas) for $\text{H}_2\text{O}(\text{a})$ (1627 cm^{-1} , open square) and $\text{HCOOH}(\text{a})$ (1724 cm^{-1} , open circle) on silica surface as a function of RH, after exposure to 100 mTorr $\text{HCOOH}(\text{g})$. For comparison adsorbed water, $\text{H}_2\text{O}(\text{a})$ (solid square), in the absence of $\text{HCOOH}(\text{g})$ is also plotted as a function of RH.

Intensities of IR peaks for $\text{H}_2\text{O}(\text{a})$ at 1627 cm^{-1} and $\text{HCOOH}(\text{a})$ at 1724 cm^{-1} are plotted in Figure 3.7 as a function of RH, further suggesting that the amount of $\text{HCOOH}(\text{a})$ decreases and $\text{H}_2\text{O}(\text{a})$ increases when RH increases. The peak areas of $\text{H}_2\text{O}(\text{a})$ in the absence of $\text{HCOOH}(\text{g})$ are also displayed in Figure 3.7 as a function of RH, suggesting that the amounts of $\text{H}_2\text{O}(\text{a})$ in the absence of $\text{HCOOH}(\text{g})$ are similar to (if not significantly larger than) those in the presence of 100 mTorr $\text{HCOOH}(\text{g})$ at the same RH.

3.4.2.2 Effect of $\text{HCOOH}(\text{g})$ concentrations

Experiments were also performed in which RH was maintained at 10% while $\text{HCOOH}(\text{g})$ pressure was varied. Figure 3.8a shows IR spectra (1500-1850 cm^{-1}) of silica particles after exposure to $\text{HCOOH}(\text{g})$ of different pressure at 10% RH. Again, we did not observe the formation of $\text{H}_3\text{O}^+(\text{a})$ or $\text{HCOO}^-(\text{a})$ ions. Intensities of IR peaks (represented by peak area) for $\text{HCOOH}(\text{a})$ (1724 cm^{-1}) and $\text{H}_2\text{O}(\text{a})$ (1627 cm^{-1}) are plotted as a function of $\text{HCOOH}(\text{g})$ pressure in Figure 3.8b. As $\text{HCOOH}(\text{g})$ pressure increases, the amounts of both $\text{HCOOH}(\text{a})$ and $\text{H}_2\text{O}(\text{a})$ increase. The peak area of $\text{HCOOH}(\text{a})$ under dry conditions are also included in Figure 3.8b for different $\text{HCOOH}(\text{g})$ pressure. For 100 mTorr $\text{HCOOH}(\text{g})$, the amount of $\text{HCOOH}(\text{a})$ at dry conditions is significantly larger than that at 10% RH. The amounts of $\text{HCOOH}(\text{a})$ become very similar at dry conditions and 10% RH for 500 mTorr $\text{HCOOH}(\text{g})$, probably because at high $\text{HCOOH}(\text{g})$ pressures the effect of $\text{H}_2\text{O}(\text{a})$ at 10% RH becomes relatively small. A close examination of Figure 3.8a suggests that two carbonyl vibration modes (at 1710 and 1724 cm^{-1}) may exist at low $\text{HCOOH}(\text{g})$ pressure. We also analyzed the peak areas at 1627, 1710 and 1724 cm^{-1} using peak fitting, and the results are not significantly different from those presented in Figure 3.8b. This is because the peak intensity at 1710 cm^{-1} is much smaller than that at 1724 cm^{-1} .

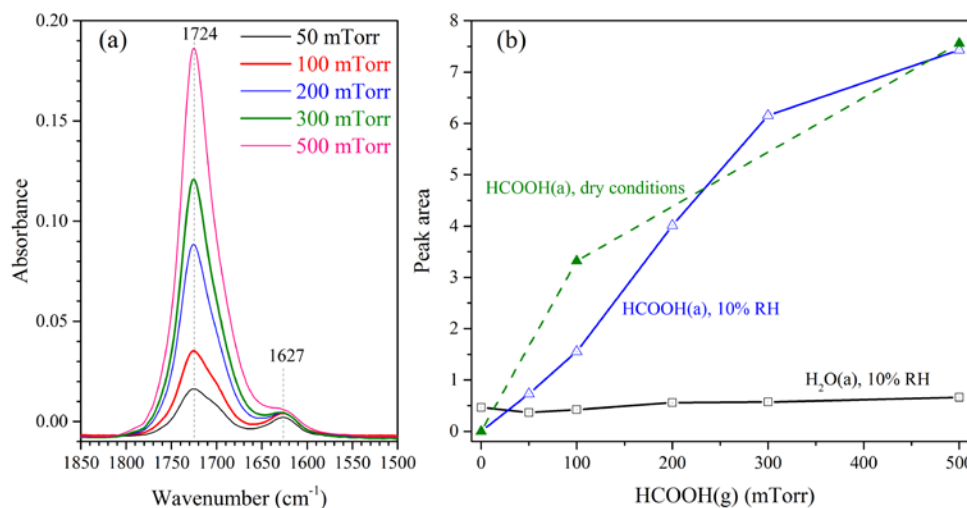
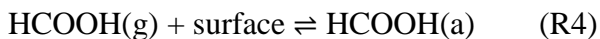


Figure 3.8. (a) FTIR spectra ($1500\text{--}1850\text{ cm}^{-1}$) of silica particles after exposure to $\text{HCOOH}(\text{g})$ of different pressure at 10% RH. (b) Intensities (represented by peak areas) of IR absorption bands for $\text{H}_2\text{O}(\text{a})$ (1627 cm^{-1} , open squares) and $\text{HCOOH}(\text{a})$ (1724 cm^{-1} , open triangles) on silica particles at 10% RH, as a function of $\text{HCOOH}(\text{g})$ pressure. For comparison $\text{HCOOH}(\text{a})$ at dry conditions (solid triangles) is also plotted as a function of $\text{HCOOH}(\text{g})$ pressure.

3.4.2.3 Mechanisms

For the most part, it is determined that HCOOH is reversibly adsorbed on silica surface, as described by Reaction (R4). In the presence of water vapor in the gas phase (and thus $\text{H}_2\text{O}(\text{a})$ on the surface), water could compete for surface adsorption sites with $\text{HCOOH}(\text{a})$ (Reaction R5), or assist the dissociation of $\text{HCOOH}(\text{a})$ (Reaction R6).



As shown by Reactions R5 and R6, both mechanisms imply the decrease of $\text{HCOOH}(\text{a})$ with increasing RH at a given $\text{HCOOH}(\text{g})$ pressure (100 mTorr in our study) as shown in Figure 3.7. Within the noise level no $\text{H}_3\text{O}^+(\text{a})$ or $\text{HCOO}^-(\text{a})$ were observed by FTIR in our

study. This suggests that the dissociation mechanism (Reaction R6) does not play a significant role while competition is the dominant mechanism for the interactions of HCOOH and water vapor with silica surface.

If Reaction R6 did not occur at all, at a given RH the amount of H₂O(a) should have decreased with increasing HCOOH(g) pressure. Nevertheless, Figure 3.8b shows that at 10% RH, the amount of H₂O(a) on silica surface slightly increases with HCOOH(g) pressure. This observation indicates that H₂O(a) assisted dissociation also occurs for HCOOH(a) adsorbed on silica. Similar to HNO₃(g), increasing HCOOH(g) pressure leads to the increase of HCOOH(a) and thus HCOO⁻(a) which is more hydrophilic and can adsorb more water. Since no H₃O⁺(a) or HCOO⁻(a) were observed, the extent of dissociation can be much smaller for HCOOH(a), compared to that for HNO₃(a).

3.4.3 Role of Adsorbed Water in Surface Displacement and Dissociation Reactions of Acids on Silica Surfaces

Surface adsorbed water and thus RH play a myriad of roles in the kinetics and mechanism of heterogeneous reactions of mineral dust particles with trace gases.⁴⁹ We find that H₂O(a) can both displace acids (in this study, HNO₃ and HCOOH) molecularly adsorbed on silica and assist their dissociation to H₃O⁺(a) and corresponding anions. It is also suggested that the extent of dissociation is much larger for HNO₃(a) than HCOOH(a). The observed difference in dissociation extents between HNO₃ and HCOOH may be mainly due to their different acidities in water. The pK_a values are -1.3 for HNO₃⁵⁴ and 3.75 for HCOOH,⁵⁵ respectively.

Though we have observed the dual roles H₂O(a) plays in the adsorption of HNO₃ and HCOOH by silica surface, the relative importance of these two pathways at various

atmospherically relevant conditions is not clear. Previous studies^{18,38,43} suggest that one monolayer of adsorbed water is formed on silica surface at ~20% RH. A close look at Figures 3.2 and 3.7 reveals that HNO₃(a) on silica shows a large decrease when RH increases from 10% to 20% (Figure 3.2) when a monolayer of adsorbed water is formed, while HCOOH(a) decreases significantly when RH is increased from 0% to 10% at which a monolayer of adsorbed water is not formed yet. This suggests that at a given pressure (100 mTorr in our study) of gaseous acids, a significant displacement of HNO₃(a) by H₂O(a) occurs at higher RH compared to that for HCOOH(a), implying that compared to HCOOH(a), HNO₃(a) is more strongly bonded to the silica surface.

To gain further insights into these two reactions, it is highly desirable to quantify the amounts of molecularly adsorbed acids (in our case, HNO₃ and HCOOH), H₂O(a), H₃O⁺, and corresponding anions (in our case, NO₃⁻ and HCOO⁻) as a function of RH. However, experiments of this type are difficult yet these studies do however suggest there is an optimal amount of water and nitric acid present on the surface simultaneously for dissociation to occur in the case of HNO₃ this occurs at approximately 10% RH. Quartz crystal microbalance (QCM) has been used in our laboratory previously to investigate the change in water adsorption properties of several minerals (including γ -Al₂O₃, α -FeOOH, and kaolinite) after their irreversible interactions with HNO₃(g)⁵⁶ and HCOOH(g).²⁸ However, it is difficult to quantitatively determine amounts when the simultaneous adsorption of two different gases is studied.

Theoretical simulation can provide insights into questions which are difficult to be directly addressed by experimental work alone, and has proven to be a valuable tool in investigating atmospheric heterogeneous and multiphase reactions.^{57,58} Previous

theoretical studies have examined the interactions of HNO_3 ³⁹ and HCOOH ^{26,52,53} with Al_2O_3 and of water with SiO_2 ^{59,60} under environmental conditions. A recent study⁶¹ simulated the heterogeneous reaction of HCl with hydroxylated (0001) α -quartz in the presence of water. It is found that⁶¹ while no ionization of HCl occurs on the dry hydroxylated silica surface, HCl ionizes rapidly on the surface covered by one monolayer adsorbed water. Similar methodologies can be applied to study the adsorption of HNO_3 and HCOOH on silica in the absence and presence of water, in order to further our understanding in these two reactions (and in general, the interactions of acidic gases with silica surface) on a more fundamental level.

3.5 Conclusion

Transmission FTIR spectroscopy was used in this study to investigate the heterogeneous reactions of HNO_3 and HCOOH with silica particles. To systematically examine the roles of RH and thus adsorbed water in these two reactions, experiments were carried out by varying RH at a given pressure of HNO_3 (or HCOOH) and by changing the pressure of HNO_3 (or HCOOH) at a given RH. Under dry conditions, HNO_3 and HCOOH are physically adsorbed on silica surface. Adsorbed water is found to play dual roles in these two reactions. It can compete with HNO_3 and HCOOH for surface adsorption sites, and can also assist their dissociation (to hydronium and corresponding anions) on the surface. Due to its much weaker acidity, the extent of dissociation is significantly smaller for HCOOH than that for HNO_3 . Our study highlights the important and complex roles of RH and surface adsorbed water play in atmospheric heterogeneous reactions of mineral dust particles.

3.6 Acknowledgement

This material is based on the work supported by the National Science Foundation under grant number CHE-1305723. Any opinions, findings, and conclusions or recommendations expressed in this material are those of the authors and do not necessarily reflect the views of National Science Foundation. Chapter 3, in full, is a reprint of the material published by American Chemical Society in: Yuan Fang, Mingjin Tang, Vicki H. Grassian, “Competition between Displacement and Dissociation of a Strong Acid Compared to a Weak Acid Adsorbed on Silica Particle Surfaces: The Role of Adsorbed Water”, *The Journal of Physical Chemistry A* **2016** *120* (23), 4016-4024. The dissertation author was the primary investigator and author of this paper.

3.7 References

- (1) Textor, C.; Schulz, M.; Guibert, S.; Kinne, S.; Balkanski, Y.; Bauer, S.; Berntsen, T.; Berglen, T.; Boucher, O.; Chin, M. *et al.* Analysis and Quantification of the Diversities of Aerosol Life Cycles within AeroCom. *Atmos. Chem. Phys.* **2006**, *6*, 1777-1813.
- (2) Usher, C. R.; Michel, A. E.; Grassian, V. H. Reactions on Mineral Dust. *Chem. Rev.* **2003**, *103*, 4883-4939.
- (3) Crowley, J. N.; Ammann, M.; Cox, R. A.; Hynes, R. G.; Jenkin, M. E.; Mellouki, A.; Rossi, M. J.; Troe, J.; Wallington, T. J. Evaluated Kinetic and Photochemical Data for Atmospheric Chemistry: Volume V - Heterogeneous Reactions on Solid Substrates. *Atmos. Chem. Phys.* **2010**, *10*, 9059-9223.
- (4) Dentener, F. J.; Carmichael, G. R.; Zhang, Y.; Lelieveld, J.; Crutzen, P. J. Role of Mineral Aerosol as a Reactive Surface in the Global Troposphere. *J. Geophys. Res.-Atmos.* **1996**, *101*, 22869-22889.
- (5) Tang, Y.; Carmichael, G. R.; Kurata, G.; Uno, I.; Weber, R. J.; Song, C. H.; Guttikunda, S. K.; Woo, J. H.; Streets, D. G.; Wei, C. *et al.* Impacts of Dust on Regional Tropospheric Chemistry during the ACE-Asia Experiment: a Model Study with Observations. *J. Geophys. Res.* **2004**, *109*, D19s21, doi: 10.1029/2003jd003806.

- (6) Sullivan, R. C.; Guazzotti, S. A.; Sodeman, D. A.; Prather, K. A. Direct Observations of the Atmospheric Processing of Asian Mineral Dust. *Atmos. Chem. Phys.* **2007**, *7*, 1213-1236.
- (7) Li, W. J.; Shao, L. Y. Observation of Nitrate Coatings on Atmospheric Mineral Dust Particles. *Atmos. Chem. Phys.* **2009**, *9*, 1863-1871.
- (8) Krueger, B. J.; Grassian, V. H.; Laskin, A.; Cowin, J. P. The Transformation of Solid Atmospheric Particles into Liquid Droplets through Heterogeneous Chemistry: Laboratory Insights into the Processing of Calcium Containing Mineral Dust Aerosol in the Troposphere. *Geophys. Res. Lett.* **2003**, *30*, 1148.
- (9) Laskin, A.; Iedema, M. J.; Ichkovich, A.; Graber, E. R.; Taraniuk, I.; Rudich, Y. Direct Observation of Completely Processed Calcium Carbonate Dust Particles. *Faraday Discuss.* **2005**, *130*, 453-468.
- (10) Sullivan, R. C.; Moore, M. J. K.; Petters, M. D.; Kreidenweis, S. M.; Roberts, G. C.; Prather, K. A. Effect of Chemical Mixing State on the Hygroscopicity and Cloud Nucleation Properties of Calcium Mineral Dust Particles. *Atmos. Chem. Phys.* **2009**, *9*, 3303-3316.
- (11) Tang, M. J.; Whitehead, J.; Davidson, N. M.; Pope, F. D.; Alfarra, M. R.; McFiggans, G.; Kalberer, M. Cloud Condensation Nucleation Activities of Calcium Carbonate and its Atmospheric Ageing Products. *Phys. Chem. Chem. Phys.* **2015**, *17*, 32194-32203.
- (12) Tang, M. J.; Cziczo, D. J.; Grassian, V. H. Interactions of Water with Mineral Dust Aerosol: Water Adsorption, Hygroscopicity, Cloud Condensation and Ice Nucleation. *Chem. Rev.* **2016**, *116*, 4205-4259.
- (13) Sullivan, R. C.; Petters, M. D.; DeMott, P. J.; Kreidenweis, S. M.; Wex, H.; Niedermeier, D.; Hartmann, S.; Clauss, T.; Stratmann, F.; Reitz, P. *et al.* Irreversible Loss of Ice Nucleation Active Sites in Mineral Dust Particles Caused by Sulphuric Acid Condensation. *Atmos. Chem. Phys.* **2010**, *10*, 11471-11487.
- (14) Kulkarni, G.; Sanders, C.; Zhang, K.; Liu, X.; Zhao, C. Ice Nucleation of Bare and Sulfuric Acid-coated Mineral Dust Particles and Implication for Cloud Properties. *J. Geophys. Res.-Atmos* **2014**, *119*, 9993-10011.
- (15) Sihvonen, S. K.; Schill, G. P.; Lykтей, N. A.; Veghte, D. P.; Tolbert, M. A.; Freedman, M. A. Chemical and Physical Transformations of Aluminosilicate Clay Minerals Due to Acid Treatment and Consequences for Heterogeneous Ice Nucleation. *J. Phys. Chem. A* **2014**, *118*, 8787-8796.
- (16) Seinfeld, J. H.; Pandis, S. N. *Atmospheric Chemistry and Physics: From Air Pollution to Climate Change*; Wiley Interscience: New York, 2006.

- (17) Chebbi, A.; Carlier, P. Carboxylic Acids in the Troposphere, Occurrence, Sources, and Sinks: A Review. *Atmos. Environ.* **1996**, *30*, 4233-4249.
- (18) Goodman, A. L.; Bernard, E. T.; Grassian, V. H. Spectroscopic Study of Nitric Acid and Water Adsorption on Oxide Particles: Enhanced Nitric Acid Uptake Kinetics in the Presence of Adsorbed Water. *J. Phys. Chem. A* **2001**, *105*, 6443-6457.
- (19) Hanisch, F.; Crowley, J. N. Heterogeneous Reactivity of Gaseous Nitric Acid on Al₂O₃, CaCO₃, and Atmospheric Dust Samples: A Knudsen Cell Study. *J. Phys. Chem. A* **2001**, *105*, 3096-3106.
- (20) Underwood, G. M.; Li, P.; Al-Abadleh, H.; Grassian, V. H. A Knudsen Cell Study of the Heterogeneous Reactivity of Nitric Acid on Oxide and Mineral Dust Particles. *J. Phys. Chem. A* **2001**, *105*, 6609-6620.
- (21) Seisel, S.; Borensen, C.; Vogt, R.; Zellner, R. The Heterogeneous Reaction of HNO₃ on Mineral Dust and Gamma-alumina Surfaces: a Combined Knudsen Cell and DRIFTS Study. *Phys. Chem. Chem. Phys.* **2004**, *6*, 5498-5508.
- (22) Mashburn, C. D.; Frinak, E. K.; Tolbert, M. A. Heterogeneous Uptake of Nitric Acid on Na-montmorillonite Clay as a Function of Relative Humidity. *J. Geophys. Res.-Atmos.* **2006**, *111*, D15213.
- (23) Vlasenko, A.; Sjogren, S.; Weingartner, E.; Stemmler, K.; Gaggeler, H. W.; Ammann, M. Effect of Humidity on Nitric Acid Uptake to Mineral Dust Aerosol Particles. *Atmos. Chem. Phys.* **2006**, *6*, 2147-2160.
- (24) Al-Hosney, H. A.; Carlos-Cuellar, S.; Baltrusaitis, J.; Grassian, V. H. Heterogeneous Uptake and Reactivity of Formic Acid on Calcium Carbonate Particles: a Knudsen Cell Reactor, FTIR and SEM Study. *Phys. Chem. Chem. Phys.* **2005**, *7*, 3587 - 3595.
- (25) Hatch, C. D.; Gough, R. V.; Tolbert, M. A. Heterogeneous Uptake of the C1 to C4 Organic Acids on a Swelling Clay Mineral. *Atmos. Chem. Phys.* **2007**, *7*, 4445-4458.
- (26) Tong, S. R.; Wu, L. Y.; Ge, M. F.; Wang, W. G.; Pu, Z. F. Heterogeneous Chemistry of Monocarboxylic Acids on α -Al₂O₃ at Different Relative Humidities. *Atmos. Chem. Phys.* **2010**, *10*, 7561-7574.
- (27) Wu, L.-Y.; Tong, S.-R.; Hou, S.-Q.; Ge, M.-F. Influence of Temperature on the Heterogeneous Reaction of Formic Acid on α -Al₂O₃. *J. Phys. Chem. A* **2012**, *116*, 10390-10396.
- (28) Rubasinghege, G.; Ogden, S.; Baltrusaitis, J.; Grassian, V. H. Heterogeneous Uptake and Adsorption of Gas-Phase Formic Acid on Oxide and Clay Particle Surfaces: The Roles of Surface Hydroxyl Groups and Adsorbed Water in Formic

- Acid Adsorption and the Impact of Formic Acid Adsorption on Water Uptake. *J. Phys. Chem. A* **2013**, *117*, 11316-11327.
- (29) Nanayakkara, C. E.; Dillon, J. K.; Grassian, V. H. Surface Adsorption and Photochemistry of Gas-Phase Formic Acid on TiO₂ Nanoparticles: The Role of Adsorbed Water in Surface Coordination, Adsorption Kinetics, and Rate of Photoproduct Formation. *J. Phys. Chem. C* **2014**, *118*, 25487-25495.
- (30) Journet, E.; Balkanski, Y.; Harrison, S. P. A New Data Set of Soil Mineralogy for Dust-cycle Modeling. *Atmos. Chem. Phys.* **2014**, *14*, 3801-3816.
- (31) Scanza, R. A.; Mahowald, N.; Ghan, S.; Zender, C. S.; Kok, J. F.; Liu, X.; Zhang, Y.; Albani, S. Modeling Dust as Component Minerals in the Community Atmosphere Model: Development of Framework and Impact on Radiative Forcing. *Atmos. Chem. Phys.* **2015**, *15*, 537-561.
- (32) Bogdan, A.; Kulmala, M. Effect of Acids on Water Vapor Uptake by Pyrogenic Silica. *J. Colloid Interface Sci.* **1997**, *191*, 95-101.
- (33) Dubowski, Y.; Sumner, A. L.; Menke, E. J.; Gaspar, D. J.; Newberg, J. T.; Hoffman, R. C.; Penner, R. M.; Hemminger, J. C.; Finlayson-Pitts, B. J. Interactions of Gaseous Nitric Acid with Surfaces of Environmental Interest. *Phys. Chem. Chem. Phys.* **2004**, *6*, 3879-3888.
- (34) Goodman, A. L.; Underwood, G. M.; Grassian, V. H. A Laboratory Study of the Heterogeneous Reaction of Nitric Acid on Calcium Carbonate Particles. *J. Geophys. Res.-Atmos.* **2000**, *105*, 29053-29064.
- (35) Goodman, A. L.; Underwood, G. M.; Grassian, V. H. Heterogeneous Reaction of NO₂: Characterization of Gas-phase and Adsorbed Products from the Reaction, 2NO₂(g)+H₂O(a)-> HONO(g)+HNO₃(a) on Hydrated Silica Particles. *J. Phys. Chem. A* **1999**, *103*, 7217-7223.
- (36) Barney, W. S.; Finlayson-Pitts, B. J. Enhancement of N₂O₄ on Porous Glass at Room Temperature: A Key Intermediate in the Heterogeneous Hydrolysis of NO₂? *J. Phys. Chem. A* **2000**, *104*, 171-175.
- (37) Seisel, S.; Borensen, C.; Vogt, R.; Zellner, R. Kinetics and Mechanism of the Uptake of N₂O₅ on Mineral Dust at 298 K. *Atmos. Chem. Phys.* **2005**, *5*, 3423-3432.
- (38) Schuttlefield, J.; Al-Hosney, H.; Zachariah, A.; Grassian, V. H. Attenuated Total Reflection Fourier Transform Infrared Spectroscopy to Investigate Water Uptake and Phase Transitions in Atmospherically Relevant Particles. *Appl. Spectrosc.* **2007**, *61*, 283-292.
- (39) Baltrusaitis, J.; Schuttlefield, J.; Jensen, J. H.; Grassian, V. H. FTIR Spectroscopy Combined with Quantum Chemical Calculations to Investigate Adsorbed Nitrate

- on Aluminium Oxide Surfaces in the Presence and Absence of Co-adsorbed Water. *Phys. Chem. Chem. Phys.* **2007**, *9*, 4970-4980.
- (40) Ritzhaupt, G.; Devlin, J. P. Infrared Spectra of Nitric and Hydrochloric Acid Hydrate Thin Films. *J. Phys. Chem.* **1991**, *95*, 90-95.
- (41) Roziere, J.; Potier, J. Infrared Evidence for the Diaquooxonium ion in Crystallized $\text{HNO}_3 \cdot 3\text{H}_2\text{O}$ and $\text{HClO}_4 \cdot 3\text{H}_2\text{O}$. *J. Inorg. Nucl. Chem.* **1973**, *35*, 1179-1183.
- (42) Bianco, R.; Wang, S.; Hynes, J. T. Infrared Signatures of HNO_3 and NO_3^- at a Model Aqueous Surface. A Theoretical Study. *J. Phys. Chem. A* **2008**, *112*, 9467-9476.
- (43) Ma, Q. X.; He, H.; Liu, Y. C. In Situ DRIFTS Study of Hygroscopic Behavior of Mineral Aerosol. *J. Environ. Sci.* **2010**, *22*, 555-560.
- (44) Rahaman, A.; Grassian, V. H.; Margulis, C. J. Dynamics of Water Adsorption onto a Calcite Surface as a Function of Relative Humidity. *J. Phys. Chem. C* **2008**, *112*, 2109-2115.
- (45) Croteau, T.; Bertram, A. K.; Patey, G. N. Simulation of Water Adsorption on Kaolinite under Atmospheric Conditions. *J. Phys. Chem. A* **2009**, *113*, 7826-7833.
- (46) Ma, G.; Liu, D. F.; Allen, H. C. Piperidine Adsorption on Hydrated Alpha-alumina (0001) Surface Studied by Vibrational Sum Frequency Generation Spectroscopy. *Langmuir* **2004**, *20*, 11620-11629.
- (47) Liu, D. F.; Ma, G.; Xu, M.; Allen, H. C. Adsorption of Ethylene Glycol Vapor on $\alpha\text{-Al}_2\text{O}_3(0001)$ and Amorphous SiO_2 Surfaces: Observation of Molecular Orientation and Surface Hydroxyl Groups as Sorption Sites. *Environ. Sci. Technol.* **2005**, *39*, 206-212.
- (48) Tang, M. J.; Camp, J. C. J.; Rkiouak, L.; McGregor, J.; Watson, I. M.; Cox, R. A.; Kalberer, M.; Ward, A. D.; Pope, F. D. Heterogeneous Interaction of SiO_2 with N_2O_5 : Aerosol Flow Tube and Single Particle Optical Levitation-Raman Spectroscopy Studies. *J. Phys. Chem. A* **2014**, *118*, 8817-8827.
- (49) Rubasinghege, G.; Grassian, V. H. Role(s) of Adsorbed Water in the Surface Chemistry of Environmental Interfaces. *Chem. Commun.* **2013**, *49*, 3071-3094.
- (50) Du, J.; Keese, R. G.; Zhu, L. Experimental Study of the Competitive Adsorption of HNO_3 and H_2O on Surfaces by Using Brewster Angle Cavity Ring-Down Spectroscopy in the 295–345 nm Region. *J. Phys. Chem. A* **2014**, *118*, 8177-8181.
- (51) Tang, M. J.; Schuster, G.; Crowley, J. N. Heterogeneous Reaction of N_2O_5 with Illite and Arizona Test Dust Particles. *Atmos. Chem. Phys.* **2014**, *14*, 245-254.

- (52) Ruan, M.; Hou, H.; Li, W.; Wang, B. Theoretical Study of the Adsorption/Dissociation Reactions of Formic Acid on the α -Al₂O₃(0001) Surface. *J. Phys. Chem. C* **2014**, *118*, 20889-20898.
- (53) Iuga, C.; Sainz-Díaz, C. I.; Vivier-Bunge, A. Interaction Energies and Spectroscopic Effects in the Adsorption of Formic Acid on Mineral Aerosol Surface Models. *J. Phys. Chem. C* **2012**, *116*, 2904-2914.
- (54) Bell, R. P. *The Proton in Chemistry*; Chapman and Hall: London, 1973.
- (55) Lange, N. A.; Dean, J. A. *Lange's Handbook of chemistry*; McGraw-Hill: London, 1979.
- (56) Wijenayaka, L. A.; Rubasinghege, G.; Baltrusaitis, J.; Grassian, V. H. Surface Chemistry of alpha-FeOOH Nanorods and Microrods with Gas-Phase Nitric Acid and Water Vapor: Insights into the Role of Particle Size, Surface Structure, and Surface Hydroxyl Groups in the Adsorption and Reactivity of alpha-FeOOH with Atmospheric Gases. *J. Phys. Chem. C* **2012**, *116*, 12566-12577.
- (57) Gerber, R. B.; Varner, M. E.; Hammerich, A. D.; Riikonen, S.; Murdachaew, G.; Shemesh, D.; Finlayson-Pitts, B. J. Computational Studies of Atmospherically-Relevant Chemical Reactions in Water Clusters and on Liquid Water and Ice Surfaces. *Accounts Chem. Res.* **2015**, *48*, 399-406.
- (58) Bianco, R.; Hynes, J. T. Heterogeneous Reactions Important in Atmospheric Ozone Depletion: A Theoretical Perspective. *Accounts Chem. Res.* **2006**, *39*, 159-165.
- (59) Marie-Pierre, G.; Michiel, S.; Marialore, S. Oxide/Water Interfaces: How the Surface Chemistry Modifies Interfacial Water Properties. *J. Phys. Condens. Matter* **2012**, *24*, 124106.
- (60) Sulpizi, M.; Gaigeot, M. P.; Sprik, M. The Silica-Water Interface: How the Silanols Determine the Surface Acidity and Modulate the Water Properties. *J. Chem. Theory Comput.* **2012**, *8*, 1037-1047.
- (61) Murdachaew, G.; Gaigeot, M.-P.; Halonen, L.; Gerber, R. B. Dissociation of HCl into Ions on Wet Hydroxylated (0001) α -Quartz. *J. Phys. Chem. Lett.* **2013**, *4*, 3500-3507.

CHAPTER 4 HETEROGENEOUS REACTIONS OF ACETIC ACID WITH OXIDE SURFACES: EFFECTS OF MINERALOGY AND RELATIVE HUMIDITY

4.1 Abstract

We have investigated the heterogeneous uptake of gaseous acetic acid on different oxides including γ -Al₂O₃, SiO₂, and CaO under a range of relative humidity conditions. Under dry conditions, the uptake of acetic acid leads to the formation of both acetate and molecularly adsorbed acetic acid on γ -Al₂O₃ and CaO, and only molecularly adsorbed acetic acid on SiO₂. More importantly, under the conditions of this study, dimers are the major form for molecularly adsorbed acetic acid on all three particle surfaces investigated, even at low acetic acid pressures under which monomers are the dominant species in the gas phase. We have also determined saturation surface coverages for acetic acid adsorption on these three oxides under dry conditions as well as Langmuir adsorption constants in some cases. Kinetic analysis shows that the reaction rate of acetic acid increases by a factor of 3 to 5 for γ -Al₂O₃ when relative humidity increases from 0% to 15%, whereas for SiO₂ particles, acetic acid and water are found to compete for surface adsorption sites.

4.2 Introduction

Mineral dust aerosol, emitted from arid and semi-arid regions due to natural and anthropogenic processes, is one of the major types of aerosol present in the troposphere^{1,2} and plays an important role in atmospheric chemistry and climate. Dust aerosol particles can scatter and absorb solar radiation,³⁻⁵ and also impact solar radiation by acting as cloud condensation nuclei and ice nuclei.⁶⁻⁹ Deposition of dust particles is also a major input pathway for several important nutrients in many remote regions.¹⁰⁻¹² After being entrained into the troposphere, dust aerosol particles can be transported over thousands of kilometres^{13,14} and undergo heterogeneous reactions with reactive trace gases.¹⁵⁻²⁰ These reactions can directly and indirectly change the abundance of trace gases in the troposphere,²¹⁻²³ as well as alter the composition of dust particles,²⁴⁻²⁸ thereby impacting their cloud condensation nucleation and ice nucleation activities.^{9,29-33}

Acetic acid is a major monocarboxylic acid in the troposphere, found to be present in the gas phase as well as within aerosol particles and cloud droplets.³⁴ Acetic acid can be produced in the troposphere by photooxidation of volatile organic compounds, and directly emitted by motor vehicles, biomass burning, vegetation and soil.³⁴ Gaseous acetic acid levels show large spatial and temporal variations in the troposphere, ranging from <0.1 ppbv in remote marine regions to >10 ppbv in urban areas.³⁴ The partitioning of acetic acid in the gas and condensed phases significantly affects the acidity of aerosol particles, cloud droplets, and precipitation.³⁴ Therefore, one may expect that heterogeneous uptake of acetic acid by mineral dust particles may play a role in the levels of gaseous acetic acid and the compositions of mineral dust aerosol.

A few previous studies have investigated the heterogeneous reaction of $\text{CH}_3\text{COOH}(\text{g})$ with mineral dust particles, as summarized by Shen et al.³⁵ Carlos-Cuellar et al.³⁶ used a Knudsen cell reactor to study the uptake of $\text{CH}_3\text{COOH}(\text{g})$ by mineral dust, and under dry conditions the initial uptake coefficients were reported to be $(1.9 \pm 0.3) \times 10^{-3}$ for $\alpha\text{-Fe}_2\text{O}_3$, $(2 \pm 1) \times 10^{-3}$ for $\alpha\text{-Al}_2\text{O}_3$, and $(2.4 \pm 0.4) \times 10^{-3}$ for SiO_2 , respectively. After exposure of CaCO_3 aerosol particles to $\text{CH}_3\text{COOH}(\text{g})$, Prince et al.³⁷ found that calcium acetate and CO_2 were formed on the particles and in the gas phase, respectively. The uptake of $\text{CH}_3\text{COOH}(\text{g})$ onto Na-montmorillonite particles was studied at 212 K,³⁸ and the uptake coefficients were found to increase from 1.3×10^{-5} at 0% relative humidity (RH) to 6.0×10^{-5} at 45% RH. Diffuse reflectance infrared Fourier transform spectroscopy (DRIFTS) was used to investigate the heterogeneous interaction of $\text{CH}_3\text{COOH}(\text{g})$ with $\alpha\text{-Al}_2\text{O}_3$ particles,³⁹ and the uptake coefficient was reported to be $(6.0 \pm 0.8) \times 10^{-7}$ at 0% RH. Another DRIFTS study suggested that the heterogeneous reaction of $\text{CH}_3\text{COOH}(\text{g})$ with MgO , $\alpha\text{-Al}_2\text{O}_3$, and CaCO_3 particles leads to the production of acetate, the formation of which is enhanced at higher RH for all the three different types of particles.⁴⁰ The effect of temperature on the uptake of $\text{CH}_3\text{COOH}(\text{g})$ by $\alpha\text{-Al}_2\text{O}_3$ has also been examined.⁴¹ Additionally, very recent study also shows that pretreatment of $\gamma\text{-Al}_2\text{O}_3$ particles with $\text{CH}_3\text{COOH}(\text{g})$ could affect subsequent heterogeneous interactions with NO_2 .⁴²

In addition to the removal of acetic acid from the gas phase and modification of the particle surface composition and reactivity, previous studies suggested that heterogeneous reaction with acetic acid could also lead to changes in hygroscopicity and cloud condensation nucleation (CCN) activity. For example, Ma et al.⁴⁰ found that the water adsorption abilities of MgO , $\alpha\text{-Al}_2\text{O}_3$, and CaCO_3 particles were significantly increased

after reaction with $\text{CH}_3\text{COOH}(\text{g})$. The single hygroscopicity parameter (κ), used to represent the CCN activity of aerosol particles, is reported to be ~ 0.50 for calcium acetate,⁴³ similar to that for $(\text{NH}_4)_2\text{SO}_4$, compared to 0.001-0.003 for CaCO_3 . Processing with acetic acid can also alter the optical properties of CaCO_3 particles⁴⁴ and enhance the solubility of Fe contained by dust through a ligand-assisted process.⁴⁵

Despite these previous studies, mechanisms for the heterogeneous reactions of $\text{CH}_3\text{COOH}(\text{g})$ with mineral dust particles are still not well understood at the molecular level, and the roles of dust mineralogy and relative humidity (and thus surface-adsorbed water) require further elucidation. In this work, transmission FTIR spectroscopy was used to investigate the heterogeneous reaction of $\text{CH}_3\text{COOH}(\text{g})$ with $\gamma\text{-Al}_2\text{O}_3$, SiO_2 , and CaO particles over a wide range of pressures. We have examined the effects of particle mineralogy and RH, and also provided insightful discussion on reaction mechanisms by interpretation of IR spectra of particle surfaces after exposure to $\text{CH}_3\text{COOH}(\text{g})$ under different conditions.

4.3 Experimental section

Experimental details can be found elsewhere,^{46,47} and only a brief description is provided here. All the experiments were carried out at 296 ± 1 K. Three types of particles were investigated in this study, including $\gamma\text{-Al}_2\text{O}_3$ (Degussa Chemical), SiO_2 (Degussa Chemical), and CaO (Alfa Aesar). The BET surface areas are 101, 230, and $4 \text{ m}^2 \text{ g}^{-1}$ for $\gamma\text{-Al}_2\text{O}_3$, SiO_2 , and CaO , as previously reported.^{46,48} For infrared studies, a Teflon-coated stainless steel reaction cell coupled to a FTIR spectrometer (Mattson GL-0621) with a mercury-cadmium-telluride (MCT) detector was used to investigate the heterogeneous

reaction of $\text{CH}_3\text{COOH}(\text{g})$ with mineral dust particles. Samples were prepared by pressing mineral particles (~ 10 mg) onto one half of a tungsten grid which was held by two Teflon-coated jaws in the reaction cell. Prior to each experiment, the reaction cell was evacuated for 6 hours to clean the mineral sample and the reaction cell. After that, $\text{CH}_3\text{COOH}(\text{g})$ and then water vapor (if used) with given pressures (measured by two absolute pressure transducers) were introduced into an evacuated glass mixing chamber, and subsequently the gas mixture was then introduced into the reaction cell to initiate its interaction with dust particles. In our experiments particles were exposed to i) $\text{CH}_3\text{COOH}(\text{g})$ alone or ii) $\text{CH}_3\text{COOH}(\text{g})$ and water vapor simultaneously.

$\text{CH}_3\text{COOH}(\text{g})$ was taken from vapor in the overhead space of a long-neck glass bulb containing several mL acetic acid (Fisher Scientific, with a purity of $\geq 99.7\%$ w/w) which was purified by several freeze-pump-thaw cycles. The reaction was stopped after no significant changes were observed for the particle surface (typically with an exposure time of 20 min) by evacuating the reaction cell. This evacuation was carried out overnight in attempt to remove weakly adsorbed surface species.

The reaction cell was mounted on a linear translator inside the FTIR spectrometer, allowing both halves of the tungsten grid (the blank half for gas phase measurements and the particle-loaded half for surface measurements) to be probed by the IR beam. Single beam FTIR spectra of the gas and surface were collected with a resolution of 4 cm^{-1} in the spectral range of $800\text{-}4000\text{ cm}^{-1}$ at $296\pm 1\text{ K}$ before and after exposure of mineral dust samples to gaseous acetic acid. 250 scans were averaged to get a single spectrum. FTIR spectra of gas and surface species were obtained by referencing single-beam spectra to these collected before introducing gaseous acetic acid into the reaction cell. IR absorption

due to gaseous species, measured through the blank half of the tungsten grid, were subtracted in order to get the spectra of the particle surfaces.

4.4 Results and Discussion

FTIR spectra of CH₃COOH(g) were collected in this study, and its vibrational modes are well understood,⁴⁹⁻⁵¹ with the following absorptions observed at 3580 cm⁻¹ assigned to $\nu(\text{OH})$, 3078 and 2955 cm⁻¹ assigned to $\nu(\text{CH})$, 1426 cm⁻¹ assigned to $\delta(\text{CH}_3)$, 1295 cm⁻¹ assigned to $\delta(\text{OH})$, and 1176 cm⁻¹ assigned to $\nu(\text{C-O})$. Acetic acid undergoes dimerization in the gas phase. The occurrence of monomers and dimers can be identified by the vibrational frequency of $\nu(\text{C=O})$, at 1733 cm⁻¹ for the dimer and 1790 cm⁻¹ for the monomer,⁵⁰⁻⁵⁴ as shown in Figure 4.1. The equilibrium between acetic acid monomers and dimers in the gas phase can be described by:⁵⁵

$$K_{eq} = \frac{P_M^2}{P_D} = 10^{(-3347/T+10.931)} \quad (\text{E4.1})$$

where K_{eq} is the equilibrium constant (in Torr) at the temperature of T (in K), and P_M and P_D are the pressure (in Torr) of monomers and dimers in the gas phase. K_{eq} is equal to 0.42 Torr at 293 K, suggesting that the ratio of monomers to dimers is 0.9 for a total pressure of 1000 mTorr, 5.0 for a total pressure of 100 mTorr, and 43 for a total pressure of 10 mTorr. As a result, in our experiments dimers also exist in the gas phase, though monomers are typically the dominant form. In this paper the acetic acid pressure if all the dimers decompose to monomers is always reported, given by

$$P = P_M + 2 \times P_D \quad (\text{E4.2})$$

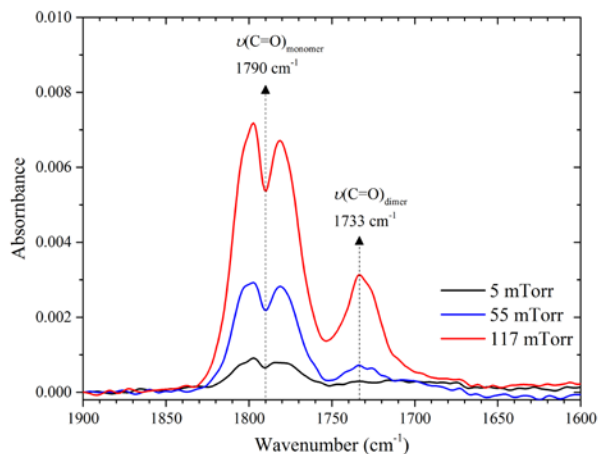


Figure 4.1. FTIR spectra (shown above from 1600 to 1900 cm^{-1}) of $\text{CH}_3\text{COOH}(\text{g})$ as a function of pressure (5, 55, and 117 mTorr) at 296 K.

4.4.1 Heterogeneous reaction with $\gamma\text{-Al}_2\text{O}_3$

The infrared spectra for $\gamma\text{-Al}_2\text{O}_3$ particles after exposure to $\text{CH}_3\text{COOH}(\text{g})$ under dry conditions as a function of pressures are displayed in Figure 4.2a from the 900 to 1900 cm^{-1} region. Additional spectra in the full range, from 800 to 4000 cm^{-1} , are provided in supporting information. The peak assignments for the vibrational modes of adsorbed acetic acid are given in Table 4.1. Infrared absorbances are observed at 1017 and 1051 cm^{-1} and attributed to $\rho_{\text{op}}(\text{CH}_3)$ and $\rho_{\text{ip}}(\text{CH}_3)$, at 1273 cm^{-1} attributed to $\delta(\text{OH})$ or $\nu(\text{C-OH})$, at 1329, 1366 and 1424 cm^{-1} attributed to $\delta(\text{CH}_3)$, at 1479 and 1586 cm^{-1} attributed to $\nu_{\text{s}}(\text{COO})$ and $\nu_{\text{as}}(\text{COO})$, and at 1716 and 1758 cm^{-1} attributed to $\nu(\text{C=O})_{\text{dimer}}$ and $\nu(\text{C=O})_{\text{monomer}}$, respectively. Further discussions on these IR peaks formed on the $\gamma\text{-Al}_2\text{O}_3$ surface due to adsorption of acetic acid are provided below.

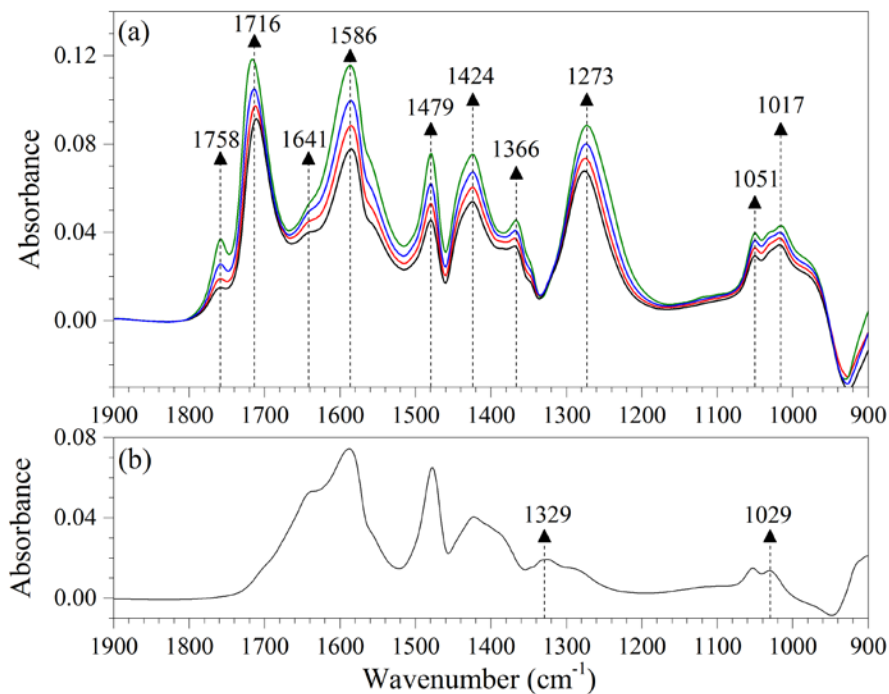


Figure 4.2. FTIR spectra (900-1900 cm^{-1}) of $\gamma\text{-Al}_2\text{O}_3$ after reaction with $\text{CH}_3\text{COOH}(\text{g})$ under dry conditions. (a) Spectra of $\gamma\text{-Al}_2\text{O}_3$ after reaction with 27, 79, 293, and 1190 mTorr $\text{CH}_3\text{COOH}(\text{g})$. (b) A typical spectrum of reacted $\gamma\text{-Al}_2\text{O}_3$ after evacuation of the reaction cell.

Tong et al.³⁹ investigated the heterogeneous reaction of $\alpha\text{-Al}_2\text{O}_3$ with $\text{CH}_3\text{COOH}(\text{g})$ and did not observe any IR peaks between 1690 and 1790 cm^{-1} for products formed on the surface, suggesting that physisorption of acetic acid on $\alpha\text{-Al}_2\text{O}_3$ is not significant. In contrast, in our study two IR peaks at 1758 and 1716 cm^{-1} , characteristic of molecularly adsorbed acetic acid, were observed. Upon evacuation, some IR peaks, at 1758, 1716 and 1273 cm^{-1} for example, disappeared, as shown in Figure 4.2b. This clearly confirms that some acetic acid is physisorbed on $\gamma\text{-Al}_2\text{O}_3$ surfaces and thus reversibly adsorbed at 295 K. Previous studies also found that acetic acid showed some amount of molecular and reversibly adsorption on TiO_2 ⁵⁴ and $\gamma\text{-}$ and $\delta\text{-Al}_2\text{O}_3$.⁵¹

Table 4.1. Vibrational mode assignments for species formed on the surfaces of γ -Al₂O₃, SiO₂, and CaO after heterogeneous interactions with CH₃COOH(g).

surface species	mode assignment	γ -Al ₂ O ₃	SiO ₂	CaO	literature
weakly bound	$\nu_s(\text{OH})$	3502	3331	3422	3465 ⁵¹
acetic acid	$\nu_{\text{as/s}}(\text{CH}_3)$	2942	2936	2924	2935, ⁵⁶ 2937 ⁴⁰
	$\nu(\text{C=O})_{\text{monomer}}$	1758	1758		1756 ⁵¹ , 1746 ⁵³
	$\nu(\text{C=O})_{\text{dimer}}$	1716	1716	1711	1714 ⁵¹ , 1701 ⁵³
	$\delta(\text{CH}_3)$	1366, 1424	1385, 1410		1420 and 1331-1327, ⁵¹ 1343 and 1424, ³⁹ 1350 and 1424 ⁴⁰
hydroxyl groups and acetate groups	$\nu(\text{OH})$		3742 ^a , 3255		3744, ⁴⁶
	$\delta(\text{OH})$ or $\nu(\text{C-OH})$	1273		1249, 1295	1279 and 1302, ⁵³ 1265, ⁴⁰ 1255 ⁵¹
strongly bound acetate species	$\nu_{\text{as/s}}(\text{CH}_3)$	2942			2935, ⁵⁶ 2937 ⁴⁰
	$\nu_{\text{as}}(\text{COO})$	1586		1613	1590, ⁵¹ 1583, ⁵³ 1608, ⁴⁰ 1578 ³⁹
	$\nu_s(\text{COO})$	1479			1470 ⁵¹ , 1456 ⁴⁰ , 1468 ³⁹
	$\delta(\text{CH}_3)$	1329, 1424		1335	1420 and 1331-1327, ⁵¹ 1343 and 1424, ³⁹ 1350 and 1424 ⁴⁰
	$P_{\text{op}}(\text{CH}_3)$	1051		1051	1051, ⁵⁶ 1049 ⁵¹ , 1053 ⁴⁰
	$P_{\text{ip}}(\text{CH}_3)$	1017		1023	1027, ⁵⁶ 1026 ⁵¹ , 1025 ⁴⁰

^a: negative peaks due to hydrogen bonding interactions with isolated Si-OH groups.

Figure 4.1 reveals that monomers are the major form when CH₃COOH(g) is less than 100 mTorr, as also confirmed by our calculations using the previously reported equilibrium constants.⁵⁵ However, Figure 4.2a shows that under the same conditions, dimers are dominant for acetic acid molecularly adsorbed on γ -Al₂O₃ surfaces. This suggests that physisorption of acetic acid on γ -Al₂O₃ surfaces favours the adsorption of dimers. Hasan et al.⁵¹ also observed the occurrence of two IR peaks at 1756 and 1714 cm⁻¹ on the γ - and δ -Al₂O₃ surfaces after exposure to gaseous acetic acid, but these two peaks

were not unambiguously attributed. A close examination of the IR spectra presented by Hasan et al.⁵¹ suggested that dimers are the dominant form for molecularly adsorbed acetic acid; however, the usage of 3 Torr gaseous acetic acid in their experiments also favors the formation of acetic acid dimers in the gas phase.⁵¹ In addition, the occurrence of a relatively small peak at 1641 cm⁻¹, as shown in Figure 4.2a, indicates that some molecularly adsorbed acetic acid may be present in the chain form on γ -Al₂O₃ surface.⁵³

Adsorbed acetate can be coordinated to the surface in different modes:^{39,53,57} 1) in a monodentate mode, only one carboxylate O atom is coordinated to a surface Al atom, 2) in a bridged bidentate mode, two carboxylate O atoms are coordinated to two different surface Al atoms, and 3) in a chelating bidentate mode, two carboxylate O atoms are coordinated to the same surface Al atom. The coordination modes can be differentiated by the difference in wavenumbers between $\nu_s(\text{COO})$ and $\nu_{as}(\text{COO})$,^{51,54,57} i.e. $\Delta(\text{COO})$. In our study, $\Delta(\text{COO})$ is determined to be 107 cm⁻¹ for acetate adsorbed on γ -Al₂O₃, significantly smaller than that for sodium acetate (156 or 143 cm⁻¹).^{58,59} This suggests that adsorbed acetate is bound to the γ -Al₂O₃ surface via the chelating bidentate mode. Previous studies found that $\Delta(\text{COO})$ is equal to 81 cm⁻¹ for acetate adsorbed on TiO₂⁵⁴ and 120 cm⁻¹ for γ - and δ -Al₂O₃,⁵¹ thereby concluding that acetate is adsorbed on both TiO₂ and γ - and δ -Al₂O₃ via the chelating bidentate configuration. In another study, Tong et al.³⁹ calculated wavenumbers of $\nu_s(\text{COO})$, $\nu_{as}(\text{COO})$ and $\delta(\text{CH})$ for acetate adsorbed on α -Al₂O₃ via three different configuration modes using density functional theory, and compared calculated wavenumbers with their measured values. The bridged bidentate mode, which gives the best agreement between measurement and calculation for all the three vibration modes, is suggested to be the mode via which adsorbed acetate is coordinated to α -Al₂O₃.³⁹

Nevertheless, $\Delta(\text{COO})$, calculated from the wavenumbers measured by Tong et al.,³⁹ is equal to 110 cm^{-1} for acetate adsorbed on $\alpha\text{-Al}_2\text{O}_3$; in this aspect it can be interpreted that adsorbed acetate is coordinated to the $\alpha\text{-Al}_2\text{O}_3$ surface via the chelating bidentate mode. Further theoretical work can help resolve this controversy and better understand the surface coordination modes of adsorbed acetate on different oxides. Please note that in their original paper, Tong et al.³⁹ used a different terminology for configuration modes.

4.4.1.1 Uptake kinetics and surface coverage

The IR absorbance of surface species, if calibrated, can be used to quantify the amount of surface species and thus to calculate surface coverages and uptake kinetics. The calibration procedure has been detailed in previous studies.^{46,57} Briefly, under dry conditions the amount of $\text{CH}_3\text{COOH}(\text{g})$ uptaken by the particles is determined by the pressure difference of $\text{CH}_3\text{COOH}(\text{g})$ with and without loading particles with a given mass on the tungsten grid. This pressure change is then converted to number of acetic acid molecules uptaken by per cm^2 particle surface, which can be used to calibrate the IR absorbance. In order to minimize the effects of dimers in the gas phase, these calibrations were carried out with $\text{CH}_3\text{COOH}(\text{g})$ pressures lower than 20 mTorr when the presence of dimers in the gas phase is negligible.

The rate of a heterogeneous reaction is usually described by the uptake coefficient, γ , defined as the ratio of the number of gas molecules uptaken by the surface to the total number of gas-surface collisions.^{15,46,60} We have determined the uptake coefficients of $\text{CH}_3\text{COOH}(\text{g})$, $\gamma(\text{CH}_3\text{COOH})$, onto $\gamma\text{-Al}_2\text{O}_3$ particles at a few different RH (0-15%) and at three different $\text{CH}_3\text{COOH}(\text{g})$ pressures (79, 183, and 398 mTorr), and the results are summarized in Table 4.2. No significant difference in the measured $\gamma(\text{CH}_3\text{COOH})$ was

found at different $\text{CH}_3\text{COOH}(\text{g})$ pressures for the same RH. The effect of RH is quite substantial, with $\gamma(\text{CH}_3\text{COOH})$ increased by a factor of about 3-5 when RH is increased from 0% to 15%. $\gamma(\text{CH}_3\text{COOH})$ for $\gamma\text{-Al}_2\text{O}_3$ particles measured by our work are similar to those determined for $\alpha\text{-Al}_2\text{O}_3$ particles by Tong et al.,³⁹ who reported that $\gamma(\text{CH}_3\text{COOH})$ for $\alpha\text{-Al}_2\text{O}_3$ particles is $(6.0 \pm 0.8) \times 10^{-7}$ at 0% RH and increases with RH for RH below 20%. Under dry conditions, the saturation coverage of acetic acid is determined to be $(4.8 \pm 0.1) \times 10^{14}$ molecules cm^{-2} for $\gamma\text{-Al}_2\text{O}_3$. Experiments at higher RH will further help elucidate the mechanism and kinetics of the heterogeneous reaction of $\text{CH}_3\text{COOH}(\text{g})$ with $\gamma\text{-Al}_2\text{O}_3$ and the effects of surface adsorbed water.

Table 4.2. Uptake coefficients of CH₃COOH(g) on γ -Al₂O₃ particles at different acetic acid pressure and RH.

Pressure (mTorr)	RH (%)	γ ($\times 10^{-7}$)
79	0	3.0 \pm 0.4
	0	0.5 \pm 0.1
	5	7.0 \pm 1.0
	7	10.0 \pm 4.0
	10	10.0 \pm 4.0
	10	9.0 \pm 2.0
	15	10.0 \pm 4.0
	15	8.0 \pm 3.0
183	0	2.0 \pm 0.4
	0	3.0 \pm 0.5
	5	10.0 \pm 4.0
	5	8.0 \pm 2.0
	10	7.0 \pm 3.0
	11	9.0 \pm 4.0
	15	10.0 \pm 6.0
	15	8.0 \pm 3.0
398	0	2.0 \pm 2.0
	0	3.0 \pm 1.0
	5	10.0 \pm 3.0
	5	4.0 \pm 3.0
	10	10.0 \pm 7.0
	10	6.0 \pm 5.0
	15	10.0 \pm 5.0
	15	7.0 \pm 4.0

4.4.2 Heterogeneous reaction with CaO

Figure 4.3a shows the spectra (900-1900 cm⁻¹) of CaO particles after reaction with 25, 82, 298, and 1175 mTorr CH₃COOH(g) under dry conditions, and full-range spectra are provided as supporting information. Important IR absorptions at 1023 and 1051 cm⁻¹ are assigned to $\rho_{op}(\text{CH}_3)$ and $\rho_{ip}(\text{CH}_3)$, at 1249 and 1295 cm⁻¹ assigned to $\delta(\text{OH})$ or $\nu(\text{C-OH})$, at 1335 cm⁻¹ attributed to $\delta(\text{CH}_3)$, at 1613 cm⁻¹ assigned to $\nu_{as}(\text{COO})$, and at 1711 cm⁻¹ assigned to $\nu(\text{C=O})_{\text{dimer}}$. A complete peak assignment is given in Table 1, and here we

only discuss important IR peaks. In addition, the absorbance feature between 1429 and 1492 cm^{-1} is due to the asymmetric stretch of surface carbonates,⁴⁶ formed by the reaction of CaO with atmospheric CO_2 during sample storage and preparation.

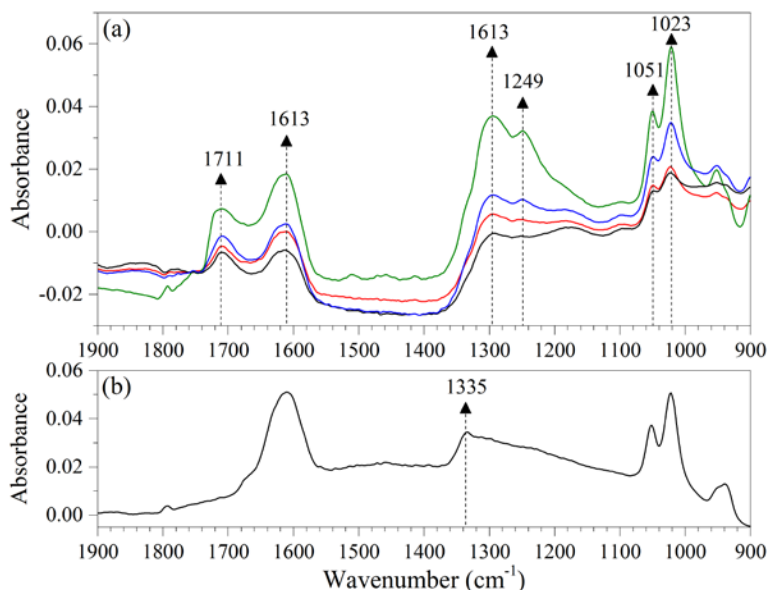


Figure 4.3. FTIR spectra ($900\text{-}1900\text{ cm}^{-1}$) of CaO after reaction with $\text{CH}_3\text{COOH}(\text{g})$ under dry conditions. (a) Spectra of CaO after reaction with 25, 82, 298, and 1175 mTorr $\text{CH}_3\text{COOH}(\text{g})$. (b) A typical spectrum of reacted CaO after evacuation of the reaction cell.

As shown in Figure 4.3b, after evacuation some peaks (e.g., at 1249, 1711 and 1758 cm^{-1}) disappeared, suggesting that they are due to weakly (or molecularly) adsorbed acetic acid on the surface. The heterogeneous uptake of $\text{CH}_3\text{COOH}(\text{g})$ on MgO was investigated by Ma et al.,⁴⁰ who also observed desorption of some adsorbed acetic acid after flushing MgO particles with dry air. Interestingly, the peak at around 1758 cm^{-1} , attributed to $\nu(\text{C}=\text{O})_{\text{monomer}}$, was not significant if existed at all, though monomers dominate in the gas phase for acetic acid pressure less than 100 mTorr. This suggests that molecularly adsorbed acetic acid on CaO surface is favored to exist in the form of dimers. Both monomers and dimers of molecularly adsorbed acetic acid were observed on MgO(100) surfaces by Xu

and Koel⁵³ using FTIR, though additional details or discussions were not provided. Under dry conditions, the saturation surface coverage of acetic acid is determined to be $(2.0 \pm 0.1) \times 10^{15}$ molecules cm^{-2} for CaO.

4.4.3 Heterogeneous uptake on SiO₂

Spectra (900-1900 cm^{-1}) of SiO₂ particles after exposure to CH₃COOH(g) of different pressures are shown in Figure 4.4. Several IR absorptions are observed at 1385 and 1410 cm^{-1} assigned to $\delta(\text{CH}_3)$, and at 1758 and 1716 cm^{-1} assigned to $\nu(\text{C=O})_{\text{monomer}}$ and $\nu(\text{C=O})_{\text{dimer}}$, respectively. No peaks attributable to surface-bound acetate or acetate ions were observed. In addition, evacuation of the reactor cell led to the complete disappearance of all the IR peaks formed on the SiO₂ surface due to interactions with gaseous acetic acid. These data clearly suggest that acetic acid is molecularly and reversibly adsorbed on SiO₂ surfaces, different from the chemistry of MgO,^{40,53} Al₂O₃,^{39,40,51} TiO₂^{51,54,56} and CaCO₃ particle surfaces.^{37,40} Our very recent work⁴⁷ also found that the adsorption of formic acid, another small monocarboxylic acid, on SiO₂ surface is completely reversible; in contrast, a fraction of adsorbed nitric acid are dissociated on SiO₂ surface,⁴⁷ due to its significantly higher acidity compared to formic and acetic acids.

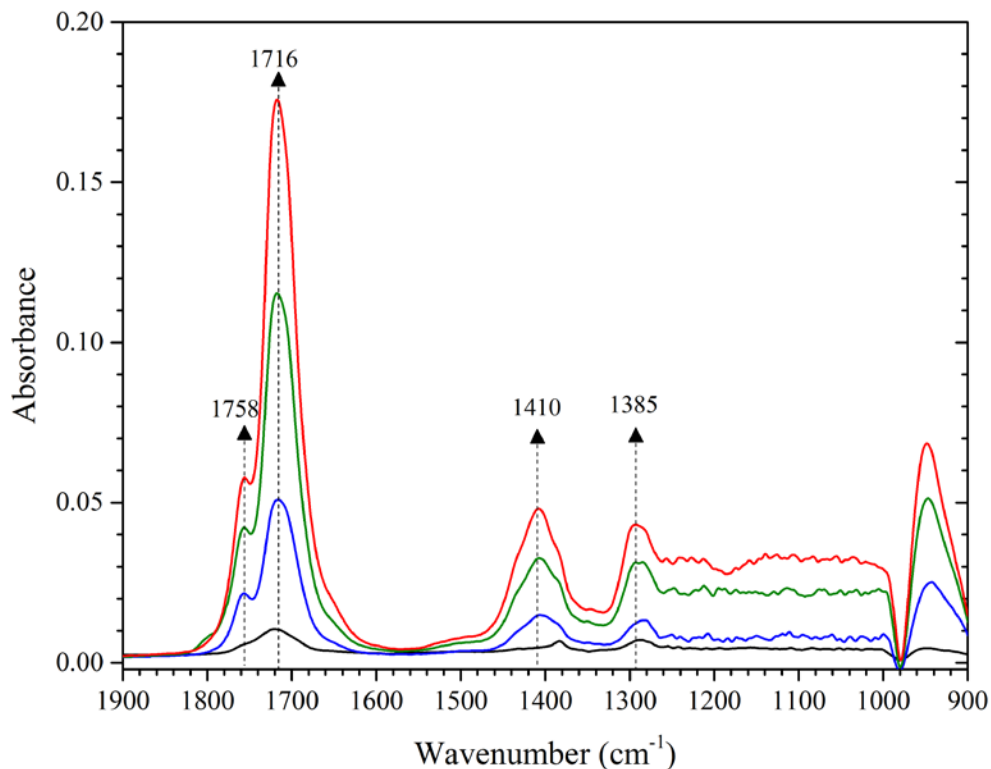


Figure 4.4. FTIR spectra (900-1900 cm^{-1}) of SiO_2 after interaction with $\text{CH}_3\text{COOH}(\text{g})$ with pressure of 5, 21, 55, and 117 mTorr in the gas phase under dry conditions. Please note that SiO_2 is opaque below 1250 cm^{-1} .

For $\text{CH}_3\text{COOH}(\text{g})$ pressure less than 100 mTorr, monomers dominate in the gas phase. However, Figure 4.4 shows that for acetic acid molecularly adsorbed on SiO_2 surface, the IR absorbance of dimers (at 1716 cm^{-1}) is much larger than that of monomers (at 1758 cm^{-1}). This suggests that similar to $\gamma\text{-Al}_2\text{O}_3$ and CaO , SiO_2 favours the formation of dimers on the surface, even under conditions when acetic acid monomers are the major form in the gas phase. We also found that the adsorption of acetic acid on SiO_2 can be described by the Langmuir isotherm, as detailed in the supporting information, and the saturation coverage and Langmuir constant are determined to be $(2.0 \pm 0.1) \times 10^{14}$ molecules cm^{-2} and $213 \pm 35 \text{ Torr}^{-1}$, respectively.

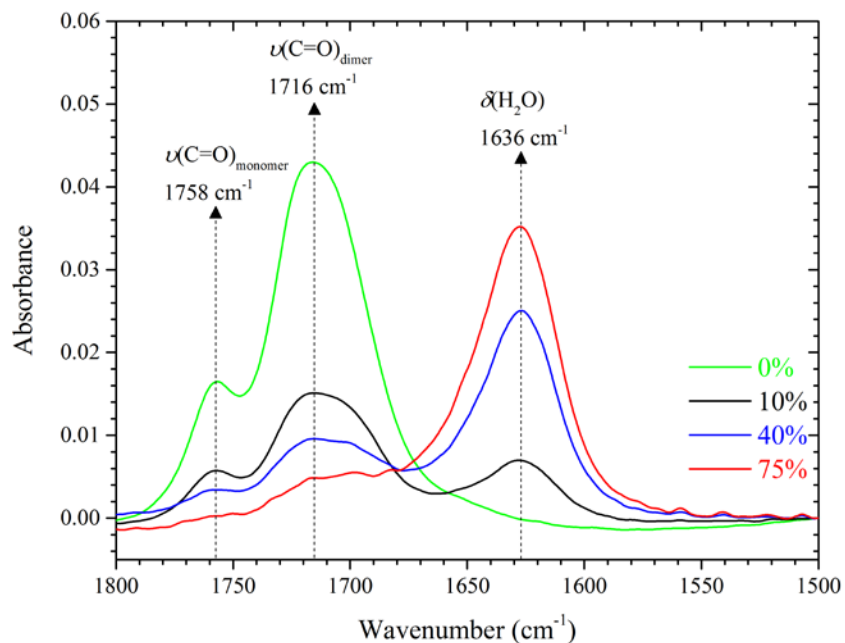


Figure 4.5. FTIR spectra (1500-1800 cm^{-1}) of SiO_2 after exposure to $\text{CH}_3\text{COOH}(\text{g})$ of 5 mTorr in the gas phase at different RH.

A series of experiments were conducted in which $\text{CH}_3\text{COOH}(\text{g})$ pressure was kept at 5 mTorr while the RH in the reaction cell was varied, in order to further understand the mechanisms of acetic acid adsorption on SiO_2 surface and the roles of RH and thus surface adsorbed water. The results are displayed in Figure 4.5, showing that increasing RH leads to the increase of surface adsorbed water (at 1636 cm^{-1}) and the decrease of molecularly adsorbed acetic acid (for both monomers at 1758 cm^{-1} and dimers at 1716 cm^{-1}). In addition, no formation of surface-bound acetate or dissolved acetate ions was observed within the detection limit. These evidences together suggest that acetic acid is molecularly adsorbed on SiO_2 surface and competes with water molecules for surface adsorption sites. Very similar adsorption behavior on SiO_2 surface has been found for formic acid in our previous study.⁴⁷

4.4.4 Discussion

Mineral surface, and surfaces of aerosol particles in general, provide unique media which can facilitate reactions which may not occur in the gas phase,^{16,61} e.g., the heterogeneous hydrolysis of NO_2 ⁶¹⁻⁶³ and N_2O_5 .^{61,64} The formation of N_2O_4 (the NO_2 dimers) on the surface due to adsorption of NO_2 is proposed to be an key intermediate for the atmospheric heterogeneous reaction of NO_2 , because N_2O_4 can undergo autoionization to form NO^+NO_3^- ,⁶⁵ further leading to the formation of HONO or ClNO which are important precursors of OH radicals and Cl atoms in the troposphere. Though N_2O_4 has been observed on surfaces at very low temperature⁶⁶ and theoretical work also predicts its formation at higher temperatures,^{61,67} to our knowledge the formation of N_2O_4 has not been observed on the surface under conditions of direct atmospheric relevance (please note that the presence of N_2O_4 is significant in the gas phase only at high NO_2 pressure,⁶³ similar to acetic acid dimers).

Our study provides direct evidence that the adsorption of acetic acid, an important reactive trace gas in the troposphere, on different mineral surfaces, leads to the formation of dimers on the surface. In addition, the formation of dimers is strongly favoured compared to monomers, even under conditions when monomers are the dominant species in the gas phase. For the first time, the dimerization of an atmospheric reactive trace gas on mineral surface is directly observed. This finding provides a new example showing the uniqueness of surfaces in facilitating reactions which are not favoured in the gas phase under the same conditions. The structure, chemical reactivity and thermodynamic properties of surface-adsorbed acetic acid dimers (and monomers as well) are still

unexplored yet, and a full understanding at the fundamental level requires the combination of experimental studies and theoretical work.

4.5 Conclusion

Acetic acid is a ubiquitous reactive trace gas in the troposphere, and its interaction with mineral dust particles has a myriad of impacts and is of great interest. In this study, transmission FTIR spectroscopy was used to investigate the heterogeneous uptake of $\text{CH}_3\text{COOH}(\text{g})$ by $\gamma\text{-Al}_2\text{O}_3$, SiO_2 , and CaO particles under atmospherically relevant conditions. The importance of particle mineralogy has been found in this work. Uptake of $\text{CH}_3\text{COOH}(\text{g})$ leads to the formation of both surface-coordinated acetate and molecularly adsorbed acetic acid on $\gamma\text{-Al}_2\text{O}_3$ and CaO surface under dry conditions, while for SiO_2 only molecularly adsorbed acetic acid is observed on the surface. The surface saturation coverages of acetic acid under dry conditions, are determined to be $(4.8 \pm 0.1) \times 10^{14}$, $(2.0 \pm 0.1) \times 10^{15}$, and $(2.0 \pm 0.1) \times 10^{14}$ molecules cm^{-2} for $\gamma\text{-Al}_2\text{O}_3$, CaO , and SiO_2 , respectively. This suggests that under dry conditions, if normalized to particle surface area, CaO has the largest capacity to uptake acetic acid while SiO_2 has the smallest capacity. In addition, the Langmuir constant of acetic acid adsorption on SiO_2 is determined to be $213 \pm 35 \text{ Torr}^{-1}$. Some metal oxides have several different structure forms (e.g., α -, γ -, and $\delta\text{-Al}_2\text{O}_3$), possibly showing different behaviors in terms of the heterogeneous reactions with trace gases including $\text{CH}_3\text{COOH}(\text{g})$ investigated in this study, and this aspect deserves further investigations in future.

Very importantly, we have found that acetic acid dimers are the major form for molecularly adsorbed acetic acid on all the three particle surfaces we investigated, even at

low acetic acid pressures (down to a few mTorr) under which monomers are dominant over monomers in the gas phase. We have also explored the roles of RH and thus surface adsorbed water in the heterogeneous uptake of acetic acid by γ -Al₂O₃ and SiO₂ particles. The uptake coefficients of acetic acid are increased by a factor of 3-5 for γ -Al₂O₃ when RH increases from 0% to 15%, whereas acetic acid and water are found to compete for surface sites for the adsorption on SiO₂ particles.

4.6 Acknowledgement

This material is based on the work supported by the National Science Foundation under grant number CHE-1639757. Any opinions, findings, and conclusions or recommendations expressed in this material are those of the authors and do not necessarily reflect the views of National Science Foundation. Chapter 4, in full, is a reprint of the material published by American Chemical Society in: Mingjin Tang, Whitney A. Larish, Yuan Fang, Aruni Gankanda, and Vicki H. Grassian, "Heterogeneous Reactions of Acetic Acid with Oxide Surfaces: Effects of Mineralogy and Relative Humidity", *The Journal of Physical Chemistry A* **2016** *120* (28), 5609-5616. The dissertation author was the investigator and author of all experimental measurements and data analysis of gas phase and adsorbed acetic acid on silica.

4.7 Appendix

4.7.1 FTIR spectra (800-4000 cm^{-1}) of $\gamma\text{-Al}_2\text{O}_3$, CaO, and SiO₂ after interaction with acetic acid

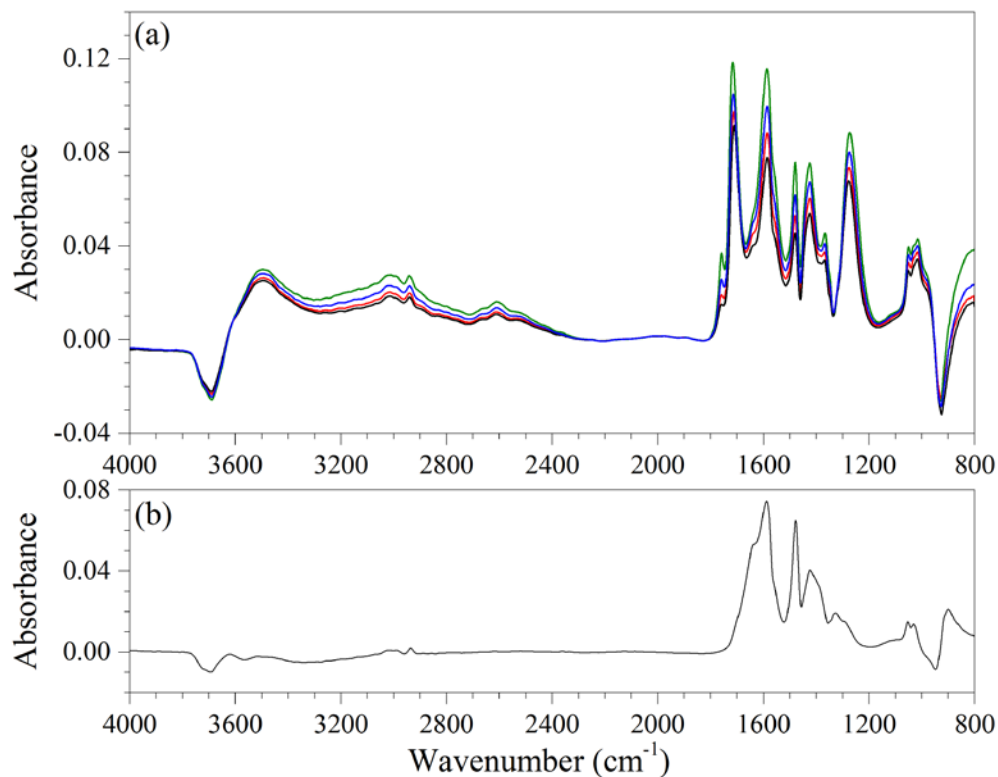


Figure 4.6. FTIR spectra (800-4000 cm^{-1}) of $\gamma\text{-Al}_2\text{O}_3$ after reaction with $\text{CH}_3\text{COOH}(\text{g})$ under dry conditions. (a) Spectra of $\gamma\text{-Al}_2\text{O}_3$ after reaction with 27, 79, 293, and 1190 mTorr $\text{CH}_3\text{COOH}(\text{g})$. (b) A typical spectrum of reacted $\gamma\text{-Al}_2\text{O}_3$ after evacuation of the reaction cell.

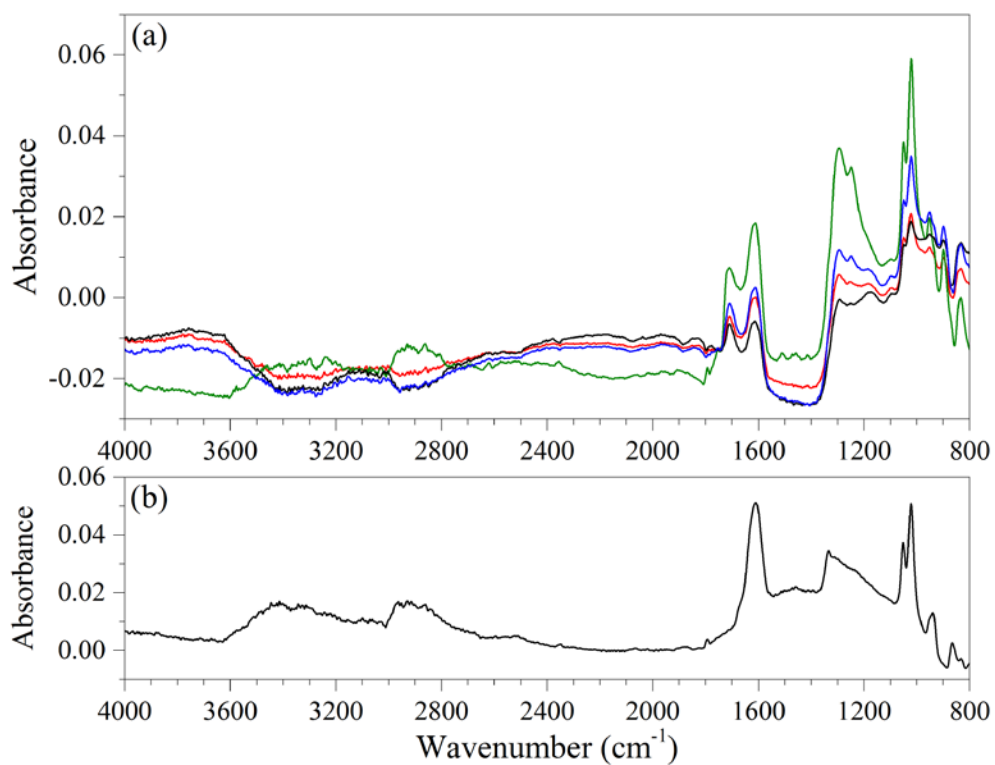


Figure 4.7. FTIR spectra (800-4000 cm⁻¹) of CaO after reaction with CH₃COOH(g) under dry conditions. (a) Spectra of CaO after reaction with 25, 82, 298, and 1175 mTorr CH₃COOH(g). (b) A typical spectrum of reacted CaO after evacuation of the reaction cell.

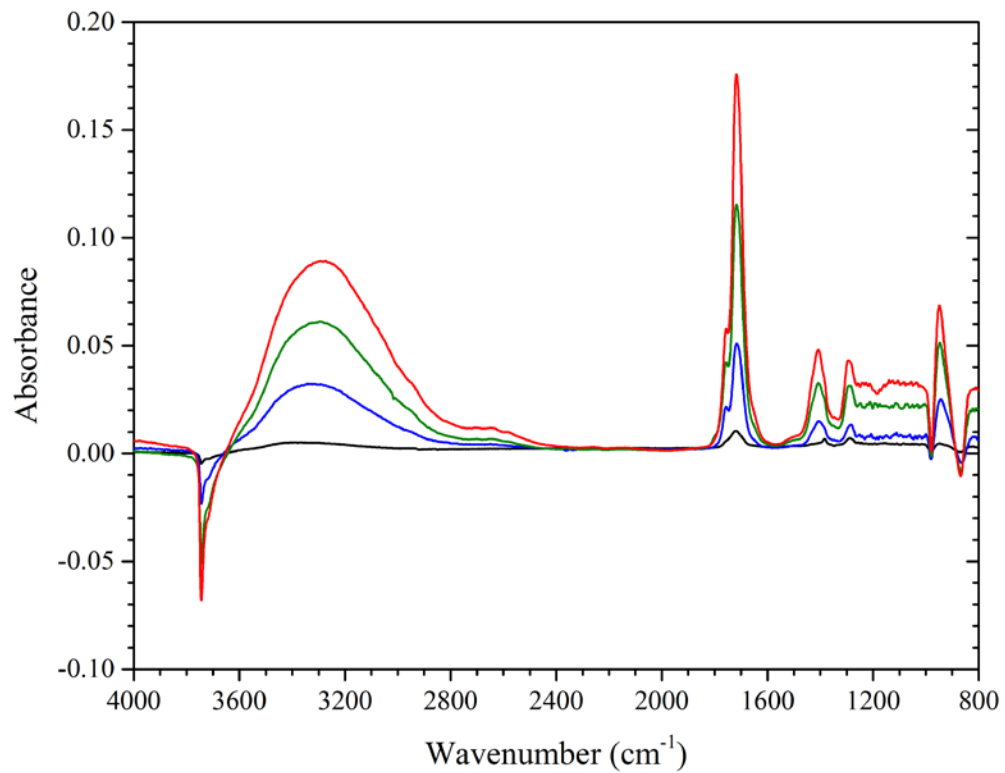


Figure 4.8. FTIR spectra (800-4000 cm⁻¹) of SiO₂ after exposure to CH₃COOH(g) with pressure of 5, 21, 55, and 117 mTorr in the gas phase under dry conditions. Please note that SiO₂ is opaque below 1250 cm⁻¹.

4.7.2 Langmuir isotherm for acetic acid adsorption on silica particles

Physisorption on a surface can usually be described by the Langmuir isotherm:

$$\theta = \frac{N}{N_s} = \frac{Kp}{1+Kp} \quad (\text{E4.3})$$

where θ is the surface coverage, K is the Langmuir constant, and P is the pressure (of gaseous acetic acid in our study), N is the number of molecules adsorbed by per area surface at the pressure of P , and N_s is the number of molecules adsorbed by per area surface at saturation. Eq. (E4.3) can be rearranged to

$$\frac{P}{N} = \frac{1}{N_s K} + \frac{P}{N_s} \quad (\text{E4.4})$$

Therefore, a plot of P/N against P should give a linear line with a slope equal to $1/N_s$ and an intercept equal to $1/(N_s \cdot K)$.

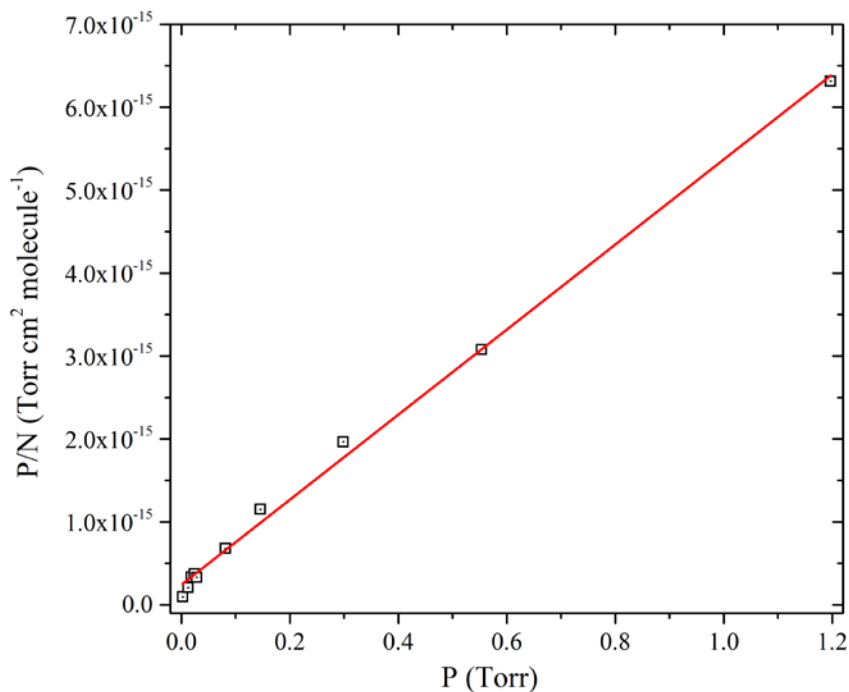


Figure 4.9. Plotting of P/N as a function of $\text{CH}_3\text{COOH}(\text{g})$ pressure (P) for SiO_2 under dry conditions.

Figure 4.9 shows that the plot of P/N against P for SiO_2 particles generates a straight line, suggesting that the Langmuir isotherm can adequately describe the adsorption of acetic acid by SiO_2 surface. The saturation coverage and Langmuir constant for SiO_2 , are determined to be $(2.0 \pm 0.1) \times 10^{14}$ molecules cm^{-2} and 213 ± 35 Torr $^{-1}$, respectively.

4.8 References

- (1) Textor, C.; Schulz, M.; Guibert, S.; Kinne, S.; Balkanski, Y.; Bauer, S.; Bernsten, T.; Berglen, T.; Boucher, O.; Chin, M. *et al.* Analysis and Quantification of the Diversities of Aerosol Life Cycles within AeroCom. *Atmos. Chem. Phys.* **2006**, *6*, 1777-1813.
- (2) Ginoux, P.; Prospero, J. M.; Gill, T. E.; Hsu, N. C.; Zhao, M. Global-scale Attribution of Anthropogenic and Natural Dust Sources and Their Emission Rates Based on MODIS Deep Blue Aerosol Products. *Rev. Geophys.* **2012**, *50*, RG3005.
- (3) Balkanski, Y.; Schulz, M.; Claquin, T.; Guibert, S. Reevaluation of Mineral Aerosol Radiative Forcings Suggests a Better Agreement with Satellite and AERONET Data. *Atmos. Chem. Phys.* **2007**, *7*, 81-95.
- (4) Huang, X.; Song, Y.; Zhao, C.; Cai, X.; Zhang, H.; Zhu, T. Direct Radiative Effect by Multicomponent Aerosol over China. *J. Climate* **2015**, *28*, 3472-3495.
- (5) Tanre, D.; Haywood, J.; Pelon, J.; Leon, J. F.; Chatenet, B.; Formenti, P.; Francis, P.; Goloub, P.; Highwood, E. J.; Myhre, G. Measurement and Modeling of the Saharan Dust Radiative Impact: Overview of the Saharan Dust Experiment (SHADE). *J. Geophys. Res.-Atmos.* **2003**, *108*, 8574.
- (6) Twohy, C. H.; Kreidenweis, S. M.; Eidhammer, T.; Browell, E. V.; Heymsfield, A. J.; Bansemer, A. R.; Anderson, B. E.; Chen, G.; Ismail, S.; DeMott, P. J. *et al.* Saharan Dust Particles Nucleate Droplets in Eastern Atlantic Clouds. *Geophys. Res. Lett.* **2009**, *36*, L01807.
- (7) Cziczo, D. J.; Froyd, K. D.; Hoose, C.; Jensen, E. J.; Diao, M.; Zondlo, M. A.; Smith, J. B.; Twohy, C. H.; Murphy, D. M. Clarifying the Dominant Sources and Mechanisms of Cirrus Cloud Formation. *Science* **2013**, *340*, 1320-1324.
- (8) Creamean, J. M.; Suski, K. J.; Rosenfeld, D.; Cazorla, A.; DeMott, P. J.; Sullivan, R. C.; White, A. B.; Ralph, F. M.; Minnis, P.; Comstock, J. M. *et al.* Dust and Biological Aerosols from the Sahara and Asia Influence Precipitation in the Western U.S. *Science* **2013**, *339*, 1572-1578.
- (9) Tang, M. J.; Cziczo, D. J.; Grassian, V. H. Interactions of Water with Mineral Dust Aerosol: Water Adsorption, Hygroscopicity, Cloud Condensation and Ice Nucleation. *Chem. Rev.* **2016**, *116*, 4205-4259.
- (10) Jickells, T. D.; An, Z. S.; Andersen, K. K.; Baker, A. R.; Bergametti, G.; Brooks, N.; Cao, J. J.; Boyd, P. W.; Duce, R. A.; Hunter, K. A. *et al.* Global Iron Connections between Desert Dust, Ocean Biogeochemistry, and Climate. *Science* **2005**, *308*, 67-71.

- (11) Mahowald, N. M.; Baker, A. R.; Bergametti, G.; Brooks, N.; Duce, R. A.; Jickells, T. D.; Kubilay, N.; Prospero, J. M.; Tegen, I. Atmospheric Global Dust Cycle and Iron Inputs to the Ocean. *Glob. Biogeochem. Cycle* **2005**, *19*, GB4025.
- (12) Schulz, M.; Prospero, J. M.; Baker, A. R.; Dentener, F.; Ickes, L.; Liss, P. S.; Mahowald, N. M.; Nickovic, S.; García-Pando, C. P.; Rodríguez, S. *et al.* Atmospheric Transport and Deposition of Mineral Dust to the Ocean: Implications for Research Needs. *Environ. Sci. Technol.* **2012**, *46*, 10390-10404.
- (13) Prospero, J. M. Long-range Transport of Mineral Dust in the Global Atmosphere: Impact of African Dust on the Environment of the Southeastern United States. *Proc. Natl. Acad. Sci. U. S. A.* **1999**, *96*, 3396-3403.
- (14) Uno, I.; Eguchi, K.; Yumimoto, K.; Takemura, T.; Shimizu, A.; Uematsu, M.; Liu, Z.; Wang, Z.; Hara, Y.; Sugimoto, N. Asian Dust Transported One Full Circuit around the Globe. *Nature Geosci.* **2009**, *2*, 557-560.
- (15) Crowley, J. N.; Ammann, M.; Cox, R. A.; Hynes, R. G.; Jenkin, M. E.; Mellouki, A.; Rossi, M. J.; Troe, J.; Wallington, T. J. Evaluated Kinetic and Photochemical Data for Atmospheric Chemistry: Volume V - Heterogeneous Reactions on Solid Substrates. *Atmos. Chem. Phys.* **2010**, *10*, 9059-9223.
- (16) Usher, C. R.; Michel, A. E.; Grassian, V. H. Reactions on Mineral Dust. *Chem. Rev.* **2003**, *103*, 4883-4939.
- (17) Tang, M. J.; Thieser, J.; Schuster, G.; Crowley, J. N. Kinetics and Mechanism of the Heterogeneous Reaction of N₂O₅ with Mineral Dust Particles. *Phys. Chem. Chem. Phys.* **2012**, *14*, 8551-8561.
- (18) Bedjanian, Y.; Romanias, M. N.; El Zein, A. Uptake of HO₂ Radicals on Arizona Test Dust. *Atmos. Chem. Phys.* **2013**, *12*, 6461-6471.
- (19) Nicolas, M.; Ndour, M.; Ka, O.; D'anna, B.; George, C. Photochemistry of Atmospheric Dust: Ozone Decomposition on Illuminated Titanium Dioxide. *Environ. Sci. Technol.* **2009**, *43*, 7347-7442.
- (20) Shang, J.; Li, J.; Zhu, T. Heterogeneous Reaction of SO₂ on TiO₂ Particles. *Sci. China Chem.* **2010**, *53*, 2637-2643.
- (21) Fairlie, T. D.; Jacob, D. J.; Dibb, J. E.; Alexander, B.; Avery, M. A.; van Donkelaar, A.; Zhang, L. Impact of Mineral Dust on Nitrate, Sulfate, and Ozone in Transpacific Asian Pollution Plumes. *Atmos. Chem. Phys.* **2010**, *10*, 3999-4012.
- (22) Zhu, S.; Butler, T.; Sander, R.; Ma, J.; Lawrence, M. G. Impact of Dust on Tropospheric Chemistry over Polluted Regions: a Case Study of the Beijing Megacity. *Atmos. Chem. Phys.* **2010**, *10*, 3855-3873.

- (23) Wang, K.; Zhang, Y.; Nenes, A.; Fountoukis, C. Implementation of Dust Emission and Chemistry into the Community Multiscale Air Quality Modeling System and Initial Application to an Asian Dust Storm Episode. *Atmos. Chem. Phys.* **2012**, *12*, 10209-10237.
- (24) Laskin, A.; Iedema, M. J.; Ichkovich, A.; Graber, E. R.; Taraniuk, I.; Rudich, Y. Direct Observation of Completely Processed Calcium Carbonate Dust Particles. *Faraday Discuss.* **2005**, *130*, 453-468.
- (25) Sullivan, R. C.; Guazzotti, S. A.; Sodeman, D. A.; Prather, K. A. Direct Observations of the Atmospheric Processing of Asian Mineral Dust. *Atmos. Chem. Phys.* **2007**, *7*, 1213-1236.
- (26) Tang, Y. H.; Carmichael, G. R.; Seinfeld, J. H.; Dabdub, D.; Weber, R. J.; Huebert, B.; Clarke, A. D.; Guazzotti, S. A.; Sodeman, D. A.; Prather, K. A. *et al.* Three-dimensional Simulations of Inorganic Aerosol Distributions in East Asia during Spring 2001. *J. Geophys. Res.-Atmos.* **2004**, *109*, D19s23.
- (27) He, H.; Wang, Y.; Ma, Q.; Ma, J.; Chu, B.; Ji, D.; Tang, G.; Liu, C.; Zhang, H.; Hao, J. Mineral Dust and NO_x Promote the Conversion of SO₂ to Sulfate in Heavy Pollution Days. *Sci. Rep.* **2014**, *4*, 4172.
- (28) Li, W.; Shao, L.; Zhang, D.; Ro, C.-U.; Hu, M.; Bi, X.; Geng, H.; Matsuki, A.; Niu, H.; Chen, J. A Review of Single Aerosol Particle Studies in the Atmosphere of East Asia: Morphology, Mixing State, Source, and Heterogeneous Reactions. *J. Clean. Prod.* **2015**, *112*, 1330-1349.
- (29) Krueger, B. J.; Grassian, V. H.; Laskin, A.; Cowin, J. P. The Transformation of Solid Atmospheric Particles into Liquid Droplets through Heterogeneous Chemistry: Laboratory Insights into the Processing of Calcium Containing Mineral Dust Aerosol in the Troposphere. *Geophys. Res. Lett.* **2003**, *30*, 1148.
- (30) Sullivan, R. C.; Moore, M. J. K.; Petters, M. D.; Kreidenweis, S. M.; Roberts, G. C.; Prather, K. A. Timescale for Hygroscopic Conversion of Calcite Mineral Particles through Heterogeneous Reaction with Nitric Acid. *Phys. Chem. Chem. Phys.* **2009**, *11*, 7826-7837.
- (31) Tobo, Y.; Zhang, D.; Matsuki, A.; Iwasaka, Y. Asian Dust Particles Converted into Aqueous Droplets under Remote Marine Atmospheric Conditions. *Proc. Natl. Acad. Sci. U. S. A.* **2010**, *107*, 17905-17910.
- (32) Kulkarni, G.; Zhang, K.; Zhao, C.; Nandasiri, M.; Shutthanandan, V.; Liu, X.; Fast, J.; Berg, L. Ice Formation on Nitric Acid Coated Dust Particles: Laboratory and Modeling Studies. *J. Geophys. Res.-Atmos* **2015**, *120*, 7682-7698.
- (33) Augustin-Bauditz, S.; Wex, H.; Kanter, S.; Ebert, M.; Niedermeier, D.; Stolz, F.; Prager, A.; Stratmann, F. The Immersion Mode Ice Nucleation Behavior of Mineral

Dusts: A Comparison of Different Pure and Surface Modified Dusts. *Geophys. Res. Lett.* **2014**, *41*, 7375-7382.

- (34) Khare, P.; Kumar, N.; Kumari, K. M.; Srivastava, S. S. Atmospheric Formic and Acetic Acids: An Overview. *Rev. Geophys.* **1999**, *37*, 227-248.
- (35) Shen, X.; Zhao, Y.; Chen, Z.; Huang, D. Heterogeneous reactions of volatile organic compounds in the atmosphere. *Atmos. Environ.* **2013**, *68*, 297-314.
- (36) Carlos-Cuellar, S.; Li, P.; Christensen, A. P.; Krueger, B. J.; Burrichter, C.; Grassian, V. H. Heterogeneous Uptake Kinetics of Volatile Organic Compounds on Oxide Surfaces Using a Knudsen Cell Reactor: Adsorption of Acetic Acid, Formaldehyde, and Methanol on α -Fe₂O₃, α -Al₂O₃, and SiO₂. *J. Phys. Chem. A* **2003**, *107*, 4250-4261.
- (37) Prince, A. P.; Kleiber, P. D.; Grassian, V. H.; Young, M. A. Reactive Uptake of Acetic Acid on Calcite and Nitric Acid Reacted Calcite Aerosol in an Environmental Reaction Chamber. *Phys. Chem. Chem. Phys.* **2008**, *10*, 142-152.
- (38) Hatch, C. D.; Gough, R. V.; Tolbert, M. A. Heterogeneous Uptake of the C1 to C4 Organic Acids on a Swelling Clay Mineral. *Atmos. Chem. Phys.* **2007**, *7*, 4445-4458.
- (39) Tong, S. R.; Wu, L. Y.; Ge, M. F.; Wang, W. G.; Pu, Z. F. Heterogeneous Chemistry of Monocarboxylic Acids on α -Al₂O₃ at Different Relative Humidities. *Atmos. Chem. Phys.* **2010**, *10*, 7561-7574.
- (40) Ma, Q. X.; Liu, Y. C.; Liu, C.; He, H. Heterogeneous Reaction of Acetic Acid on MgO, α -Al₂O₃, and CaCO₃ and the Effect on the Hygroscopic Behavior of These Particles. *Phys. Chem. Chem. Phys.* **2012**, *14*, 8403-8409.
- (41) Hou, S. Q.; Tong, S. R.; Zhang, Y.; Tan, F.; Guo, Y. C.; Ge, M. F. Heterogeneous uptake of gas-phase acetic acid on α -Al₂O₃ particle surface: the impact of temperature. *Chem. Asian J.* **2016**.
- (42) Sun, Z.; Kong, L.; Ding, X.; Du, C.; Zhao, X.; Chen, J.; Fu, H.; Yang, X.; Cheng, T. The effects of acetaldehyde, glyoxal and acetic acid on the heterogeneous reaction of nitrogen dioxide on gamma-alumina. *Phys. Chem. Chem. Phys.* **2016**, *18*, 9367-9376.
- (43) Tang, M. J.; Whitehead, J.; Davidson, N. M.; Pope, F. D.; Alfarra, M. R.; McFiggans, G.; Kalberer, M. Cloud Condensation Nucleation Activities of Calcium Carbonate and its Atmospheric Ageing Products. *Phys. Chem. Chem. Phys.* **2015**, *17*, 32194-32203.
- (44) Alexander, J. M.; Grassian, V. H.; Young, M. A.; Kleiber, P. D. Optical Properties of Selected Components of Mineral Dust Aerosol Processed with Organic Acids and Humic Material. *J. Geophys. Res.-Atmos* **2015**, *120*, 2437-2452.

- (45) Chen, H.; Grassian, V. H. Iron Dissolution of Dust Source Materials during Simulated Acidic Processing: The Effect of Sulfuric, Acetic, and Oxalic Acids. *Environ. Sci. Technol.* **2013**, *47*, 10312-10321.
- (46) Goodman, A. L.; Bernard, E. T.; Grassian, V. H. Spectroscopic Study of Nitric Acid and Water Adsorption on Oxide Particles: Enhanced Nitric Acid Uptake Kinetics in the Presence of Adsorbed Water. *J. Phys. Chem. A* **2001**, *105*, 6443-6457.
- (47) Fang, Y.; Tang, M. J.; Grassian, V. H. Competition between Surface Displacement and Dissociative Adsorption of a Strong Acid Compared to a Weak Acid on Silica Particle Surfaces: The Role of Adsorbed Water *J. Phys. Chem. A* **2016**, *120*.
- (48) Rubasinghege, G.; Ogden, S.; Baltrusaitis, J.; Grassian, V. H. Heterogeneous Uptake and Adsorption of Gas-Phase Formic Acid on Oxide and Clay Particle Surfaces: The Roles of Surface Hydroxyl Groups and Adsorbed Water in Formic Acid Adsorption and the Impact of Formic Acid Adsorption on Water Uptake. *J. Phys. Chem. A* **2013**, *117*, 11316-11327.
- (49) Weltner, W. The Vibrational Spectrum, Associative and Thermodynamic Properties of Acetic Acid Vapor. *J. Am. Chem. Soc.* **1955**, *77*, 3941-3950.
- (50) Maréchal, Y. IR Spectra of Carboxylic Acids in the Gas Phase: A Quantitative Reinvestigation. *J. Chem. Phys.* **1987**, *87*, 6344-6353.
- (51) Hasan, M. A.; Zaki, M. I.; Pasupulety, L. Oxide-catalyzed conversion of acetic acid into acetone: an FTIR spectroscopic investigation. *Appl. Catal., A* **2003**, *243*, 81-92.
- (52) Chocholoušová, J.; Vacek, J.; Hobza, P. Acetic Acid Dimer in the Gas Phase, Nonpolar Solvent, Microhydrated Environment, and Dilute and Concentrated Acetic Acid: Ab Initio Quantum Chemical and Molecular Dynamics Simulations. *J. Phys. Chem. A* **2003**, *107*, 3086-3092.
- (53) Xu, C.; Koel, B. E. Adsorption and Reaction of CH₃COOH and CD₃COOD on the MgO(100) Surface: A Fourier Transform Infrared and Temperature Programmed Desorption Study. *J. Chem. Phys.* **1995**, *102*, 8158-8166.
- (54) Liao, L.-F.; Lien, C.-F.; Lin, J.-L. FTIR Study of Adsorption and Photoreactions of Acetic Acid on TiO₂. *Phys. Chem. Chem. Phys.* **2001**, *3*, 3831-3837.
- (55) Taylor, M. D. The Vapor Phase Dissociation of Some Carboxylic Acids. I. Acetic Acid_{1,2,3,4}. *J. Am. Chem. Soc.* **1951**, *73*, 315-317.
- (56) Pei, Z. F.; Ponec, V. On the Intermediates of the Acetic Acid Reactions on Oxides: an IR Study. *Appl. Surf. Sci.* **1996**, *103*, 171-182.
- (57) Nanayakkara, C. E.; Dillon, J. K.; Grassian, V. H. Surface Adsorption and Photochemistry of Gas-Phase Formic Acid on TiO₂ Nanoparticles: The Role of

- Adsorbed Water in Surface Coordination, Adsorption Kinetics, and Rate of Photoproduct Formation. *J. Phys. Chem. C* **2014**, *118*, 25487-25495.
- (58) Ito, K.; Bernstein, H. J. The Vibrational Spectra of the Formate, Acetate, and Oxalate Ions. *Can. J. Chem.* **1956**, *34*, 170-178.
- (59) Kakihana, M.; Kotaka, M.; Okamoto, M. Infrared Spectra of Carbon-13-Substituted Species of Solid Sodium Acetate at 80 K. *J. Phys. Chem.* **1982**, *86*, 4385-4387.
- (60) Tang, M. J.; Cox, R. A.; Kalberer, M. Compilation and Evaluation of Gas Phase Diffusion Coefficients of Reactive Trace Gases in the Atmosphere: Volume 1. Inorganic Compounds. *Atmos. Chem. Phys.* **2014**, *14*, 9233-9247.
- (61) Raff, J. D.; Njegic, B.; Chang, W. L.; Gordon, M. S.; Dabdub, D.; Gerber, R. B.; Finlayson-Pitts, B. J. Chlorine Activation Indoors and Outdoors via Surface-mediated Reactions of Nitrogen Oxides with Hydrogen Chloride. *Proc. Natl. Acad. Sci. U. S. A.* **2009**, *106*, 13647-13654.
- (62) Finlayson-Pitts, B. J.; Wingen, L. M.; Sumner, A. L.; Syomin, D.; Ramazan, K. A. The heterogeneous hydrolysis of NO₂ in laboratory systems and in outdoor and indoor atmospheres: An integrated mechanism. *Phys. Chem. Chem. Phys.* **2003**, *5*, 223-242.
- (63) Finlayson-Pitts, B. J. Reaction of NO₂ with NaCl and Atmospheric Implications of NOCl Formation. *Nature* **1983**, *306*, 676-677.
- (64) Finlayson-Pitts, B. J.; Ezell, M. J.; Pitts, J. N. Formation of Chemically Active Chlorine Compounds by Reactions of Atmospheric NaCl Particles with Gaseous N₂O₅ and ClONO₂. *Nature* **1989**, *337*, 241-244.
- (65) Miller, Y.; Finlayson-Pitts, B. J.; Gerber, R. B. Ionization of N₂O₄ in Contact with Water: Mechanism, Time Scales and Atmospheric Implications. *J. Am. Chem. Soc.* **2009**, *131*, 12180-12185.
- (66) Wang, J.; Koel, B. E. IRAS Studies of NO₂, N₂O₃, and N₂O₄ Adsorbed on Au(111) Surfaces and Reactions with Coadsorbed H₂O. *J. Phys. Chem. A* **1998**, *102*, 8573-8579.
- (67) Gerber, R. B.; Varner, M. E.; Hammerich, A. D.; Riikonen, S.; Murdachaew, G.; Shemesh, D.; Finlayson-Pitts, B. J. Computational Studies of Atmospherically-Relevant Chemical Reactions in Water Clusters and on Liquid Water and Ice Surfaces. *Accounts Chem. Res.* **2015**, *48*, 399-406.

CHAPTER 5 HETEROGENEOUS INTERACTIONS BETWEEN GAS-PHASE PYRUVIC ACID AND HYDROXYLATED SILICA SURFACES: A COMBINED EXPERIMENTAL AND THEORETICAL STUDY

5.1 Abstract

The adsorption of gas-phase pyruvic acid ($\text{CH}_3\text{COCO}(\text{OH})$) on hydroxylated silica particles has been investigated at 296 K. Under dry conditions ($< 1\%$ RH), both the Tc and Tt pyruvic acid conformers are observed on the surface as well as the (hydrogen-bonded) pyruvic acid dimer. Under higher relative humidity conditions (above 10% RH), adsorbed water competes for surface adsorption sites. Adsorbed water is observed to change the relative composition of the different adsorbed pyruvic acid configurations. Overall, this study provides valuable insights into the interaction of gas-phase pyruvic acid with the silica surface on the molecular level from both experimental and theoretical view. Furthermore, these results highlight the importance of the environment (relative humidity) in the surface adsorption and surface chemistry of organic acids.

5.2 Introduction

Pyruvic acid (PA), $\text{CH}_3\text{COCO}(\text{OH})$, an important atmospheric α – keto, is formed in the atmosphere primarily via the particle-phase aqueous reaction between the hydroxyl radical ($\text{OH}\cdot$) and hydrated methylglyoxal (an abundant oxidation product of precursors such as isoprene and aromatic compounds).¹ Numerous field studies have detected pyruvic

acid in the gas-phase (10-100 ppt), in aerosols (up to 140 ng m⁻³), in snow and in rainwater²⁻¹³. A variety of reactions have been investigated for pyruvic acid including gas- and condensed- phase photolysis¹⁴⁻²³, hydroxyl radical oxidation²⁴⁻²⁶, thermal decomposition^{27,28} and vibrational overtone induced decarboxylation²⁹⁻³¹. Computational studies³²⁻³⁴ on pyruvic acid's electronic structure, conformation possibilities, and barriers to decarboxylation provide insights into experimental findings.

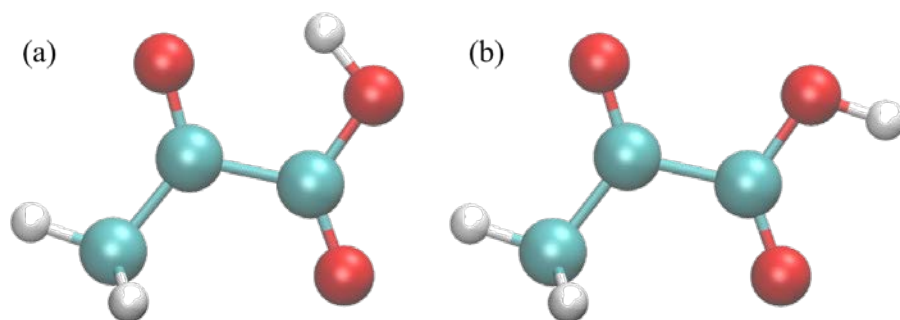


Figure 5.1. Conformers of pyruvic acid. (a) Tc and (b) Tt conformer.

The structure of pyruvic acid is interesting as it is an α -dicarbonyl acid that possesses several conformers due to the intramolecular rotation around the C–C and C–O bonds²⁹. Reva et al.³⁵ investigated the infrared spectroscopic features of the rotational conformers of pyruvic acid. These conformers have also been studied using theoretical approaches^{27,34-38} and for gaseous pyruvic acid, the two lowest energy conformers are separated by only 2.08 kcal mol⁻¹, while other conformers lie at much higher energy.^{27,35,39,40} The lowest energy conformer is labelled as the trans – cis (Tc) conformer, while the higher energy conformer is the trans – trans (Tt) conformer as shown in Figure 5.1. The Tt conformer has the acidic hydrogen rotated away from the ketonic oxygen while the most stable conformer form, the Tc conformer, forms an intramolecular hydrogen bond

between the acidic hydrogen and the α – carbonyl. Since the Tt conformer is close enough in energy to the most stable Tc conformer, there is a significant thermal population of both at ambient temperatures.^{27,29,34,41–44} Plath et al.²⁹ revealed the differences between the Tt and Tc conformers by studying the OH vibrational overtone transitions and Reva et al.⁴⁴ showed conformational switching between pyruvic acid Tt and Tc conformers by selective pumping of the first OH stretching vibration overtone.

Since mineral aerosol surfaces are ubiquitous in the atmosphere and play an important role in atmospheric chemistry^{45–47}, we are interested in how organic acids such as pyruvic acid interacts with these surfaces. Silica (SiO_2), an oxide with abundant surface hydroxyl groups, is an important component of mineral dust particles in the atmosphere⁴⁸. Silica can also represent indoor glass surface. In addition, pyruvic acid has been identified in human emanation and has been recently detected as one of the dominant gas phase carboxylic acids in occupied classrooms.⁴⁹ Several studies have investigated the heterogeneous reaction of atmospheric acidic gases with silica^{48,50–54}. The uptake of organic acids including HCOOH and CH_3COOH on SiO_2 has been examined previously^{48,54,55}, as well as inorganic acids such as HNO_3 ⁵¹. Since there is an abundance of water vapor in the atmosphere, the role of co-adsorbed water of in the interaction of these acids with silica has been probed as well. These studies reveal that adsorbed water both competes for surface adsorption sites with HNO_3 and HCOOH , as well as promotes their dissociation to hydronium ions and the corresponding anions^{51,56} the case of pyruvic acid, few studies have investigated the surface chemistry of this molecule, however, Schnitzler et al.⁵⁷ studied the intermolecular interactions between pyruvic acid and water

complex and suggested hydrogen-bonded water affects pyruvic acid conformation and stability.

To date, heterogenous interactions of pyruvic acid with mineral aerosol particle surfaces, such as SiO₂, are not well understood. Given the importance of heterogeneous reactions of mineral dust aerosol particle surfaces with trace atmospheric gases, the interaction of pyruvic acid requires further investigation. The current limited knowledge necessitates this study of surface adsorption of pyruvic acid on SiO₂ surfaces to better understand how adsorption impacts the molecular structure of pyruvic acid and if co-adsorbed water changes that structure.

5.3 Methods

5.3.1 Experimental Setup

The adsorption of pyruvic acid on silica surfaces as a function of pyruvic acid pressure at 296 ± 1 K and different relative humidity (RH), was studied using a modified Teflon coated infrared cell coupled with transmission Fourier transform infrared (FTIR) spectroscopy, as described in detail previous studies.^{51,52,58} In these experiments, approximately 5 mg of silica (Degussa), having a BET area of 230 m² g⁻¹, was pressed onto one half of a tungsten grid held by two Teflon coated jaws in the sample cell compartment. The sample cell was then evacuated for 6 hours using a turbo-molecular pump to clean the cell and sample surface. After evacuation, the sample was exposed to the desired pressure of dry, gaseous pyruvic acid for 20 minutes under dry conditions (RH < 1%). The gaseous pyruvic acid was produced from CH₃COCOOH (97%, Alfa Aesar) by degassing at least three times with consecutive freeze-pump-thaw cycles.

To investigate the effects of relative humidity, the oxide sample was first exposed to the desired pressures of pyruvic acid for 20 minutes, followed by the introduction of the desired pressure of water vapor (produced from degassed HPLC grade water, Fisher Chemicals) for an additional 20 minutes. Fixing the relative humidity while varying the pressure of pyruvic acid which the sample was exposed to allowed for the effects of pyruvic acid pressure to be studied. After each experiment, the IR cell was evacuated overnight using a turbo-molecular pump. Prior to and after the exposure of pyruvic acid, the single beam spectra of surface- and gas- phase (250 scans) were acquired at 296 K using a resolution of 4 cm^{-1} and covering the spectral range of 800 to 4000 cm^{-1} . As silica is opaque below $\sim 1200\text{ cm}^{-1}$, spectra are shown only above 1200 cm^{-1} . During and following exposure to pyruvic acid, single beam spectra of the silica surface (10 scans) were acquired using a Macro (OMNIC Macro Basics) for 60s intervals. Absorbance spectra of pyruvic acid on silica particles are reported as the difference in the silica spectra before and after exposure to pyruvic acid. Absorption bands due to gas-phase pyruvic acid, measured through the blank half of the tungsten grid, were subtracted to obtain FTIR spectra of the particles loaded on the tungsten grid.

5.3.2 Theoretical Methods

The geometry optimizations and the ab initio Born-Oppenheimer molecular dynamics (BOMD) simulations were performed using the Quickstep module⁵⁹ within the CP2K package, with the nuclei treated as classical particles. The DFT^{60,61} exchange-correlation functional was used, supplemented by the dispersion correction Grimme (BLYP-D).

The silica model^{62,63} representing the (0001) face of hydroxylated α -quartz consisted of a periodic tetragonal slab with dimension (xyz) of $19.64 \times 17.008 \times 80 \text{ \AA}^3$, with 6 O-Si-O layers, thus leaving a vacuum of about 69 \AA between periodic images in the z – direction. Both bottom and top surfaces were fully hydroxylated. The top surface, which contains 32 silanol groups, was used to examine reactivity.

The systems studied were pyruvic acid interacting with dry or wetted hydroxylated silica: (1) dry silica (zero physisorbed water molecules, 0% coverage), (2) fully wetted silica with one full monolayer of water (16 molecules, 100% coverage).

Tc and Tt conformers in gas phase, CSVr 1ps thermostat, 298 K, 15 ps trajectory. Tc and Tt conformer on silica, CSVr 1ps, 298 K, parallel to the surface. For the one monolayer case, molecular dynamics simulations (MD) were performed at 330 K.

5.4 Results and Discussion

5.4.1 Adsorption of Pyruvic Acid on SiO₂ Surfaces

The FTIR spectrum of gas-phase pyruvic acid ($\text{C}_3\text{H}_4\text{O}_3(\text{g})$) seen in Figure 5.2 was collected at 298 K for a pressure of 1 Torr (4 cm^{-1} resolution). The spectrum and the vibrational modes of gas-phase pyruvic acid are well understood²⁹. The modes are assigned as follows: 3579 cm^{-1} for O-H stretching of the Tt conformer; 3463 cm^{-1} for O-H stretching of the Tc conformer; 1805 cm^{-1} for C=O acid stretching; 1737 cm^{-1} for C=O ketone stretching; 1360 cm^{-1} for CH₃ symmetric bending; 1211 cm^{-1} for COH bending; 1134 cm^{-1} for C-O stretching, and 970 cm^{-1} is assigned to CH₃ rocking. Adjacent to the C=O ketone stretching frequency (centred at 1737 cm^{-1}), a small shoulder (at 1760 cm^{-1}) is

observed (inset in Figure 5.1), corresponding to the non-hydrogen bonded Tt conformer. The main part of this peak, however, is due to the more stable intramolecular hydrogen bonded Tc conformer²⁹.

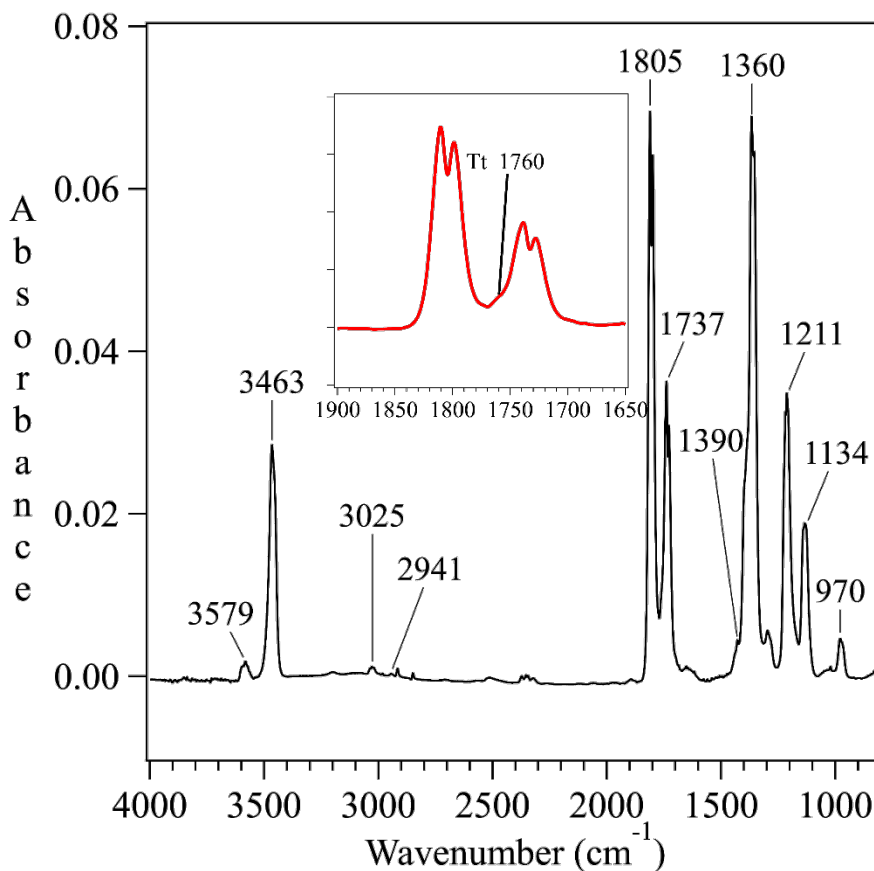


Figure 5.2. FTIR spectrum of gas-phase pyruvic acid in the spectral range of 800 to 4000 cm^{-1} and inset from 1650 to 1900 cm^{-1} . The small shoulder observed in the inset (at 1760 cm^{-1} , shown in red) corresponds to the non-hydrogen bonded Tt conformer, while the main part of this peak is due to the more stable intramolecular hydrogen bonded Tc conformer³¹.

5.4.1.1 Pyruvic Acid Adsorption Under Dry Conditions ($RH < 1\%$)

Shown in Figure 5.3 is infrared spectra for hydroxylated silica particles after exposure to gaseous pyruvic acid as a function of varying pyruvic acid pressure. For this

set of experiments, dry conditions were employed ($\text{RH} < 1\%$) at 296 K. The clean silica surface serves as the background reference spectrum. Observed infrared absorption band frequencies are assigned as follows: C=O stretching at 1737 cm^{-1} ; CH_3 asymmetric bending at 1428 cm^{-1} ; C-C asymmetric stretching at 1389 cm^{-1} ; and CH_3 symmetric bending at 1280 cm^{-1} . Pyruvic acid adsorption was also carried out at lower pyruvic acid pressures (5, 10, 15 and 25 mTorr) as shown in Figure 5.3b. A small shoulder (1776 cm^{-1}) to the left of the peak centered at 1737 cm^{-1} is clear at lower pyruvic acid coverages and can be assigned to the Tc conformer acid stretch, shifted from the gas-phase position (1805 cm^{-1}). The peak shift is due to weaker intramolecular hydrogen bonding following adsorption. Note that at higher pressures, the peak at 1776 cm^{-1} has been merged into the highest intensity peak (centered at 1737 cm^{-1}) and become less clear. Except for this band, all other observed band frequencies are in excellent agreement with the gas-phase pyruvic acid spectrum. Only a few wavenumber differences are observed. The negative peak at 3742 cm^{-1} is due to silica surface isolated silanol groups hydrogen bonded with pyruvic acid, with the broad band below 3600 cm^{-1} assigned to the hydrogen bonded Si – OH groups. Absorption peaks due to adsorbed pyruvic acid (1737 , 1428 , 1389 , and 1355 cm^{-1}) disappear upon evacuation, while the negative peak attributed to isolated O-H groups (3742 cm^{-1}) reappears, suggesting that pyruvic acid is molecularly adsorbed on the silica surface via a reversible process.

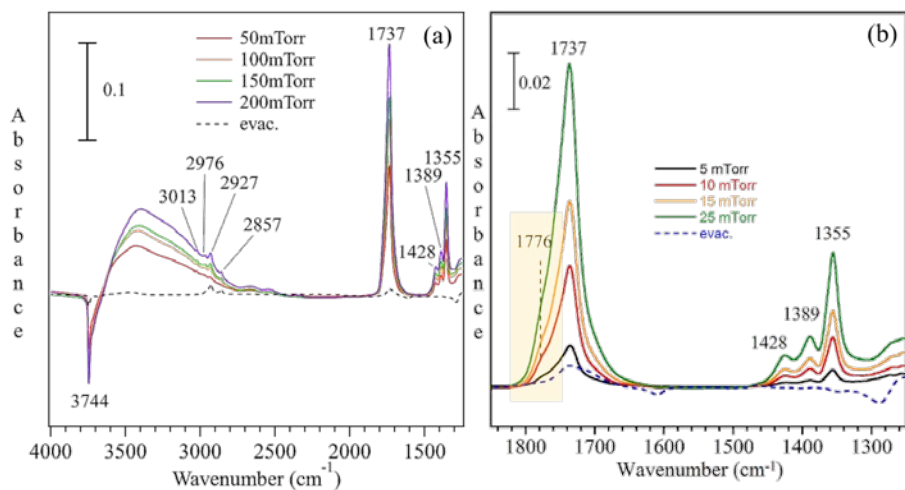


Figure 5.3. (a) Absorbance spectra (1280 to 4000 cm^{-1}) of pyruvic acid adsorbed on silica under dry conditions ($\text{RH} < 1\%$). Note that SiO_2 is opaque below 1280 cm^{-1} due to lattice vibrations. Spectral subtraction was performed using gas-phase absorption spectra. Shown as a dashed line (- -) is the surface spectrum following overnight evacuation. (b) Absorbance spectra (1250 to 1850 cm^{-1}) for lower pressures (5, 10, 15 and 25 mTorr) of pyruvic acid adsorbed on silica under dry conditions.

Table 5.1. Vibrational mode assignment for pyruvic acid (PA), CH₃COCOOH(g) and adsorbed species on SiO₂ particle surfaces.

mode assignment	gas phase	SiO ₂	literature ²⁹
$\nu(\text{OH, surface})$		3744	3742 ⁵¹
$\nu(\text{OH, Tt})$	3579		3579
$\nu(\text{OH, Tc})$	3463		3463
$\nu_{as/s}(\text{CH}_3)$	3025, 2941	3013, 2976, 2927, 2857	3025, 2941
$\nu(\text{C=O}_{\text{acid, Tc}})$	1805	1776	1804
$\nu(\text{C=O}_{\text{acid, Tt}})$	1760	1756	1765, 1751 ⁴⁴
$\nu(\text{C=O}_{\text{ketone}})$	1737	1737	1737
$\nu(\text{C=O}_{\text{dimer}})$		1710	1720, 1747 ⁶⁴
$\delta_{as}(\text{CH}_3)$	1422	1428	1424
$\nu_{as}(\text{C-C})$	1390	1389	1391
$\delta_s(\text{CH}_3)$	1360	1355	1360
$\delta(\text{COH})$	1211		1211
$\nu_{as}(\text{C-O})$	1134		1133

5.4.1.2 Pyruvic Acid Adsorption in the Presence of Water Vapor

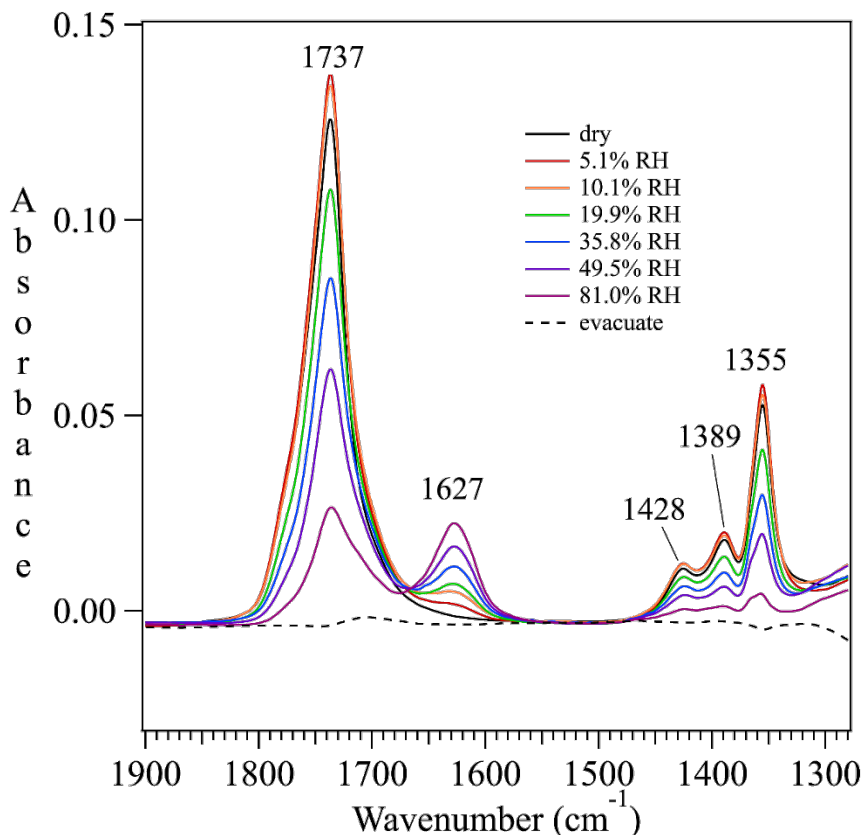


Figure 5.4. Absorbance spectra (1280 to 1900 cm^{-1}) of silica particles after first exposure to 100 mTorr pyruvic acid and then water vapor as a function of relative humidity (RH). The dashed line (- - -) indicates the surface adsorbed species disappear after evacuation of both water and pyruvic acid.

To investigate the effect of surface-adsorbed water ($\text{H}_2\text{O}(\text{a})$), the adsorption of pyruvic acid (100 mTorr) on silica was systematically studied at the following RHs: < 1% (dry), 5.1%, 10.1%, 19.9%, 35.8%, 49.5%, and 81%. The amount of water adsorbed on the surface increases with RH (see Figure 5.4), as evident from the observed increase in intensity of the band at 1627 cm^{-1} (OH bending mode of water). The intensities of peaks attributed to adsorbed pyruvic acid (1737, 1428, 1389 and 1355 cm^{-1}), however, decreased above 19.9% RH, suggesting that water competes for surface adsorption sites with pyruvic

acid/displaced adsorbed pyruvic acid. This displacement role dominates at higher RH (>20%). An absence of pyruvate peaks around 1400 – 1600 cm^{-1} (C=O stretching of pyruvate) was observed, indicating that adsorbed pyruvic acid did not deprotonate on the silica surface even in the presence of water. The disappearance of surface adsorbed species following evacuation suggests that the adsorption of pyruvic acid in the presence of water vapor is a reversible process as well.

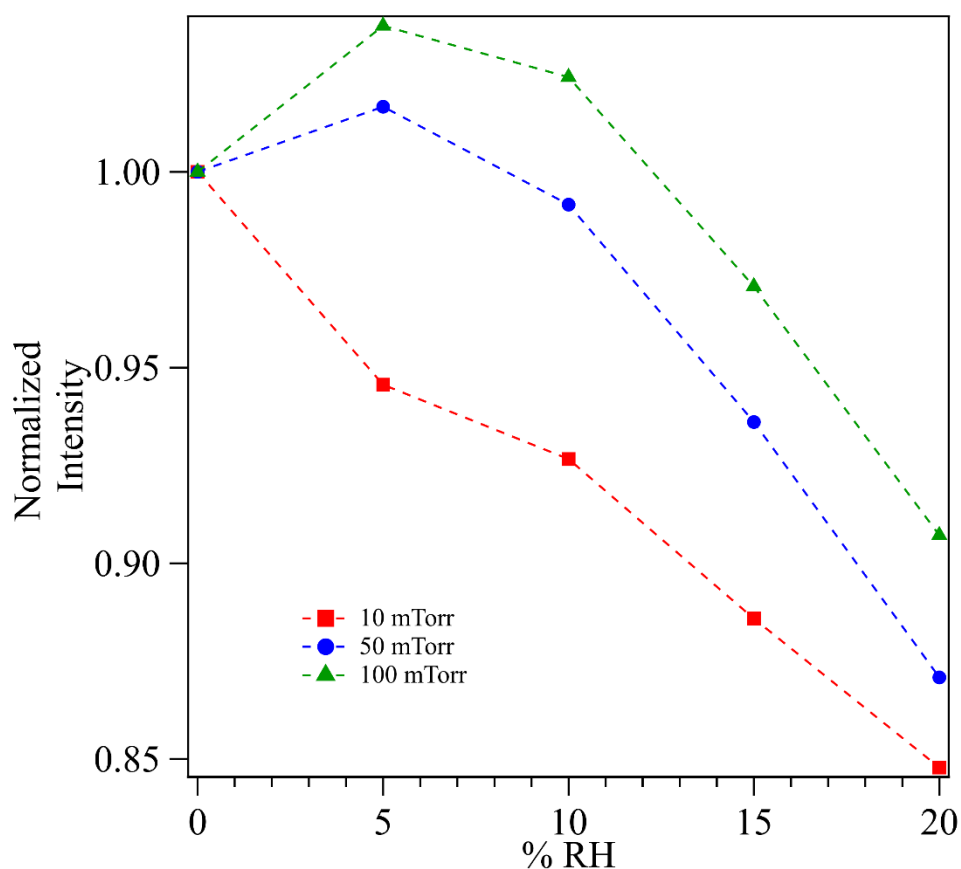


Figure 5.5. Normalized intensity (peak height at 1737 cm^{-1}) of 10, 50, 100 mTorr pyruvic acid adsorbed on the silica surface as a function of RH (< 1%, 5%, 10%, 15% and 20%).

The role of water on the adsorption of pyruvic acid on silica was studied for 10, 50, and 100 mTorr pyruvic acid and relative humidity up to 20%. Water can enhance surface

adsorption by providing more hydroxyl groups as available adsorption sites. Water can also prohibit adsorption by competing for surface hydroxyl groups with pyruvic acid. As shown in Figure 5.5, when pyruvic acid gas-phase pressure is low (at 10 mTorr), adsorbed pyruvic acid (1737 cm^{-1}) decreases with increasing RH even at the very beginning. At higher pyruvic acid pressure (50 mTorr), when the RH is increased up to 5%, the amount of adsorbed pyruvic acid increases. At 10% RH, the adsorbed pyruvic acid intensity is very close to that of the original dry conditions. For 50 mTorr pyruvic acid, the enhanced adsorption role dominates at low water vapor pressure (initial RH), while adsorbed water displacement of pyruvic acid becomes dominant for RHs $> 10\%$. At 100 mTorr, on the other hand, the enhanced adsorption role dominates until 10% RH, while for RH $> 15\%$, adsorbed pyruvic acid decreased with RH. Therefore, the pressure of gas-phase pyruvic acid affects the extent of water competition. For a small gas-phase pressure, water competes for adsorbed surface sites and displaces pyruvic acid at the very beginning. As the gas-phase pressure increases, and more pyruvic acid is in the gas-phase, water will provide surface sites sooner (at lower RH). Our results agree with previous studies which have revealed that water can enhance surface adsorption by providing more hydroxyl groups as available adsorption sites, assist dissociation, as well as prohibit adsorption by competing for surface hydroxyl groups with other adsorbed acidic gases.^{51,58}

5.4.2 Theoretical Modeling

Theoretical modeling of pyruvic acid interacting with dry or wetted hydroxylated silica has been investigated using geometry optimizations and the ab initio Born-Oppenheimer molecular dynamics (BOMD) simulations. Binding energies between

pyruvic acid with a dry silica surface were calculated as shown in Table 5.2. The Tt conformer interacting with a silica surface shows similar binding energy (16 kcal/mol) to that of the Tc conformer (17 kcal/mol). With the small gas phase energy difference (2.58 kcal/mol) calculated in this study, the Tt conformer is found to have the ability to form intramolecular hydrogen bonds and transform to the Tc conformer. However, when adsorbed on the surface, the Tt conformer does not change its configuration to Tc, suggestive that no obvious preference (between Tc and Tt conformer) exists on the surface. Vibrational frequencies of adsorbed pyruvic acid species were also calculated as shown in Table 5.3. The Tc conformer C=O ketone shifts slightly by only 1 cm^{-1} following adsorption, while the C=O acid shifts by 44 cm^{-1} , suggesting that the Tc conformer hydrogen bonds strongly between C=O acid and surface hydroxyl groups. This can be supported by the large shift of C=O acid from 1805 cm^{-1} to the shoulder at 1776 cm^{-1} as seen from vibrational measurements (Figure 5.3). When adsorbed on the silica surface from the gas phase, pyruvic acid Tt conformer C=O acid shifts by 6 cm^{-1} with a much larger redshift of C=O ketone by 27 cm^{-1} , suggesting that the Tt conformer adsorbed on SiO_2 with -COOH and C=O keto group partially hydrogen bonded with the silica surface. Simulation of the interactions of Tc and Tt conformers with the silica surface show that the Tc conformer has three main minima, (Figure 5.6 (a) – (c)) forming two hydrogen bonds between C=O acid and OH group from -COOH group. Figure 5.6 (d) and (e) show the two lowest energy minima of the pyruvic acid Tt conformer interacting with the silica surface. There are two different binding modes between the Tt conformer and the silica surface: (1) Tt C=O ketone and OH from -COOH (Figure 5.6(d)) (2) Tt C=O acid OH from -COOH (Figure 5.6(e)) interacting with surface hydroxyl groups.

In addition, Tt – Ct conformer is calculated to be the only stable pyruvic acid dimer found on the silica surface with a binding energy (27 kcal/mol). Therefore, adsorbed pyruvic dimer is also energetically possible on silica surfaces. A snapshot of the simulated pyruvic acid dimer Tt – Ct on silica surface is shown in Figure 5.7.

Table 5.2. Calculated binding energies of different pyruvic acid species on hydroxylated silica. (From Dr. Dominika Lesnicki)

Pyruvic Acid Species	Binding Energy (kcal/mol)
Tc	17
Tt	16
Tt-Ct	27

Table 5.3. Calculated vibrational frequencies of different adsorbed pyruvic acid species. (Adapted from Dr. Dominika Lesnicki)

Species	Mode	exp	gas	on dry surface	on wet surface
Tc	v(C=O) acid	1805	1740	1696	1651
	v(C=O) ketone	1737	1677	1694	1657
Tt	v(C=O) acid	1760	1700	1676	1629
	v(C=O) ketone		1700	1673	1668
Tt-Ct	v(C=O) acid			1649	
	v(C=O) ketone			1694	

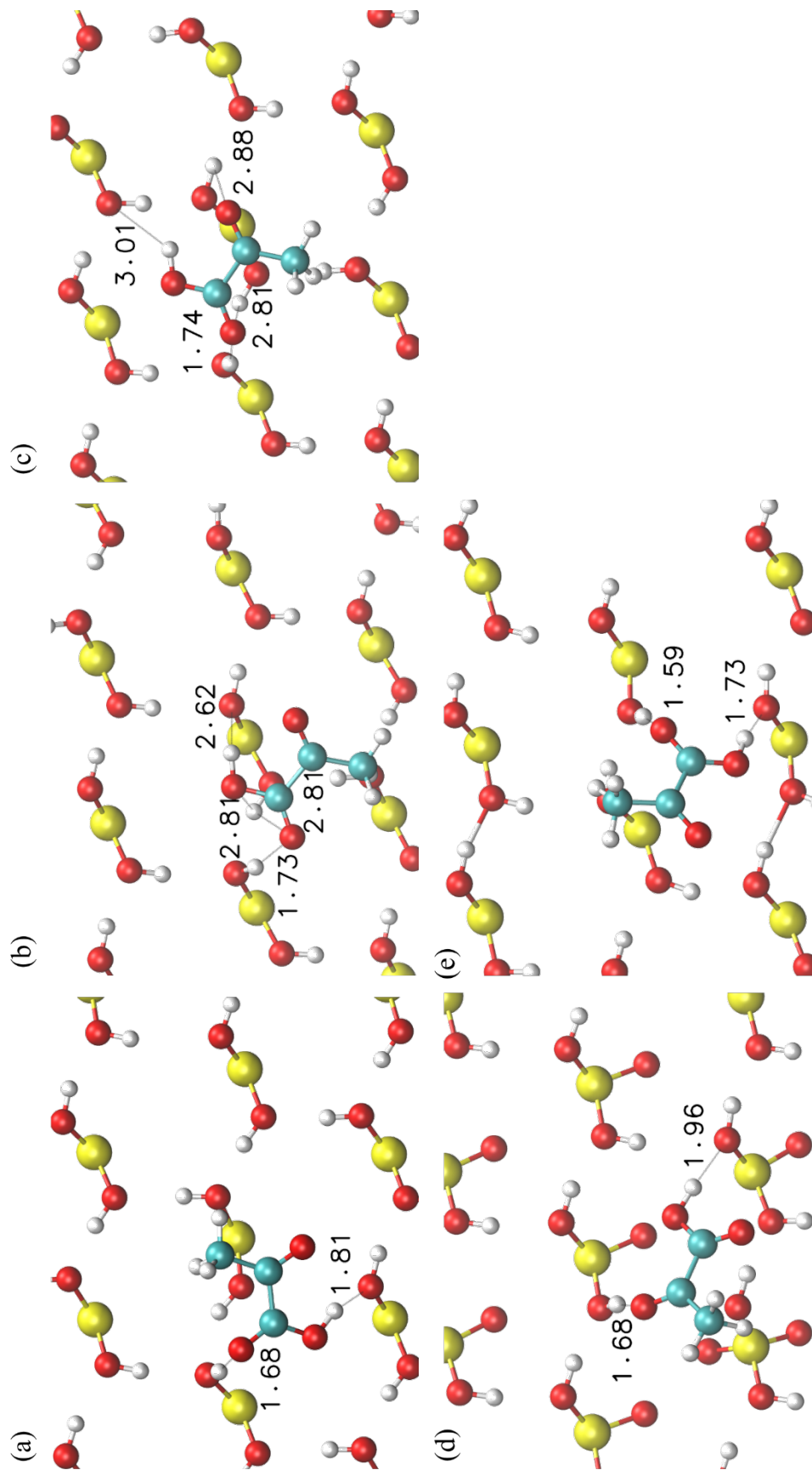


Figure 5.6. (a) – (c) Tc conformer interacting with silica surface from geometry optimization: the lowest three energy minima. (d) – (e) The two lowest energy minima of Tt conformer interacting with silica surface. (From Dr. Dominika Lesnicki)

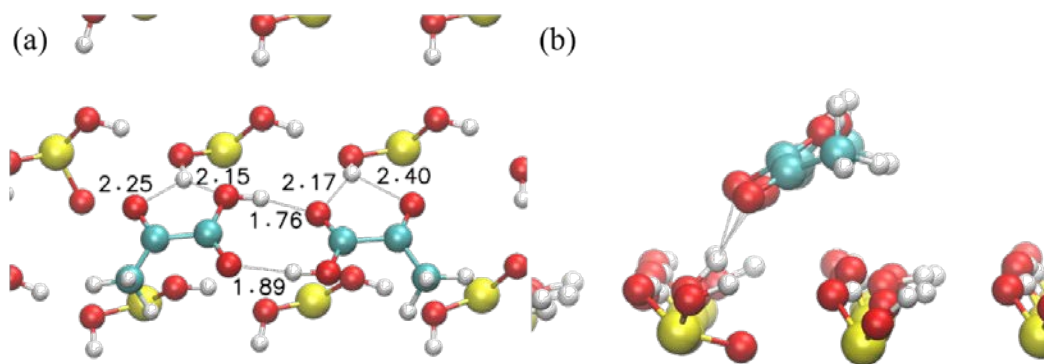


Figure 5.7. Interaction between Tt-Ct pyruvic acid dimer on silica surface from (a) top and (b) side view. (From Dr. Dominika Lesnicki)

Pyruvic acid interacting with a wet silica surface has also been investigated using the same method. As shown in Figure 5.8, the binding between pyruvic acid and the surface silanol groups is not direct but mediated by a water bridge. Vibrational frequencies of Tt and Tc conformers in the presence of water are shown in Table 5.3. It has been found that further redshift has been observed for both C=O acid and C=O ketone stretching modes of the Tc conformer by 45 and 37 cm^{-1} respectively in the presence of water. However, in the case of the Tt conformer, C=O acid mode is redshifted by 47 cm^{-1} while C=O keto is only shifted by 5 cm^{-1} . In addition, the adsorbed pyruvic acid dimer is minimized in the presence of water.

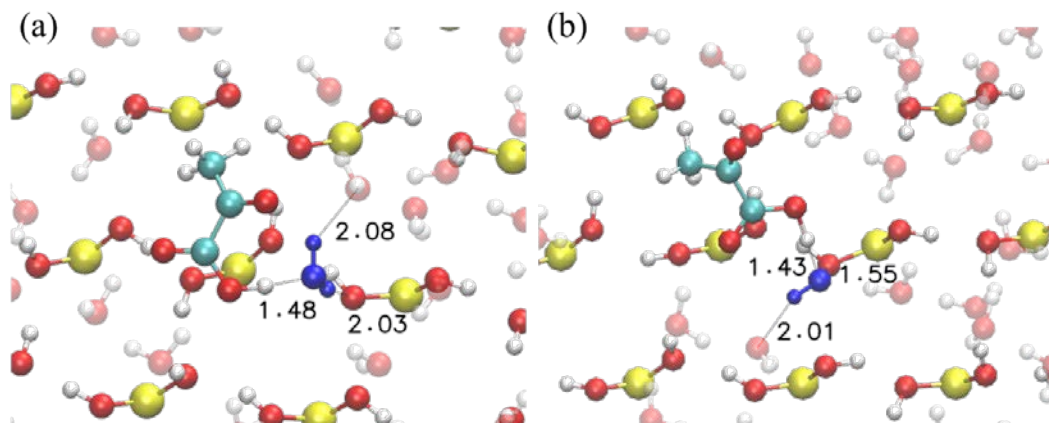


Figure 5.8. Pyruvic acid (a) Tc and (b) Tt conformer interacting with wet silica surface through a water bridge (dark blue). (From Dr. Dominika Lesnicki)

5.4.3 Curve fitting based on theoretical simulation

5.4.3.1 Dry conditions

To further determine correct peak compositions and areas from experimental results, peak fitting was applied based on the vibrational frequencies calculated in Section 5.4.2. In the gas-phase, an overlap was observed for C=O stretching of the pyruvic acid ketone stretching at 1737 cm^{-1} and the Tt conformer (1760 cm^{-1}), respectively as shown in Figure 5.2. When adsorbed on the surface, gas-phase Tc conformer acid stretching is also red shifted from 1805 cm^{-1} to the shoulder at 1776 cm^{-1} , further overlapping with other C=O stretching species. Applying peak fitting to spectra ($1550 - 1900\text{ cm}^{-1}$) observed for silica particles after exposure to pyruvic acid ($\text{RH} < 1\%$), based on blueshift of the theoretical modeling calculated vibrational frequencies corrected by 60 cm^{-1} at 1756 , 1754 , 1736 , 1733 and 1709 cm^{-1} , respectively. Note that the experimental measured gas phase pyruvic acid vibrational frequencies are $60 \sim 65\text{ cm}^{-1}$ higher than calculated value. The adsorption band at 1756 cm^{-1} is assigned to C=O acid stretching of the adsorbed pyruvic acid Tc conformer, while 1754 cm^{-1} is due to C=O ketone stretching of adsorbed Tc

conformer and pyruvic acid dimers (Tt – Ct). C=O acid stretching of the pyruvic acid Tc conformer has been shifted by 49 cm^{-1} from the gas-phase as the acid -COOH group is now involved in hydrogen bonding with hydroxyl groups on the silica surface. In contrast, Tt conformer C=O acid and ketone stretching shifted by 24 and 27 cm^{-1} , respectively, suggestive that both Tt acid -COOH and ketone groups are involved in weak binding with surface hydroxyl groups. The broader peak at 1709 cm^{-1} is due to C=O acid stretching of hydrogen-bonded pyruvic acid dimers (Tt – Ct). A previous laboratory study⁵⁵ has shown that other carboxylic acids, such as acetic acid can form dimers on the silica surface. Pyruvic acid can form dimers^{43,59,60}, supporting our observation of the formation of a pyruvic acid dimer with a vibrational frequency at 1709 cm^{-1} . This observation can also be supported by theoretical modeling as discussed in Section 5.4.2.

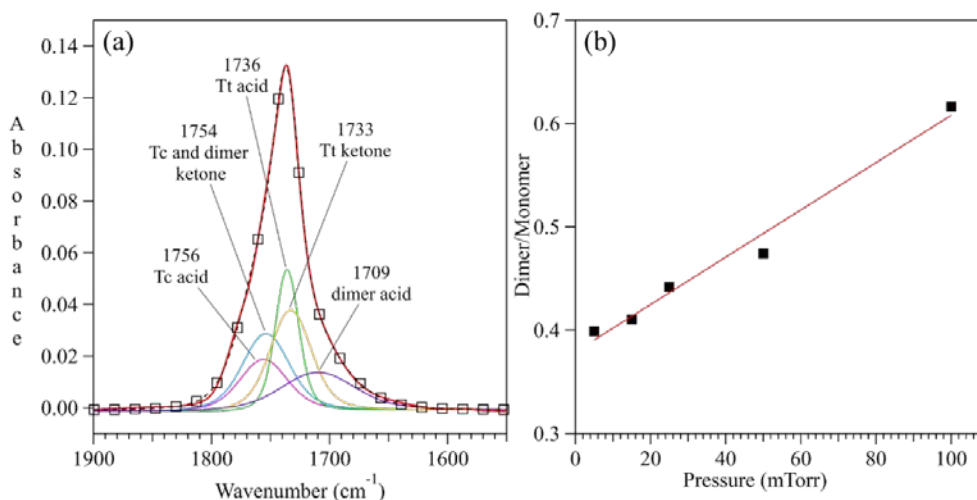


Figure 5.9. (a) Absorbance spectra ($1550 - 1900 \text{ cm}^{-1}$) after peak fitting, for SiO_2 particles following exposure to 100 mTorr pyruvic acid ($\text{RH} < 1\%$). Absorbance bands correspond to $\text{C}=\text{O}$ stretching of multiple species present on the surface, including: adsorbed pyruvic acid Tc conformer $\text{C}=\text{O}$ acid stretch (1756 cm^{-1}); dimer and Tc conformer $\text{C}=\text{O}$ ketone stretch (1754 cm^{-1}); Tt conformer $\text{C}=\text{O}$ acid stretch (1736 cm^{-1}); Tt conformer $\text{C}=\text{O}$ ketone stretch (1733 cm^{-1}); and dimer acid $\text{C}=\text{O}$ stretch (1709 cm^{-1}). Red line (—) represents the original spectrum and the dashed line with open square marker (—□—) represents the overall fit. (b) Ratio of peak area of $\text{C}=\text{O}$ acid stretch from hydrogen-bonded pyruvic acid dimers (1709 cm^{-1}) to total peak area of monomers (the sum of peak areas of the Tc acid (1756 cm^{-1}) + Tt acid (1736 cm^{-1})) as a function of gas-phase pyruvic acid pressure.

The relative composition (%) (after peak fitting) of adsorbed pyruvic acid (Tt, Tc and dimer) on the silica surface as a function of gas-phase pyruvic acid pressure is represented as the ratio of peak areas of dimer to monomers (sum of Tt and Tc conformers) in Figure 5.9b. The $\text{C}=\text{O}$ acid stretch is used to calculate the dimer/monomer ratio owing to the fact that the $\text{C}=\text{O}$ ketone stretch of Tc and dimer overlap at 1754 cm^{-1} . The relative amount of pyruvic acid dimer formed on the silica surface increases with pressure (see Figure 5.9(b)), while the total amount of pyruvic acid monomers decreases. Even at 1 Torr of pyruvic acid, no dimer is observed in the gas phase. Pyruvic acid is unlikely to form the dimer in the gas-phase due to the intramolecular hydrogen bonding in the most stable Tc

conformer. Figure 5.9(b) shows that for molecularly-adsorbed pyruvic acid on SiO₂, the intensity of the infrared absorbance (represented by the peak area after peak fitting) due to dimers (at 1709 cm⁻¹) is comparable with the sum of monomers even for very low pyruvic acid pressure (5 mTorr). This suggests that SiO₂ favors the formation of dimers on the surface. Tang et al⁵⁵ investigated heterogeneous reactions of acetic acid on SiO₂ surfaces and suggested that the acetic acid dimer is favorable in the presence of silica surfaces even under conditions when monomers are the major species in the gas-phase. This supports our observations for pyruvic acid (another carboxylic acid) adsorption on silica surfaces. As predicted by theoretical modeling (refer to Figure 5.7) hydroxyl groups from the silica surface form more than one hydrogen bond with the pyruvic acid Tc conformer.

5.4.3.2 Role of adsorbed water

To further determine the experimental vibrational frequencies of the conformers of pyruvic acid in the presence of water, curve fitting has been applied based on calculated vibrational frequencies in Section 5.4.2. As shown in Figure 5.10, Tc conformer water bridged with the silica surface has been observed at 1711 and 1717 cm⁻¹ for acid and ketone stretches respectively, while Tt conformer water bridged with the silica surface results in two C=O stretches at 1728 (ketone) and 1689 (acid) cm⁻¹. The peak at 1627 cm⁻¹ can be assigned to the OH bending mode of water. Note that water vapor is introduced following pyruvic acid adsorption and reaches equilibrium on the silica surface. Therefore, the adsorbed Tt conformer (1736 cm⁻¹) and Tc conformer (1756 cm⁻¹) still exist on the surface. Note that acid and ketone stretches are not distinguished here as they are close when Tt and Tc conformers are directly interacting with the silica surface. Water-bridged pyruvic acid Tc conformer redshifted by 45 (acid) and 37 (ketone) cm⁻¹, suggests that the Tc conformer

acid and ketone C=O are both involved in hydrogen bonding with adsorbed water. On the other hand, the Tt pyruvic acid conformer interacts with water by its acid C=O group, suggested by the 47 cm⁻¹ redshift of acid group and the 5 cm⁻¹ shift of ketone stretch. The redshift of Tc and Tt conformers suggests that pyruvic acid forms a significantly stronger hydrogen bond with adsorbed water.

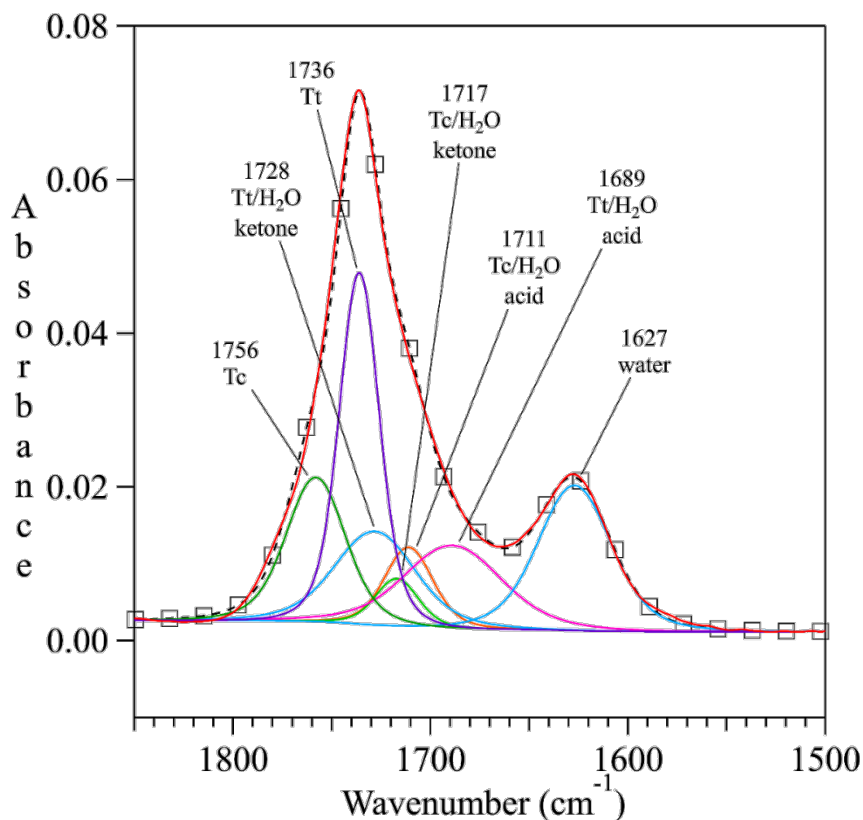


Figure 5.10. Absorbance spectra (1500 – 1900 cm^{-1}) after peak fitting, for SiO_2 particles following exposure to 100 mTorr pyruvic acid ($\text{RH} = 50\%$). Absorbance bands correspond to C=O stretching of multiple species present on the surface, including: the adsorbed pyruvic acid Tc conformer (1756 cm^{-1}); Tt conformer (1736 cm^{-1}); water bridged Tt conformer ketone stretch (1728 cm^{-1}); water bridged Tc conformer ketone stretch (1717 cm^{-1}); water bridged Tc conformer acid stretch (1711 cm^{-1}); and water bridged Tt conformer acid stretch (1689 cm^{-1}). The absorbance band centered at 1627 cm^{-1} is assigned to the OH bending mode of water. Red line (—) represents the original spectrum and the dashed line with open square marker (- \square -) represents the overall fit.

5.5 Conclusion

Transmission FTIR spectroscopy and theoretical simulations were used to investigate the heterogeneous interactions of pyruvic acid with SiO_2 particles. To investigate the effect of SiO_2 on the configuration of pyruvic acid, experiments were carried out by exposing the silica surface to pyruvic acid as a function of pressure. Pyruvic

acid adsorption on the silica surface is a molecularly reversible process. Pyruvic acid has two stable configurations in the gas phase: Tc and Tt conformers. Following adsorption, both conformers (Tc and Tt) exist on the surface forming two hydrogen bonds. The Tc conformer binds through C=O and OH (from -COOH) with silica surface hydroxyl groups, while the Tt conformer binds through both C=O acid and C=O ketone groups. Even at very low pyruvic acid pressure where no pyruvic acid dimer has been observed in the gas phase, pyruvic acid dimer is observed on the surface following adsorption. Tt – Ct is calculated to be the only stable adsorbed pyruvic acid dimer on the silica surface. The role of water was studied as a function of relative humidity. Water is found to compete for surface adsorption sites with pyruvic acid at all RHs studied. In addition, calculations reveal that adsorbed pyruvic acid Tt and Tc conformers bind with silica surface hydroxyl groups through a “water bridge” in the presence of adsorbed water.

5.6 Acknowledgement

This material is the Alfred P. Sloan Foundation under grant number G-2017-9692. The contents of this study do not necessarily reflect the official views of the Alfred P. Sloan Foundation. The Alfred P. Sloan Foundation does not endorse the purchase of the commercial products used in this report. The dissertation author was the primary investigator of all experimental measurements and data analysis. The author would like to thank Dr. Dominika Lesnicki for all theoretical simulations of pyruvic acid on silica surface. Chapter 5, in full is currently being prepared for submission for publication of the material. Yuan Fang, Dominika Lesnicki, Kristin Wall, Marialore Sulpizi and Vicki H. Grassian. The dissertation author was the primary investigator and author of this material.

5.7 Reference

- (1) Reed Harris, A. E.; Pajunoja, A.; Cazaunau, M.; Gratien, A.; Pangui, E.; Monod, A.; Griffith, E. C.; Virtanen, A.; Doussin, J. F.; Vaida, V. Multiphase Photochemistry of Pyruvic Acid under Atmospheric Conditions. *J. Phys. Chem. A* **2017**, *121* (18), 3327–3339.
- (2) Reed Harris, A. E.; Doussin, J. F.; Carpenter, B. K.; Vaida, V. Gas-Phase Photolysis of Pyruvic Acid: The Effect of Pressure on Reaction Rates and Products. *J. Phys. Chem. A* **2016**, *120* (51), 10123–10133.
- (3) Andreae, M. O.; Talbot, R. W.; Li, S.-M. . Atmospheric Measurements of Pyruvic and Formic Acid. *J. Geophys.* **1987**, *92*, 6635–6641.
- (4) Talbot, R. W.; Andreae, M. O.; Berresheim, H.; Jacob, D. J.; Beecher, K. M. Sources and Sinks of Formic, Acetic, and Pyruvic Acids over Central Amazonia: 2. Wet Season. *J. Geophys. Res. Atmos.* **1990**, *95* (D10), 16799–16811.
- (5) Kawamura, K.; Bikkina, S. A Review of Dicarboxylic Acids and Related Compounds in Atmospheric Aerosols: Molecular Distributions, Sources and Transformation. *Atmos. Res.* **2016**, *170*, 140–160.
- (6) Baboukas, E. D.; Kanakidou, M.; Mihalopoulos, N. Carboxylic Acids in Gas and Particulate Phase above the Atlantic Ocean. *J. Geophys. Res. Atmos.* **2000**, *105* (D11), 14459–14471.
- (7) Bao, L.; Matsumoto, M.; Kubota, T.; Sekiguchi, K.; Wang, Q.; Sakamoto, K. Gas/Particle Partitioning of Low-Molecular-Weight Dicarboxylic Acids at a Suburban Site in Saitama, Japan. *Atmos. Environ.* **2012**, *47*, 546–553.
- (8) Bardouki, H.; Liakakou, H.; Economou, C.; Sciare, J.; Smolík, J.; Ždímal, V.; Eleftheriadis, K.; Lazaridis, M.; Dye, C.; Mihalopoulos, N. Chemical Composition of Size-Resolved Atmospheric Aerosols in the Eastern Mediterranean during Summer and Winter. *Atmos. Environ.* **2003**, *37* (2), 195–208.
- (9) Chebbi, a; Carlier, P. Carboxylic Acids in the Troposphere, Occurrence, Sources and Sinks: A Review. *Atmos. Environ.* **1996**, *30* (24), 4223–4249.
- (10) Ho, K. F.; Lee, S. C.; Cao, J. J.; Kawamura, K.; Watanabe, T.; Cheng, Y.; Chow, J. C. Dicarboxylic Acids, Ketocarboxylic Acids and Dicarbonyls in the Urban Roadside Area of Hong Kong. *Atmos. Environ.* **2006**, *40* (17), 3030–3040.
- (11) Khwaja, H. A. Atmospheric Concentrations of Carboxylic Acids and Related Compounds at a Semiurban Site. *Atmos. Environ.* **1995**, *29* (1), 127–139.
- (12) Limbeck, A.; Puxbaum, H.; Otter, L.; Scholes, M. C. Semivolatile Behavior of Dicarboxylic Acids and Other Polar Organic Species at a Rural Background Site (Nylsvley, RSA). *Atmos. Environ.* **2001**, *35* (10), 1853–1862.

- (13) Kawamura, K.; Kasukabe, H.; Barrie, L. A. Source and Reaction Pathways of Dicarboxylic Acids, Ketoacids and Dicarbonyls in Arctic Aerosols: One Year of Observations. *Atmos. Environ.* **1996**, *30* (10–11), 1709–1722.
- (14) Reed Harris, A. E.; Ervens, B.; Shoemaker, R. K.; Kroll, J. A.; Rapf, R. J.; Griffith, E. C.; Monod, A.; Vaida, V. Photochemical Kinetics of Pyruvic Acid in Aqueous Solution. *J. Phys. Chem. A* **2014**, *118* (37), 8505–8516.
- (15) Hall, G. E.; Muckerman, J. T.; Preses, J. M.; Weston, R. E.; Flynn, G. W. Time-Resolved FTIR Studies of the Photodissociation of Pyruvic Acid at 193 Nm. *Chem. Phys. Lett.* **1992**, *193* (1–3), 77–83.
- (16) Rincón, A. G.; Guzman, M. I.; Hoffmann, M. R.; Colussi, A. J. Optical Absorptivity versus Molecular Composition of Model Organic Aerosol Matter. *J. Phys. Chem. A* **2009**, *113* (39), 10512–10520.
- (17) Guzmán, M. I.; Colussi, A. J.; Hoffmann, M. R. Photoinduced Oligomerization of Aqueous Pyruvic Acid. *J. Phys. Chem. A* **2006**, *110* (10), 3619–3626.
- (18) Griffith, E. C.; Carpenter, B. K.; Shoemaker, R. K.; Vaida, V. Photochemistry of Aqueous Pyruvic Acid. *Proc. Natl. Acad. Sci.* **2013**, *110* (29), 11714–11719.
- (19) O’Neill, J. A.; Kreutz, T. G.; Flynn, G. W. IR Diode Laser Study of Vibrational Energy Distribution in CO₂ Produced by UV Excimer Laser Photofragmentation of Pyruvic Acid. *J. Chem. Phys.* **1987**, *87* (8), 4598.
- (20) Grosjean, D. Atmospheric Reactions of Pyruvic Acid. *Atmos. Environ.* **1983**, *17* (11), 2379–2382.
- (21) Yamamoto, S.; Back, R. A. The Photolysis and Thermal Decomposition of Pyruvic Acid in the Gas Phase. *Can. J. Chem.* **1985**, *63* (2), 549–554.
- (22) Davidson, R. S.; Goodwin, D.; Violet, D. E. And Ph. FORNIER DE VIOLET. **1981**, *78* (3), 1–4.
- (23) Wood, C. F.; O’Neill, J. A.; Flynn, G. W. Infrared Diode Laser Probes of Photofragmentation Products: Bending Excitation in CO₂ Produced by Excimer Laser Photolysis of Pyruvic Acid. *Chem. Phys. Lett.* **1984**, *109* (4), 317–323.
- (24) Mellouki, A.; Mu, Y. On the Atmospheric Degradation of Pyruvic Acid in the Gas Phase. *J. Photochem. Photobiol. A Chem.* **2003**, *157* (2–3), 295–300.
- (25) Carlton, A. G.; Turpin, B. J.; Lim, H. J.; Altieri, K. E.; Seitzinger, S. Link between Isoprene and Secondary Organic Aerosol (SOA): Pyruvic Acid Oxidation Yields Low Volatility Organic Acids in Clouds. *Geophys. Res. Lett.* **2006**, *33* (6), 2–5.
- (26) Stefan, M. I.; Bolton, J. R. Reinvestigation of the Acetone Degradation Mechanism in Dilute Aqueous Solution by the UV/H₂O₂ Process. *Environ. Sci. Technol.* **1999**,

33 (6), 870–873.

- (27) Saito, K.; Sasaki, G.; Okada, K.; Tanaka, S. Unimolecular Decomposition of Pyruvic Acid: An Experimental and Theoretical Study. *J. Phys. Chem.* **1994**, *98*, 3756–3761.
- (28) Taylor, R. The Mechanism of Thermal Eliminations Part XXIII: [1] The Thermal Decomposition of Pyruvic Acid. *Int. J. Chem. Kinet.* **1987**, *19* (8), 709–713.
- (29) Plath, K. L.; Takahashi, K.; Skodje, R. T.; Vaida, V. Fundamental and Overtone Vibrational Spectra of Gas-Phase Pyruvic Acid. *J. Phys. Chem. A* **2009**, *113* (26), 7294–7303.
- (30) Larsen, M. C.; Vaida, V. Near Infrared Photochemistry of Pyruvic Acid in Aqueous Solution. *J. Phys. Chem. A* **2012**, *116* (24), 5840–5846.
- (31) Takahashi, K.; Plath, K. L.; Skodje, R. T.; Vaida, V. Dynamics of Vibrational Overtone Excited Pyruvic Acid in the Gas Phase: Line Broadening through Hydrogen-Atom Chattering. *J. Phys. Chem. A* **2008**, *112* (32), 7321–7331.
- (32) Chang, X. P.; Fang, Q.; Cui, G. Mechanistic Photodecarboxylation of Pyruvic Acid: Excited-State Proton Transfer and Three-State Intersection. *J. Chem. Phys.* **2014**, *141* (15), 2–10.
- (33) Da Silva, G. Decomposition of Pyruvic Acid on the Ground-State Potential Energy Surface. *J. Phys. Chem. A* **2016**, *120* (2), 276–283.
- (34) Murto, J.; Raaska, T.; Kunttu, H.; Räsänen, M. Conformers and Vibrational Spectra of Pyruvic Acid: An Ab Initio Study. *J. Mol. Struct. THEOCHEM* **1989**, *200* (C), 93–101.
- (35) Reva, I. D.; Stepanian, S. G.; Adamowicz, L.; Fausto, R. Combined FTIR Matrix Isolation and Ab Initio Studies of Pyruvic Acid: Proof for Existence of the Second Conformer. *J. Phys. Chem. A* **2001**, *105* (19), 4773–4780.
- (36) Kakkar, R.; Pathak, M.; Radhika, N. P. A DFT Study of the Structures of Pyruvic Acid Isomers and Their Decarboxylation. *Org. Biomol. Chem.* **2006**, *4* (5), 886–895.
- (37) Raczyńska, E. D.; Duczmal, K.; Darowska, M. Experimental (FT-IR) and Theoretical (DFT-IR) Studies of Keto-Enol Tautomerism in Pyruvic Acid. *Vib. Spectrosc.* **2005**, *39* (1), 37–45.
- (38) Ellison, G. B.; Tuck, A. F.; Vaida, V. Atmospheric Processing of Organic Aerosols. *J. Geophys. Res. Atmos.* **1999**, *104* (D9), 11633–11641.
- (39) Kaluza, C. E.; Bauder, A.; Günthard, H. H. The Microwave Spectrum of Pyruvic Acid. *Chem. Phys. Lett.* **1973**, *22* (3), 454–457.

- (40) Marstokk, K.-M.; Møllendal, H. Microwave Spectrum, Conformation, Barrier to Internal Rotation and Dipole Moment of Pyruvic Acid. *J. Mol. Struct.* **1974**, *20* (2), 257–267.
- (41) Ray, W.; Katon, J.; Phillips, D. Structure, Hydrogen Bonding and Vibrational Spectra of Pyruvic Acid. *J. Mol. Struct.* **1981**, *74* (1), 75–84.
- (42) Tarakeshwar, P.; Manogaran, S. An Ab Initio Study of Pyruvic Acid. *J. Mol. Struct. THEOCHEM* **1998**, *430* (1–3), 51–56.
- (43) Plath, K. L.; Axson, J. L.; Nelson, G. C.; Takahashi, K.; Skodje, R. T.; Vaidaa, V. Gas-Phase Vibrational Spectra of Glyoxylic Acid and Its Gem Diol Monohydrate. Implications for Atmospheric Chemistry. *React. Kinet. Catal. Lett.* **2009**, *96* (2), 209–224.
- (44) Reva, I.; M. Nunes, C.; Biczysko, M.; Fausto, R. Conformational Switching in Pyruvic Acid Isolated in Ar and N₂ Matrixes: Spectroscopic Analysis, Anharmonic Simulation, and Tunneling. *J. Phys. Chem. A* **2015**, *119* (11), 2614–2627.
- (45) Rosenfeld, R. N.; Weiner, B. Energy Disposal in the Photofragmentation of Pyruvic Acid in the Gas Phase. *J. Am. Chem. Soc.* **1983**, *105* (11), 3485–3488.
- (46) Leermakers, P. A.; Vesley, G. F. The Photochemistry of α -Keto Acids and α -Keto Esters. I. Photolysis of Pyruvic Acid and Benzoylformic Acid. *J. Am. Chem. Soc.* **1963**, *85* (23), 3776–3779.
- (47) Textor, C.; Schulz, M.; Guibert, S.; Kinne, S.; Balkanski, Y.; Bauer, S.; Berntsen, T.; Berglen, T.; Boucher, O.; Chin, M.; et al. Analysis and Quantification of the Diversities of Aerosol Life Cycles within AeroCom. *Atmos. Chem. Phys.* **2006**, *6* (7), 1777–1813.
- (48) Usher, C. R.; Michel, A. E.; Grassian, V. H. Reactions on Mineral Dust. *Chem. Rev.* **2003**, *103* (12), 4883–4939.
- (49) Liu, S.; Thompson, S. L.; Stark, H.; Ziemann, P. J.; Jimenez, J. L. Gas-Phase Carboxylic Acids in a University Classroom: Abundance, Variability, and Sources. *Environ. Sci. Technol.* **2017**, *51* (10), 5454–5463.
- (50) Crowley, J. N.; Ammann, M.; Cox, R. A.; Hynes, R. G.; Jenkin, M. E.; Mellouki, A.; Rossi, M. J.; Troe, J.; Wallington, T. J. Evaluated Kinetic and Photochemical Data for Atmospheric Chemistry: Volume v -Heterogeneous Reactions on Solid Substrates. *Atmos. Chem. Phys.* **2010**, *10* (18), 9059–9223.
- (51) Fang, Y.; Tang, M.; Grassian, V. H. Competition between Displacement and Dissociation of a Strong Acid Compared to a Weak Acid Adsorbed on Silica Particle Surfaces: The Role of Adsorbed Water. *J. Phys. Chem. A* **2016**, *120* (23), 4016–4024.

- (52) Goodman, A. L.; Bernard, E. T.; Grassian, V. H. Spectroscopic Study of Nitric Acid and Water Adsorption on Oxide Particles: Enhanced Nitric Acid Uptake Kinetics in the Presence of Adsorbed Water. *J. Phys. Chem. A* **2001**, *105* (26), 6443–6457.
- (53) Underwood, G. M.; Li, P.; Al-Abadleh, H.; Grassian, V. H. A Knudsen Cell Study of the Heterogeneous Reactivity of Nitric Acid on Oxide and Mineral Dust Particles. *J. Phys. Chem. A* **2001**, *105* (27), 6609–6620.
- (54) Vlasenko, A.; Sjogren, S.; Weingartner, E.; Stemmler, K.; Gäggeler, H. W.; Ammann, M. Effect of Humidity on Nitric Acid Uptake to Mineral Dust Aerosol Particles. *Atmos. Chem. Phys.* **2006**, *6* (8), 2147–2160.
- (55) Rubasinghege, G.; Ogden, S.; Baltrusaitis, J.; Grassian, V. H. Heterogeneous Uptake and Adsorption of Gas-Phase Formic Acid on Oxide and Clay Particle Surfaces: The Roles of Surface Hydroxyl Groups and Adsorbed Water in Formic Acid Adsorption and the Impact of Formic Acid Adsorption on Water Uptake. *J. Phys. Chem. A* **2013**, *117* (44), 11316–11327.
- (56) Tang, M.; Cziczo, D. J.; Grassian, V. H. Interactions of Water with Mineral Dust Aerosol: Water Adsorption, Hygroscopicity, Cloud Condensation, and Ice Nucleation. *Chem. Rev.* **2016**, *116* (7), 4205–4259.
- (57) Schnitzler, E. G.; Seifert, N. A.; Ghosh, S.; Thomas, J.; Xu, Y.; Jäger, W. Hydration of the Simplest α -Keto Acid: A Rotational Spectroscopic and Ab Initio Study of the Pyruvic Acid-Water Complex. *Phys. Chem. Chem. Phys.* **2017**, *19* (6), 4440–4446.
- (58) Tang, M.; Larish, W. A.; Fang, Y.; Gankanda, A.; Grassian, V. H. Heterogeneous Reactions of Acetic Acid with Oxide Surfaces: Effects of Mineralogy and Relative Humidity. *J. Phys. Chem. A* **2016**, *120* (28), 5609–5616.
- (59) VandeVondele, J.; Krack, M.; Mohamed, F.; Parrinello, M.; Chassaing, T.; Hutter, J. Quickstep: Fast and Accurate Density Functional Calculations Using a Mixed Gaussian and Plane Waves Approach. *Comput. Phys. Commun.* **2005**, *167* (2), 103–128.
- (60) Lee, C.; Yang, W.; Parr, R. G. Development of the Colle-Salvetti Correlation-Energy Formula into a Functional of the Electron Density. *Phys. Rev. B* **1988**, *37* (2), 785–789.
- (61) Becke, A. D. Density-Functional Exchange-Energy Approximation with Correct Asymptotic Behavior. *Phys. Rev. A* **1988**, *38* (6), 3098–3100.
- (62) Sulpizi, M.; Gaigeot, M. P.; Sprik, M. The Silica-Water Interface: How the Silanols Determine the Surface Acidity and Modulate the Water Properties. *J. Chem. Theory Comput.* **2012**, *8* (3), 1037–1047.
- (63) Gaigeot, M. P.; Sprik, M.; Sulpizi, M. Oxide/Water Interfaces: How the Surface Chemistry Modifies Interfacial Water Properties. *J. Phys. Condens. Matter* **2012**, *24*

(12).

- (64) Yang, X.; Orlova, G.; Zhou, X. J.; Leung, K. T. A DFT Study on the Radical, Monomer and Dimer of α -Keto Pyruvic Acid: Equilibrium Structures and Vibrational Analysis of Stable Conformers. *Chem. Phys. Lett.* **2003**, 380 (1–2), 34–41.

CHAPTER 6 SURFACE ADSORPTION AND HETEROGENEOUS PHOTOCHEMISTRY OF PYRUVIC ACID ON OXIDE SURFACES: Al_2O_3 AND TiO_2

6.1 Abstract

The adsorption of gas-phase pyruvic acid (CH_3COCOOH) on oxides, Al_2O_3 and TiO_2 , and the effect of adsorbed water have been investigated using transmission Fourier Transform Infrared Spectroscopy (FTIR). Pyruvic acid uptake on Al_2O_3 and TiO_2 are found to be mostly irreversible processes. The FTIR spectra show that pyruvic acid adsorbs onto Al_2O_3 and TiO_2 from the gas phase and forms predominately pyruvate as well as other more chemically complex molecular species. Broadband photolysis of adsorbed pyruvate on Al_2O_3 and TiO_2 surfaces, respectively, was also investigated. Mass spectrometry analysis has been applied to identify unique products formed following irradiation.

This study provides valuable insights into the interaction of pyruvic acid with different oxides (Al_2O_3 , and TiO_2) on the molecular level. High resolution mass spectrometry was used in this study to identify photochemical and non-photochemical products of pyruvic acid on oxide surfaces. Oxygen to carbon ratios (O:C) of adsorbed pyruvic acid photochemical reactions show that TiO_2 samples formed more oxidized products compared to that for Al_2O_3 . Zymonic acid was found in dark and light conditions and was identified as a major product. Other products form following irradiation and include parapyruvic acid and 2, 4- dihydroxy-2-methyl-5-oxohexanoic acid (DMOHA).

6.2 Introduction

Sunlight, the major source of energy in the atmosphere, drives the complex physical and chemical cycles which determine the atmospheric compositions through directly photolysis as well as the formation of reactive species.¹⁻⁷ It is crucial to understand the photochemical processes as they affect the lifetime of atmospherically relevant molecules.

Pyruvic acid (PA), CH_3COCOOH , an important atmospheric α – keto acid, is formed primarily between the hydroxyl radical ($\text{OH}\bullet$) and hydrated methylglyoxal via the particle-phase aqueous reaction in the atmosphere.⁶ Protonated form of pyruvic acid (pyruvate), serving as an intermediate for both aerobic and anaerobic metabolism, has been proposed to be a promising prebiotic molecule initializing primitive metabolism.⁸⁻¹¹ Photolysis is the major tropospheric sink of pyruvic acid, with wet deposition and its reaction with $\text{OH}\bullet$ acting as secondary sinks.⁵ Pyruvic acid has been detected in numerous field studies in the gas-phase (10-100 ppt), in aerosols (up to 140 ng m^{-3}), in snow, and in rainwater.^{5,12-22} Pyruvic acid gas- and condensed- phase photolysis²³⁻³², hydroxyl radical oxidation³³⁻³⁵, thermal decomposition^{36,37} and vibrational overtone induced decarboxylation³⁸⁻⁴⁰ have been investigated over the past 30 years while little heterogeneous study of pyruvic acid on surfaces has been investigated. Computational studies⁴¹⁻⁴³ on pyruvic acid's configurations, reaction barriers, and electronic structure have also been used to provide insights into these experimental findings.

Early studies on the photochemistry of pyruvic acid vapor, using higher energy photons, were carried out at approximately 1 Torr of pyruvic acid at room temperature using low buffer gas pressures.^{31,44,45} The most energetically favorable mechanism for the photolysis of gas-phase pyruvic acid involves a hydrogen atom transfer and C–C bond

cleavage, processing through a five-membered cyclic transition state.^{41,42} Acetic acid and CO were detected as photolysis products via a lactone intermediate by Harris et al.⁵ for lower concentrations of pyruvic acid.

Aqueous-phase pyruvic acid has a dramatically different photochemistry from that in the gas phase due to energetic and conformational changes. When dissolved in water, approximately 60% of pyruvic acid hydrates to 2, 2-dihydroxypropanoic acid (DHPA), a geminal-diol form of pyruvic acid which is not photoactive at wavelengths present near the Earth's surface.^{46,47} In addition, pyruvic acid undergoes intersystem crossing after its keto form adsorbs a photon in water, from the $S_1^1(n, \pi^*)$ state, followed by internal conversion to a $T_1^3(n, \pi^*)$ state because interactions with water changed pyruvic acid electronic structure and pyruvic acid photochemical mechanisms.⁴⁸ Multiple photochemical pathways for aqueous-phase pyruvic acid have been proposed, all of which involve excitation and intersystem crossing to the T_1 state of pyruvic acid. Griffith et al.²⁷ proposed a mechanism, in which the $T_1(n, \pi^*)$ state of pyruvic acid acts as a radical initiator by abstracting the acidic hydrogen atom from DHPA. The presence of oxygen has also been studied by Harris et al.⁵, who demonstrated that O_2 quickly quenches the radicals, favoring the formation of acetic acid and inhibiting the radical recombination reactions which generate dimethyl tartaric acid (DMTA). More complex oligomeric species, including covalently-bonded dimers and trimers of pyruvic acid are found to be the main products via major aqueous photochemical pathways, results in a significant contribution to SOA formation due to the decrease in volatility.⁴⁸

Since pyruvic acid undergoes photochemistry in the troposphere in both aqueous and gas phases, the multiphase photochemistry of pyruvic acid has been studied using an

environmental simulation chamber.⁶ Upon irradiation of nebulized pyruvic acid, acetic acid and CO₂ were generated as the two major products, consistent with studies on bulk photolysis reactions.^{5,41,42} However, more interestingly, a new higher carbon number product, a C₆ product, zymonic acid was also observed.⁶

There is great interest in the mechanistic details of the interaction of organic acids (including pyruvic acid) with surfaces as they are ubiquitous in the atmosphere and play an important role in atmospheric chemistry.⁴⁹⁻⁵¹ Al₂O₃ is a major component of mineral dust particles, occupying 10 – 15 % of the oxide fraction.⁵² Heterogeneous reactions between atmospheric trace gases and Al₂O₃, as well as the photochemistry of Al₂O₃ have been widely studied.⁵²⁻⁵⁸

Mineral dust has been reported to contain TiO₂, a photoactive semiconductor oxide, in the range of 1 – 10% by mass.^{59,60} Previous studies have focused on heterogeneous reactions of atmospheric trace gases on TiO₂ surfaces, including: nitrogen oxides (NO_x), nitric acid (HNO₃), sulfur dioxide (SO₂), ozone (O₃), hydrogen peroxide (H₂O₂), and volatile organic compounds (VOCs). Studies have also shown that organic acids can be readily adsorbed by mineral dust particles.^{59,61} The adsorption of formic acid (HCOOH, a carbonyl acid) on SiO₂ has been observed to be a reversible, molecular process, while adsorbed bridged bidentate formate (HCOO⁻) is irreversibly formed on a TiO₂ surface.^{61,62} Photochemical reactions of atmospheric trace gases on TiO₂ were also investigated as TiO₂ can interact with radiation, with the potential to initiate numerous photochemical processes. In addition, surfaces composed of oxides in indoor environments can also play a major role in air quality indoors.⁶³⁻⁶⁶ TiO₂ is a component of self-cleaning surfaces and paints.⁶⁷⁻⁷⁰

TiO₂ has three major stable forms: anatase, rutile and brookite. Degussa P25 TiO₂, which is composed of 75% anatase and 25% rutile, exhibits better photocatalytic efficiency compared with other forms because anatase has shown the highest photocatalytic activity among the three polymorphs.^{59,71} Additionally, it has been suggested that the presence of rutile in an anatase sample can increase catalytic activity.^{59,72} An electron-hole pair can be generated when excited with light of wavelength no less than the band gap energy of TiO₂ (~ 3.2 eV; λ ~390 nm).^{59,60} The three major pathways following the photogeneration of electron-hole pairs include: recombination of electrons and holes on the surface; reduction of electron acceptors; and oxidation of electron donors by photogenerated holes.^{59,72,73} Electrons and holes transported to the particle surface can also initiate redox chemistry.

Heterogenous interactions of pyruvic acid with oxide surfaces, such as Al₂O₃ and TiO₂, and their photochemical reactions, are not currently well understood. Given the importance of heterogeneous interactions and photochemical reactions of atmospheric trace gases with mineral dust surfaces and the role of surface chemistry in indoor environments, the interaction of pyruvic acid with Al₂O₃ and TiO₂ requires further investigation. In this study, the adsorption of pyruvic acid on Al₂O₃ and TiO₂ surfaces is investigated via both FTIR and high resolution mass spectrometry (HRMS) to better understand how mineral dust surfaces affects the composition of pyruvic acid and derived molecules.

6.3 Experimental Methods

Transmission Fourier transform infrared (FTIR) spectroscopy, coupled with a modified Teflon-coated infrared cell, was used to study the adsorption of pyruvic acid on

mineral dust oxides surfaces at 296 ± 1 K. Additional details of this procedure has been described in previous studies.^{62,74,75} Approximately 5 mg of metal oxide, Al_2O_3 , (Degussa, AlumOxid C, $101 \text{ m}^2 \text{ g}^{-1}$) and TiO_2 (Sigma Aldrich, $50 \text{ m}^2 \text{ g}^{-1}$), was pressed separately onto one half of a tungsten grid in the sample cell compartment, held by two Teflon coated jaws. To clean the IR cell and sample surface, the system is evacuated for 6 hours using a turbo-molecular pump. After evacuation, the sample was exposed to the desired pressure of dry, gaseous pyruvic acid (97%, Alfa Aesar) degassed at least three times with consecutive freeze-pump-thaw cycles) for 20 minutes under dry conditions ($\text{RH} < 1\%$).

Photochemistry experiments were carried out using a broadband 500 W Hg arc lamp (Oriel, Model 66033) simulating the solar spectrum. Infrared radiation was removed via a water filter placed directly after the lamp output. After 6 h of evacuation, Al_2O_3 and TiO_2 surfaces were exposed to 100 mTorr pyruvic acid vapor for 25 minutes, followed by overnight evacuation to remove all weakly-bonded species. Isolation of the reaction mixing chamber from the evacuation system is achieved by closing the valve between the customized infrared cell and the glass mixing chamber.

Prior to and following the exposure of pyruvic acid, the single beam spectra (250 scans) of surface- and gas- phase were acquired using a resolution of 4 cm^{-1} and covering the spectral range of 800 to 4000 cm^{-1} . During the exposure, single beam spectra of the silica surface (10 scans) were acquired using a Macro (OMNIC Macro Basics) for 60 s intervals. Absorbance spectra of pyruvic acid on oxide particles are reported as the difference in the oxide spectra before and after exposure to pyruvic acid. Absorption bands due to gas-phase pyruvic acid, measured through the blank half of the tungsten grid, were subtracted to obtain FTIR spectra of the particles loaded on the tungsten grid.

Insights into oxidation products formed on these surfaces were obtained using direct-injection linear ion trap (ThermoFisher Orbitrap) high resolution mass spectrometry (HRMS). Samples taken prior to and following absorption-desorption processes for the selected solid nanoparticles were removed from the substrate using acetonitrile (LC-MS Optima-grade) and methanol (Fisher Scientific). Sample vial, syringe, and all other glassware used in the transfer process were cleaned prior to use with acetonitrile and Milli-Q water [18.2 M Ω .cm] and baked in an oven at 500 °C to further remove trace organics. All samples were stored at -20 °C and analyzed within 24 hours of collection.

Analysis in both positive and negative mode was used, although the majority of detected ions were observed in negative mode ($[M-H]^-$). The heated electrospray ionization (HESI) source was operated at 50°C. The ESI capillary was set to a voltage of 2.8 kV at 325°C. Internal standards in negative mode included high-purity deuterated Hexanoic-d₁₁ Acid and Octanoic-d₁₅ Acid (CDN Isotopes). Positive mode internal standards included Hexylamine (99%) and Hexadecylamine (98%) (both purchased from Sigma-Aldrich). The HESI-Orbitrap MS was calibrated prior to use. Spectra were acquired with a mass range of 80-2000 Da. Peaks with a mass error > 2 ppm were rejected and were calculated for composition with the following element ranges: ¹²C, 0–30; ¹H, 0–50; ¹⁶O, 0–10. The list of mass signatures having no labelled composition are found in Supporting Information (SI). Contamination was minimized by employing consistent method and instrumental blanks.

6.4 Results and Discussion

6.4.1 Pyruvic acid adsorption on Al₂O₃

Table 6.1. Vibrational mode assignments for species formed on the surface of Al₂O₃ and TiO₂, respectively, following heterogeneous interaction with pyruvic acid.

Species	Mode	Al ₂ O ₃	TiO ₂	literature (sodium pyruvate)
Molecularly adsorbed	v(C=O) acid	1822		
	v(C=O) keto	1737		
	δ _{as} (CH ₃)	1427		
	v _{as} (C-CH ₃)	1389		
	δ _s (CH ₃)	1357		
	δ(COH)	1210		
	v(C-O)	1147		
	ρ(CH ₃)	1021, 973		
Adsorbed pyruvate	v _{as} (CH ₃)	3013, 2987	3012, 2989	3026 and 2991 ⁷⁶ , 3021.2 ⁷⁷ , 3021 ⁷⁸
	v _s (CH ₃)	2928	2929	2932, 2922 ⁷⁶
	v(C=O)	1737	1732	1709 ⁷⁶⁻⁷⁸
	v _{as} (CO ₂ ⁻)	1607, 1566	1610, 1585, 1570, 1564	1657 ⁷⁶ , 1634 ⁷⁸ , 1633 ⁷⁷
	δ _{as} (CH ₃)	1406	1428, 1411	1460 and 1422 ⁷⁸ , 1425.8 ⁷⁷ , 1381 ⁷⁶ , 1454
	δ _s (CH ₃)	1360	1359	1430 and 1354 ⁷⁶ , 1406 and 1353.9 ⁷⁷ , 1355 ⁷⁸ , 1361 ⁷⁹
	v _s (CO ₂ ⁻)	1473, 1454	1460, 1450	1420.8 ⁸⁰ , 1407 ⁷⁶ , 1406 ⁷⁸ , 1405.9 ⁷⁷
	v(C-CH ₃)	1176	1180	1188.4 ⁷⁷ , 1188 ⁷⁸
	ρ(CH ₃)	1022, 978	1023, 980	1017.5 ⁷⁷ , 1017 ⁷⁸ , 1016 ⁷⁶ , 983 ⁷⁸

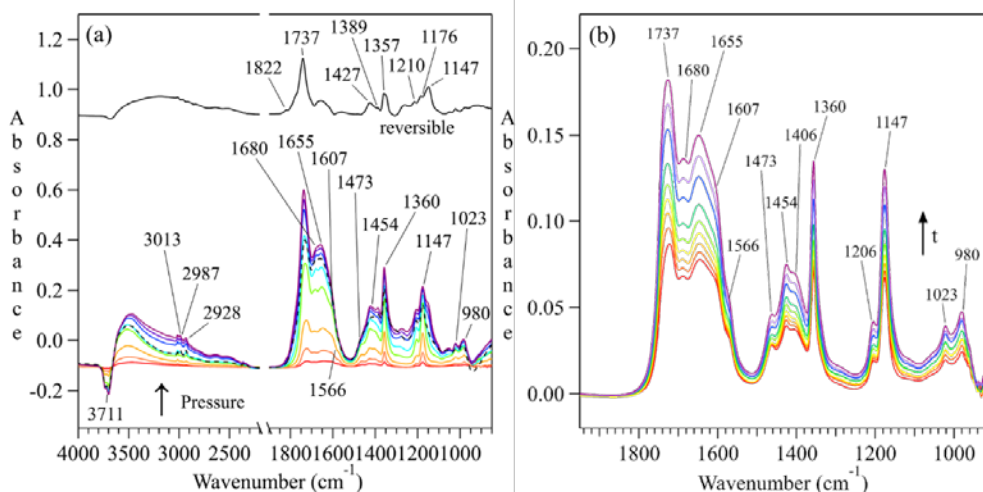


Figure 6.1. FTIR spectra of (a) Al_2O_3 following exposure to pyruvic acid for 20 minutes under dry conditions as a function of pyruvic acid pressure (5, 10, 20, 50, 100, 634, 856 and 1124 mTorr) in the spectral range of 850 to 4000 cm^{-1} and (b) 20 mTorr Al_2O_3 adsorption as a function of time in the spectral range of 900 to 1950 cm^{-1} . Evacuation of the sample cell and surface yields loss of weakly-bound species leaving a strongly-bound chemisorbed pyruvic acid species adsorbed on Al_2O_3 surface (shown by dashed line (---)). Reversible adsorbed spectrum (—, labeled as “reversible”) was obtained by subtracting evacuation spectra (---) from adsorption spectra collected at 1124 mTorr. The peaks can be assigned to molecularly-adsorbed pyruvic acid and adsorbed pyruvate (refer to Table 6.1).

A typical spectrum observed for Al_2O_3 particles following exposure to pyruvic acid under dry conditions ($\text{RH} < 1\%$) is displayed in Figure 6.1. Infrared absorbances are given the following assignments: $\rho(\text{CH}_3)$ at 1022 and 978 cm^{-1} ; $\nu(\text{C-CH}_3)$ at 1178 cm^{-1} ; $\nu_s(\text{CO}_2^-)$ and $\nu_{as}(\text{CO}_2^-)$ at 1481 and 1606 cm^{-1} , respectively; $\delta_s(\text{CH}_3)$ at 1357 cm^{-1} ; $\delta_{as}(\text{CH}_3)$ at 1427 cm^{-1} ; $\nu_s(\text{CH}_3)$ at 2928 cm^{-1} and $\nu_{as}(\text{CH}_3)$ at 2987 and 3013 cm^{-1} .

Figure 6.1 suggests that upon evacuation, most of the adsorbed pyruvic acid remains on the Al_2O_3 surface. The intensity of some infrared peaks, for example at 1737 cm^{-1} , decreases, suggesting that a small amount of pyruvic acid is molecularly- and reversibly-adsorbed on the Al_2O_3 surface at 296 K (as shown by “reversible” spectrum in

Figure 6.1). The detailed peak assignments for both adsorbed pyruvate and molecularly-adsorbed pyruvic acid on Al₂O₃ are shown in Table 6.1.

Adsorbed pyruvate can be coordinated to the metal (M) oxides (M_xO_y) surface in three different modes: (1) monodentate mode in which only one carboxylate O atom is coordinated to a surface M atom; (2) bridged bidentate mode in which two carboxylate O atoms are coordinated to two different surface M atoms; and (3) chelating bidentate mode in which two carboxylate O atoms are coordinated to the same surface M atom.⁸¹⁻⁸³ The coordination modes can be differentiated by the difference in wavenumbers between $\nu_s(\text{CO}_2^-)$ and $\nu_{as}(\text{CO}_2^-)$, i.e., $\Delta(\text{CO}_2^-)$. In this study, $\Delta(\text{CO}_2^-)$ is determined to be 125 cm⁻¹ for pyruvate adsorbed on Al₂O₃, significantly smaller than that for sodium pyruvate (250 or 228 cm⁻¹)^{76,78}, suggesting that adsorbed pyruvate is bound to the Al₂O₃ surface via the bidentate mode. It has been reported that acetic acid coordinates to the Al₂O₃ surface via the chelating bidentate mode, suggesting that pyruvic acid (an α -carbonyl acid), has similar adsorption behavior.

Other absorbance bands centered at 1680 cm⁻¹ and 1655 cm⁻¹ were also observed here, which could be assigned to zymonic acid, a closed enol ring dimer of pyruvic acid reported by Harris et al (2017), as well as other tautomers of zymonic acid^{6,84}, suggesting that zymonic acid and other pyruvic acid dimers formed when pyruvic acid adsorbed on Al₂O₃ surfaces. These peaks remaining on the surface after overnight evacuation, suggesting these large molecules (pyruvic acid dimers) are mostly irreversible on the surface. HRMS shows zymonic acid as one of the major products produced when pyruvic acid adsorbs on Al₂O₃ (Table 6.2). Mass spectrometry has been applied to further identify and analyze the products and will be discussed in Section 6.3.3.

6.4.2 Surface adsorption of pyruvic acid on TiO₂

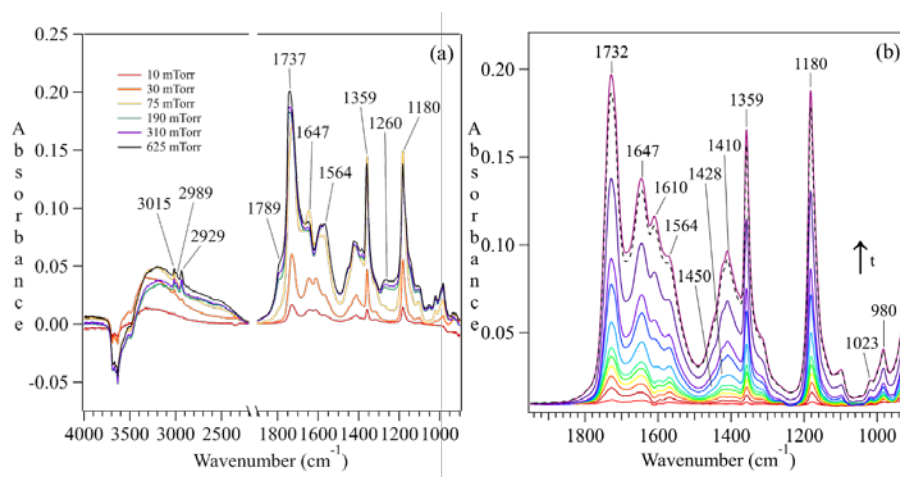


Figure 6.2. (a) FTIR spectra (800 to 4000 cm⁻¹) of TiO₂ following exposure to pyruvic acid under dry conditions as a function of pressure (10, 30, 75, 190, 310 and 625 mTorr). Each spectrum was taken 20 minutes after introduction of each pressure. (b) FTIR spectra (800 to 2000 cm⁻¹) of TiO₂ following exposure to 50 mTorr pyruvic acid under dry conditions as a function of time. Evacuation spectra (---) collected after 30 minutes of evacuation.

Figure 6.2 shows spectra observed for TiO₂ particles following exposure to pyruvic acid under dry conditions (RH < 1%). The peak assignments for the vibrational modes of adsorbed pyruvic acid on TiO₂ particles are given in Table 6.1. Pyruvic acid deprotonates on TiO₂ surface after adsorption, forming adsorbed pyruvate. Evacuation spectra in Figure 6.2(b) suggests that pyruvic acid adsorption on TiO₂ is an irreversible process. According to Figure 6.2(a), the intensity of most absorbance bands, which can be assigned to adsorbed pyruvate, remain stable above 75 mTorr, suggesting that the TiO₂ surface is almost saturated following exposure to above 75 mTorr pyruvic acid. However, absorbance bands at 1789 cm⁻¹ and 1260 cm⁻¹ which can be assigned to C=O acid stretching and C-OH from carboxylic acid respectively, still shows an increasing trend, suggesting that the extra

pyruvic acid forms dimers or other large molecules on the TiO₂ surface (including zymonic acid, C₇H₉O₆, and C₉H₁₁O₆, as shown in MS result (Table 6.2b)).

The coordination modes of surface-adsorbed pyruvate can be differentiated by the difference in wavenumbers between $\nu_s(\text{CO}_2^-)$ and $\nu_{as}(\text{CO}_2^-)$, i.e., $\Delta(\text{CO}_2^-)$. In this study, $\Delta(\text{CO}_2^-)$ is determined to be 114 – 135 cm⁻¹ for pyruvate adsorbed on TiO₂ (after the TiO₂ surface is saturated), significantly smaller than that for sodium pyruvate (250 or 228 cm⁻¹)^{76,78}, suggesting that adsorbed pyruvate is bound to TiO₂ surface via a chelating bidentate mode. However, prior to surface saturation (at lower coverages), $\Delta(\text{CO}_2^-)$ is determined to be 160 cm⁻¹, indicative that a bridged bidentate mode of adsorbed pyruvate also existed on the TiO₂ surface. Following exposure of 75 mTorr pyruvic acid to the TiO₂ surface, the observed peak position of CO₂⁻ shifts, suggesting that the binding mode of adsorbed pyruvate might change during surface saturation.

6.4.3 Photochemistry of Adsorbed Pyruvic Acid on Al₂O₃ and TiO₂

The photochemistry of adsorbed pyruvic acid on Al₂O₃ and TiO₂, respectively, was investigated using FTIR following 150 minutes of irradiation. Sample collection was performed following experiments, as well as after evacuation for further MS analysis. As seen in both Figure 6.3(a) and 6.3(b), the intensity of infrared peaks attributed to C=O ketone stretching of adsorbed pyruvate (1736 cm⁻¹ and 1741 cm⁻¹), C-CH₃ stretching (1175 cm⁻¹ and 1173 cm⁻¹), as well as the bending mode (1342 cm⁻¹ and 1356 cm⁻¹) on Al₂O₃ and TiO₂, respectively decrease with irradiation time suggesting that adsorbed pyruvic acid photolyzed during the irradiation. However, several infrared bands (1637, 1595, 1516, 1477, 1448, 1385 cm⁻¹ in Figure 6.5(a); and 1568, 1535, 1464, 1381 in Figure 6.3(b))

appeared during the irradiation, indicative of the formation of new photochemical products. Peaks at 1516 and 1477 cm^{-1} on Al_2O_3 , and peaks at 1568 and 1464 cm^{-1} on TiO_2 can be assigned to COO^- stretching of a carboxylic acid such as adsorbed lactic acid. However, detail product identification is needed because these infrared bands are broad and complicated.

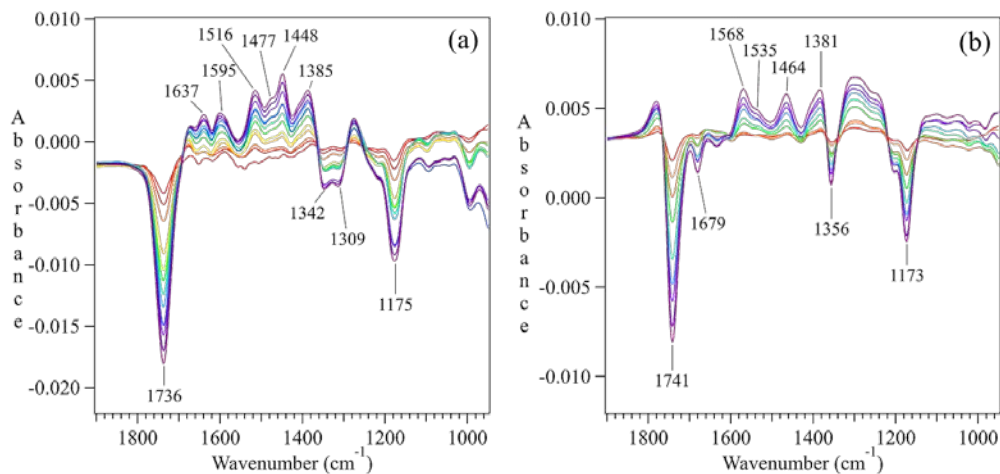


Figure 6.3. FTIR difference spectra ($950 - 1900 \text{ cm}^{-1}$) of 100 mTorr adsorbed pyruvic acid on the (a) Al_2O_3 and (b) TiO_2 surface, respectively, as a function of irradiation time. Difference spectra were obtained by subtracting the spectrum taken prior to irradiation.

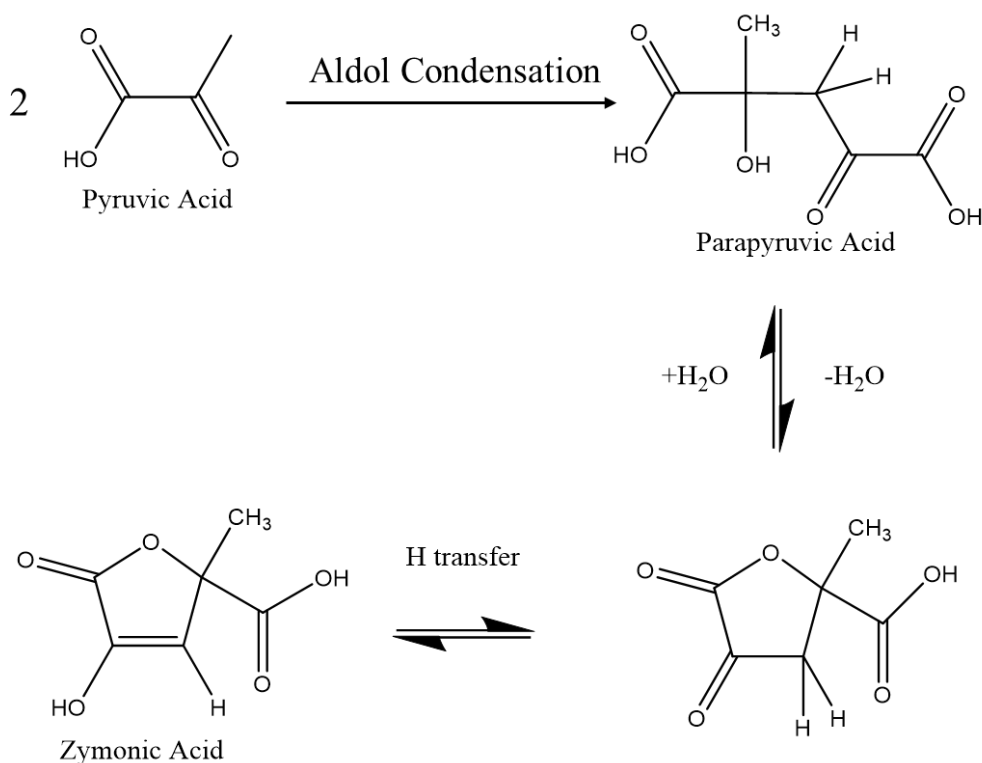
Table 6.2. Selected Compiled Photochemistry HRMS Data of Adsorbed Pyruvic Acid on Al₂O₃. (From Michael Alves)

Assigned formula [M-H]-	Assigned structure	Average experimental m/z	Mass error (ppm)	Dark with desorption	Irradiated with desorption
C ₃ H ₃ O ₃	pyruvic acid	87.00903	3.04	Medium	Strong
C ₄ H ₇ O ₄	2-methyl-2,3-dihydroxy-propanoic acid	119.03526	2.3	Below threshold	Below threshold
C ₅ H ₃ O ₃	Unassigned	111.00904	2.46	Medium	Below threshold
C ₅ H ₅ O ₃	Unassigned	113.02469	2.42	Medium	Medium
C ₅ H ₇ O ₄	acetolactic acid	131.03529	2.35	Below threshold	Medium
C ₅ H ₉ O ₄	Unassigned	133.05090	2.02	Strong	Weak
C ₆ H ₅ O ₅	zymonic acid	157.01440	1.00	Medium	Medium
C ₆ H ₇ O ₆	parapyruvic acid*	175.02495	0.8	Below threshold	Medium
C ₆ H ₉ O ₄	Unassigned	145.05082	1.3	Weak	Strong
C ₇ H ₇ O ₅	Unassigned	171.02993	0.21	Weak	Below threshold
C ₇ H ₉ O ₅	Unassigned	173.04572	1.03	Below threshold	Strong
C ₇ H ₁₁ O ₅	DMOHA	175.06134	0.81	Below threshold	Strong
C ₇ H ₉ O ₆	Unassigned	189.04046	-0.02	Medium	Weak
C ₈ H ₁₁ O ₆	Unassigned	203.05603	-0.38	Weak	Below threshold
C ₉ H ₁₁ O ₆	Unassigned	215.05611	-0.02	Below threshold	Below threshold
C ₁₂ H ₁₃ O ₄	Unassigned	221.08200	0.32	Below threshold	Strong

Table 6.3. Selected Compiled Photochemistry HRMS Data of Adsorbed Pyruvic Acid on TiO₂. (From Michael Alves)

Assigned formula [M-H]-	Assigned structure	Average experimental m/z	Mass error (ppm)	Dark with desorption	Irradiated with desorption
C ₃ H ₃ O ₃	pyruvic acid	87.00902	2.91	Medium	Strong
C ₄ H ₇ O ₄	2-methyl-2,3-dihydroxy-propanoic acid	119.03526	2.3	Below threshold	Weak
C ₅ H ₅ O ₃	Unassigned	113.02468	2.36	Strong	Medium
C ₅ H ₇ O ₄	acetolactic acid	131.03526	2.11	Below threshold	Weak
C ₅ H ₉ O ₄	Unassigned	133.05089	1.96	Medium	Weak
C ₆ H ₅ O ₅	zymonic acid	157.01443	1.17	Strong	Strong
C ₆ H ₇ O ₆	parapyruvic acid*	175.02495	0.8	Below threshold	Medium
C ₆ H ₉ O ₄	Unassigned	145.05082	1.27	Below threshold	Medium
C ₇ H ₇ O ₅	Unassigned	171.02996	0.38	Medium	Below threshold
C ₇ H ₁₁ O ₅	DMOHA	175.06134	0.84	Below threshold	Medium
C ₇ H ₉ O ₆	Unassigned	189.04052	0.31	Strong	Strong
C ₈ H ₁₁ O ₆	Unassigned	203.05611	-0.01	Medium	Below threshold
C ₉ H ₁₁ O ₆	Unassigned	215.05611	-0.02	Medium	Medium
C ₁₂ H ₁₃ O ₄	unassigned	221.08189	-0.18	Weak	Weak

To further determine the photochemical reaction products and possible pathways of adsorbed pyruvic acid on Al_2O_3 and TiO_2 , extracts of adsorbed pyruvic acid on oxide surfaces, before and after irradiation, were analysed via mass spectrometry. Either pure or aqueous pyruvic acid has been proved to spontaneously dimerize, likely through an aldol addition reaction, forming parapyruvic acid and zymonic acid, as well as their tautomers and hydrates, in a known equilibrium dependent on pH and concentration as shown in Scheme 1.^{48,84}



Scheme 6.1. Pyruvic acid dimerized to form parapyruvic acid and zymonic acid. (Adapted from Perkins et al (2016)).

Therefore, the study of adsorbed pyruvic acid on oxide surfaces in dark conditions is crucial to understand as it is necessary to consider the contribution from the oligomerization processes that will provide insight into more complex photochemical

pathways. HRMS used in this study shows that adsorbed pyruvic acid on oxide surfaces, in dark conditions, produced many such oligomers found in Table 6.2 and Table 6.3.

Rapf and coworkers⁴⁸ studied pyruvic acid aqueous photochemical reactions and observing pyruvic acid derived dimers and trimers as products. Such products can then undergo further photochemical reactions to form larger oligomeric products such as DMOHA. Zymonic acid has also been found in multiphase photochemical reactions of pyruvic acid under atmospheric relevant conditions using an environmental simulation chamber.⁶ Among many other produced oligomers from this study, zymonic acid was specifically observed in our mass spectra as one of the major products in all of the pyruvic acid-oxide surface (Al_2O_3 and TiO_2) experiments. This supports our FTIR observations shown in Figure 6.1 and Figure 6.2. After evacuation to remove weakly bonded surface species, zymonic species (zymonic acid and its tautomers) exhibit a much higher intensity in TiO_2 compared to Al_2O_3 , suggesting that the zymonic species are more stable on TiO_2 . The most stable adsorption geometry, calculated by theoretical work on adsorption of oxalic acid on TiO_2 , is expected to be deprotonation of both carboxyl groups.^{85,86} In another study, attenuated total reflection Fourier-transform infrared spectroscopy (ATR-FTIR) was used to investigate malonic acid adsorbed on particulate TiO_2 (P25 Degussa), suggesting adsorption of malonic acid on the TiO_2 surface occurred via one bridging bidentate and one monodentate carboxylate group.^{86,87} We speculate that the pyruvic acid oligomers such as zymonic species, those with two carboxyl groups or more, will be the more energetically stable (irreversible adsorbed) as doubly deprotonated products on metal oxide surfaces. Both zymonic acid and other C_5 species were observed in aqueous pyruvic acid dark conditions (see Table 6.2 and Table 6.3). Zymonic acid has also been detected in

multiphase pyruvic acid photochemistry and can be formed by dehydration of parapyruvic acid.⁶

Samples were extracted from oxide surfaces after pyruvic acid adsorption following 150 mins of irradiation for HRMS analysis. Parapyruvic acid (and its other forms) is below threshold before irradiation from both surfaces. Selected oligomers of pyruvic acid, previously observed by Rapf and coworkers⁴⁸ were also detected in this study, oligomers not detected such as CDMOHA/DMTA was most likely due to the nature of the experiment. Parapyruvic acid, a dimer of pyruvic acid is detected at m/z 175.02495 (0.80 ppm mass error) by MS, in good agreement with previous photochemical studies by Rapf et al.⁴⁸ who calculated that it is energetically possible to photochemically generate parapyruvic acid. Zymonic acid, a closed enol ring dimer of pyruvic acid, is also detected here using MS at m/z 157.01440 (1.17 ppm mass error). However, in our studies, zymonic acid has been detected in both light and dark conditions, while parapyruvic acid is only seen as a photoproduct. This finding suggests that zymonic acid is the product of a spontaneous oligomerization process on the surface, but parapyruvic acid is only being produced in substantial amounts in the photochemical processes.

Pyruvic acid on oxide surfaces have specific and previously observed photochemical pathways, further details can be found in photolysis studies of aqueous pyruvic acid by Rapf et al and Guzman et al.^{26,48} Briefly, for deprotonated pyruvate molecules, such as adsorbed pyruvate on Al_2O_3 and TiO_2 surfaces, only the methyl group is available for abstraction. Furthering photochemical processing, after generating and combining the $CH_3C(OH)_2$ (GD) and $CH_2C(O)CO_2H$ (OA) radicals, recombination products, dimethyltartaric acid and 2, 5- dioxohexanedioic acid, are not detected within the

threshold of our HRMS results suggesting that intersystem crossing back to the singlet state was the dominant pathway for photochemistry of adsorbed pyruvate. It is important to note, though, that oligomeric species can decompose into smaller product species. In the aqueous-phase, products resulting from the GD radical were also not detected (above threshold) in the HRMS analysis, suggesting that a GD radical pathway is not favorable for adsorbed pyruvic acid surface photochemistry.

Analysis of the surface-adsorbed species following 150 mins of irradiation and subsequent overnight evacuation was also performed. Zymonic acid and DMOHA are still present as major photoproducts on both TiO_2 and Al_2O_3 surfaces. Parapyruvic acid is reported to undergo further photolysis, forming pyruvic acid trimers and other larger molecules. However, parapyruvic acid is still observed after irradiation (for all studies), suggesting that Al_2O_3 and TiO_2 surfaces and absorbed irradiated pyruvic acid proceeds in an alternate pathway not previously suggested. The observation that the formation of more complex, oligomeric species, including: zymonic acid, DMOHA, parapyruvic acid, C_5 unassigned species, $\text{C}_9\text{H}_{11}\text{O}_6$, and $\text{C}_{12}\text{H}_{13}\text{O}_4$ are favored under anoxic conditions raises intriguing possibilities for the relevance of this chemistry in the ancient, prebiotic environment, which contained very little O_2 and ozone, allowing more UV light to reach the troposphere and Earth's surface. Heterogenous reactions between pyruvic acid and oxide surfaces under prebiotically relevant conditions forms oligomers, suggesting that sunlight can be trapped by pyruvic acid and converted into usable chemical energy stored in larger molecules.

6.5 Conclusion

Transmission FTIR spectroscopy was used to investigate the heterogeneous reactions between pyruvic acid and mineral dust aerosol particles. Pyruvate was observed when pyruvic acid adsorbed on Al₂O₃ and TiO₂. Upon irradiation, adsorbed pyruvic acid reacted to form other compounds on both surfaces. HRMS was applied to study the products and mechanisms for pyruvic acid in both light and dark conditions. Parapyruvic acid has been found on both surfaces in light conditions while zymonic species were found in both light and dark conditions, suggesting that the production of zymonic acid and its tautomers is an oligomerization process in both conditions and parapyruvic acid is being produced via photochemical processes. Other compounds such as DMOHA, C₉H₁₂O₆, and C₁₂H₁₄O₄ were also detected using MS, suggesting that pyruvic acid photochemistry on surfaces formed various larger products.

This study highlights the complex nature of surface-adsorbed systems by identifying compounds which are not produced from single gas- or aqueous-phase photochemical studies. The formation of the various oligomers discussed in this study, produced from currently unidentified reaction pathways, emphasizes the need for further studies on the detailed mechanisms and subsequent products.

6.6 Acknowledgement

This material is the Alfred P. Sloan Foundation under grant number G-2017-9692. The contents of this study do not necessarily reflect the official views of the Alfred P. Sloan Foundation. The Alfred P. Sloan Foundation does not endorse the purchase of the commercial products used in this report. The dissertation author was the primary

investigator of all FTIR measurements and data analysis. The author would like to thank Michael Alves for HRMS analysis. Chapter 6, in full is currently being prepared for submission for publication of the material. Yuan Fang, Michael Alves, Kristin Wall and Vicki H. Grassian. The dissertation author was the primary investigator and author of this material.

6.7 References

- (1) George, C.; D'Anna, B.; Herrmann, H.; Weller, C.; Vaida, V.; Donaldson, D. J.; Bartels-Rausch, T.; Ammann, M. Emerging Areas in Atmospheric Photochemistry. In *Atmospheric and Aerosol Chemistry*; McNeill, V. F., Ariya, P. A., Eds.; Springer Berlin Heidelberg: Berlin, Heidelberg, 2014; pp 1–53.
- (2) George, C.; Ammann, M.; D'Anna, B.; Donaldson, D. J.; Nizkorodov, S. A. Heterogeneous Photochemistry in the Atmosphere. *Chem. Rev.* **2015**, *115* (10), 4218–4258.
- (3) Rapf, R. J.; Vaida, V. Sunlight as an Energetic Driver in the Synthesis of Molecules Necessary for Life. *Phys. Chem. Chem. Phys.* **2016**, *18* (30), 20067–20084.
- (4) Vaida, V. Spectroscopy of Photoreactive Systems: Implications for Atmospheric Chemistry. *J. Phys. Chem. A* **2009**, *113* (1), 5–18.
- (5) Reed Harris, A. E.; Doussin, J. F.; Carpenter, B. K.; Vaida, V. Gas-Phase Photolysis of Pyruvic Acid: The Effect of Pressure on Reaction Rates and Products. *J. Phys. Chem. A* **2016**, *120* (51), 10123–10133.
- (6) Reed Harris, A. E.; Pajunoja, A.; Cazaunau, M.; Gratien, A.; Pangui, E.; Monod, A.; Griffith, E. C.; Virtanen, A.; Doussin, J. F.; Vaida, V. Multiphase Photochemistry of Pyruvic Acid under Atmospheric Conditions. *J. Phys. Chem. A* **2017**, *121* (18), 3327–3339.
- (7) Gligorovski, S.; Strekowski, R.; Barbati, S.; Vione, D. Environmental Implications of Hydroxyl Radicals ($\bullet\text{OH}$). *Chem. Rev.* **2015**, *115* (24), 13051–13092.
- (8) Griffith, E. C.; Shoemaker, R. K.; Vaida, V. Sunlight-Initiated Chemistry of Aqueous Pyruvic Acid: Building Complexity in the Origin of Life. *Orig. Life Evol. Biosph.* **2013**, *43* (4–5), 341–352.

- (9) Shapiro, R. Small Molecule Interactions Were Central to the Origin of Life. *Q. Rev. Biol.* **2006**, *81* (2), 105–126.
- (10) Guzman, M. I.; Martin, S. T. Prebiotic Metabolism: Production by Mineral Photoelectrochemistry of α -Ketocarboxylic Acids in the Reductive Tricarboxylic Acid Cycle. *Astrobiology* **2009**, *9* (9), 833–842.
- (11) Orgel, L. E. The Implausibility of Metabolic Cycles on the Prebiotic Earth. *PLoS Biol.* **2008**, *6* (1), 0005-0013.
- (12) Andreae, M. O.; Talbot, R. W.; Li, S.-M. . Atmospheric Measurements of Pyruvic and Formic Acid. *J. Geophys.* **1987**, *92*, 6635–6641.
- (13) Talbot, R. W.; Andreae, M. O.; Berresheim, H.; Jacob, D. J.; Beecher, K. M. Sources and Sinks of Formic, Acetic, and Pyruvic Acids over Central Amazonia: 2. Wet Season. *J. Geophys. Res. Atmos.* **1990**, *95* (D10), 16799–16811.
- (14) Kawamura, K.; Bikkina, S. A Review of Dicarboxylic Acids and Related Compounds in Atmospheric Aerosols: Molecular Distributions, Sources and Transformation. *Atmos. Res.* **2016**, *170*, 140–160.
- (15) Baboukas, E. D.; Kanakidou, M.; Mihalopoulos, N. Carboxylic Acids in Gas and Particulate Phase above the Atlantic Ocean. *J. Geophys. Res. Atmos.* **2000**, *105* (D11), 14459–14471.
- (16) Bao, L.; Matsumoto, M.; Kubota, T.; Sekiguchi, K.; Wang, Q.; Sakamoto, K. Gas/Particle Partitioning of Low-Molecular-Weight Dicarboxylic Acids at a Suburban Site in Saitama, Japan. *Atmos. Environ.* **2012**, *47*, 546–553.
- (17) Bardouki, H.; Liakakou, H.; Economou, C.; Sciare, J.; Smolík, J.; Ždímal, V.; Eleftheriadis, K.; Lazaridis, M.; Dye, C.; Mihalopoulos, N. Chemical Composition of Size-Resolved Atmospheric Aerosols in the Eastern Mediterranean during Summer and Winter. *Atmos. Environ.* **2003**, *37* (2), 195–208.
- (18) Chebbi, a; Carlier, P. Carboxylic Acids in the Troposphere, Occurrence, Sources and Sinks: A Review. *Atmos. Environ.* **1996**, *30* (24), 4223–4249.
- (19) Ho, K. F.; Lee, S. C.; Cao, J. J.; Kawamura, K.; Watanabe, T.; Cheng, Y.; Chow, J. C. Dicarboxylic Acids, Ketocarboxylic Acids and Dicarbonyls in the Urban Roadside Area of Hong Kong. *Atmos. Environ.* **2006**, *40* (17), 3030–3040.
- (20) Khwaja, H. A. Atmospheric Concentrations of Carboxylic Acids and Related Compounds at a Semiurban Site. *Atmos. Environ.* **1995**, *29* (1), 127–139.
- (21) Limbeck, A.; Puxbaum, H.; Otter, L.; Scholes, M. C. Semivolatile Behavior of Dicarboxylic Acids and Other Polar Organic Species at a Rural Background Site (Nylsvley, RSA). *Atmos. Environ.* **2001**, *35* (10), 1853–1862.

- (22) Kawamura, K.; Kasukabe, H.; Barrie, L. A. Source and Reaction Pathways of Dicarboxylic Acids, Ketoacids and Dicarbonyls in Arctic Aerosols: One Year of Observations. *Atmos. Environ.* **1996**, *30* (10–11), 1709–1722.
- (23) Reed Harris, A. E.; Ervens, B.; Shoemaker, R. K.; Kroll, J. A.; Rapf, R. J.; Griffith, E. C.; Monod, A.; Vaida, V. Photochemical Kinetics of Pyruvic Acid in Aqueous Solution. *J. Phys. Chem. A* **2014**, *118* (37), 8505–8516.
- (24) Hall, G. E.; Muckerman, J. T.; Preses, J. M.; Weston, R. E.; Flynn, G. W. Time-Resolved FTIR Studies of the Photodissociation of Pyruvic Acid at 193 Nm. *Chem. Phys. Lett.* **1992**, *193* (1–3), 77–83.
- (25) Rincón, A. G.; Guzman, M. I.; Hoffmann, M. R.; Colussi, A. J. Optical Absorptivity versus Molecular Composition of Model Organic Aerosol Matter. *J. Phys. Chem. A* **2009**, *113* (39), 10512–10520.
- (26) Guzmán, M. I.; Colussi, A. J.; Hoffmann, M. R. Photoinduced Oligomerization of Aqueous Pyruvic Acid. *J. Phys. Chem. A* **2006**, *110* (10), 3619–3626.
- (27) Griffith, E. C.; Carpenter, B. K.; Shoemaker, R. K.; Vaida, V. Photochemistry of Aqueous Pyruvic Acid. *Proc. Natl. Acad. Sci.* **2013**, *110* (29), 11714–11719.
- (28) O’Neill, J. A.; Kreutz, T. G.; Flynn, G. W. IR Diode Laser Study of Vibrational Energy Distribution in CO₂ Produced by UV Excimer Laser Photofragmentation of Pyruvic Acid. *J. Chem. Phys.* **1987**, *87* (8), 4598.
- (29) Wood, C. F.; O’Neill, J. A.; Flynn, G. W. Infrared Diode Laser Probes of Photofragmentation Products: Bending Excitation in CO₂ Produced by Excimer Laser Photolysis of Pyruvic Acid. *Chem. Phys. Lett.* **1984**, *109* (4), 317–323.
- (30) Grosjean, D. Atmospheric Reactions of Pyruvic Acid. *Atmos. Environ.* **1983**, *17* (11), 2379–2382.
- (31) Yamamoto, S.; Back, R. A. The Photolysis and Thermal Decomposition of Pyruvic Acid in the Gas Phase. *Can. J. Chem.* **1985**, *63* (2), 549–554.
- (32) Davidson, R. S.; Goodwin, D.; Violet, D. E. And Ph. FORNIER DE VIOLET. **1981**, *78* (3), 1–4.
- (33) Mellouki, A.; Mu, Y. On the Atmospheric Degradation of Pyruvic Acid in the Gas Phase. *J. Photochem. Photobiol. A Chem.* **2003**, *157* (2–3), 295–300.
- (34) Carlton, A. G.; Turpin, B. J.; Lim, H. J.; Altieri, K. E.; Seitzinger, S. Link between Isoprene and Secondary Organic Aerosol (SOA): Pyruvic Acid Oxidation Yields Low Volatility Organic Acids in Clouds. *Geophys. Res. Lett.* **2006**, *33* (6), 2–5.
- (35) Stefan, M. I.; Bolton, J. R. Reinvestigation of the Acetone Degradation Mechanism in Dilute Aqueous Solution by the UV/H₂O₂ Process. *Environ. Sci. Technol.* **1999**,

33 (6), 870–873.

- (36) Saito, K.; Sasaki, G.; Okada, K.; Tanaka, S. Unimolecular Decomposition of Pyruvic Acid: An Experimental and Theoretical Study. *J. Phys. Chem.* **1994**, *98*, 3756–3761.
- (37) Taylor, R. The Mechanism of Thermal Eliminations Part XXIII: [1] The Thermal Decomposition of Pyruvic Acid. *Int. J. Chem. Kinet.* **1987**, *19* (8), 709–713.
- (38) Plath, K. L.; Takahashi, K.; Skodje, R. T.; Vaida, V. Fundamental and Overtone Vibrational Spectra of Gas-Phase Pyruvic Acid. *J. Phys. Chem. A* **2009**, *113* (26), 7294–7303.
- (39) Larsen, M. C.; Vaida, V. Near Infrared Photochemistry of Pyruvic Acid in Aqueous Solution. *J. Phys. Chem. A* **2012**, *116* (24), 5840–5846.
- (40) Takahashi, K.; Plath, K. L.; Skodje, R. T.; Vaida, V. Dynamics of Vibrational Overtone Excited Pyruvic Acid in the Gas Phase: Line Broadening through Hydrogen-Atom Chattering. *J. Phys. Chem. A* **2008**, *112* (32), 7321–7331.
- (41) Chang, X. P.; Fang, Q.; Cui, G. Mechanistic Photodecarboxylation of Pyruvic Acid: Excited-State Proton Transfer and Three-State Intersection. *J. Chem. Phys.* **2014**, *141* (15), 2–10.
- (42) Da Silva, G. Decomposition of Pyruvic Acid on the Ground-State Potential Energy Surface. *J. Phys. Chem. A* **2016**, *120* (2), 276–283.
- (43) Murto, J.; Raaska, T.; Kunttu, H.; Räsänen, M. Conformers and Vibrational Spectra of Pyruvic Acid: An Ab Initio Study. *J. Mol. Struct. THEOCHEM* **1989**, *200* (C), 93–101.
- (44) Rosenfeld, R. N.; Weiner, B. Energy Disposal in the Photofragmentation of Pyruvic Acid in the Gas Phase. *J. Am. Chem. Soc.* **1983**, *105* (11), 3485–3488.
- (45) Leermakers, P. A.; Vesley, G. F. The Photochemistry of α -Keto Acids and α -Keto Esters. I. Photolysis of Pyruvic Acid and Benzoylformic Acid. *J. Am. Chem. Soc.* **1963**, *85* (23), 3776–3779.
- (46) Hans-Jürgen, B.; Edward, D.; Wilhelm, K. The Reversible Hydration of Carbonyl Compounds in Aqueous Solution Part II: The Kinetics of the Keto/Gem-diol Transition. *Berichte der Bunsengesellschaft für Phys. Chemie* **2018**, *86* (2), 129–134.
- (47) Pocker, Y.; Meany, J. E.; Nist, B. J.; Zadorojny, C. The Reversible Hydration of Pyruvic Acid. I. Equilibrium Studies. *J. Phys. Chem.* **1969**, *73* (9), 2879–2882.
- (48) Rapf, R. J.; Perkins, R. J.; Carpenter, B. K.; Vaida, V. Mechanistic Description of Photochemical Oligomer Formation from Aqueous Pyruvic Acid. *J. Phys. Chem. A*

2017, 121 (22), 4272–4282.

- (49) Textor, C.; Schulz, M.; Guibert, S.; Kinne, S.; Balkanski, Y.; Bauer, S.; Bernsten, T.; Berglen, T.; Boucher, O.; Chin, M.; et al. Analysis and Quantification of the Diversities of Aerosol Life Cycles within AeroCom. *Atmos. Chem. Phys.* **2006**, 6 (7), 1777–1813.
- (50) Usher, C. R.; Michel, A. E.; Grassian, V. H. Reactions on Mineral Dust. *Chem. Rev.* **2003**, 103 (12), 4883–4939.
- (51) Crowley, J. N.; Ammann, M.; Cox, R. A.; Hynes, R. G.; Jenkin, M. E.; Mellouki, A.; Rossi, M. J.; Troe, J.; Wallington, T. J. Evaluated Kinetic and Photochemical Data for Atmospheric Chemistry: Volume v -Heterogeneous Reactions on Solid Substrates. *Atmos. Chem. Phys.* **2010**, 10 (18), 9059–9223.
- (52) Gankanda, A.; Grassian, V. H. Nitrate Photochemistry on Laboratory Proxies of Mineral Dust Aerosol: Wavelength Dependence and Action Spectra. *J. Phys. Chem. C* **2014**, 118 (50), 29117–29125.
- (53) Rubasinghege, G.; Grassian, V. H. Surface-Catalyzed Chlorine and Nitrogen Activation: Mechanisms for the Heterogeneous Formation of ClNO, NO, NO₂, HONO, and N₂O from HNO₃ and HCl on Aluminum Oxide Particle Surfaces. *J. Phys. Chem. A* **2012**, 116 (21), 5180–5192.
- (54) Rubasinghege, G.; Grassian, V. H. Photochemistry of Adsorbed Nitrate on Aluminum Oxide Particle Surfaces. *J. Phys. Chem. A* **2009**, 113 (27), 7818–7825.
- (55) Baltrusaitis, J.; Schuttlefield, J.; Jensen, J. H.; Grassian, V. H. FTIR Spectroscopy Combined with Quantum Chemical Calculations to Investigate Adsorbed Nitrate on Aluminium Oxide Surfaces in the Presence and Absence of Co-Adsorbed Water. *Phys. Chem. Chem. Phys.* **2007**, 9 (36), 4970–4980.
- (56) Li, P.; Perreau, K. A.; Covington, E.; Song, C. H.; Carmichael, G. R.; Grassian, V. H. Heterogeneous Reactions of Volatile Organic Compounds on Oxide Particles of the Most Abundant Crustal Elements: Surface Reactions of Acetaldehyde, Acetone, and Propionaldehyde on SiO₂, Al₂O₃, Fe₂O₃. *J. Geophys. Res. Atmos.* **2001**, 106 (D6), 5517–5529.
- (57) Hanisch, F.; Crowley, J. N. Heterogeneous Reactivity of Gaseous Nitric Acid on Al₂O₃, CaCO₃, and Atmospheric Dust Samples: A Knudsen Cell Study. *J. Phys. Chem. A* **2001**, 105, 3096–3106.
- (58) Liu, Y.; He, H.; Mu, Y. Heterogeneous Reactivity of Carbonyl Sulfide on α -Al₂O₃ and γ -Al₂O₃. *Atmos. Environ.* **2008**, 42 (6), 960–969.
- (59) Chen, H.; Nanayakkara, C. E.; Grassian, V. H. Titanium Dioxide Photocatalysis in Atmospheric Chemistry. *Chem. Rev.* **2012**, 112 (11), 5919–5948.

- (60) Nanayakkara, C. E.; Larish, W. A.; Grassian, V. H. Titanium Dioxide Nanoparticle Surface Reactivity with Atmospheric Gases, CO₂, SO₂, and NO₂: Roles of Surface Hydroxyl Groups and Adsorbed Water in the Formation and Stability of Adsorbed Products. *J. Phys. Chem. C* **2014**, *118* (40), 23011–23021.
- (61) Tang, M.; Larish, W. A.; Fang, Y.; Gankanda, A.; Grassian, V. H. Heterogeneous Reactions of Acetic Acid with Oxide Surfaces: Effects of Mineralogy and Relative Humidity. *J. Phys. Chem. A* **2016**, *120* (28), 5609–5616.
- (62) Fang, Y.; Tang, M.; Grassian, V. H. Competition between Displacement and Dissociation of a Strong Acid Compared to a Weak Acid Adsorbed on Silica Particle Surfaces: The Role of Adsorbed Water. *J. Phys. Chem. A* **2016**, *120* (23), 4016–4024.
- (63) Weschler, C. J.; Shields, H. C. Potential Reactions among Indoor Pollutants. *Atmos. Environ.* **1997**, *31* (21), 3487–3495.
- (64) Yu, B. F.; Hu, Z. B.; Liu, M.; Yang, H. L.; Kong, Q. X.; Liu, Y. H. Review of Research on Air-Conditioning Systems and Indoor Air Quality Control for Human Health. *Int. J. Refrig.* **2009**, *32* (1), 3–20.
- (65) Tham, K. W.; Zuraimi, M. S. Size Relationship between Airborne Viable Bacteria and Particles in a Controlled Indoor Environment Study. *Indoor Air* **2005**, *15 Suppl 9* (Suppl 9), 48–57.
- (66) Cox, S. S.; Little, J. C.; Hodgson, A. T. Predicting the Emission Rate of Volatile Organic Compounds from Vinyl Flooring. *Environ. Sci. Technol.* **2002**, *36* (4), 709–714.
- (67) Fujishima, A.; Rao, T. N.; Tryk, D. A. Titanium Dioxide Photocatalysis. *J. Photochem. Photobiol. C Photochem. Rev.* **2000**, *1* (1), 1–21.
- (68) Romeas, V.; Pichat, P.; Guillard, C.; Chopin, T.; Lehaut, C. Testing the Efficacy and the Potential Effect on Indoor Air Quality of a Transparent Self-Cleaning TiO₂-Coated Glass through the Degradation of a Fluoranthene Layer. *Ind. Eng. Chem. Res.* **1999**, *38* (10), 3878–3885.
- (69) Paz, Y.; Luo, Z.; Rabenberg, L.; Heller, A. Photooxidative Self-Cleaning Transparent Titanium Dioxide Films on Glass. *J. Mater. Res.* **1995**, *10* (11), 2842–2848.
- (70) Anandan, S.; Narasinga Rao, T.; Sathish, M.; Rangappa, D.; Honma, I.; Miyauchi, M. Superhydrophilic Graphene-Loaded TiO₂ thin Film for Self-Cleaning Applications. *ACS Appl. Mater. Interfaces* **2013**, *5* (1), 207–212.
- (71) Hanaor, D. A. H.; Sorrell, C. C. Review of the Anatase to Rutile Phase Transformation. *J. Mater. Sci.* **2011**, *46* (4), 855–874.

- (72) Hurum, D. C.; Agrios, A. G.; Gray, K. A.; Rajh, T.; Thurnauer, M. C. Explaining the Enhanced Photocatalytic Activity of Degussa P25 Mixed-Phase TiO₂ Using EPR. *J. Phys. Chem. B* **2003**, *107* (19), 4545–4549.
- (73) Linsebigler, A. L.; Lu, G.; Yates, J. T. Photocatalysis on TiO₂ Surfaces: Principles, Mechanisms, and Selected Results. *Chem. Rev.* **1995**, *95* (3), 735–758.
- (74) Goodman, A. L.; Bernard, E. T.; Grassian, V. H. Spectroscopic Study of Nitric Acid and Water Adsorption on Oxide Particles: Enhanced Nitric Acid Uptake Kinetics in the Presence of Adsorbed Water. *J. Phys. Chem. A* **2001**, *105* (26), 6443–6457.
- (75) Goodman, A. L.; Underwood, G. M.; Grassian, V. H. A Laboratory Study of the Heterogeneous Reaction of Nitric Acid on Calcium Carbonate Particles. *J. Geophys. Res.* **2000**, *105* (D23), 29053–29064.
- (76) Katon, J. E.; Covington, D. T. The Vibrational Spectra of Crystalline Sodium Pyruvate. *Spectrosc. Lett.* **1979**, *12* (10), 761–766.
- (77) Kakihana, M.; Okamoto, M. Vibrational Analysis of Pyruvate Ion Molecules and Estimation of Equilibrium Constants for Their Hydrogen Isotopic Exchange Reactions. *J. Phys. Chem.* **1984**, *88* (9), 1797–1804.
- (78) Long, B. D. A.; George, W. Spectroscopic Study of the Pyruvate Ion. **1960**.
- (79) Ray, W.; Katon, J.; Phillips, D. Structure, Hydrogen Bonding and Vibrational Spectra of Pyruvic Acid. *J. Mol. Struct.* **1981**, *74* (1), 75–84.
- (80) Hanai, K.; Kuwae, A.; Sugawa, Y.; Kunimoto, K. K.; Maeda, S. Vibrational and NMR Spectra and Structures of Lithium Pyruvate Monohydrate. *J. Mol. Struct.* **2007**, *837* (1–3), 101–106.
- (81) Sokolow, J. D.; Trzop, E.; Chen, Y.; Tang, J.; Allen, L. J.; Crabtree, R. H.; Benedict, J. B.; Coppens, P. Binding Modes of Carboxylate- and Acetylacetonate-Linked Chromophores to Homodisperse Polyoxotitanate Nanoclusters. *J. Am. Chem. Soc.* **2012**, *134* (28), 11695–11700.
- (82) Dobson, K. D.; McQuillan, A. J. In Situ Infrared Spectroscopic Analysis of the Adsorption of Aromatic Carboxylic Acids to TiO₂, ZrO₂, Al₂O₃, and Ta₂O₅ from Aqueous Solutions. *Spectrochim. Acta - Part A Mol. Biomol. Spectrosc.* **2000**, *56* (3), 557–565.
- (83) Dobson, K. D.; McQuillan, A. J. In Situ Infrared Spectroscopic Analysis of the Adsorption of Aliphatic Carboxylic Acids to TiO₂, ZrO₂, Al₂O₃, and Ta₂O₅ from Aqueous Solutions. *Spectrochim. Acta Part A Mol. Biomol. Spectrosc.* **1999**, *55* (7–8), 1395–1405.
- (84) Perkins, R. J.; Shoemaker, R. K.; Carpenter, B. K.; Vaida, V. Chemical Equilibria and Kinetics in Aqueous Solutions of Zymonic Acid. *J. Phys. Chem. A* **2016**, *120*

(51), 10096–10107.

- (85) Fahmi, A.; Minot, C.; Fourre, P.; Nortier, P. A Theoretical Study of the Adsorption of Oxalic Acid on TiO₂. *Surf. Sci.* **1995**, *343*, 261–272.
- (86) Thomas, A. G.; Syres, K. L. Adsorption of Organic Molecules on Rutile TiO₂ and Anatase TiO₂ Single Crystal Surfaces. *Chem. Soc. Rev.* **2012**, *41* (11), 4207.
- (87) Dolamic, I.; Bürgi, T. Photoassisted Decomposition of Malonic Acid on TiO₂ Studied by in Situ Attenuated Total Reflection Infrared Spectroscopy. *J. Phys. Chem. B* **2006**, *110* (30), 14898–14904.

CHAPTER 7 UNDERSTANDING THE INTERACTION BETWEEN INDOOR AIR RELEVANT VOLATILE ORGANIC COMPOUNDS WITH SILICA SURFACES

7.1 Abstract

Adsorption and desorption kinetics of limonene, a terpene commonly found in indoor environments, on silica, which is representative of glass surfaces, were investigated here as a function of coverage (at 296 K), as well as a function of temperature at fixed pressure for under dry conditions (< 1 % RH). Limonene adsorption on silica is found to be a molecular, reversible process via hydrogen bonding with surface hydroxyl groups. By combining experimental (Transmission Fourier transform infrared (FTIR) spectroscopy), kinetics modeling and atomistic computer simulations, we developed a method to study limonene adsorption/desorption kinetics on silica surfaces. The methods developed for studying this molecule and the surface can be further applied to other relevant indoor organic vapors and surfaces. The role adsorbed water plays in limonene adsorption on SiO₂ surfaces was also investigated.

7.2 Introduction

In developed nations, people spend almost 90% of their total time indoors, especially in their own residences, which consists of myriad of surfaces such as walls, windows and floors.^{1,2} Given the large surface to volume ratios and long reactive lifetimes in the indoor environment, interfacial chemistry can play a significant role indoors.^{1,3,4}

Indoor surfaces may provide substrates for reactions to occur which may lead to the formation of new molecular species that can desorb into the gas phase, and/or these surfaces could also remove gas phase species via adsorption.² However, little is known about these reactions and there remains a lack of knowledge concerning the detailed chemistry and molecular processes involving indoor surfaces.

Three main surface processes including oxidation, acid-base reactions and adsorption/desorption can influence indoor air chemistry.¹ Given the presence of oxidants such as ozone, hydroxyl radicals and nitrates, the indoor environment can be highly oxidized to form secondary organic aerosols and nitrous acid (HONO).^{5,6} Since carbon dioxide and ammonia are also present indoors (at parts per million levels), with their concentrations varying as occupants change activities, acid-base reactions are potentially important.^{7,8} Depending on factors such as the volatility of the molecular species, nature of the surface and relative humidity (RH) indoors, adsorption/desorption processes can also influence indoor air concentrations.⁹ Among the various surface interactions occurring in the indoor environment, we focus on understanding the kinetics of the adsorption/desorption process of a common indoor gas, d-limonene, on silica, a model indoor surface for glass. The role of RH on surface adsorbed species is also studied.

Limonene, a terpene commonly found in the indoor environment, is an active ingredient in a variety of consumer products such as cleaning products and odorants.^{10,11} The average reported indoor concentration of limonene is 5-15 ppb^{12,13}, however, the concentration can escalate up to 175 ppb immediately following product use.¹¹ Limonene also has the potential to form secondary organic aerosols (SOA) via reactions with oxidants such as ozone because it is an unsaturated hydrocarbon.^{11,14} Given the ability of limonene

to interact with various components in indoor environments, we used limonene as one of our indoor gases of interest. Carvone (p-mentha-6,8-diene-2-one), an ingredient in turpentine balsam, can also be produced from limonene oxidation.^{15,16} Dihydromyrcenol (2,6-dimethyl-7-octen-2-ol) has been widely used in fragrances for detergents, bath preparations, soaps as well as other household products.^{10,17,18} Ham et al. (2009) and Shu et al. (2012) investigated heterogeneous reactions between dihydromyrcenol and ozone on various indoor surfaces including glass and vinyl flooring tiles.^{18,19}

Furthermore, silica (SiO_2) was chosen as the model indoor surface in this study since it can represent the chemistry occurring on glass surfaces. The SiO_2 sample used in our studies is in powder form, having a high surface area to obtain information on surface adsorption mechanisms. The adsorption of organic molecules including DL-menthol, limonene, citronellal and carvone has been studied using flow microcalorimetry and infrared spectroscopy on preheated gel silicas to investigate the varying adsorptive properties owing to different functional groups.²⁰ In this work, we investigate the interaction type and strength of limonene vapor adsorption on SiO_2 , along with the kinetics of the adsorption/desorption process by integrating surface adsorption measurements obtained from vibrational spectroscopy with theoretical calculations and kinetic modeling. The methods developed, and kinetics model built for studying this molecule and surface can then be applied to other indoor organic vapors (such as dihydromyrcenol) and surfaces. We also studied the role of water vapor of adsorbed limonene on silica surfaces.

7.3 Experimental Section

The adsorption of limonene on silica surfaces as a function of limonene pressure at 296 ± 1 K, as well as from 298 to 308 K for temperature dependence experiments were studied using transmission Fourier transform infrared (FTIR) spectroscopy coupled with a modified Teflon coated infrared cell.^{21,22} In these experiments, approximately 5 mg of silica particles (Degussa, BET surface area of $230 \text{ m}^2 \text{ g}^{-1}$), was pressed onto one half of a tungsten grid held by two Teflon coated jaws in the FTIR cell compartment (177 ± 2 mL). The customized Teflon coated infrared cell is connected to a glass mixing chamber (1329 ± 2 mL) via Teflon tubing (75 cm long, with a diameter of 3.3 mm). The sample cell and mixing chamber were then evacuated for 6 hours using a turbo-molecular pump to clean the cell and the sample surface. After evacuation, the sample was exposed to the desired pressures of dry, gaseous limonene for 20 minutes under dry conditions ($\text{RH} < 1\%$). The gaseous limonene was produced from (+) - Limonene (>99%, Fisher Scientific) by degassing at least three times with consecutive freeze-pump-thaw cycles. Limonene adsorption/desorption at 296 K were studied at a series of 14 pressures (7, 8, 9, 10, 11, 14, 15, 16, 18, 20, 24, 25, 26, and 32 mTorr), with 3 replicas carried out at 8, 16, and 25 mTorr. Limonene adsorption on silica as a function of RH was carried out by introducing the desired amount of water vapor after 100 mTorr limonene adsorption reached equilibrium. To investigate the effects of temperature, the silica sample was held by a custom heated sample holder as described in a previous study.^{23,24} Thermocouple wires are welded to the tungsten grid to measure the temperature of the sample and the tungsten grid, with the sample coated on the grid resistively heated by an external heater. With the heated sample holder, the volume of the FTIR cell increased to $327 (\pm 3)$ mL. The coated surface samples

were evacuated for at least 6 hours and pre-heated to the desired temperature before introduction of limonene.

Prior to and after the exposure of limonene, the single-beam spectra of surface- and gas- phases (300 scans) were acquired at 296 K, as well as from 298 K to 308 K for temperature dependence experiments. The following temperatures were employed for these experiments: 298, 300.5, 303, 305.5 and 308 K. A resolution of 4 cm^{-1} was used over the spectral range of 800 to 4000 cm^{-1} . As silica is opaque below $\sim 1200\text{ cm}^{-1}$, spectra are shown only above 1200 cm^{-1} . During and following exposure to limonene, single-beam spectra (10 scans) of the respective silica and gas phase surfaces were automatically acquired using a Macro (OMNIC Macro Basics software) to study the kinetics of limonene adsorption until equilibrium was reached. The IR cell and sample surface were evacuated after adsorption had reached equilibrium. Desorption information was then obtained by acquiring single-beam spectra (10 scans) for 30 minutes. Absorbance spectra of limonene on the silica surface are reported as the difference in the silica spectra before and following exposure to limonene. Absorption bands attributed to gas phase limonene (measured through the blank half of the tungsten grid) were subtracted from the surface absorbance spectra to obtain the FTIR spectra of the adsorbed particle species loaded on the tungsten grid.

Other gaseous compounds used in this study were produced from (R) - (-) - Carvone (98%, Aldrich) and dihydromyrcenol ($\geq 99\%$, Sigma-Aldrich), respectively, by degassing at least three times with consecutive freeze-pump-thaw cycles.

7.4 Results and Discussion

7.4.1 Limonene Adsorption and Desorption Kinetics on Silica

The FTIR spectrum of high pressure gas-phase limonene (1.6 Torr) was collected at 296 K with a resolution of 4 cm^{-1} (see Figure 7.1). The spectrum and the vibrational modes of gas-phase limonene are well understood.²⁵ The modes are assigned as follows: 3084 cm^{-1} for C-H sp^2 stretching motion; 3015 cm^{-1} for C-H (from ring) sp^2 stretching mode; 2847 , 2861 , 2928 and 2974 cm^{-1} for C-H sp^3 symmetric and asymmetric stretching mode; 1782 cm^{-1} is assigned to a vibrational overtone; 1645 cm^{-1} for C=C (alkene) stretching motion; 1380 and 1451 cm^{-1} for CH_2 and CH_3 bending vibrations, respectively; 1151 cm^{-1} for C-H in plane rocking motion; 1020 and 1050 cm^{-1} for methyl rocking plus C-C stretching motions; and 891 cm^{-1} for CH_2 out of plane bending.²⁵⁻²⁹

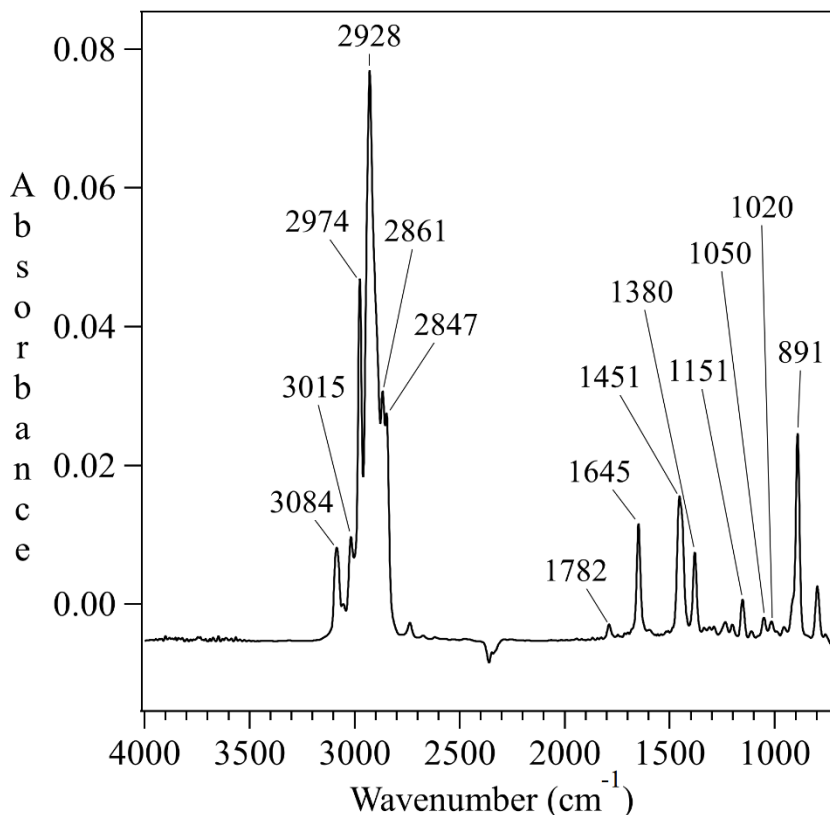


Figure 7.1. FTIR spectrum of gas phase limonene (1.6 Torr) from 800 to 4000 cm^{-1} .

7.4.1.1 Adsorption and Desorption Kinetics as a Function of Pressure

Infrared spectra for silica particles following exposure to gaseous limonene as a function of varying limonene pressure at 296 K are shown in Figure 7.2. Observed infrared absorption band frequencies are in good agreement with gas phase limonene vibrational frequencies (with only a few wavenumbers difference) and assigned as follows: C-H sp^2 stretching at 3074 cm^{-1} ; C-H (ring) sp^2 stretching at 3010 cm^{-1} ; C-H sp^3 stretching at 2834, 2860, 2922 and 2967 cm^{-1} ; C=C (alkene) stretching at 1645 cm^{-1} ; CH_2 and CH_3 bending at 1380, 1439 and 1451 cm^{-1} . The negative peak at 3742 cm^{-1} is due to silica surface isolated silanol groups hydrogen bonded with limonene, and the broad band near 3504 cm^{-1} is

Table 7.1. Vibrational mode assignment for limonene and adsorbed species on SiO₂ particle surfaces.

Mode assignment	Gas phase	SiO ₂	Literature
$\nu_s(\text{CH}, \text{sp}^2)$	3084, 3015(ring)	3074, 3010	3084, 3015 ²⁵
$\nu(\text{CH}, \text{sp}^3)$	2847, 2861, 2928, 2974	2834, 2860, 2922, 2967	2836 – 2966 ²⁸
Overtone	1782		1780 ²⁶
$\nu(\text{C}=\text{C},$ alkenene)	1645	1645	1645 ^{25,26,29}
$\delta(\text{CH}_2, \text{CH}_3)$	1380, 1451	1380, 1439, 1451	1377, 1453 ²⁶
$\rho(\text{C-H})$	1151		1162 ^{26,30}
Methyl rocking + C-C stretching	1020, 1050		1020, 1039 ²⁵
$\delta(\text{CH}_2)$	891		886 ^{26,29}

Additionally, we have investigated the kinetics of limonene adsorption/desorption on SiO₂ surfaces. Calibration of surface coverage was achieved by combining volumetric measurements with absorption band peak intensities for the adsorbed species as previously described.^{21,31} Kinetics measurements were carried out for 14 different pressures. Triplicate measurements have been applied to 8, 16 and 25 mTorr only. The time-dependent surface coverage (molecules/cm²) of 25 mTorr limonene adsorbed on silica particles is plotted in Figure 7.3(a). The time-dependent surface coverage for all 14 pressures can be found in Figure 7.3(b) – 7.3(o). Limonene was introduced to the system at $t = 0$ s, with increasing coverage observed until the adsorption of limonene on the surface was in equilibrium with the gas phase ($t > 600$ s). Desorption was then immediately initiated, and from that point

onward, the surface coverage of limonene decreased with time.

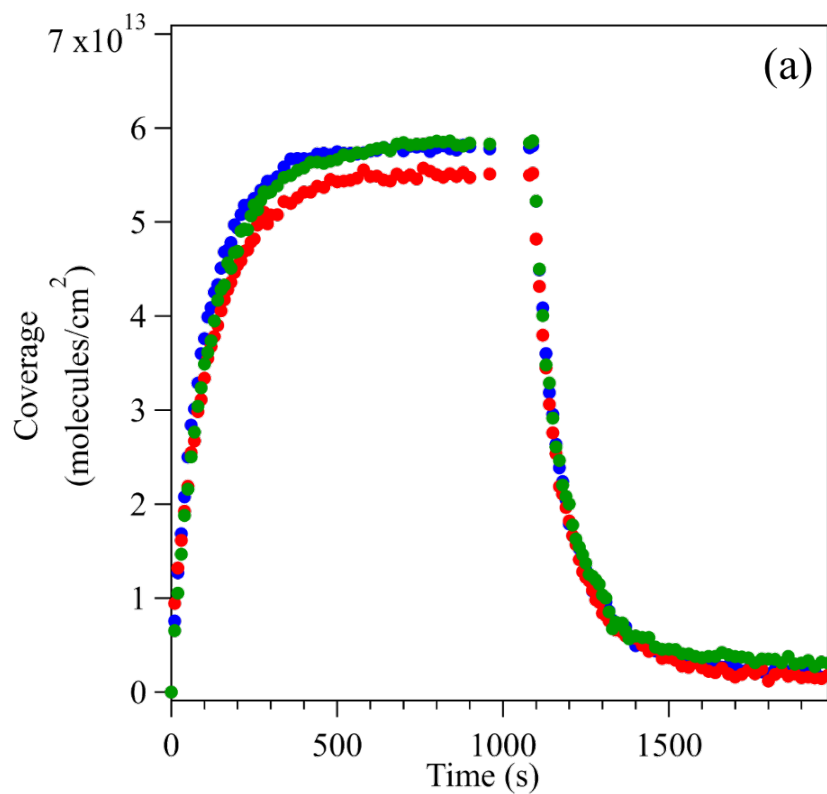


Figure 7.3. Temporal evolution of (a) 25 mTorr (3 replicates) limonene on silica. Gas-phase contribution has been subtracted.

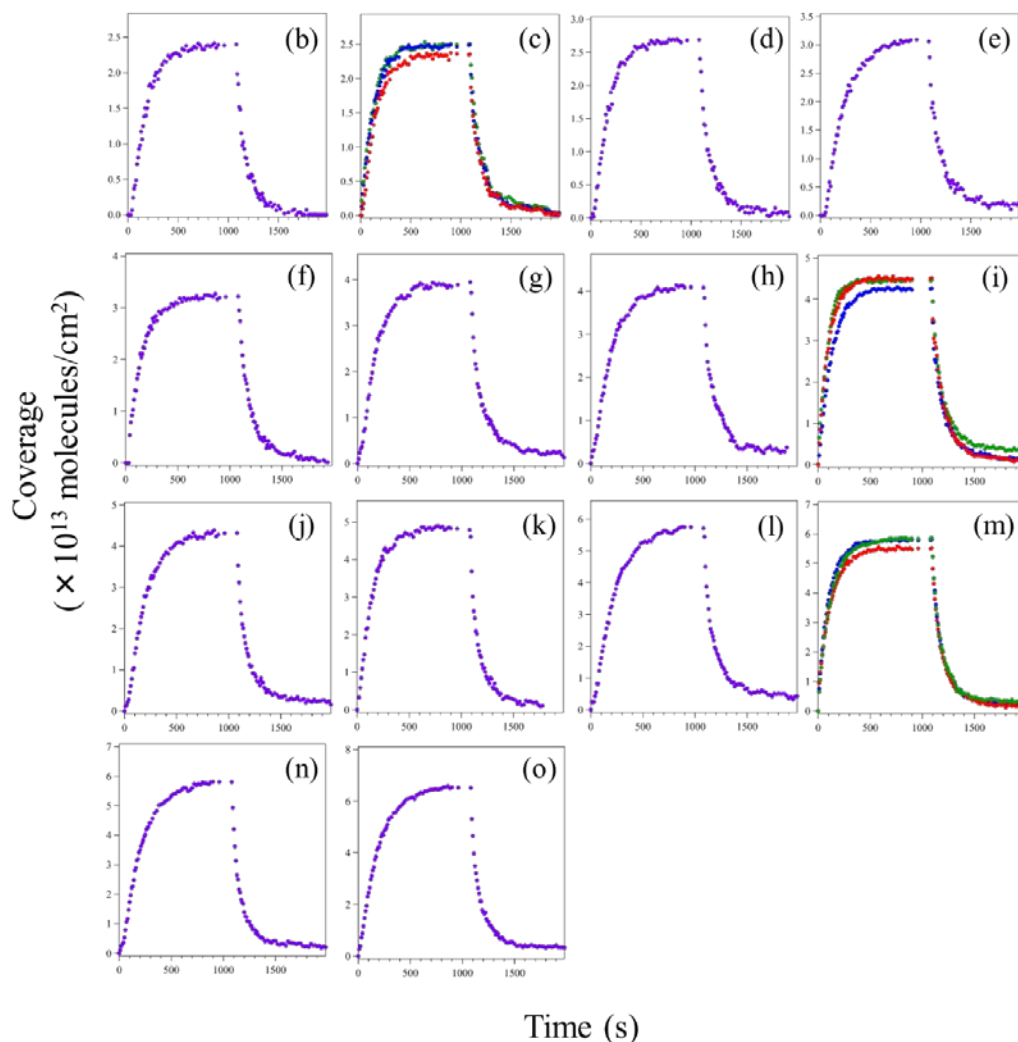


Figure 7.3. (continued) Temporal evolution of (b) – (o) 14 different pressures (7, 8, 9, 10, 11, 14, 15, 16, 18, 20, 24, 25, 26 and 32 mTorr) of limonene on silica. Gas-phase contribution has been subtracted.

The amount of limonene adsorbed on silica surface is determined by volumetric measurements, as described in previous studies.^{21,31} Equations (E8.1) to (E8.3) allow for calculation of the pressure represents the pressure calculation corresponding to the amount of adsorption which occurred on the silica surface. The amount of adsorption on the walls of the sample cell and mixing chamber, represented by the change of pressure in blank measurements (E8.1), has been subtracted from the amount adsorbed on the walls of the

system as well as the sample loading (represented by the change in pressure during experiments (E8.2):

$$P_{\text{blank, i}} - P_{\text{blank, eq}} = \Delta P_{\text{blank}} \quad (\text{E8.1})$$

$$P_{\text{exp, i}} - P_{\text{exp, eq}} = \Delta P_{\text{exp}} \quad (\text{E8.2})$$

$$\Delta P = \Delta P_{\text{exp}} - \Delta P_{\text{blank}} \quad (\text{E8.3})$$

$P_{\text{blank, i}}$ and $P_{\text{blank, eq}}$ represent the initial pressure and equilibrium pressure of blank measurements, respectively. In the same manner, $P_{\text{exp, i}}$ and $P_{\text{exp, eq}}$ represent the pressures, but for experimental measurements, and ΔP represents the change in pressure corresponding to the amount adsorbed by the sample only. By applying the ideal gas equation, this change in pressure can be converted to the number of molecules adsorbed on the surface. Note that this calibration was only done for a 100 mTorr initial introduction pressure. A conversion factor (in terms of molecules) is then applied by dividing the number of molecules adsorbed on the surface by the integrated absorbance peak area of the vibrational modes (from 2785 to 3115 cm^{-1}) using the spectrum collected at equilibrium (with the gas-phase contribution subtracted). This is subsequently used to determine the temporal evolution of the number of molecules adsorbed on the surface for other pressures, according to the integrated peak area which has been corrected for gas-phase diffusion (as described in Section 2.1.5) for the same vibrational modes. Surface coverages were obtained by dividing the number of molecules adsorbed by the total surface area of the sample (BET surface area \times mass of sample). Table 7.2 summarizes the observed coverages of limonene on silica for low initial pressures limonene.

Table 7.2. Calculated coverages of limonene on silica for different pressures using volumetric measurements.

Initial Pressure (mTorr)	Coverage ($\times 10^{13}$ molecules/cm ²)
7	2.4 ± 0.1
8	2.4 ± 0.1
9	2.7 ± 0.1
10	3.1 ± 0.2
11	3.2 ± 0.2
14	3.9 ± 0.2
15	4.1 ± 0.2
16	4.4 ± 0.2
18	4.3 ± 0.2
20	4.8 ± 0.2
24	5.7 ± 0.3
25	5.7 ± 0.3
26	5.8 ± 0.3
32	6.5 ± 0.3

The calculated surface coverage of limonene as a function of pressure is shown in Table 7.2. Assuming monolayer adsorption for the pressure range studied, the three-parameter BET equation (E7.4) can be reduced to the Langmuir equation (E7.5) when $n = 1$:

$$V = \frac{V_m c \frac{P}{P_0} \frac{1 - (n+1)\left(\frac{P}{P_0}\right)^n + n\left(\frac{P}{P_0}\right)^{n+1}}{1 - \left(\frac{P}{P_0}\right)}}{1 + (c-1)\left(\frac{P}{P_0}\right) - c\left(\frac{P}{P_0}\right)^{n+1}} \quad (\text{E7.4})$$

$$V = \frac{V_m c \left(\frac{P}{P_0}\right)}{1 + c\left(\frac{P}{P_0}\right)} \quad (\text{E7.5})$$

$$\frac{P}{N} = \frac{1}{N_s K} + \frac{P}{N_s} \quad (\text{E7.6})$$

The Langmuir equation (E7.5) could then be further simplified to a linear form where: P is pressure; N is surface coverage; N_s is the Langmuir saturation coverage; and K is the Langmuir constant as shown in (E7.6). Plotting $[P/N]$ versus pressure produces a linear

relationship as shown in Figure 7.4. The fitted linear equation can be correlated to (E7.6), the simplified linear relationship between P/N and P, where the slope can be defined as $1/N_s$ as shown in (E7.7).

$$\text{Slope} = \frac{1}{N_s} \text{ or } N_s = \frac{1}{\text{slope}} \quad (\text{E7.7})$$

According to Figure 7.4 and (E7.6), the Langmuir saturation coverage and Langmuir constant K of limonene adsorption on silica is determined to be $(1.37 \pm 0.07) \times 10^{14}$ molecules/cm² and (0.032 ± 0.02) respectively. Diaz et al. (2005) studied the adsorption of limonene and other organic molecules onto gel silicas and reported a theoretical monolayer coverage of limonene on the silica surface as $3.23 \mu\text{mol m}^{-2}$ (equivalent to 1.95×10^{14} molecules/cm²) obtained by molecular modeling.²⁰ Our experimental data of Langmuir saturated coverage is in good agreement with the calculated monolayer coverage. Experimentally, the molecules were not expected to tessellate perfectly on the silica surface since some active sites are inaccessible owing to the shape of molecules and hindering interactions. Therefore, the experimental coverage is expected to be lower than the theoretical value.²⁰

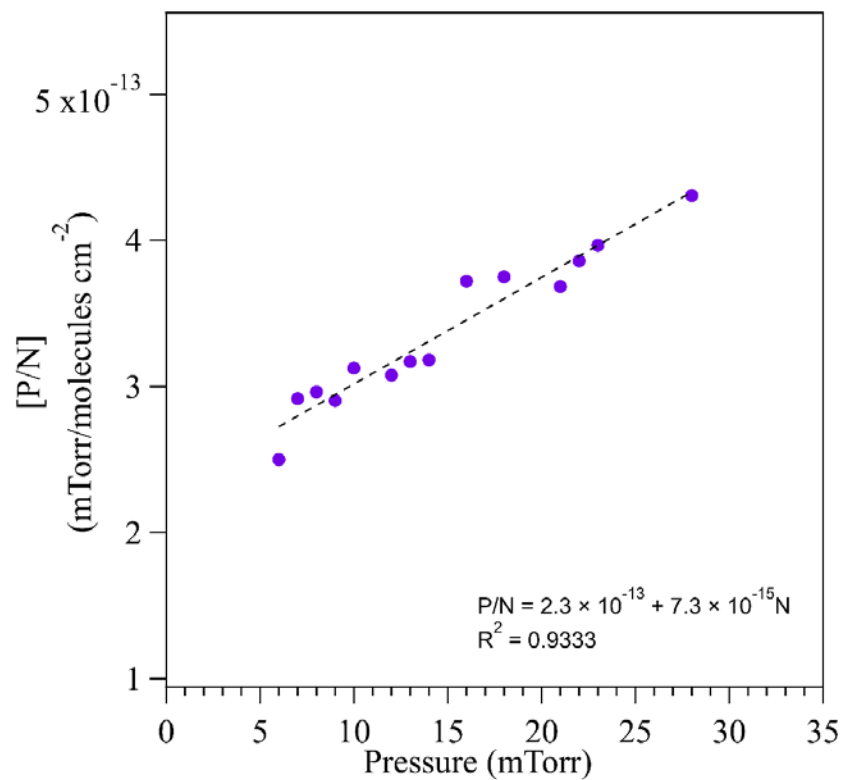


Figure 7.4. [P/N] versus pressure for limonene adsorbed on silica using integrated peak area from 2785 to 3115 cm^{-1} .

7.4.1.2 Adsorption and Desorption Kinetics as a Function of Temperature

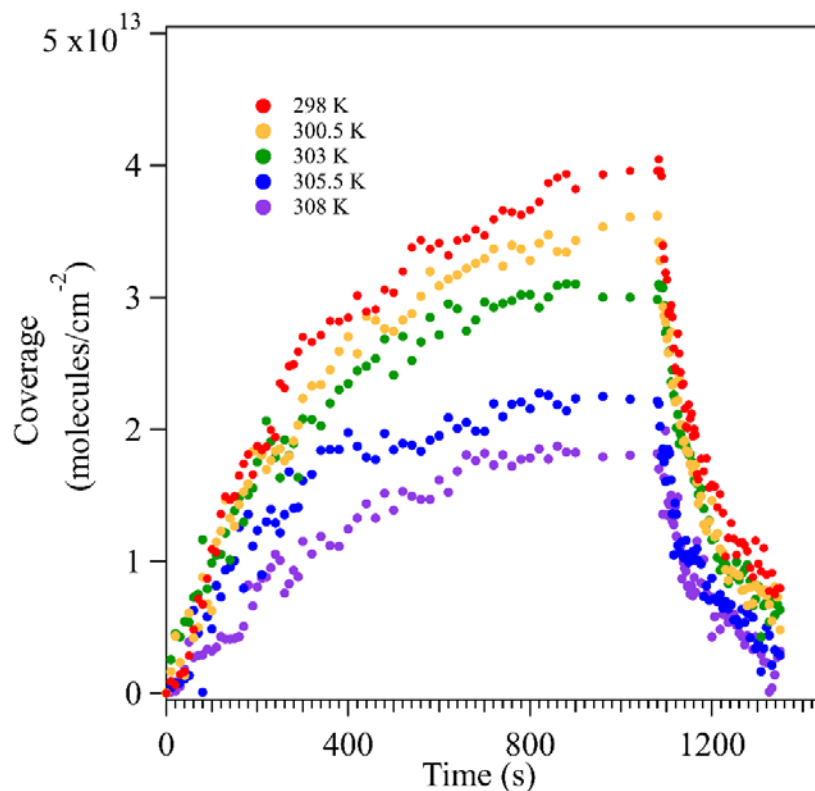
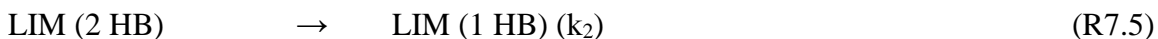
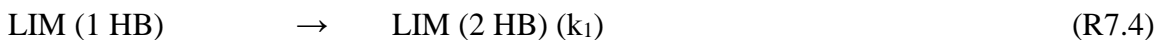
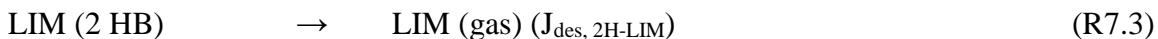
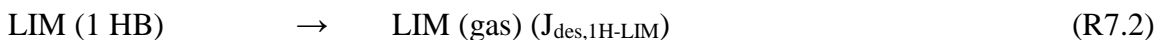


Figure 7.5. Temporal evolution of limonene (16 mTorr) adsorption and desorption for the following temperatures: 298, 300.5, 303, 305.5, 308 K (± 1 K).

Kinetics of limonene adsorption/desorption on the silica surface were also studied as a function of temperature (298, 300.5, 303, 305.5 and 308K). The time-dependent surface coverage (molecules/cm²) of limonene on silica is shown in Figure 7.5. Prior to the introduction of 16 mTorr limonene, the silica surface was heated to the desired temperature. The desorption process started after 1080 s, the time at which limonene adsorption reaches equilibrium. The limonene coverage at equilibrium decreases with temperature, suggesting that at higher temperatures, less limonene can be adsorbed on the silica. Kinetics modeling with energy parameters obtained from molecular dynamic simulations was applied to further understand the adsorption/desorption kinetics of limonene on silica.

7.4.1.3 Kinetics Modeling of Limonene Adsorption on Silica

The kinetic double-layer of aerosol surface chemistry and gas-particle interactions (K2-SURF), previously described in detail³², was used to reproduce experimental measurements of adsorbed limonene concentrations on a silica surface as a function of pressure and temperature (as shown in Section 7.3.1.1 and 7.3.1.2). Figure 7.6 shows the adsorption mechanism employed in this model, which involves a multi-step mechanism, not just a simple adsorption/desorption process. Adsorbed limonene could be either bound to the surface by one or two hydrogen bonds and the interconversion between the singly and doubly hydrogen bound limonene was explicitly treated in the model. The first-order desorption rate coefficient was assumed to follow Arrhenius kinetics. The gas-phase limonene pressure in the reaction cell as a function of time was constrained to experimental measurements. It was also assumed that gas-phase diffusion into the silica matrix, which was ~150 μm thick, was fast and therefore did not affect the measured adsorption and desorption kinetics. In the mechanism below, gas molecules (limonene(LIM)) are proposed to undergo adsorption on the surface forming one or two hydrogen bonds (HB) (R7.1). These molecules can then thermally desorb back to the gas phase (R7.2 and R7.3) or switch between one or two hydrogen bonds (R7.4 and R7.5):



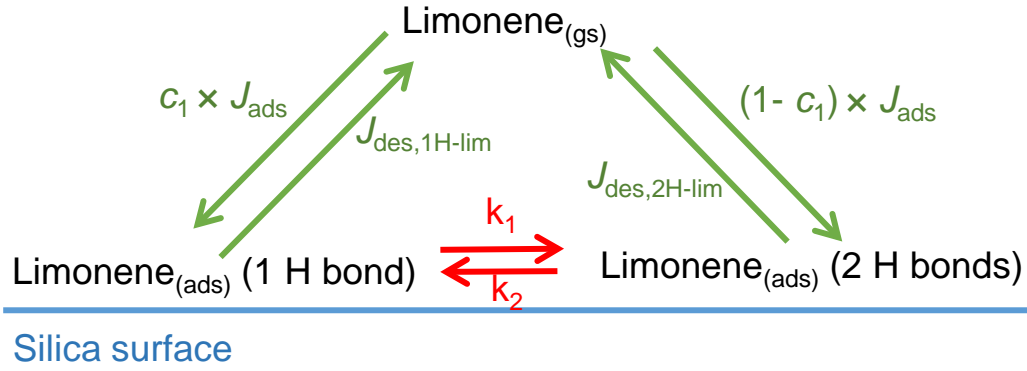


Figure 7.6. Schematic of the K2-SURF model for adsorption and desorption of limonene to a silica surface. The subscripts ‘ads’ and ‘gs’ represent adsorbed molecules and near surface gas-phase molecules, respectively. J_{ads} is the adsorption flux which is equal to $\alpha_{s,0,lim} \times W/4 \times (1-\theta) \times [Lim_{(gs)}]$ while J_{des} is desorption flux which is equal to $(1/\tau_{d,lim}) \times [Lim_{(ads)}]$. W is the mean thermal velocity and θ is the surface coverage. A description of all other parameters can be found in Table 1. (From Dr. Pascale Lakey)

In the mechanism,

$$J_{ads} = \frac{\alpha_{s,0,lim} \times W}{4 \times (1-\theta) \times [Limonene(g_s)]} \quad (E7.6), \text{ and}$$

$$J_{des} = \frac{1}{\tau_{d,lim}} \times [Limonene(ads)] \quad (E7.7),$$

where: $\alpha_{s,0,lim}$ is the initial surface mass accommodation; W is the mean thermal velocity of limonene; $\tau_{d,lim}$ is the desorption lifetime on the surface in the absence of surface reaction and surface-bulk transport; θ is the surface coverage, equivalent to $([limonene (1 HB)] + [limonene (2 HB)]) \times \sigma_{limonene}$, $\sigma_{limonene}$ represents the average space that one adsorbed limonene takes up on the surface; and k_1 and k_2 are rate constants for the reversible process (R7.4 and R7.5).

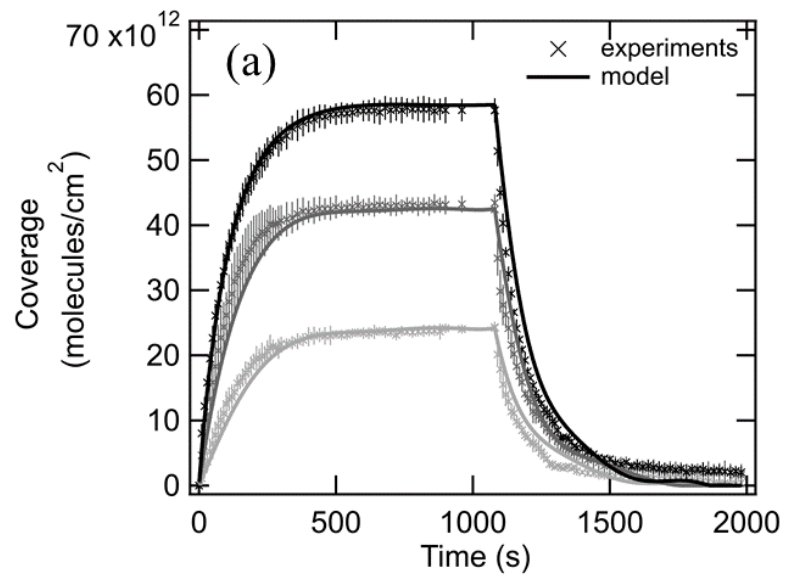


Figure 7.7. (a) Example of experimental kinetics data (×) at 3 different pressures (8, 16 and 25 mTorr, triplicate measurements) fitted with K2-SURF model (—). (Fitted curve from Dr. Pascale Lakey)

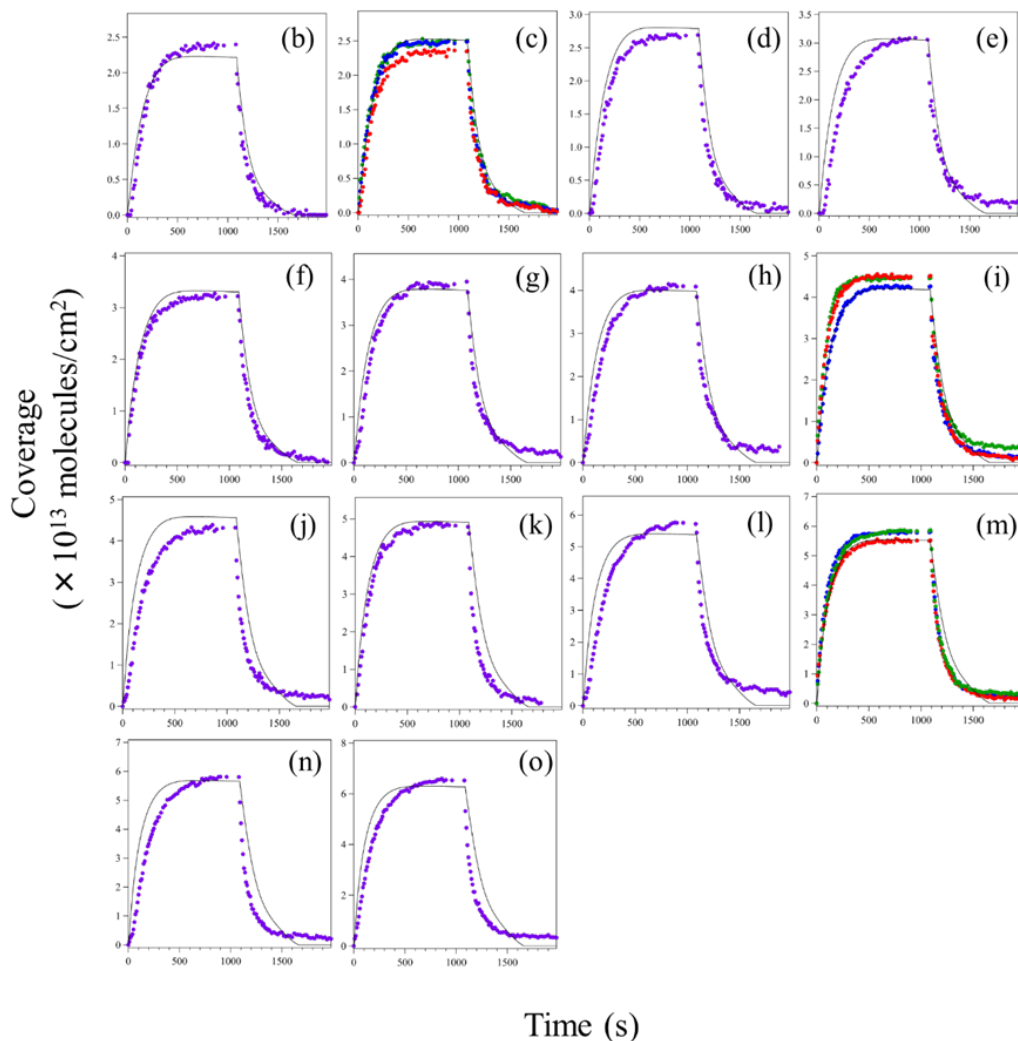


Figure 7.7. (continued) (b) – (o) Experimental kinetics data (•) for 14 different pressures: 7, 8, 9, 10, 11, 14, 15, 16, 18, 20, 24, 25, 26 and 32 mTorr limonene on silica, respectively, fitted with the K2–SURF model (—). (Fitted curve from Dr. Pascale Lakey)

The best-fit curves for some of the experimental kinetics data using the proposed two-step mechanism are shown in Figure 7.6. As evident from Figure 7.7, the modeling can accurately predict our experimental results. The best-fit parameters obtained from the model are summarized in Table 7.3. The K2-SURF model and the proposed mechanism fit our experimental kinetics data very well using the given kinetic parameters including the

desorption lifetime (T_d) and effective adsorption enthalpy (ΔH_{ads}) (obtained from the fitting)

Table 7.3. Parameters used in the K2-SURF model. (From Dr. Pascale Lakey)

Parameter	Parameter description	Parameter value
$\alpha_{s,0,\text{lim}}$	surface mass accommodation coefficient on an adsorbate-free surface	1
$\tau_{d,\text{lim}}$	lifetime of limonene on the surface	2.3×10^4 ns (Figure 7.7: 8, 16, 25 mTorr) 2.6×10^4 ns (Figure 7.7 other pressures) *
$k_{\text{lim},1\text{H},2\text{H}}$	first-order rate coefficient for the conversion of singly hydrogen bound limonene to doubly hydrogen bound limonene	1×10^{12} s ⁻¹ **
$k_{\text{lim},2\text{H},1\text{H}}$	first-order rate coefficient for the conversion of doubly hydrogen bound limonene to singly hydrogen bound limonene	1×10^{10} s ⁻¹ ***
σ_{lim}	effective adsorption cross-section of a limonene molecule	0.55 nm ² (Figure 7.7: 8, 16, 25 mTorr) 0.79 nm ² (Figure 7.7 other pressures and Figure 7.8)
c_1	fraction of limonene adsorbed as singly hydrogen bonded, (1- c_1) is the fraction adsorbed as doubly hydrogen bonded.	0.5

* For simplicity, the same value is assumed for singly and doubly hydrogen bonded limonene. Also note that these values are for room temperature (~296 K). At other temperatures the following equation is used: $(1/\tau_{d,\text{lim}}) = \exp(-6423 \times (1/T) + 32.24)$.

** The activation energy associated with this rate coefficient is 5.7 kJ mol^{-1} assuming a pre-exponential factor of $1 \times 10^{13} \text{ s}^{-1}$.

*** The activation energy associated with this rate coefficient is 17.0 kJ mol^{-1} assuming a pre-exponential factor of $1 \times 10^{13} \text{ s}^{-1}$.

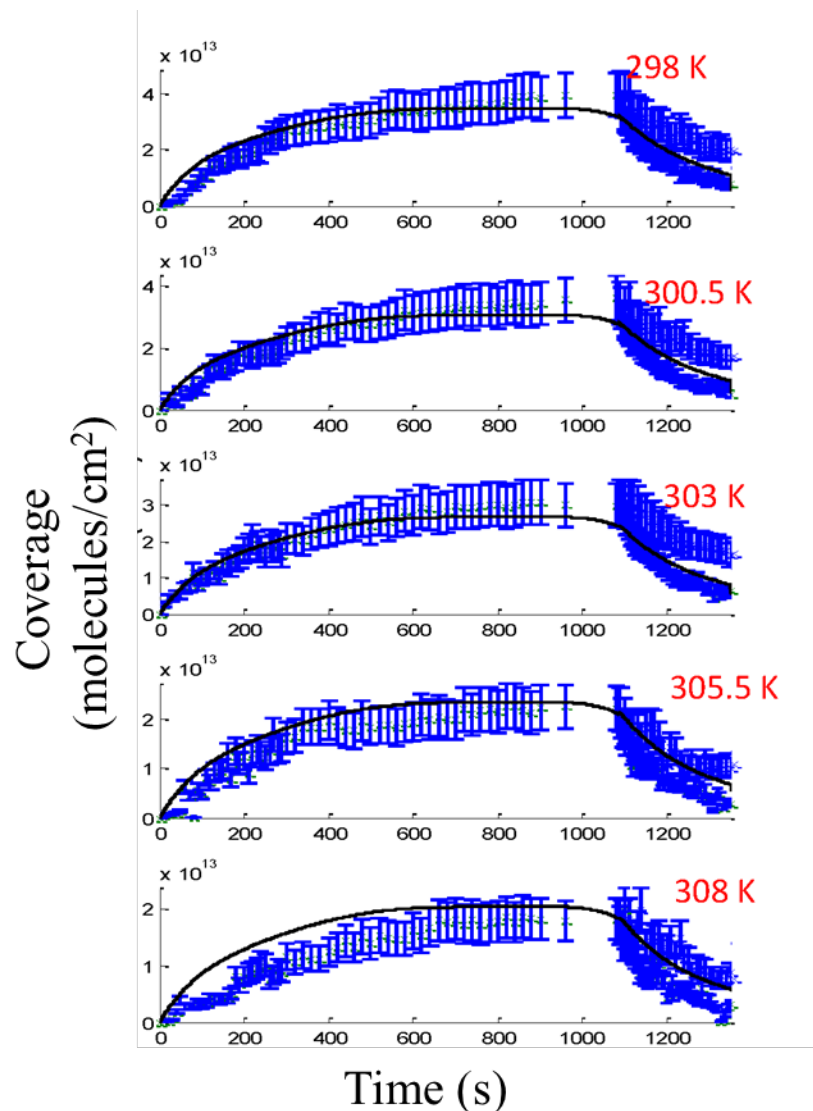


Figure 7.8. Adsorbed limonene concentrations on silica as a function of time at an equilibrium pressure of 16 mTorr and at five different temperatures (a) 298 K, (b) 300.5 K, (c) 303 K, (d) 305.5 K and (e) 308 K. A 20% error has been assumed for the adsorption part of the graphs while for the desorption part of the graphs a range of values are shown, representing experimental uncertainty. (From Dr. Pascale Lakey)

Figure 7.8 shows experimental data and model lines for limonene adsorption and desorption onto a silica surface as a function of time for different temperatures. Similar to the previous data, the model limonene gas-phase concentration as a function of time was

constrained to experimental measurements. The decrease in the maximum adsorbed limonene concentration as the temperature increases can be explained by the first-order desorption rate coefficient following Arrhenius kinetics. The Arrhenius equation which was used to fit the data ($1/\tau_{d,\text{lim}} = \exp(-6423 \times (1/T) + 32.24)$) had a pre-exponential factor (A) which was fixed to $1 \times 10^{14} \text{ s}^{-1}$, allowing the adsorption enthalpy (ΔH_{ads}) to be calculated as $-53.4 \text{ kJ mol}^{-1}$. This is consistent with the pressure data, as when setting A to equal $1 \times 10^{14} \text{ s}^{-1}$ the value of ΔH_{ads} can be calculated as $-(53.0 - 53.4 \text{ kJ mol}^{-1})$. The values of ΔH_{ads} are larger than may be expected for purely physisorbed molecules, although this may be due to hydrogen bonding, and the values are lower than would be expected for strongly chemisorbed species.

7.4.2 Limonene Adsorption as a Function of RH

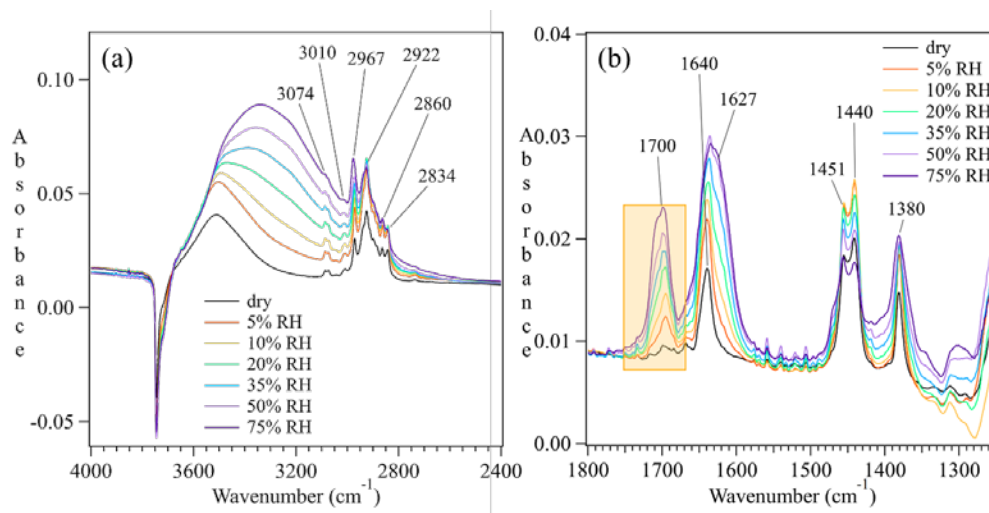


Figure 7.9. FTIR spectra (a) 2400 to 4000 cm^{-1} and (b) 1250 to 1800 cm^{-1} for silica particles following initial exposure to 100 mTorr limonene, then water vapor at varying RH (5%, 10%, 20%, 35%, 50% and 75% RH). The peak at 1700 cm^{-1} increases as a function of RH (highlighted in light yellow), suggesting an increasing formation of oxidized with RH.

The role of adsorbed water on limonene adsorption on SiO₂ was investigated systematically at the following RH values: < 1% (dry), 5%, 10%, 20%, 35%, 50%, and 75%. The amount of water adsorbed on the surface increases with RH (as shown in Figure 7.9) as suggested by the increase in the adsorbed water OH bending peak at 1627 cm⁻¹. Adsorbed limonene coverage decreases, indicative by the loss of peaks at 1440 and 1451 cm⁻¹, which can be assigned to the CH₂ and CH₃ bending mode of limonene. The CH stretching region from 2800 to 3000 cm⁻¹ also decreases with RH. The infrared peak centered at 1640 cm⁻¹ increases with RH indicating that other C=C species are formed on the surface in the presence of adsorbed water. Furthermore, a new absorption band at 1700 cm⁻¹ is observed, which increases with RH, most likely due to the carbonyl group stretching vibration from an oxidized adsorbed species such as carvone, carveol, limonene oxide(LimOx) or limonene-1, 2-diol (LimDiol).²⁸

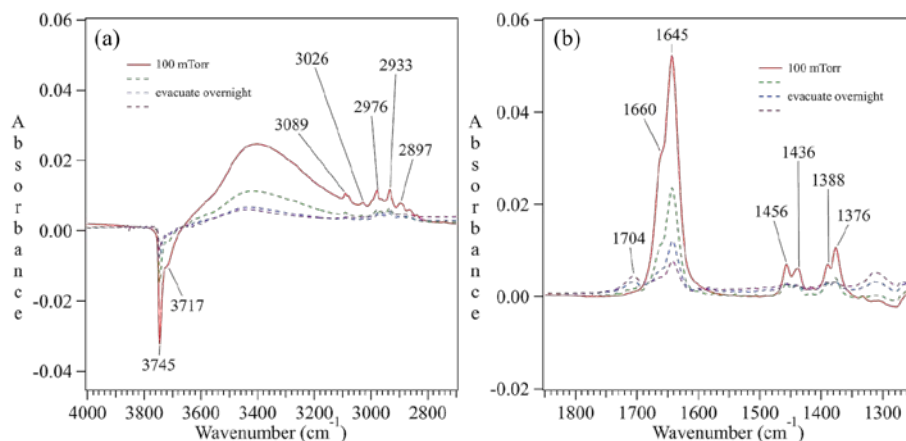


Figure 7.10. FTIR spectra over the spectral range (a) 2600 to 4000 cm⁻¹ and (b) 1250 to 1850 cm⁻¹ for silica particles following exposure to 100 mTorr carvone, then evacuation.

Carvone, a terpenoid, has been found in many essential oils and is most abundant in the oils from seeds of caraway, spearmint and dill.³³ Carvone adsorption on silica under

dry conditions has been investigated using FTIR to further confirm the oxidized products from the water-assisted oxidization process of adsorbed limonene on silica. As shown in Figure 7.10, carvone also molecularly adsorbs on silica surface via hydrogen bonding, as suggested by the loss of surface hydroxyl groups at 3745 cm^{-1} . Carvone adsorption is also a reversible process, with a decrease in adsorbed species observed after evacuation. However, after overnight evacuation, there remains a small amount of carvone on the silica surface, whereas limonene desorption is usually completed within 10 minutes of evacuation. Carvone desorption is a much slower process, suggesting that the interactions between carvone and surface hydroxyl groups are stronger in comparison to the hydrogen bonding occurring between limonene and silica surface. Infrared bands at 1645 cm^{-1} and 1660 cm^{-1} can be assigned to C=C and C=O stretching vibrations of the vinyl group and carbonyl groups, respectively.³⁴ However, since the carbonyl peak of adsorbed carvone is observed at 40 wavenumbers lower, the intense C=O band at 1700 cm^{-1} (shown in Figure 7.10) might result from other limonene oxidation products. Here, we confirmed that carvone is not the oxidation product of limonene on an inert surface (silica) in the presence of adsorbed water.

7.4.3 Adsorption and Desorption of Other Indoor Relevant Molecules

Infrared spectra (using transmission FTIR) obtained for the adsorption/desorption of dihydromyrcenol on silica particles as a function of varying dihydromyrcenol pressure at 296 K are shown in Figure 7.11. Observed infrared absorption band frequencies are assigned as follows: C-H sp^2 stretching at 3080 cm^{-1} ; C-H sp^3 stretching at 2848, 2868, 2911, 2938 and 2970 cm^{-1} ; C=C (alkene) stretching at 1642 cm^{-1} ; CH₂ and CH₃ bending at

1375, 1420, 1454 and 1466 cm^{-1} . The negative peak at 3745 cm^{-1} is due to adsorption of dihydromyrcenol on the silica surface via hydrogen bonding with isolated silanol groups. Absorption peaks due to adsorbed dihydromyrcenol decrease upon evacuation, while the negative peak at 3745 cm^{-1} attributed to isolated O-H groups, reappears, suggesting that adsorption of dihydromyrcenol on silica is also a reversible process.

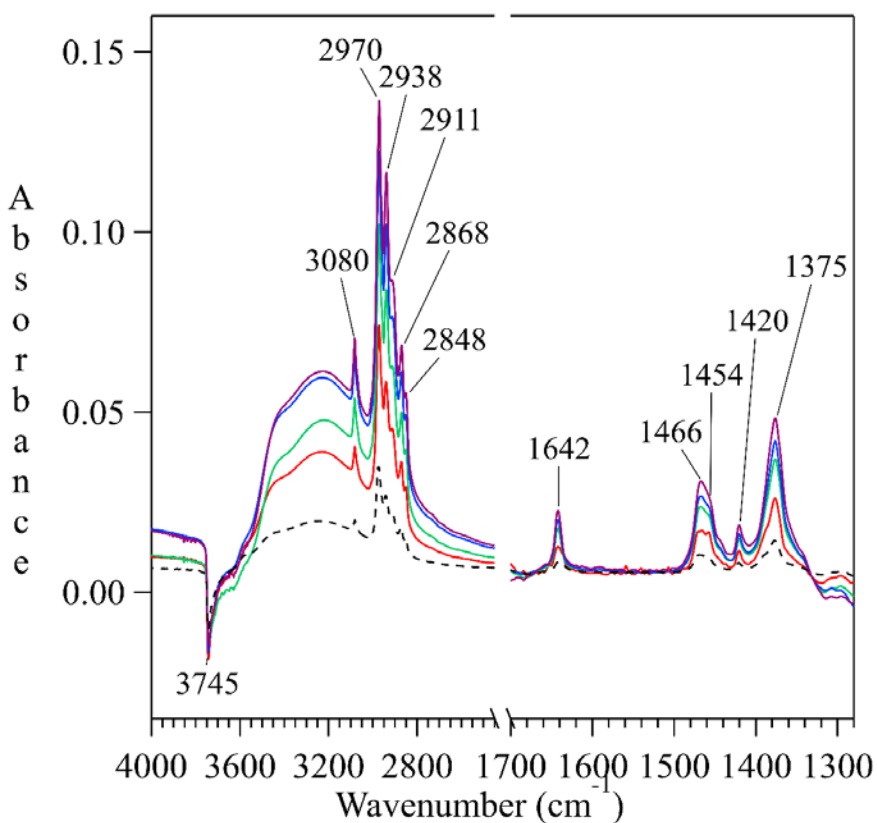


Figure 7.11. Absorbance spectra of dihydromyrcenol adsorbed on silica under dry conditions ($\text{RH} < 1\%$) as a function of dihydromyrcenol pressure (16, 34, 100 and 150 mTorr) in the 1280 ~ 4000 cm^{-1} spectral regions. The surface spectrum following evacuation is shown as a dashed line (---). Gas-phase dihydromyrcenol has been subtracted from these spectra.

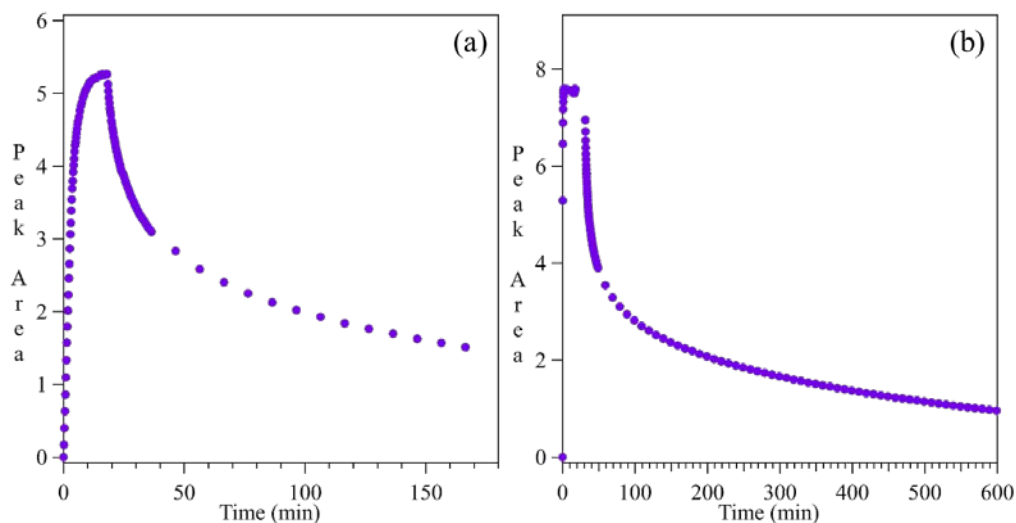


Figure 7.12. Temporal evolution of (a) 34 mTorr and (b) 150 mTorr dihydromyrcenol on silica. Gas-phase contribution has been subtracted.

The time-dependent integrated peak area (absorbance bands from 2800 to 3050 cm^{-1}) of 34 and 150 mTorr dihydromyrcenol adsorbed on silica particles is plotted in Figure 7.12. Dihydromyrcenol was introduced into the system at $t = 0\text{s}$, with increasing peak area observed. The desorption process started following equilibrium of dihydromyrcenol adsorption on the surface with the gas phase. Limonene desorption was usually completed within 10 minutes of the initiation of desorption, as discussed in Section 7.3.1. However, as shown in Figure 7.12, a fraction of the adsorbed dihydromyrcenol remained on the surface even after hours, suggesting that desorption of dihydromyrcenol is a much slower process in comparison to limonene. It has been reported that ozone reacts with α -terpineol on surfaces more than in the gas phase.³⁵ The low desorption rate of adsorbed dihydromyrcenol on surfaces results in a long lifetime and therefore, can be further oxidized by various oxidants present in the indoor environment.

7.5 Conclusion and Implications for Indoor Air

Limonene is a common terpene found in the indoor environment, and its interaction with indoor oxidants, such as ozone, can form secondary organic aerosols. However, the detailed chemistry between limonene and indoor surfaces is lacking in knowledge. In this study, transmission FTIR spectroscopy was used to investigate the heterogeneous adsorption and desorption of limonene on SiO₂ under dry conditions. Uptake of limonene on the silica surface is found to be a molecular, reversible process, via hydrogen bonding between limonene and surface hydroxyl groups on the silica surface. The kinetics of the limonene adsorption/desorption processes have been investigated using a combination of surface experimental measurements obtained from vibrational spectroscopy, kinetic modeling, as well as theoretical calculations. The K2-SURF model and the proposed mechanism are in good agreement with experimental coverage results obtained from vibrational spectroscopy. The kinetic model built here and developed methods could be applied to study other relevant indoor organic vapors and surfaces.

Even though limonene adsorbed onto SiO₂ can eventually desorb back to the gas phase under dry conditions, we found that adsorbed limonene on SiO₂, an inert surface, can be oxidized in the presence of adsorbed water. The unsaturated products formed remain reactive on the surfaces and can be further reacts by various oxidants present in the indoor environment, leading to a much slower reversible/partially reversible adsorption having stronger surface interactions. Future work includes: identification of the detailed limonene oxidation products; elucidation of the reaction mechanisms using FTIR and Mass Spectrometry analysis and ¹⁸O-labeled water; and application of the methods developed

here to study limonene to further understand the adsorption/desorption kinetics of dihydromyrcenol as well as other indoor relevant gases on the silica surface.

7.6 Acknowledgement

This material is based on the work supported by the Alfred P. Sloan Foundation under grant number G-2017-9692. The contents of this study do not necessarily reflect the official views of the Alfred P. Sloan Foundation. The Alfred P. Sloan Foundation does not endorse the purchase of the commercial products used in this report. The dissertation author was the primary investigator of all experimental measurements and data analysis. The author would like to thank Dr. Pascale Lakey for kinetics modeling and Saleh Riahi for molecular dynamic simulations. Chapter 7, in full is currently being prepared for submission for publication of the material. Yuan Fang, Pascale Lakey, Saleh Riahi, Mona Shrestha, Andrew McDonald, Manabu Shiraiwa, Douglas J. Tobias, and Vicki H. Grassian. The dissertation author was the primary investigator and author of this material.

7.7 References

- (1) Nazaroff, W. W.; Goldstein, A. H. Indoor Chemistry: Research Opportunities and Challenges. *Indoor Air* **2015**, *25* (4), 357–361.
- (2) Morrison, G. Interfacial Chemistry in Indoor Environments. *Environ. Sci. Technol.* **2008**, *42* (10), 3495–3499.
- (3) Singer, B. C.; Hodgson, A. T.; Hotchi, T.; Ming, K. Y.; Sextro, R. G.; Wood, E. E.; Brown, N. J. Sorption of Organic Gases in Residential Rooms. *Atmos. Environ.* **2007**, *41* (15), 3251–3265.
- (4) Weschler, C. J.; Carslaw, N. Indoor Chemistry. *Environ. Sci. Technol.* **2018**, *52* (5), 2419–2428.

- (5) Gligorovski, S.; Weschler, C. J. The Oxidative Capacity of Indoor Atmospheres. *Environ. Sci. Technol.* **2013**, *47* (24), 13905–13906.
- (6) Waring, M. S.; Wells, J. R. Volatile Organic Compound Conversion by Ozone, Hydroxyl Radicals, and Nitrate Radicals in Residential Indoor Air: Magnitudes and Impacts of Oxidant Sources. *Atmos. Environ.* **2015**, *106* (3), 382–391.
- (7) Atkins, D. H. F.; Lee, D. S. Indoor Concentrations of Ammonia and the Potential Contribution of Humans to Atmospheric Budgets. *Atmos. Environ. Part A. Gen. Top.* **1993**, *27* (1), 1–7.
- (8) Ongwande, M.; Morrison, G. C. Influence of Ammonia and Carbon Dioxide on the Sorption of a Basic Organic Pollutant to Carpet and Latex-Painted Gypsum Board. *Environ. Sci. Technol.* **2008**, *42* (15), 5415–5420.
- (9) Ongwande, M.; Chatsuvan, T.; Suksawas Na Ayudhya, W.; Morris, J. Understanding Interactions in the Adsorption of Gaseous Organic Compounds to Indoor Materials. *Environ. Sci. Pollut. Res.* **2017**, *24* (6), 5654–5668.
- (10) Nazaroff, W. W.; Weschler, C. J. Cleaning Products and Air Fresheners: Exposure to Primary and Secondary Air Pollutants. *Atmos. Environ.* **2004**, *38* (18), 2841–2865.
- (11) Wainman, T.; Zhang, J.; Weschler, C. J.; Lioy, P. J. Ozone and Limonene in Indoor Air: A Source of Submicron Particle Exposure. *Environ. Health Perspect.* **2000**, *108* (12), 1139–1145.
- (12) Wolkoff, P.; Wilkins, C. K.; Clausen, P. A.; Nielsen, G. D. Organic Compounds in Office Environments - Sensory Irritation, Odor, Measurements and the Role of Reactive Chemistry. *Indoor Air* **2006**, *16* (1), 7–19.
- (13) Tamás, G.; Weschler, C. J.; Toftum, J.; Fanger, P. O. Influence of Ozone-Limonene Reactions on Perceived Air Quality. *Indoor Air* **2006**, *16* (3), 168–178.
- (14) Weschler, C. J.; Shields, H. C. Indoor Ozone/Terpene Reactions as a Source of Indoor Particles. *Atmos. Environ.* **1999**, *33* (15), 2301–2312.
- (15) Uhde, E.; Salthammer, T. Impact of Reaction Products from Building Materials and Furnishings on Indoor Air Quality-A Review of Recent Advances in Indoor Chemistry. *Atmos. Environ.* **2007**, *41* (15), 3111–3128.
- (16) Clausen, P. A.; Wilkins, C. K.; Wolkoff, P.; Nielsen, G. D. Chemical and Biological Evaluation of a Reaction Mixture of R-(+)-Limonene/Ozone. *Environ. Int.* **2001**, *26* (7–8), 511–522.
- (17) Colombo, A.; De Bortoli, M.; Knöppel, H.; Schauenburg, H.; Vissers, H. Small Chamber Tests and Headspace Analysis of Volatile Organic Compounds Emitted from Household Products. *Indoor Air* **1991**, *1* (1), 13–21.

- (18) Shu, S.; Morrison, G. C. Rate and Reaction Probability of the Surface Reaction between Ozone and Dihydromyrcenol Measured in a Bench Scale Reactor and a Room-Sized Chamber. *Atmos. Environ.* **2012**, *47*, 421–427.
- (19) Ham, J. E.; Raymond Wells, J. Surface Chemistry of Dihydromyrcenol (2,6-Dimethyl-7-Octen-2-Ol) with Ozone on Silanized Glass, Glass, and Vinyl Flooring Tiles. *Atmos. Environ.* **2009**, *43* (26), 4023–4032.
- (20) Diaz, L.; Liauw, C. M.; Edge, M.; Allen, N. S.; McMahon, A.; Rhodes, N. Investigation of Factors Affecting the Adsorption of Functional Molecules onto Gel Silicas: 1. Flow Microcalorimetry and Infrared Spectroscopy. *J. Colloid Interface Sci.* **2005**, *287* (2), 379–387.
- (21) Goodman, A. L.; Bernard, E. T.; Grassian, V. H. Spectroscopic Study of Nitric Acid and Water Adsorption on Oxide Particles: Enhanced Nitric Acid Uptake Kinetics in the Presence of Adsorbed Water. *J. Phys. Chem. A* **2001**, *105* (26), 6443–6457.
- (22) Fang, Y.; Tang, M.; Grassian, V. H. Competition between Displacement and Dissociation of a Strong Acid Compared to a Weak Acid Adsorbed on Silica Particle Surfaces: The Role of Adsorbed Water. *J. Phys. Chem. A* **2016**, *120* (23), 4016–4024.
- (23) Goodman, A. L.; Miller, T. M.; Grassian, V. H. Heterogeneous Reactions of NO₂ on NaCl and Al₂O₃ Particles. *J. Vac. Sci. Technol. A Vacuum, Surfaces, Film.* **1998**, *16* (4), 2585–2590.
- (24) Miller, T. M.; Grassian, V. H. Adsorption and Decomposition of Nitrous Oxide on Zirconia Nanoparticles. *Colloids Surfaces A Physicochem. Eng. Asp.* **1995**, *105* (1), 113–122.
- (25) Partal Ureña, F.; Moreno, J. R. A.; López González, J. J. Conformational Study of (R)-(+)-Limonene in the Liquid Phase Using Vibrational Spectroscopy (IR, Raman, and VCD) and DFT Calculations. *Tetrahedron Asymmetry* **2009**, *20* (1), 89–97.
- (26) O'Connor, R. T.; Goldblatt, L. A. Correlation of Ultraviolet and Infrared Spectra of Terpene Hydrocarbons. *Anal. Chem.* **1954**, *26* (11), 1726–1737.
- (27) Wolkoff, P.; Clausen, P. A.; Larsen, S. T.; Hammer, M.; Nielsen, G. D. Airway Effects of Repeated Exposures to Ozone-Initiated Limonene Oxidation Products as Model of Indoor Air Mixtures. *Toxicol. Lett.* **2012**, *209* (2), 166–172.
- (28) Lederer, M. R.; Staniec, A. R.; Coates Fuentes, Z. L.; Van Ry, D. A.; Hinrichs, R. Z. Heterogeneous Reactions of Limonene on Mineral Dust: Impacts of Adsorbed Water and Nitric Acid. *J. Phys. Chem. A* **2016**, *120* (48), 9545–9556.
- (29) Subramanian, A.; Rodriguez-Saona, L. Chapter 7 - Fourier Transform Infrared (FTIR) Spectroscopy; Sun, D.-W. B. T.-I. S. for F. Q. A. and C., Ed.; Academic Press: San Diego, 2009; pp 145–178.

- (30) Plath, K. L.; Axson, J. L.; Nelson, G. C.; Takahashi, K.; Skodje, R. T.; Vaidaa, V. Gas-Phase Vibrational Spectra of Glyoxylic Acid and Its Gem Diol Monohydrate. Implications for Atmospheric Chemistry. *React. Kinet. Catal. Lett.* **2009**, *96* (2), 209–224.
- (31) Tang, M.; Larish, W. A.; Fang, Y.; Gankanda, A.; Grassian, V. H. Heterogeneous Reactions of Acetic Acid with Oxide Surfaces: Effects of Mineralogy and Relative Humidity. *J. Phys. Chem. A* **2016**, *120* (28), 5609–5616.
- (32) Shiraiwa, M.; Garland, R. M.; Pöschl, U. Kinetic Double-Layer Model of Aerosol Surface Chemistry and Gas-Particle Interactions (K2-SURF): Degradation of Polycyclic Aromatic Hydrocarbons Exposed to O₃, NO₂, H₂O, OH and NO₃. *Atmos. Chem. Phys.* **2009**, *9* (24), 9571–9586.
- (33) De Carvalho, C. C. C. R.; Da Fonseca, M. M. R. Carvone: Why and How Should One Bother to Produce This Terpene. *Food Chem.* **2006**, *95* (3), 413–422.
- (34) Avilés Moreno, J. R.; Partal Ureña, F.; López González, J. J. Conformational Landscape in Chiral Terpenes from Vibrational Spectroscopy and Quantum Chemical Calculations: S-(+)-Carvone. *Vib. Spectrosc.* **2009**, *51* (2), 318–325.
- (35) Shu, S.; Morrison, G. C. Surface Reaction Rate and Probability of Ozone and Alpha-Terpineol on Glass, Polyvinyl Chloride, and Latex Paint Surfaces. *Environ. Sci. Technol.* **2011**, *45* (10), 4285–4292.

CHAPTER 8 THE DRIVING FORCE BEHIND ADSORPTION OF HYDROPHOBIC MOLECULES ON HYDROPHILIC SURFACES

8.1 Abstract

The driving force behind adsorption of hydrophobic molecules, such as limonene, on hydrophilic surfaces (SiO_2) is studied using a combination of vibrational spectroscopy measurements and molecular dynamic (MD) simulation modeling. Limonene adsorption on silica surfaces is found to form 1 or 2 hydrogen bonds of sp^2 unsaturated carbon with silica surface hydroxyl groups. In addition, the hydrogen bond between limonene and silica surfaces shifts to lower wavenumbers as limonene coverage increases. Other cyclic molecules, such as cyclohexane, benzene and cyclohexene were studied to further understand the interactions between hydrophobic molecules and hydrophilic surfaces. All three molecules adsorb on silica under dry conditions while benzene is found to have the most intense interaction with silica at lower pressures. The π -cloud from benzene is involved in adsorption, while hydroxyl groups from silica are found to point to the center of the π -cloud instead of a single unsaturated carbon. Owing to the unsaturated sp^2 carbons, cyclohexene readily adsorbed on silica. For the adsorption of cyclohexane on silica, no specific interaction has been found from MD simulations. Adsorption of limonene on other indoor relevant surfaces including gypsum and TiO_2 were also investigated by vibrational spectroscopy.

8.2 Introduction

People spend approximately 90% of their total time indoors, which consists of a myriad of surfaces such as walls, windows and floors with a large surface-to-volume (S/V) ratios.^{1,2} Indoor interfacial chemistry can play a significant role due to the large S/V ratios and long reactive lifetimes.^{3,4} Indoor air chemistry can be affected by three main surface processes, including oxidation, acid-base reactions and adsorption/desorption.¹ Limonene, a terpene commonly found in the indoor environment, is widely used in consumer products such as cleaning products and odorants.^{5,6} Limonene concentrations can reach up to 175 ppb immediately following product use, with an average reported concentration of 5-15 ppb.⁶ Because limonene is an unsaturated hydrocarbon, it has the potential to form secondary organic aerosols (SOAs) when oxidized by oxidants such as ozone.^{6,7} The interaction type and strength of limonene adsorption/desorption kinetics on silica, a model indoor surface (represent glass) has been investigated using a combination of surface adsorption measurements from vibrational spectroscopy with theoretical calculations and kinetic modeling (details in Chapter 7). Limonene is found to reversibly adsorb on the silica surface by hydrogen bonding with surface hydroxyl groups. However, details of the formation of the hydrogen bond between limonene and hydroxyl groups from silica surface, is still unclear.

Adsorption of organic molecules on silica surfaces have been investigated by numerous studies.⁸⁻¹⁶ Interactions between surfaces and the adsorbed species may due to: (1) chemical bonding; (2) hydrogen bonding; (3) hydrophobic bonding; and (4) van der Waals force. Bondosz et al.⁹ and Magnacca et al.¹⁰ studied the adsorption of butane and butene on the silica as a function of temperature to investigate the chemical and physical

changes in the system. A model system of conjugated π -electron aromatic substitution on silica was proposed from the investigation of phenyl acetylene with Si(100)-2 \times 1.¹¹ Surface molecular macroclusters (hydrogen bonds between the silanol groups and -OH groups) were proposed by Mizukarni et al.¹² in their study of 1-,2-propanol and ethanol adsorption on silica surfaces. The adsorption of 4-picoline and piperidine onto amorphous SiO₂ surface were studied using vibrational sum frequency generation (SFG) spectroscopy.¹³ Weak hydrogen bonds formed between nitrogen atoms of 4-picoline and the hydrogen from surface hydroxyl groups, with protonation of piperidine molecules is observed for piperidone chemisorbed on silica.¹³ Zhao et al.¹⁴ investigated the adsorption isotherms for aromatic molecules on silica and proposed the possible formation of three hydrogen bonds between the silica surface and aromatic molecules: (i) π -electron of a benzene ring and the hydrogen atom from hydroxyl groups; (ii) oxygen from aromatics and hydrogen atoms of the silanol groups; (iii) hydrogen atom attached to the oxygen atom of aromatics and oxygen atoms of the silanol groups. Adsorption of cyclohexane and benzoic acid on pre-treated silica gel have been studied and cyclohexanone is proposed to vertically adsorb.¹⁵ In addition, flow microcalorimetry and infrared spectroscopy were used to study the effect of functional groups on the adsorption of dl-menthol, (R)-(+)-limonene, (\pm)-citronellal and carvone on calcined and uncalcined porous silica.¹⁶ Adsorption of limonene on silica was reported to be rather insignificant, with Diaz et al.¹⁶ suggesting no interaction between limonene and silanol groups as limonene contains no electronegative atoms. They also proposed that limonene could likely interact with silica surface by the π -bonding of C=C and p-d π -bonding system of the siloxane linkages. However, we observe hydrogen

bonding between adsorbed limonene and hydroxylated silica surfaces (see Chapter 7). To date, the formation of such hydrogen bonding is still lacking in knowledge.

In this work, we use a combination of spectroscopic experimental measurements (Transmission FTIR) and atomistic simulations (Ab initio molecular dynamics) to better understand the interactions between limonene on silica, as well as other molecular species, including cyclohexane, benzene and cyclohexene, which are structurally similar to limonene. Heterogeneous reactions between limonene and silica, as well as other indoor surfaces, such as TiO₂ (a component of self-cleaning surfaces and paints¹⁷⁻²⁰) and gypsum (represents walls) are also investigated in this study using attenuated total reflection (ATR) - FTIR. A greater understanding of the interactions between these molecules with surfaces can improve the current knowledge concerning the forces between other organic compounds adsorbed on silica and other indoor surfaces.

8.3 Methods

The adsorption of limonene on silica surfaces at 296 ± 1 K was studied using transmission Fourier transform infrared (FTIR) spectroscopy coupled with a modified Teflon coated infrared cell.^{21,22} In these experiments, approximately 5 mg of silica particles (Degussa, BET surface area of $230 \text{ m}^2 \text{ g}^{-1}$), was pressed onto one-half of a tungsten grid held by two Teflon coated jaws in the FTIR cell compartment. The sample cell was then evacuated for 6 hours using a turbo-molecular pump to clean the cell and the sample surface. After evacuation, the sample was exposed to the desired pressures of dry, gaseous limonene for 20 minutes under dry conditions ($\text{RH} < 1\%$). The gaseous limonene was

produced from (+) - Limonene (>99%, Fisher Scientific) by degassing at least three times with consecutive freeze-pump-thaw cycles.

Prior to and following the exposure of limonene, the single-beam spectra of surface- and gas- phases (300 scans) were acquired at 296 K. A resolution of 4 cm^{-1} was used over the spectral range of 800 to 4000 cm^{-1} . As silica is opaque below $\sim 1200\text{ cm}^{-1}$, spectra are shown only above 1200 cm^{-1} . The IR cell and sample surface were evacuated after adsorption had reached equilibrium. Absorbance spectra of limonene on the silica surface are reported as the difference in the silica spectra before and following exposure to limonene. Absorption bands attributed to gas-phase limonene (measured through the blank half of the tungsten grid) were subtracted from the surface absorbance spectra to obtain the FTIR spectra of the adsorbed particle species loaded on the tungsten grid. The adsorption of other three cyclic molecules (cyclohexane, benzene and cyclohexene) was studied using the same method above.

The adsorption of limonene on SiO_2 (Degussa), TiO_2 (P25, Sigma Aldrich) and gypsum ($\text{CaSO}_4 \cdot 2\text{H}_2\text{O}$, from MP Biomedicals) were studied using a custom-build flow system coupled with a single beam Thermo Nicolet 6700 FTIR Spectrometer, equipped with a liquid-nitrogen-cooled narrow-band mercury cadmium telluride (MCT) detector. The details of the flow system can be found elsewhere.²³ A commercially available purge air generator (Nano Purification Solutions, CO_2 Adsorption Dryer NDC-600) was used to purge the FTIR spectrometer and the sample compartment to reduce H_2O and CO_2 concentrations. Typically, an ATR-FTIR single beam spectrum was acquired by averaging 300 scans over the spectral region from 750 to 4000 cm^{-1} with a resolution of 4 cm^{-1} . A thin film (15 mg) of the sample (TiO_2 and $\text{CaSO}_4 \cdot 2\text{H}_2\text{O}$, respectively) was prepared by

suspending the particles in 1mL of Milli-Q water (Milli-Q Advantage A10 System, Millipore SAS, resistivity = 18.2 M Ω .cm, 298 K). The suspension was sonicated for at least 10 minutes and then applied to the ATR cell. The water was allowed to evaporate under dry air purge overnight in the sample compartment, allowing a uniform dispersion of particles on the cell. Spectra were referenced to the ATR-FTIR crystal without applying any sample under dry conditions (RH < 3%).

The gaseous compounds were produced from (+) - Limonene (>99%, Fisher Scientific), cyclohexane (99.9% Fisher Scientific), benzene (\geq 99.9%, Sigma Aldrich) and cyclohexene (99%, Sigma Aldrich), respectively, by degassing at least three times with consecutive freeze-pump-thaw cycles.

8.4 Results and Discussion

8.4.1 FTIR Studies and Ab Initio Molecular Dynamics Study for Limonene Adsorption on SiO₂

8.4.1.1 Experimental Results

Shown in Figure 8.1 are the comparison of gas phase limonene spectra and infrared spectra for hydroxylated silica particles following exposure to gaseous limonene at 1000 mTorr. Single-beam FTIR spectra of the gas and surface, respectively, were collected using a resolution of 4 cm⁻¹ over the spectral range of 800 – 4000 cm⁻¹ at 296 K, prior to and following exposure of the silica surface to gaseous limonene. A single spectrum was obtained by averaging 300 scans. By referencing single-beam spectra to the single beam spectrum collected prior to the introduction of gas phase limonene into the reaction cell, FTIR spectra of gas and surface species were obtained. The spectra of the silica particle

surfaces were obtained by subtracting out the IR absorption due to gas-phase species. For this set of experiments, dry conditions were employed ($\text{RH} < 1\%$) at room temperature (296 K). The negative peak at 3742 cm^{-1} is due to silica surface isolated silanol groups hydrogen-bonded with limonene, and the broad band near 3504 cm^{-1} is assigned to the hydrogen bonded Si-OH groups. Absorption peaks due to adsorbed limonene disappear upon evacuation, while the negative peak attributed to isolated O-H groups (at 3745 cm^{-1}) reappears, suggesting that limonene is molecularly adsorbed on the silica surface via a reversible process. Other absorbance bands due to limonene adsorption on silica has been discussed in detail in Chapter 7. As shown in Figure 8.1 and Table 8.1, not much absorbance bands shift has been observed between gas phase limonene and adsorbed limonene.

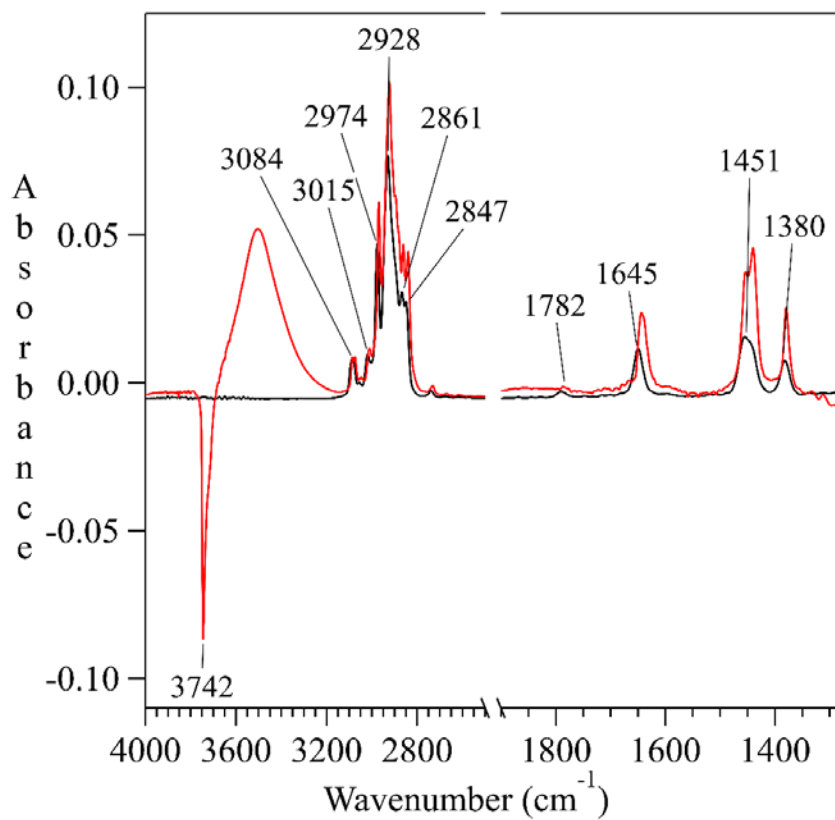


Figure 8.1. Absorbance spectra of 1000 mTorr limonene in gas phase (—) and adsorbed (—) on silica under dry conditions (RH < 1%) in the 1280 to 4000 cm⁻¹ spectral region. Gas-phase limonene has been subtracted from adsorbed limonene spectra.

Table 8.1. Vibrational mode assignment for limonene, cyclohexane, benzene and cyclohexene on SiO₂ particle surfaces.

Mode Assignment	Limonene		Cyclohexane		Benzene		Cyclohexene		
	Gas	Surface	Literature	Gas	Literature ^{24,25}	Gas	Literature ²⁶⁻²⁹	Gas	Literature ³⁰
$\nu_s(\underline{\text{C}}\text{H}, \text{sp}^2)$	3084, 3015(ring)	3074, 3010	3084, 3015			3091, 3046 (aromatic)	3100 – 3000	3030	3040, 3026
$\nu(\underline{\text{C}}\text{H}, \text{sp}^3)$	2847, 2861, 2928, 2974	2834, 2860, 2922, 2967	2836 – 2966	2933, 2862	2937, 2852, 2888			2934, 2850	2942, 2858
Overtone	1782		1780			1809	1815		
$\nu(\underline{\text{C}}=\text{C},$ alkene)	1645	1645	1645					1650	1660
$\delta(\underline{\text{C}}\text{H}_2, \text{CH}_3)$	1380, 1451	1380, 1439, 1451	1377, 1453	1456	1443, 1451, 1457	1482 (aromatic)	1479	1451	1450

The transmission FTIR spectra for limonene adsorption on silica at different coverages are shown in Figure 8.2. These spectra were obtained by referencing single-beam spectra of the surface to the gas phase single beam spectra collected prior to the introduction of gas-phase limonene. Baseline correction was applied to all absorbance spectra. Monolayer limonene coverage on silica was obtained using a Langmuir model as discussed in Chapter 7. As shown in Figure 8.2, the intensity of the sharp peak centered at 3742 cm^{-1} , which is attributed to the surface hydroxyl groups, decreases with increasing gaseous limonene coverage. This observation suggests that limonene interacted with the silica surface via hydrogen bonding with the surface hydroxyl groups. The broad band ranging from $3200 - 3700\text{ cm}^{-1}$, which can be assigned to the OH stretching mode from hydrogen bonding, also shifted with coverage, forming a peak centered at 3516 cm^{-1} at 110% coverage. This result indicates that bonded Si – OH groups red shifted at higher coverages. To better elucidate the interaction between limonene and the silica surface, we performed ab initio molecular dynamic (MD) studies.

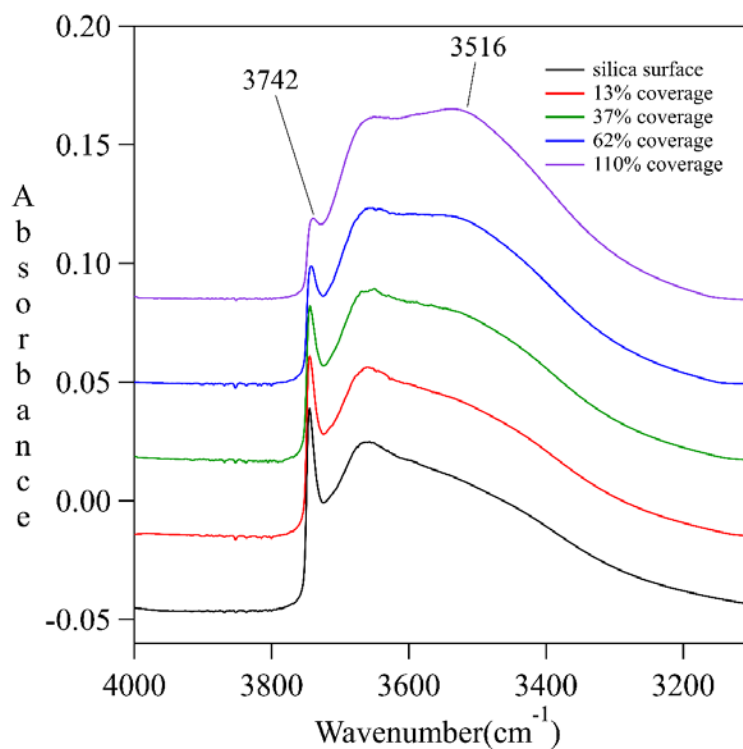


Figure 8.2. Baseline-corrected FTIR spectra displaying the loss of surface hydroxyl groups (at 3742 cm^{-1}) as a function of coverage. The broad band from 3200 to 3700 cm^{-1} , which is assigned to the OH stretching mode of hydrogen bonding, also shifts with increasing coverage.

8.4.1.2 Molecular Dynamics (MD) Results

As shown in Figure 8.3, limonene interaction with silica surface is calculated to be 1 to 2 hydrogens from surface hydroxyl groups interacting with the sp^2 carbons from limonene. The limonene molecule can flip on the surface, as suggested by the chiral carbon (marked as green) points down (Figure 8.3(a)) or points up (Figure 8.3(b)). The limonene sp^2 carbon from the cyclohexene structure is found to be involved in the interaction with the silica surface every time. However, the sp^2 carbon in the tail does not interact with surface hydroxyl groups when the chiral carbon points down, forming one hydrogen bond between adsorbed limonene and the silica surface. When the chiral carbon points up,

limonene forms the second hydrogen bond with the silica surface as the sp^2 carbon in the tail is also involved in hydrogen bonding with silica surfaces.

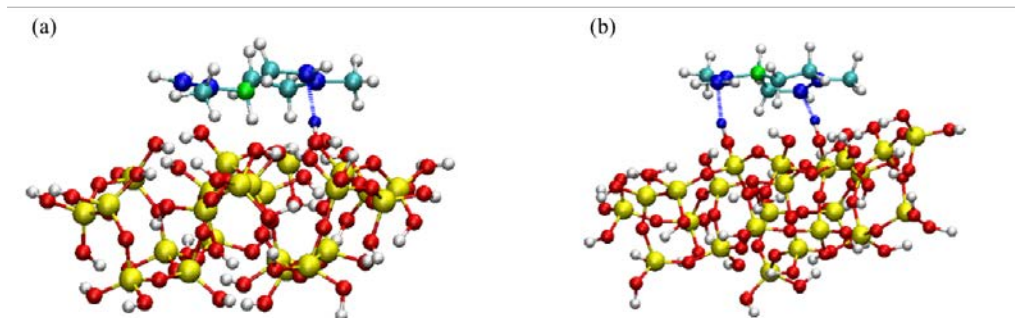


Figure 8.3. Interaction between limonene and hydroxyl groups on the silica surface. (a) Chiral carbon points down, forming 1 hydrogen bond. (b) Chiral carbon points up, forming 2 hydrogen bonds. Si (●), O (●), H (○), non-chiral C (●) and chiral C (●). Dash line (- -) represents hydrogen bonding between limonene and the silica surface. (From Saleh Riahi)

Simulated vibrational frequencies of limonene interacting with silica surface from ab initio molecular dynamics study are shown in Figure 8.4, where (—) represents vibrational frequencies of limonene forming 1 hydrogen bond (HB) with the silica surface, and (---) represents limonene forming 2 hydrogen bonds with the silica surface. Limonene forming 2 hydrogen bonds with the silica surface is expected to have a higher intensity than 1 hydrogen-bonded limonene (as seen in Figure 8.4).

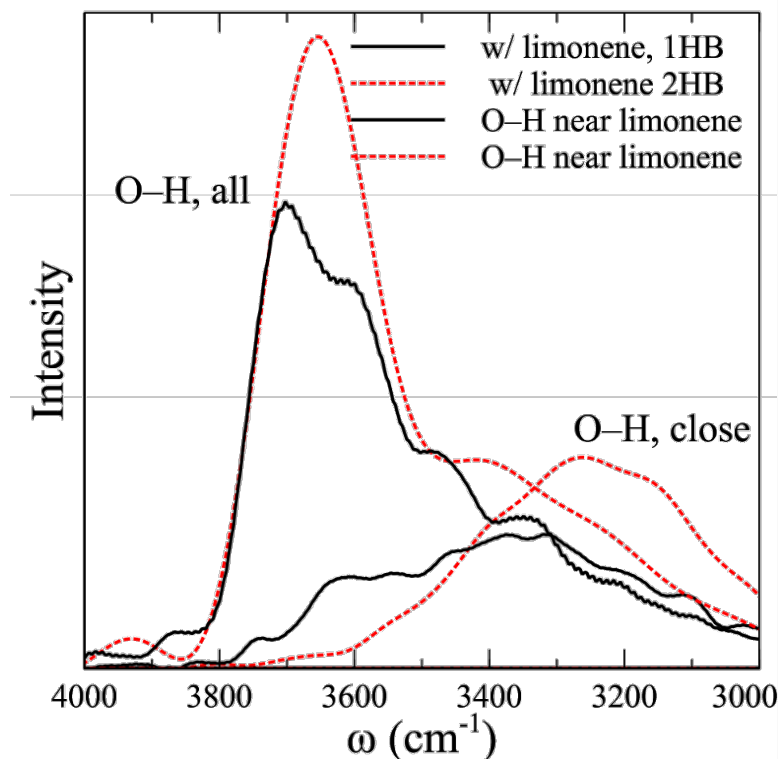


Figure 8.4. Simulated vibrational frequency, ω (cm^{-1}) for the interaction of limonene with surface hydroxyl groups via 1 (—) or 2 (---) hydrogen bonds. (From Saleh Riahi)

8.4.1.3 Peak fitting results

In this study, peak fitting has been applied to FTIR spectral absorption bands from 3000 to 4000 cm^{-1} based on the results obtained from MD simulations (Section 8.3.1.2), to further distinguish the binding mode of adsorbed limonene on the silica surface. As seen in Figure 8.5, there is a good agreement between the fitted experimental and theoretical results. The broad band between 3000 to 4000 cm^{-1} consists of the following assignments: 3742 cm^{-1} (sharp) is due to free surface hydroxyl groups; 3679 cm^{-1} is assigned to surface OH groups; 3710 and 3600 cm^{-1} are due to adsorbed limonene with a single hydrogen bond; 3631 cm^{-1} is due to adsorbed limonene with 2 hydrogen bonds; 3521 and 3375 cm^{-1} result

from the OH groups near adsorbed limonene with a single hydrogen bond; and 3266 cm^{-1} results from the OH groups near adsorbed limonene with 2 hydrogen bonds.

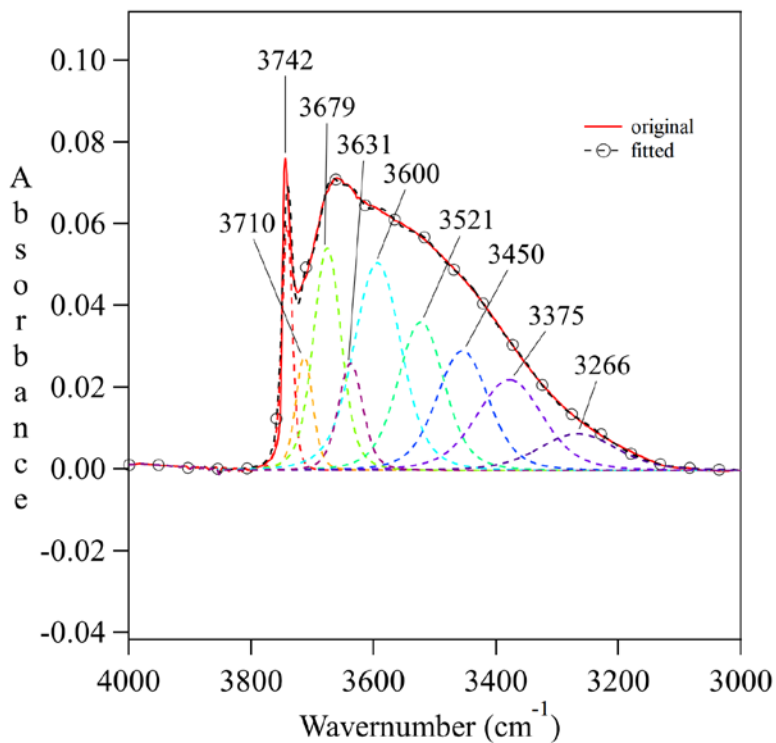


Figure 8.5. Peak fitting results for experimental FTIR spectra in the $3000 - 4000\text{ cm}^{-1}$ spectral region, with 13% of the silica surface covered with limonene (based on theoretical calculated vibrational frequencies and assignments). (—) represents the original experimental spectrum, while (-○-) represents the overall fit. The other dashed lines represent the component bands following peak fitting.

Table 8.2. Vibrational mode assignment for limonene on SiO₂ particle surfaces. (From Saleh Riahi)

Peak Position (cm ⁻¹)	Assignments
3742	Free OH on the surface
3710	with LIM 1HB
3679	Bonded OH on the surface
3631	with LIM 2HB
3600	with LIM 1HB
3521	OH near LIM, 1HB
3450	with LIM
3375	OH near LIM, 1HB
3266	OH near LIM, 2HB

8.4.2 Study of Other Cyclic Compounds on SiO₂ using FTIR and MD

The cyclic compounds, cyclohexane (C₆H₁₂), benzene (C₆H₆) and cyclohexene (C₆H₁₀) were selected to further understand the interactions between limonene with SiO₂ as cyclohexene shares the same key structure as limonene. Cyclohexane is selected as one of the saturated molecules similar to cyclohexene, and benzene is a natural constituent of crude oil which has a cyclic continuous π bond in its ring structure.

8.4.2.1 MD Results

Force field-based MD simulations were used to calculate desorption enthalpies and free energies of limonene as well as cyclic organic compounds such as cyclohexane, benzene and cyclohexene. As shown in Figure 8.6(a), the desorption enthalpy (excluding the entropic contribution to the desorption process) is predicted to be about 14 kcal/mol for limonene and 7 to 10 kcal/mol for benzene, cyclohexene, and cyclohexane. The free energy of desorption of these molecules from the silica surface was predicted by MD simulations, as shown in Figure 8.6(b). The free energy of desorption of limonene from the silica surface

is predicted to be approximately 8 kcal/mol and decreases to ~ 4 - 6 kcal/mol in benzene, cyclohexene and cyclohexane. Both calculated enthalpy and free energy follow the trend of limonene (1 HB > 2HB) > benzene > cyclohexene > cyclohexane, which suggests that limonene forms the strongest interaction with silica surfaces. The interaction between cyclohexane and silica is observed to be the weakest among all organic molecules of interest.

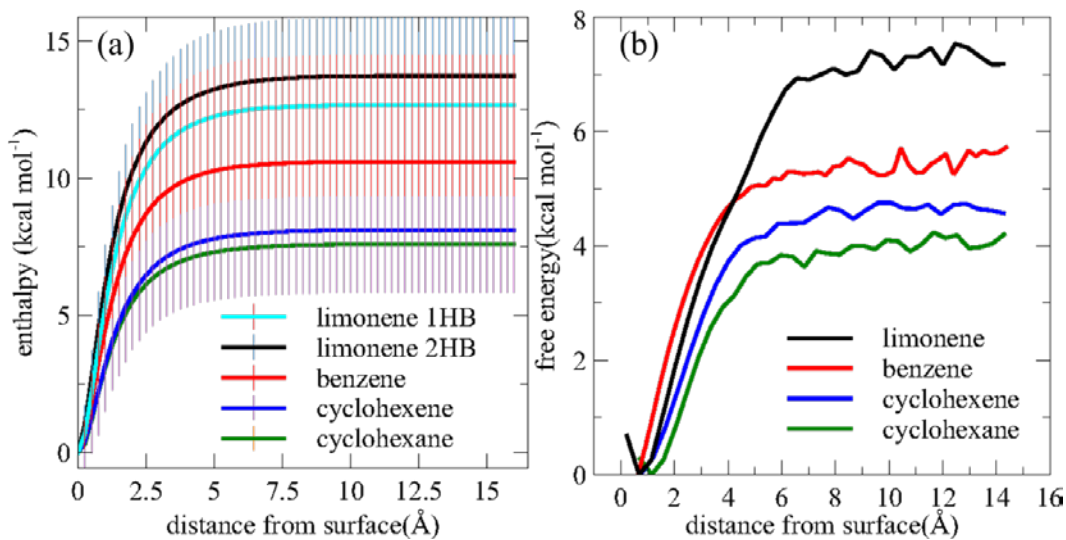


Figure 8.6. Force field MD simulations of (a) enthalpy and (b) free energy of desorption of organic molecules from the silica surface. (From Saleh Riahi)

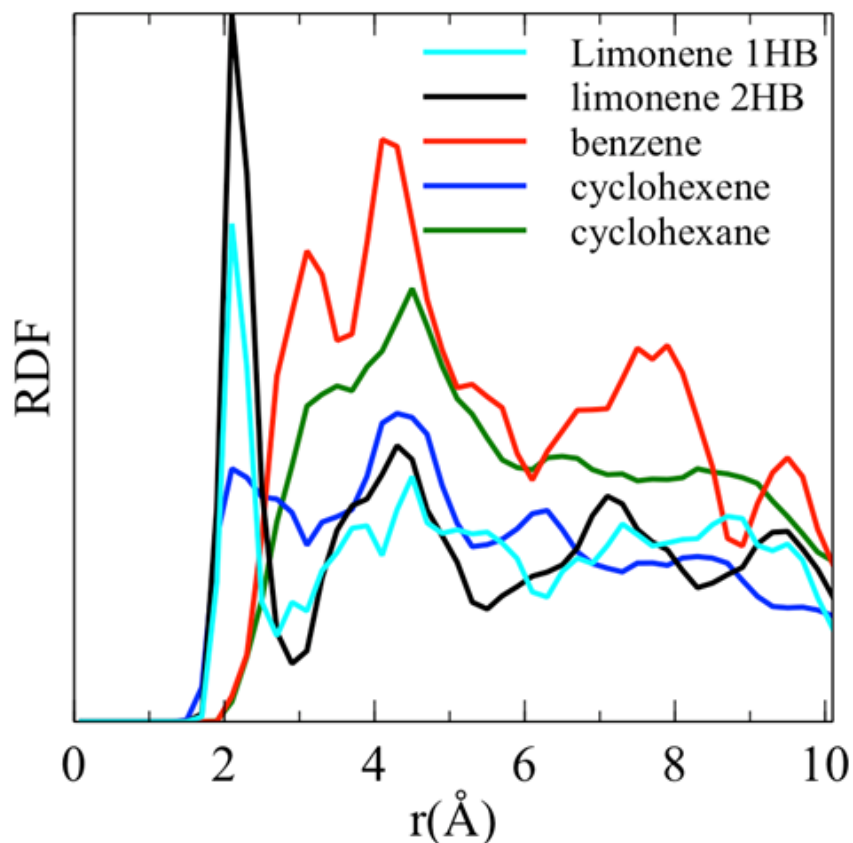


Figure 8.7. Radical distribution functions (RDFs) of hydrogen atoms on the silica surface and the carbon atoms on the organic molecules (benzene (—): center of the ring; limonene (1HB (—) and 2HB (—)) and cyclohexene (—): C=C atoms; cyclohexane (—): all carbon atoms) calculated by ab initio (DFT) MD simulations. (From Saleh Riahi)

Ab initio (DFT) MD simulations were also carried out to calculate the radial distribution function (RDFs) for hydrogen atoms on the silica surface and carbon atoms: C=C atoms from limonene and cyclohexene, all carbon atoms from cyclohexane and ring center for benzene as shown in Figure 8.7. Limonene (1HB and 2HB) appear at the closest distance among all the molecules, suggesting that hydrogen atoms interact the strongest with limonene. Cyclohexene, structurally similar to limonene, appear close to limonene in Figure 8.7 while benzene and cyclohexane peaks appear further, suggesting that the interaction strength of hydrogen atoms follow this trend: limonene > cyclohexene >

benzene > cyclohexane. There is no specific interaction between cyclohexane and silica as shown by the broadband of cyclohexane in Figure 8.7. In addition, limonene (2HB) is more favourable than limonene (1HB) since the intensity of limonene (2HB) is higher than limonene (1HB) at $\sim 2 \text{ \AA}$. A graphical representation of cyclohexane, benzene and cyclohexene on the silica surface is shown in Figure 8.8.

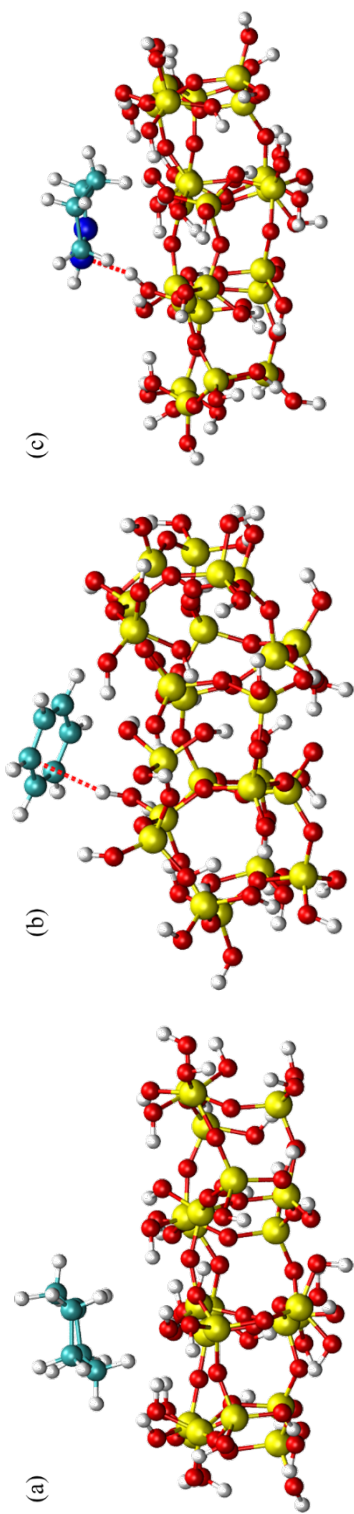


Figure 8.8. Graphical representation of (a) cyclohexane, (b) benzene, and (c) cyclohexene on the silica surface. Si (●), O (●), H (○), C (double bond from cyclohexene, ●) and C (●). Hydrogen bonding between organic molecules and the silica surface is represented by (---). (From Saleh Riahi)

8.4.2.2 Experimental Results

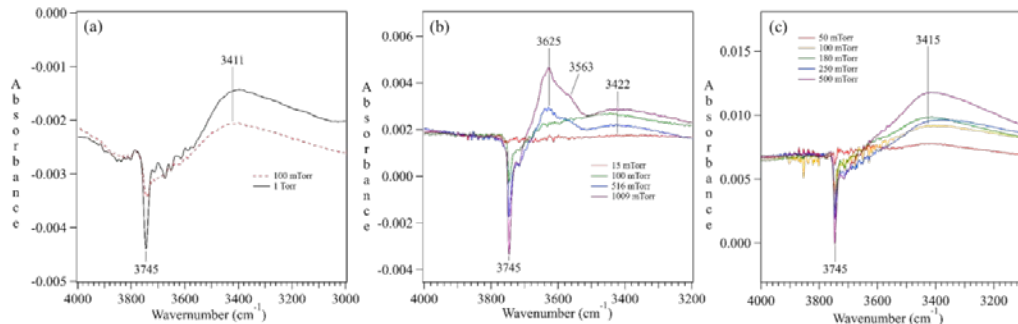


Figure 8.9. FTIR spectra of: (a) cyclohexane (3000 to 4000 cm^{-1}); (b) benzene (3200 to 4000 cm^{-1}); and (c) cyclohexene (3080 to 4000 cm^{-1}). (From Saleh Riahi)

All three cyclic compounds form hydrogen bonds with the silica surface hydroxyl groups. Such an interaction is suggested by the negative peak centered at 3745 cm^{-1} , which is attributed to the loss of surface OH groups as shown in Figure 8.9. Detail peak assignment of gas phase can be found in Table 8.1. Adsorbed surface species appear in very low intensity for these three cyclic compounds. Figure 8.10 shows the normalized loss of the integrated peak area of surface hydroxyl groups as a function of pressure for each cyclic compound. Among the three compounds, the loss of surface hydroxyl groups is smallest when cyclohexane is introduced, indicative that cyclohexane is weakly adsorbed on the silica surface. When benzene is adsorbed on the silica surface, a much larger loss of surface hydroxyl groups is observed, reaching a plateau at $> 100\text{ mTorr}$. This suggests that the interaction between benzene and the surface hydroxyl groups is significantly more favorable in comparison to cyclohexane, which is also in good agreement with MD simulation results. At low pressures ($< 100\text{ mTorr}$), cyclohexene adsorption results in a much smaller loss compared with benzene, suggesting that compared with benzene, less cyclohexene has been adsorbed at low pressures. Thus, the interaction strength of the three

cyclic compounds at lower pressures is assigned as follows: benzene > cyclohexene > cyclohexane. These experimental results are in excellent agreement with theoretical simulations as discussed in Section 8.4.2.1. However, cyclohexene adsorption on the silica surface results in the largest loss of surface hydroxyl groups at very high pressures, indicating that cyclohexene forms more hydrogen bonds with the surface hydroxyl groups than the other two cyclic compounds. Even though this observation differs from theoretical calculations, note that only one molecule was employed in the MD simulations which might not apply to the very high coverage cases here.

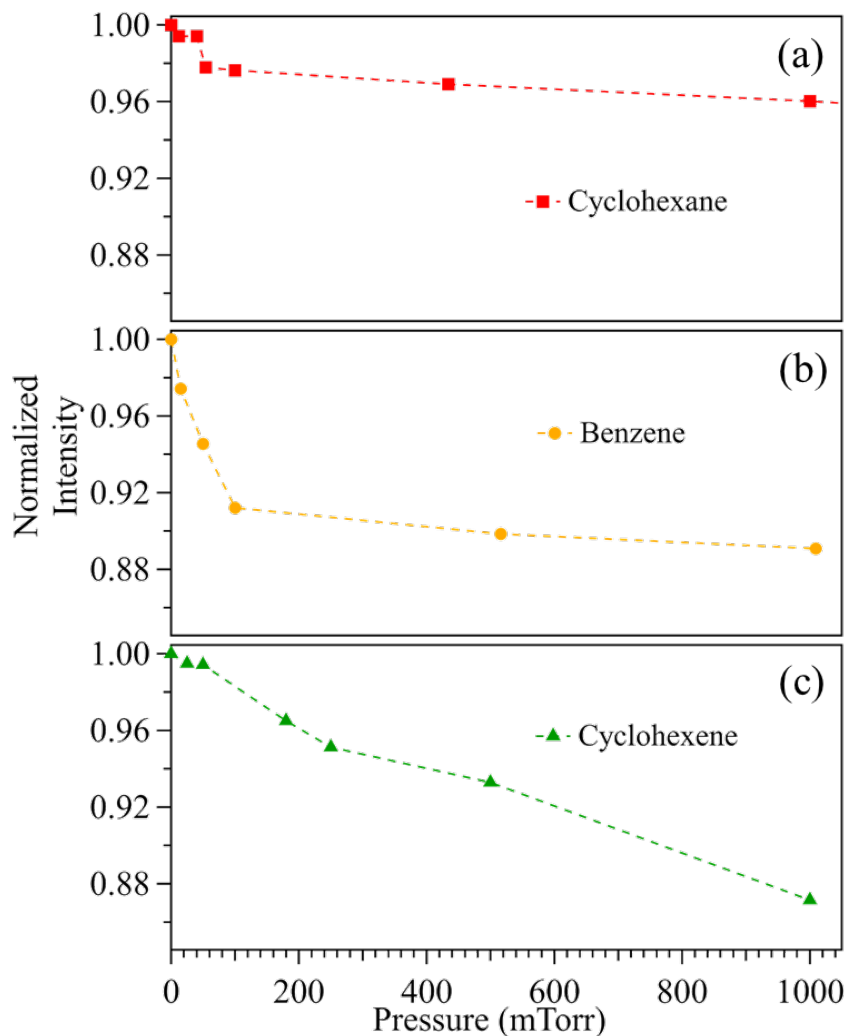


Figure 8.10. Normalized peak area of surface hydroxyl group (integrated using peak centered at 3745 cm⁻¹) loss as a function of pressure for the adsorption of the cyclic molecules of interest on the silica surface: (a) cyclohexane; (b) benzene; and (c) cyclohexene.

8.4.3 Study of Limonene Adsorption Using Flowing System

In addition to performing adsorption studies of vapor phase limonene on SiO₂ surfaces using transmission FTIR spectroscopy, we also conducted these experiments employing ATR-FTIR spectroscopy on surfaces including SiO₂, TiO₂ and gypsum using

the flowing system. This system is more atmospherically relevant than the transmission FTIR setup where the experiments are conducted in vacuum. As shown in Figure 8.11, the adsorption and desorption of limonene vapor on SiO₂ surfaces are found to be comparable using transmission FTIR and ATR-FTIR spectroscopy. Detailed peak assignments can be found in Table 8.3. Thus, it can be concluded that limonene is molecularly adsorbed on SiO₂ surfaces and can be removed upon desorption, which is done by flowing dry air instead of limonene vapor through the IR sample cell under vacuum for ATR-FTIR experiments.

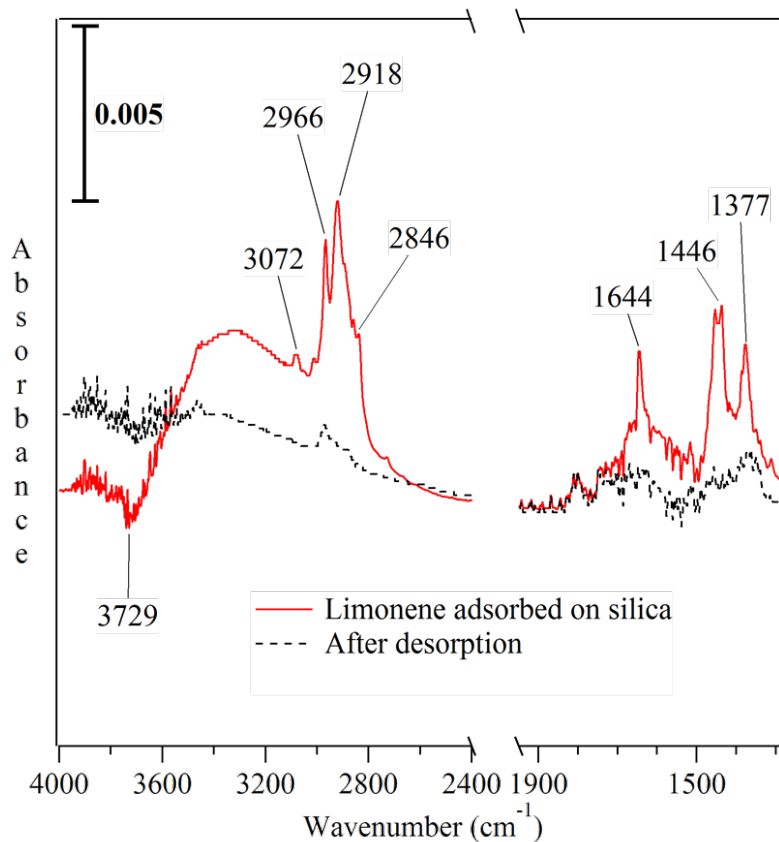


Figure 8.11. ATR-FTIR spectra for limonene adsorption (—) and desorption (---) on SiO₂ in the spectral range of 1280 – 4000 cm⁻¹.

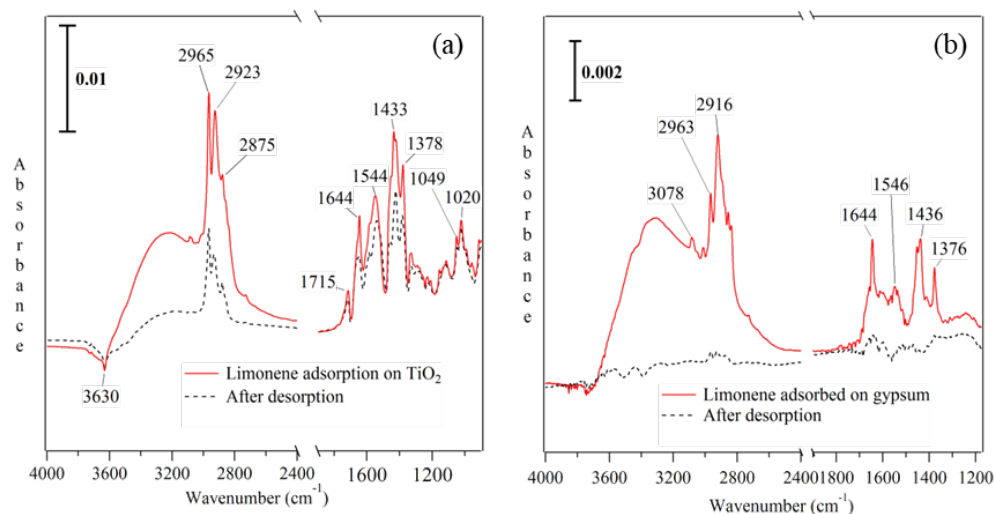


Figure 8.12. ATR-FTIR spectra for limonene adsorption (—) and desorption (---) on (a) TiO_2 and (b) $\text{CaSO}_4 \cdot 2\text{H}_2\text{O}$.

Similar adsorption experiments of limonene were also conducted for TiO_2 and gypsum surfaces. Limonene was flowed through the IR sample cell until the surface was completely saturated. Figure 8.12 (a) shows that when limonene is adsorbed on TiO_2 surfaces, a new peak appears at 1715 cm^{-1} , attributed to the carbonyl stretching vibration from the oxidized adsorbed species such as limonic acid. This assignment was determined by initial mass spectrometry analyses. Desorption spectra show a small decrease in the IR spectral intensity after dry air was flowed through the IR cell for desorption, suggesting that limonene adsorption on TiO_2 is an irreversible process. Adsorption studies of limonene on gypsum also showed limonene to be molecularly adsorbed on the surface (see Figure 8.12(b)). Analogous to SiO_2 surfaces, the adsorption is completely reversible. Detailed peak assignments for limonene adsorption on TiO_2 and $\text{CaSO}_4 \cdot 2\text{H}_2\text{O}$ can be found in Table 8.3. A summary of our adsorption studies of limonene on various surfaces using ATR- FTIR spectroscopy can be found in Table 8.4.

Table 8.3. Vibrational mode assignments for limonene adsorption on SiO₂, TiO₂ and CaSO₄·2H₂O, respectively using the flowing system coupled with ATR-FTIR.

Species	Mode	SiO ₂	TiO ₂	CaSO ₄ ·2H ₂ O
Adsorbed limonene	v(OH) from surface	3729	3630	3729
	v _s (CH, sp ²)	3072	3072	3078
	v(CH, sp ³)	2966, 2918, 2846	2875, 2923, 2965	2963, 2916, 2846
	v(C=C alkene)	1644	1644	1644
	δ(CH ₂ , CH ₃)	1377, 1446	1378, 1433	1376, 1436
	Methyl rocking + v(C-C)	1147	1020	
Oxidized Products	v(C=O)		1715	
	v _{as} (COO)		1544	
	v(C-O)		1049	

Table 8.4. Summary of ATR-FTIR studies of limonene adsorption on various surfaces conducted herein.

Surface	TiO ₂	SiO ₂	Gypsum
<i>Is the process reversible?</i>	Irreversible	Reversible	Reversible
<i>Adsorbed surface species</i>	Molecularly adsorbed limonene and oxidized products (likely limononic acid)	Molecularly adsorbed limonene	Molecularly adsorbed limonene

8.5 Conclusion

Limonene is a common terpene found indoors, and the kinetics of limonene adsorption on silica are well understood (details in Chapter 7). However, the interaction mode between limonene and the surface is poorly understood. In this study, transmission FTIR spectroscopy measurements and molecular dynamic simulation (MD) modeling is

combined to study: the driving force behind hydrophobic molecules (such as limonene); the adsorption on hydrophilic surfaces (SiO_2); and the effect of coverage. Limonene is found to form 1 or 2 hydrogen bonds with surface hydroxyl groups on silica via sp^2 carbons, with the vibrational absorbance bands shifting to lower wavenumbers at higher coverages. Other cyclic molecules, such as cyclohexane, benzene and cyclohexene were studied to further understand the interactions between hydrophobic molecules and hydrophilic surfaces. Limonene, with a cyclohexene structure and an additional $\text{C}=\text{C}$ bond is found to form the strongest interaction among all these four molecules. Benzene is found to be the strongest among the three remaining cyclic molecules due to the interaction between surface hydroxyl groups and π -cloud from the ring structure. The interactions between limonene, as well as the three selected cyclic molecules with silica studied here could help improve our understanding of the interaction of other relevant hydrophobic indoor molecules with hydrophilic surfaces. Adsorption of limonene on different surfaces in a more atmospheric relevant environment suggests that limonene is molecularly adsorbed on some indoor surfaces such as glass (SiO_2) and wall ($\text{CaSO}_4 \cdot 2\text{H}_2\text{O}$). However, on more reactive surfaces, such as TiO_2 , limonene irreversibly adsorbed, forming oxidized products.

8.6 Acknowledgement

This material is based on the work supported by the Alfred P. Sloan Foundation under grant number G-2017-9692. The contents of this study do not necessarily reflect the official views of the Alfred P. Sloan Foundation. The Alfred P. Sloan Foundation does not endorse the purchase of the commercial products used in this report. The dissertation author

was the primary investigator of all experimental measurements and data analysis. The author would like to thank Saleh Riahi for all molecular dynamic simulations. Chapter 8, in full is currently being prepared for submission for publication of the material. Yuan Fang, Saleh Riahi, Mona Shrestha, Andrew McDonald, Douglas J. Tobias, and Vicki H. Grassian. The dissertation author was the primary investigator and author of this material.

8.7 References

- (1) Nazaroff, W. W.; Goldstein, A. H. Indoor Chemistry: Research Opportunities and Challenges. *Indoor Air* **2015**, *25* (4), 357–361.
- (2) Morrison, G. Interfacial Chemistry in Indoor Environments. *Environ. Sci. Technol.* **2008**, *42* (10), 3495–3499.
- (3) Singer, B. C.; Hodgson, A. T.; Hotchi, T.; Ming, K. Y.; Sextro, R. G.; Wood, E. E.; Brown, N. J. Sorption of Organic Gases in Residential Rooms. *Atmos. Environ.* **2007**, *41* (15), 3251–3265.
- (4) Weschler, C. J.; Carslaw, N. Indoor Chemistry. *Environ. Sci. Technol.* **2018**, *52* (5), 2419–2428.
- (5) Nazaroff, W. W.; Weschler, C. J. Cleaning Products and Air Fresheners: Exposure to Primary and Secondary Air Pollutants. *Atmos. Environ.* **2004**, *38* (18), 2841–2865.
- (6) Wainman, T.; Zhang, J.; Weschler, C. J.; Lioy, P. J. Ozone and Limonene in Indoor Air: A Source of Submicron Particle Exposure. *Environ. Health Perspect.* **2000**, *108* (12), 1139–1145.
- (7) Weschler, C. J.; Shields, H. C. Indoor Ozone/Terpene Reactions as a Source of Indoor Particles. *Atmos. Environ.* **1999**, *33* (15), 2301–2312.
- (8) Parida, S. K.; Dash, S.; Patel, S.; Mishra, B. K. Adsorption of Organic Molecules on Silica Surface. *Adv. Colloid Interface Sci.* **2006**, *121* (1–3), 77–110.
- (9) Bandosz, T. J. Analysis of Silica Surface Heterogeneity Using Butane and Butene Adsorption Data. *J. Colloid Interface Sci.* **1997**, *193* (1), 127–131.
- (10) Magnacca, G.; Morterra, C. The Adsorption of C₄ Unsaturated Hydrocarbons on Highly Dehydrated Silica. An IR-Spectroscopic and Thermodynamic Study. *Langmuir* **2005**, *21* (9), 3933–3939.
- (11) Li, Z. H.; Huang, H. G.; Tao, F.; Xu, G. Q.; Dai, Y. J.; Yang, L.; Qiao, M. H. Adsorption of Phenylacetylene on Si(100)-2×1: Reaction Mechanism and Formation of a Styrene-like π -Conjugation System. *Phys. Rev. B - Condens. Matter Mater. Phys.* **2003**, *67* (11), 7.
- (12) Mizukami, M.; Moteki, M.; Kurihara, K. Hydrogen-Bonded Macrocluster Formation of Ethanol on Silica Surfaces in Cyclohexane. *J. Am. Chem. Soc.* **2002**, *124* (43), 12889–12897.
- (13) Liu, D.; Ma, G.; Allen, H. C. Adsorption of 4-Picoline and Piperidine to the Hydrated SiO₂ Surface: Probing the Surface Acidity with Vibrational Sum Frequency Generation Spectroscopy. *Environ. Sci. Technol.* **2005**, *39* (7), 2025–

2032.

- (14) Zhao, Z.-G.; Zhang, L.-H.; Lin, Y. Thermodynamics of Adsorption of Organic Compounds at the Silica Gel/Nonpolar Solvent Interfaces. *J. Colloid Interface Sci.* **1994**, *166* (1), 23–28.
- (15) Kagiya, T.; Sumida, Y.; Tachi, T. Liquid-Phase Adsorption from Binary Solutions on Silica Gel. Separation Factors and Orientation of Adsorbed Components on the Surface. *Bull. Chem. Soc. Jpn.* **1971**, *44* (5), 1219–1223.
- (16) Diaz, L.; Liauw, C. M.; Edge, M.; Allen, N. S.; McMahon, A.; Rhodes, N. Investigation of Factors Affecting the Adsorption of Functional Molecules onto Gel Silicas: 1. Flow Microcalorimetry and Infrared Spectroscopy. *J. Colloid Interface Sci.* **2005**, *287* (2), 379–387.
- (17) Fujishima, A.; Rao, T. N.; Tryk, D. A. Titanium Dioxide Photocatalysis. *J. Photochem. Photobiol. C Photochem. Rev.* **2000**, *1* (1), 1–21.
- (18) Romeas, V.; Pichat, P.; Guillard, C.; Chopin, T.; Lehaut, C. Testing the Efficacy and the Potential Effect on Indoor Air Quality of a Transparent Self-Cleaning TiO₂-Coated Glass through the Degradation of a Fluoranthene Layer. *Ind. Eng. Chem. Res.* **1999**, *38* (10), 3878–3885.
- (19) Paz, Y.; Luo, Z.; Rabenberg, L.; Heller, A. Photooxidative Self-Cleaning Transparent Titanium Dioxide Films on Glass. *J. Mater. Res.* **1995**, *10* (11), 2842–2848.
- (20) Anandan, S.; Narasinga Rao, T.; Sathish, M.; Rangappa, D.; Honma, I.; Miyauchi, M. Superhydrophilic Graphene-Loaded TiO₂ thin Film for Self-Cleaning Applications. *ACS Appl. Mater. Interfaces* **2013**, *5* (1), 207–212.
- (21) Goodman, A. L.; Bernard, E. T.; Grassian, V. H. Spectroscopic Study of Nitric Acid and Water Adsorption on Oxide Particles: Enhanced Nitric Acid Uptake Kinetics in the Presence of Adsorbed Water. *J. Phys. Chem. A* **2001**, *105* (26), 6443–6457.
- (22) Fang, Y.; Tang, M.; Grassian, V. H. Competition between Displacement and Dissociation of a Strong Acid Compared to a Weak Acid Adsorbed on Silica Particle Surfaces: The Role of Adsorbed Water. *J. Phys. Chem. A* **2016**, *120* (23), 4016–4024.
- (23) Schuttlefield, J.; Al-Hosney, H.; Zachariah, A.; Grassian, V. H. Attenuated Total Reflection Fourier Transform Infrared Spectroscopy to Investigate Water Uptake and Phase Transitions in Atmospherically Relevant Particles. *Appl. Spectrosc.* **2007**, *61* (3), 283–292.
- (24) Dows, D. A. Normal Vibrations of Cyclohexane. Infrared Spectrum of the Crystal. *J. Mol. Spectrosc.* **1965**, *16* (2), 302–308.

- (25) Takahashi, H.; Shimanouchi, T.; Fukushima, K.; Miyazawa, T. Infrared Spectrum and Normal Vibrations of Cyclohexane. *J. Mol. Spectrosc.* **1964**, *13* (1–4), 43–56.
- (26) Lehwald, S.; Ibach, H.; Demuth, J. E. Vibration Spectroscopy of Benzene Adsorbed on Pt(111) and Ni(111). *Surf. Sci.* **1978**, *78* (3), 577–590.
- (27) Alcolea Palafox, M. Scaling Factors for the Prediction of Vibrational Spectra. I. Benzene Molecule. *Int. J. Quantum Chem.* **2000**, *77* (3), 661–684.
- (28) Bertolini, J. C.; Rousseau, J. On the Vibrational Electron Energy Loss Spectra of Benzene Chemisorbed on the (111) and (100) Nickel Faces. *Surf. Sci.* **1979**, *89* (1–3), 467–476.
- (29) Mair, R. D.; Hornig, D. F. The Vibrational Spectra of Molecules and Complex Ions in Crystals. II. Benzene. *J. Chem. Phys.* **1949**, *17* (12), 1236–1247.
- (30) Neto, N.; Di Lauro, C.; Castellucci, E.; Califano, S. Vibrational Spectra and Molecular Conformation of Cyclenes—I Vibrational Assignment and Valence Force Field of Cyclohexene and Cyclohexene-D10. *Spectrochim. Acta Part A Mol. Spectrosc.* **1967**, *23* (6), 1763–1774.

CHAPTER 9 CONCLUSION AND FUTURE WORK

This dissertation study focused on understanding the heterogeneous chemistry from both outdoor (mineral dust aerosol particles and atmospheric trace gases) and indoor (indoor relevant gases and indoor model surfaces). Mineral dust aerosol particles can affect the chemical balance of the atmosphere via heterogeneous reactions and the global climate. Understanding heterogeneous reactions between atmospheric trace gases and mineral dust oxide particles is necessary for the development of models for climate predictions. In addition, understanding indoor chemistry is vital because people spend most of their time indoors. Given the fact that indoor environments consist of surfaces which have large surface-to-volume ratios, investigations on heterogeneous interactions between indoor air and indoor surfaces would help improve our understanding of the molecular details of the chemistry occurring indoors, allowing scientists to build an overarching comprehensive indoor chemistry model. The role of water was also studied in these heterogeneous reactions since water vapor is ubiquitous in both outdoor and indoor air and plays a significant role in the heterogeneous reaction chemistry.

In Chapters 3 and 4, heterogeneous reactions of inorganic acids such as HNO_3 and organic acids such as HCOOH , CH_3COOH with silica particles were investigated using transmission FTIR spectroscopy. All three acids are found to be reversibly, physically adsorbed on the silica surface via hydrogen bonding under dry conditions. Even at low acetic acid pressures (< 10 mTorr), where monomers dominate over dimers in the gas phase, acetic acid dimers are found to be the major form for molecularly adsorbed acetic

acid on silica surfaces. The roles of adsorbed water were systematically examined by varying RH at a given partial pressure of acidic gases (HNO_3 , HCOOH and CH_3COOH), as well as by changing the partial pressure of the selected acidic gas at a fixed RH. Water can assist with the dissociation of adsorbed acids on the surface (to hydronium and corresponding anions) as well as compete for surface adsorption sites. Due to the much weaker acidity, the extent of dissociation for a weak acid is observed to be significantly smaller than a strong acid (such as HNO_3). This dissertation study highlights the important and complex roles that RH and surface adsorbed water play in atmospheric heterogeneous reactions of mineral dust particles, as well as the role the surface plays to mediate the configurations of carboxylic acids when adsorbed on the surface.

In Chapter 5, a combination of experimental measurements and theoretical simulations were used to investigate the heterogeneous interactions of pyruvic acid with SiO_2 particles. Pyruvic acid adsorption on the silica surface under dry conditions as well as in the presence of varying RH was studied using transmission FTIR. Theoretical simulations determined the lowest energy binding mode, binding energies and relative vibrational frequencies. Curve fitting has been applied to the experimental vibrational spectra based on calculated vibrational frequencies to further determine the observed species vibrational frequencies. Both pyruvic acid Tc and Tt conformers exist on the surface following adsorption. Even though Tc conformer is more stable because of the intramolecular hydrogen bonding, adsorbed Tc and Tt conformer have a similar binding energy on the surface. The pyruvic acid dimer is also observed on the surface. In the presence of adsorbed water, Tt and Tc conformers bind through a water bridge rather than directly adsorbing on the surface.

In Chapter 6, the studied heterogeneous reactions between pyruvic acid and oxide surfaces using transmission FTIR are discussed. Following adsorption, pyruvate, zymonic acid and other pyruvic acid dimers are observed on both Al_2O_3 and TiO_2 surfaces. HRMS was applied to study the products and mechanisms for pyruvic acid in both light and dark conditions. The production of zymonic acid and its tautomers is found to be an oligomerization process for both light and dark conditions. Parapyruvic acid is found to be a product of photochemical processes. Pyruvic acid photochemistry on surfaces formed various larger products suggested by other compounds such as DMOHA ($\text{C}_7\text{H}_{13}\text{O}_3$), $\text{C}_9\text{H}_{12}\text{O}_6$, and $\text{C}_{12}\text{H}_{14}\text{O}_4$ as detected using MS. By identifying compounds which are not produced from single gas- or aqueous-phase photochemical studies, the complex nature of surface-adsorbed systems is highlighted by this study.

Indoor surface chemistry including indoor air interacting with indoor surfaces is also investigated in this dissertation in Chapters 7 and 8. The detailed chemistry between limonene, a terpene found in the indoor environment which can form secondary organic aerosols by interacting with oxidants, and indoor surfaces such as silica, gypsum and TiO_2 (representing glass, walls and self-cleaning materials respectively) is studied. Transmission FTIR, kinetics modeling and dynamic simulations were used to study the kinetics of limonene adsorption/desorption processes under dry conditions. Adsorption of limonene on the silica surface is a reversible, physical process via 1 to 2 hydrogen bonds between limonene sp^2 carbon and silica surface hydroxyl groups. The kinetic model built here and the developed methods could be applied to study other relevant indoor organic vapors (i.e., dihydromyrcenol) and surfaces. Although limonene adsorption is found to be a reversible process on silica, an oxidized product of limonene has been detected in this study in the

presence of water on the silica surface, leading to a much slower reversible/partially reversible process. Interactions between limonene and indoor surfaces such as SiO₂, TiO₂ and gypsum were also studied under more atmospheric relevant conditions using a flowing system coupled with ATR-FTIR. Adsorption of limonene on SiO₂ and gypsum is found to be a reversible process while on more reactive surfaces, such as TiO₂, limonene irreversibly adsorbs, forming oxidized products. The interaction mode between a hydrophilic surface, such as silica with hydrophobic compounds of indoor relevance, such as limonene (as well as other cyclic compounds including: cyclohexane, benzene and cyclohexene) is studied using a combination of transmission FTIR spectroscopy and molecular dynamic simulations. The driving force between these compounds with silica surfaces was investigated. With a cyclohexene structure and an additional C=C bond, limonene is found to form the strongest interaction among the four molecules. The interactions between limonene, as well as the three selected cyclic molecules with silica studied here could help improve our understanding of the interaction of other relevant hydrophobic indoor molecules with hydrophilic surfaces.

In conclusion, this dissertation research provides an important contribution to the understanding of the heterogeneous chemical and photochemical reactions between: (i) atmospheric trace gases and mineral dust oxide surfaces; and (ii) indoor relevant gases with indoor surfaces. Combining vibrational spectroscopy measurements and molecular dynamic simulations provides a better understanding of the interactions between gaseous molecules and surfaces. A kinetics model has been developed to study the adsorption of limonene (an organic gas relevant indoors), on silica (an indoor modeling surface) using the combination of spectroscopy measurements, kinetics modeling and molecular dynamic

simulations and can be further applied to study the adsorption/desorption kinetics of other indoor gases on indoor surfaces.

However, there remain several areas that require further investigation to fully understand the heterogeneous and photochemical processes occurring in both outdoor and indoor environments, as well as their impacts. Future work and directions include:

1. Conducting laboratory studies under atmospherically relevant partial gas phase pressure and relative humidity conditions in the presence of O_2/O_3 and solar irradiation;
2. Using the method developed in this study to build kinetics models for the adsorption/desorption of other gases of indoor relevance on indoor (modelled) surfaces under dry conditions;
3. Investigating the kinetics of adsorption/desorption of different gases of indoor relevance from the surface in the presence of adsorbed water to understand the role of water in kinetics modeling and build a kinetics model at wet surfaces;
4. Further investigation of the interaction of limonene with silica and other indoor modeling surfaces at varying RHs is crucial to determine the oxidation products in the absence/presence of oxidants such as O_2 and O_3 ; and
5. Combining experimental measurements, field measurements as well as computer models of the principal chemical and physical processes to quantitatively understand indoor chemistry.

Further investigation in these areas will elevate our understanding of both Earth's atmosphere and indoor air.